(NASA-TM-86247) ADVANCES IN PLANETARY
GEOLOGY (National Aeronautics and Space
Administration) 421 p HC A18/MF A01
CSCL 03B
G3/91

N84-25567
THRU
N84-25582
Unclas
19314

NASA TM-86247

Advances in Planetary Geology

NASA Scientific and Technical Information Branch 1984
National Aeronautics and Space Administration
Washington, DC

FOREWORD

This document is a compilation of reports from Principal Investigators and their Associates of NASA's Office of Space Science and Applications, Solar System Exploration Division, Planetary Geology Program. The reports present research that adds to our knowledge of the origin and evolution of the solar system and to our understanding of the earth as a planet. Advances in Planetary Geology was established as a complement to the abstract document "Reports of Planetary Geology Program" and to professional journals. This document provides a method of publishing research results which are in a form that would not normally be published elsewhere. The research reports may be in the form of lengthy research reports, progress reports, Ph.D. dissertations, or master's theses.

Joseph M. Boyce
Discipline Scientist
Planetary Geology and Geophysics Program
Office of Space Science and Applications

PRECEDING PAGE BLANK NOT FILMED

CONTENTS

Page

SECTION I:

THE CRUSTAL TECTONICS AND HISTORY OF EUROPA: A STRUCTURAL, MORPHOLOGICAL, AND COMPARATIVE ANALYSIS 3
Paul M. Schenk

SECTION II:

REPORTS OF THE "PLANETARY GEOLOGY INTERN PROGRAM" 113

Analysis of Permafrost Depths on Mars 115
Gennaro H. Crescenti

Spectral Analysis of Groove Spacing on Ganymede 133
Robert E. Grimm

Stratigraphy of the Crater Copernicus 136
Rita Paquette

Geologic Observations of the Martian Highland Boundary in the Mamers Valles Region 149
James H. Persky

The Source of Mangalla Vales 152
Gerchard Edmund Pfau and R. Stevens Saunders

Spatial Distribution of Craters on the Moon and Callisto 157
Alex Ruzicka and R. G. Strom

Callisto: A Lunar-Like Bombardment? 160
Alex Ruzicka

L Chondrite Meteorites: A Compilation and Preliminary Analyses 167
Alan Silliman

The Crater Density of a Linear Feature 172
Lawrence Spong

Nitrogen Threshold Experiment 180
Cheryl L. Treat

The Geology of Thaumasia-Northeast Quadrant 205
Marlene F. Tuesink

Planet-Crossing Asteroid Survey 208
Peter D. Wilder

Preliminary Results of Albedo Correlation Between Europa and Ganymede 212
Sandra E. Yuter

SECTION III:

THE GEOLOGY OF MARE ACIDALIUM QUADRANGLE MARS 219
Nanci E. Witbeck

PRECEDING PAGE BLANK NOT FILMED

To Contributors:

A wider variety of manuscripts can be accommodated by Advances in Planetary Geology than by most journals. Particularly appropriate are completed theses, dissertations, and research reports reliant on extensive presentations of supporting data. All contributions must be of direct interest to planetary geologists and must be of high scientific quality. Manuscripts must be typed, preferably single spaced, in a camera-ready format. Inquiries concerning contributions as well as submissions of contributions should be made to:

Dr. Alex Woronow
Geosciences Department
University of Houston, University Park
Houston, TX 77004

PRECEDING PAGE BLANK NOT FILMED

SECTION I

N84 25568

NORTHERN ILLINOIS UNIVERSITY

THE CRUSTAL TECTONICS AND HISTORY OF EUROPA: A STRUCTURAL, MORPHOLOGICAL, AND COMPARATIVE ANALYSIS

A THESIS SUBMITTED TO THE GRADUATE SCHOOL
IN PARTIAL FULFILLMENT OF THE REQUIREMENTS
FOR THE DEGREE
MASTER OF SCIENCE

DEPARTMENT OF GEOLOGY

BY

PAUL M. SCHENK

DEKALB, ILLINOIS

MAY 1983

PRECEDING PAGE BLANK NOT FILMED

ACKNOWLEDGEMENTS

I would like to thank Leslie Pieri and Andy Collins of the Jet Propulsion Lab, Pasadena, for their assistance; Dr. Clarence Casella, Dr. Carl Seyfert and Drs. C. Montgomery and J. Clements for helpful comments and review; and Leslie and Alice M. Schenk for their contributions.

TABLE OF CONTENTS

Page

ACKNOWLEDGEMENTS 4

LIST OF TABLES 7

LIST OF ILLUSTRATIONS 8

CHAPTER I: INTRODUCTION 12

1.1 Statement of Intent and Purpose 12

1.2 The Data Set 15

1.3 Pre-Voyager Work 23

1.4 Global Morphology 27

1.5 Europa in the Galilean System 29

CHAPTER II: LINEAMENT TYPES AND FRACTURE PATTERNS 31

2.1 Introduction 31

2.2 Simple Lineaments 31

2.3 Wedge-shaped Bands 36

2.4 Triple Bands 46

2.5 Bright Bands 52

2.6 Ridges 56

2.7 Gray Bands 62

2.8 Bright Lineaments 63

2.9 Fracturing Mechanisms and Origins 64

Page

CHAPTER III: TERRAIN TYPES AND DISTRIBUTIONS 69

3.1 Introduction 69

3.2 Plains 69

3.3 Brown Spots 71

3.4 Mottled Terrain 72

3.5 Minor Terrain Units 73

3.6 Terrain Origin 75

CHAPTER IV: COMPARISONS AND ANALOGS 79

4.1 Sea Ice 79

4.2 Lava Lakes 82

4.3 Ganymede vs. Europa 86

CHAPTER V: DISCUSSION AND CONCLUSIONS 89

5.1 Crustal Models 89

5.2 Origin and Evolution of Europa's Surface 92

5.3 Conclusions 96

References Cited 100

LIST OF TABLES

Page

Table 1.1 Galilean Satellites - Physical Properties 13

1.2 Galilean Satellites - Orbital Properties 14

1.3 Voyager Images Used For This Study 17

2.1 Lineament Classifications 32

LIST OF ILLUSTRATIONS

(Plates 1-6 are in pocket)

Plate 1 Europa - Simple Lineaments

2 Europa - Wedge-shaped Bands

3 Europa - Triple Bands

4 Europa - Bright Bands, Bright Lineaments and Gray Bands

5 Europa - Ridges

6 Europa - Terrain Units

Page

Figure 1.1 Europa from Voyager 2 18

1.2 High-resolution Mosaic of Europa from Voyager 2 . . . 19

1.3 Geometrically Registered Mosaic of Europa 20

1.4 High-resolution Mosaic of Europa from Voyager 2 . . . 22

2.1 Mosaic Showing Simple Lineaments 33

2.2 Histograms of Lineament Trends 35

2.3 Mosaic Showing Wedge-shaped Bands 37

2.4 Reconstruction of Wedge-shaped Bands 38

2.5 Schematic Diagrams of Wedge-shaped Bands and Triple Bands 39

2.6 Wedge-shaped Bands Fracture Zone 44

2.7 Histograms of a) Wedge-shaped Bands and Simple Lineaments and b) Wedge-shaped Bands, Simple Lineaments, Linear Ridges and Triple Bands . . . 47

2.8 Mosaic Showing Triple Bands 49

2.9 Mosaic Showing the Bright Band Agenor Linea 53

Page

Figure 2.10 Mosaic Showing Ridges (dominantly cycloidal) 57

2.11 Stereo Pair of Simple Lineaments and Ridges Near the Terminator 59

3.1 Stereo Pair of Region North-northeast of Thrace Macula 74

4.1 Selected Photographs of Terrestrial Arctic Sea Ice 80

4.2 Alae Lava Lake, Hawaii, during 1963 Eruption 83

4.3 Solidified Crack in a Kilauea Lava Flow 85

4.4 Antarctic Ice Sheet, Vicinity of Ross Sea and the Transantarctic Mtns. 87

5.1 Comparison of Models of Europa's Interior 90

ABSTRACT

Lineament and terrain patterns on the ice-covered Galilean satellite Europa were studied with the aid of enhanced Voyager 2 images and mosaics. New mercator maps of Europa were made from rectified images. Several questions raised by previous studies of Europa were addressed. These included: Are thin-ice or thick-ice crustal models valid? Was there ever liquid water on Europa? Was there plate tectonics on Europa?

Simple lineaments, narrow, dark linear markings, are interpreted as filled crustal fractures. These appear to be the oldest and most abundant lineaments. Several other lineament types may be related to these. Wedge-shaped bands are similar but wider. Offset of older simple lineaments has been associated with the opening of several wedge-shaped bands, indicating the rotation of crustal blocks. These bands occur in a broad belt that appears to be a major fracture zone in Europa's crust, for which a pole of rotation has been determined. Triple bands are more enigmatic but, as they are often associated with simple lineaments, probably evolved from them. Linear ridges are found near the terminator where they are highlighted by low sun angles. In earlier images they show as simple lineaments. Cycloid ridges occur in southern regions and are interpreted as compressional features. Terrain units include: plains, brown spots and brown mottled terrain. Plains are smooth but frac-

tured. Mottled terrain can be locally resolved into coalesced brown spots. This terrain may represent icy flows onto the plains, but this cannot be confirmed.

The fracture style in Europa's crust mimics that of terrestrial sea ice, suggesting that Europa's icy crust was relatively thin and underlain by a liquid water layer during fracturing. Lava lake crusts display similar features. Histograms of lineament trends show a simple, orthogonal pattern, suggesting structural control. Fracturing may have been linked to the creation of the present orbital resonance locks and increased tidal flexing or thermal fracturing of the floating icy crust or to an internal volume increase. A type of plate tectonics may have occurred in the opening of the wedge-shaped bands. This may be evidence that a convection cell operated beneath the wedge-shaped band fracture zone.

CHAPTER I: INTRODUCTION

1.1 Statement of Intent and Purpose

Europa is the second outward of the four Galilean satellites of Jupiter. It is the smallest of these, but it is also the brightest, whitest, smoothest, and has the highest surface water-ice content (Smith et al., 1979b). See Table 1.1. It is believed to be covered by an icy layer 10-100 km thick. Because of these unusual properties, study of Europa's geology could provide valuable insights into the behavior of water ice on a global scale.

The intent of this study is to make as thorough as feasible an evaluation of surface features and structures on the Galilean moon Europa using the available high resolution Voyager imagery, low resolution support imaging, and what understanding of ice structure and mechanical behavior science has that is applicable to the problem. A general discussion of the history of Europa studies and the fundamental global morphology is undertaken. The visible lineament and terrain patterns will be described, and possible origins will be discussed. Observations of faulting and block rotation previously described by Schenk and Seyfert (1980) will be amplified. A comparison of Europa's structures to terrestrial sea ice and lava lake crust features is also included. Finally, an attempt is made at synthesizing a unified model for the evolution of Europa's crust, which is to be compared with models

Table 1.1

Galilean Satellites - Physical Properties*

	Radius (km)	Mass (moon=1)	Density (g/cc)	Albedo	Water content (wt. %) bulk	Water content (wt. %) surface	Maximum surface temp. (° K)	Best Voyager resolution (km/lp)
Io	1820	1.21	3.53	0.63	0	0	125–130 (290)**	< 1
Europa	1565	0.66	3.03	0.64	~10	> 95	125	~4
Ganymede	2640	2.03	1.93	0.43	40–50	80–90	145	~1
Callisto	2420	1.45	1.79	0.17	50–60	30–90	155	~2
Moon	1738	.1.00	3.34	0.12	0	0	395	-
Earth	6371	81.30	5.52	0.39	< 1	71	320	-
Mercury	2432	4.36	5.42	0.12	0?	0?	700	~0.25 (Mariner 10)

*Radii and densities for the Galilean moons are from Smith et al. (1979a), surface temperatures from Hanal et al. (1979), surface water content from Clark (1980).
**Volcanic hotspot temperature (Hanal et al., 1979).

Table 1.2 Galilean Satellites - Orbital Properties

	Semi-major axis*	Orbital period (days)	Forced eccentricity**	Inclination (degrees)
Io	5.90 R_j	1.77	0.0041	0.027
Europa	9.40 R_j	3.55	0.0101	0.468
Ganymede	14.99 R_j	7.16	0.0006	0.183
Callisto	26.33 R_j	16.69	?	0.253
Moon	60.34 R_e	27.32	0.0549	6.68

*R_j = 71,396 km (one Jovian radius); R_e = 6,371 km (one Earth radius).

**Yoder (1979).

developed by others.

A critical limitation of this, and of all Europa studies, is the insufficient resolving power of the highest quality imaging, as explained below. As a result, the following discussions will be of a somewhat conjectural nature, and caveats will be repeated where this problem is severe. Nevertheless, certain features are imaged clearly enough for there to be little doubt as to their proper interpretation. Certain other features are suggestive enough to warrant additional speculation. Discussions are also hampered by the limited high-resolution photographic coverage, which is restricted to approximately 20% of the surface. This limits the ability to extrapolate observations to possible global processes. Mercator-projected images were obtained in order to construct detailed maps of the structures within this high-resolution area (Plates 1-6).

Some of the overriding questions that will be addressed in this study include: does the surface geology of Europa support thin-ice or thick-ice crustal models? Did liquid water ever exist in significant amounts beneath the icy crust? What type of dynamic processes are/were modifying the surface, i.e., are there plate tectonics on Europa? A tentative geologic history will be outlined and discussed.

1.2 The Data Set

The primary data set for this study included a series of images recorded by the Voyager II spacecraft as it approached and passed Europa on July 8-9, 1979 (Table 1.3). Each image consists of 800 x 800 pixels, or picture elements. At closest approach, approximately 208,000 km, each pixel, at the sub-spacecraft point, corresponds to a surface distance of ~2 km. Best resolution is often quoted as 4 km per (pixel) line pair (km/lp), which is the effective limit to which linear or structural features can be resolved. Distortions in the scale and geometry increase as the limb of the planet is approached. Although mercator projections of images can eliminate geometric distortions, scale distortions of these images are permanent. The resolution limit and areal imaging coverage for Europa are the poorest for any of the Galilean satellites.

The images used for this study include one medium-range global image with resolution of ~12 km/lp, taken July 8, 1979 (Fig. 1.1), and two close-range global mosaics, with a set of repeated east-west scans for support imaging of ultraviolet spectrometer (UVS) observations between. The first mosaic (Fig. 1.2; 1.3), using four filters for color coverage, consists of 20 narrow angle camera frames covering the quarter-phase disk. Resolution approached 4 km/lp. The area covered extends from 130 to 210° W longitude, and from 75° N to 90° S latitude. Reliable morphological information is restricted to a zone within ~10 degrees of the terminator. Beyond this, as the solar incidence angle decreases, albedo variations become prominent as topographic highlighting and shadowing effects diminish.

Table 1.3 Voyager Images Used For This Study

Picture number	FDS count	Range ($\times 10^3$ km)	Filter	Figure number
1549J2-002	20625.16	1242.67	Violet	1.1
1183J2-001*	20649.10	245.80	Violet	1.2
1198J2-001*	20649.25	241.48	Blue	1.2
1207J2-001*	20649.34	238.74	Violet	1.2
1231J2-001	20649.58	232.54	Violet	1.2
80/02/07/180218**	20650.01	231.83	Blue	1.2
1255J2-001	20650.22	226.69	Clear	1.4
1279J2-001	20650.46	222.81	Clear	1.4
1348J2-001	20651.55	211.96	Clear	1.4
1352J2-001	20651.59	210.77	Clear	1.4
1356J2-001	20652.03	211.05	Clear	1.4
1364J2-001	20652.11	209.10	Clear	1.4
1368J2-001	20652.15	208.35	Clear	1.4
1372J2-001	20652.19	208.53	Clear	1.4

*Mercator projected versions of these images were also used.
**Mercator version only used for this study.

ORIGINAL PAGE IS
OF POOR QUALITY

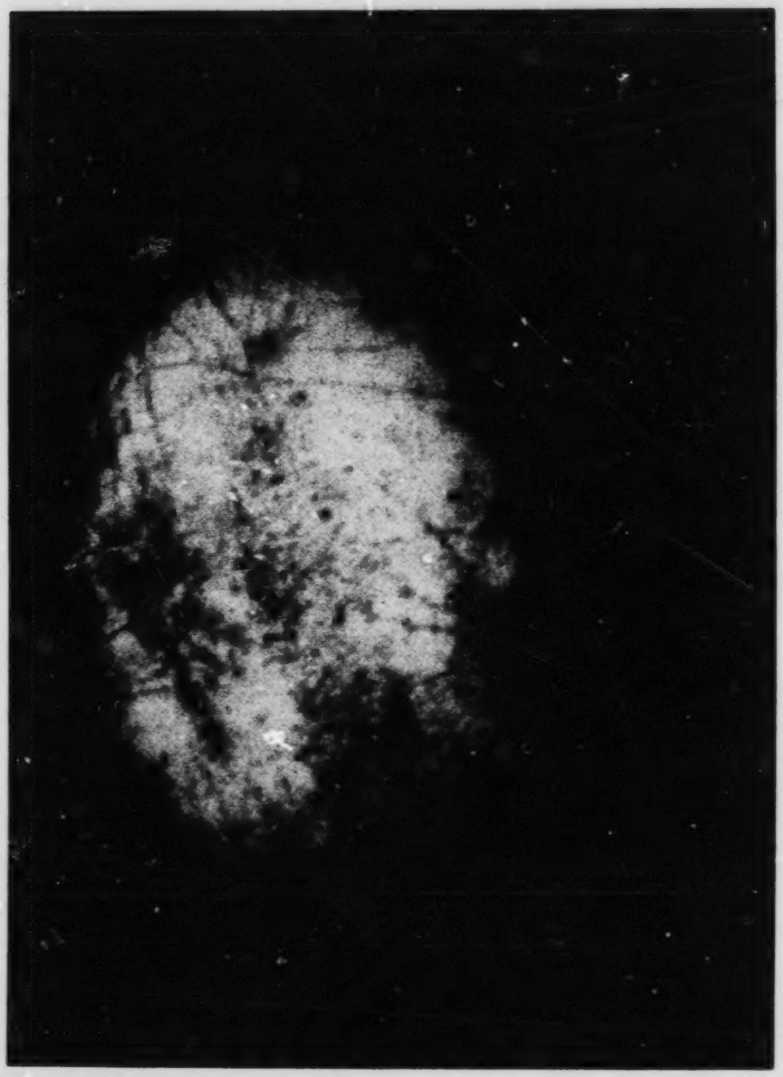

Fig. 1.1 Europa from Voyager 2. Image taken through blue filter July 8, 1979. Area of high-resolution mosaics (Figs. 1.2-1.4) is along western limb; north is up.

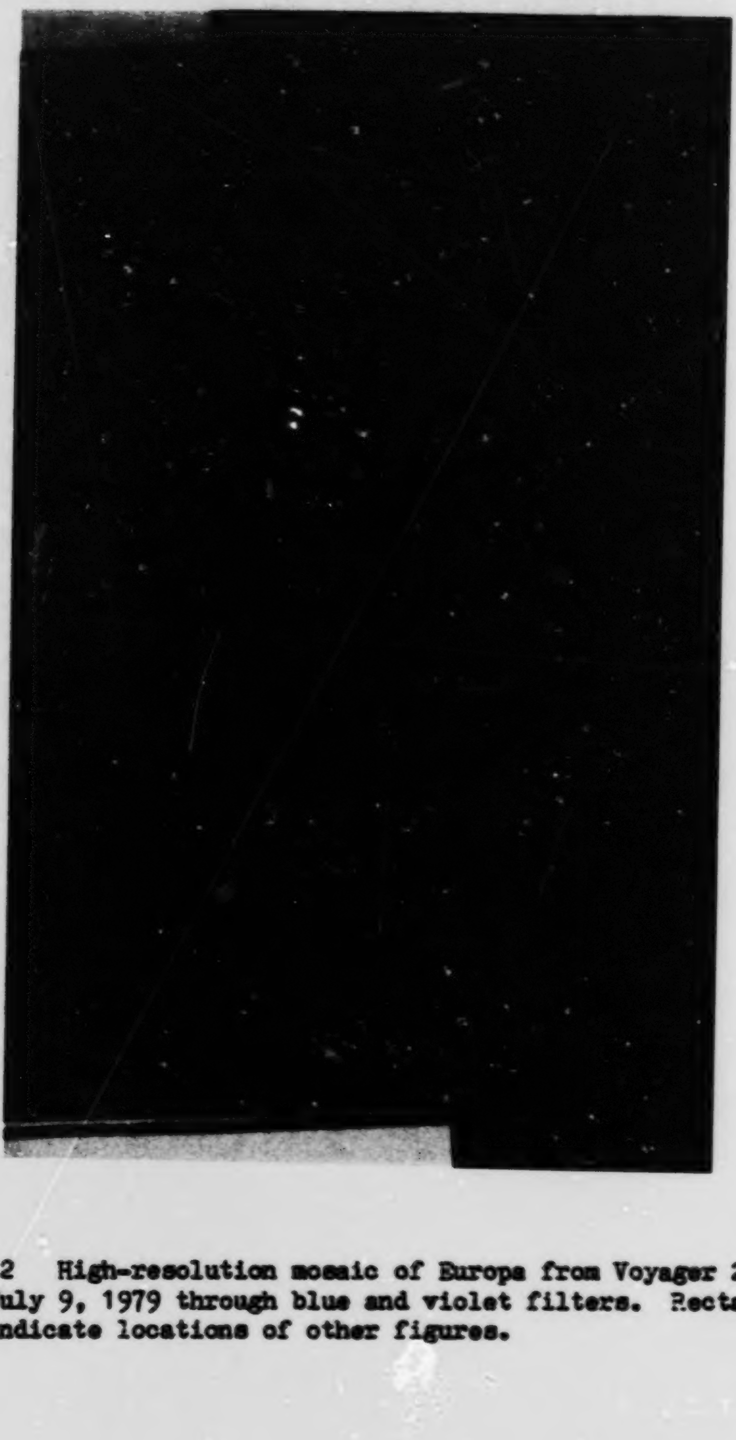

Fig. 1.2 High-resolution mosaic of Europa from Voyager 2. Images taken July 9, 1979 through blue and violet filters. Rectangular areas indicate locations of other figures.

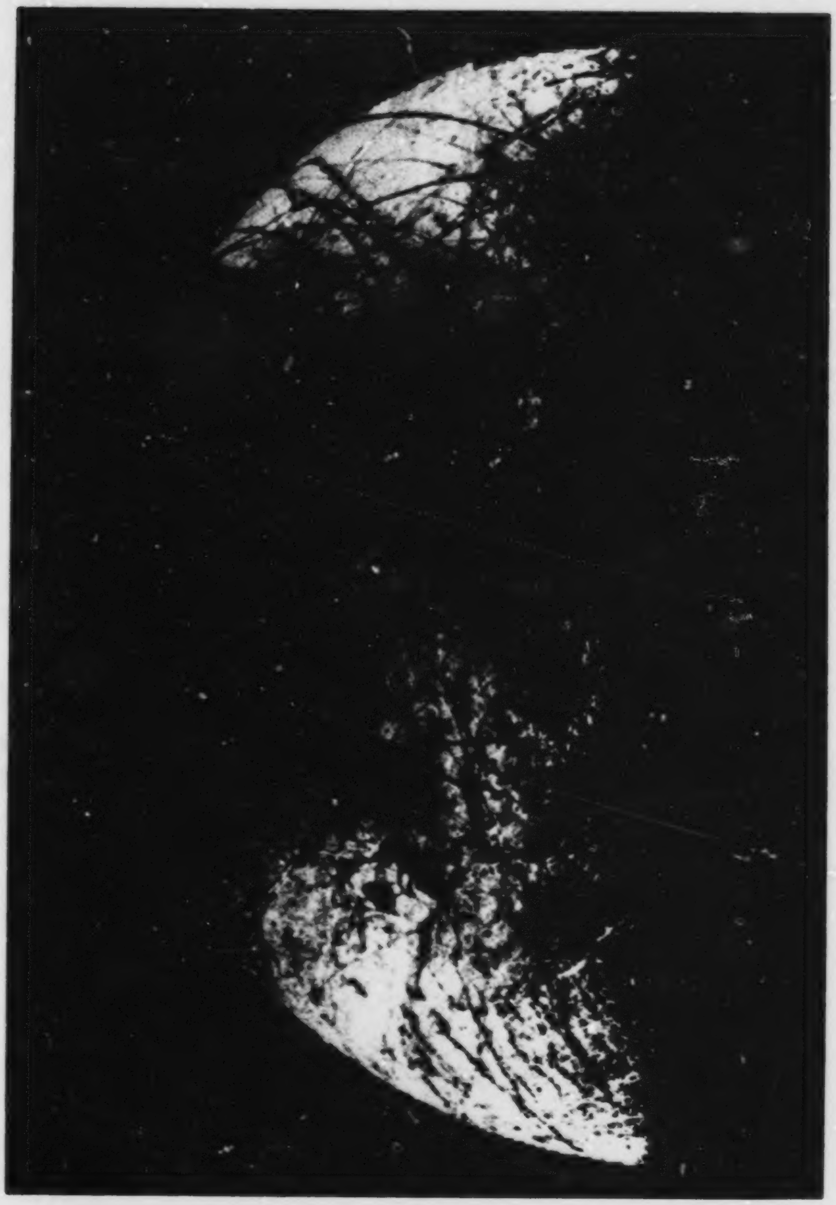

Fig. 1.3 Geometrically registered mosaic of Europa. Images taken July 9, 1979 through blue filter.

The second mosaic (Fig. 1.4) was taken about 6 hrs. after the start of the first. Taken through clear filters, it consisted of 18 alternating narrow and wide angle camera images, and was executed shortly after closest approach. The terminator had advanced 15 degrees west, transforming the disk into a distinct crescent. Resolution was just under 4 km/lp.

Approximately 20% of the surface was imaged at high resolution. This area includes the anti-jove point, and corresponds roughly with the area of mapping for this project. The mercator maps of this area (Plates 1-6) were produced by assembly of mercator-projected images (Table 1.3) and use of mylar overlays. The coordinate grid employed was developed by the author using control points determined by Davies and Katayama (1981). Feature locations on the maps are estimated to be accurate to within 20 km.

The maps (Plates 1-6) were constructed on mercator projections because suitable images were available, and because mercator projection allows convenient trend determinations (see below). These maps are useful in that they allow easily comprehensible presentation of lineament orientation and distribution patterns and also comparison among the lineament types and terrains.

Histograms of lineament trends were constructed from the mercator maps. Trends were measured over entire lineament lengths and were summed over 10 degree azimuth intervals. Histograms cover the entire mapped area.

During the summer of 1981, I had access to the Voyager project

Fig. 1.4 High-resolution mosaic of Europa from Voyager 2. Images taken July 9, 1979 through clear filter. These images were part of the second imaging mosaic.

interactive computers. The Europa images were put on tape and examined, contrast enhanced and enlargements of up to 8x made and copied. These frames were very useful in mapping. Voyager photo and figure numbers are listed in Table 1.3.

In addition to the photographic data, a significant amount of Earth-based information about Europa that is relevant to this study is in the literature and is reviewed below. The bulk physical properties of Europa have been summarized in Tables 1.1 and 1.2.

1.3 Pre-Voyager Work

Prior to Voyager, data on the Galilean moons were limited to Earth-based telescopic observations, and crudely known bulk physical characteristics. The first significant advancement in the study of Europa came with the spectroscopic confirmation of abundant water frost on Europa's surface by Pilcher et al. (1972). Subsequent observations refined the data and led to the conclusion that Europa's surface is composed of 95 to 100% water ice and frost (Clark and McCord, 1980), a conclusion consistent with Europa's high albedo (see Table 1.1).

Clark (1980) suggested that the shapes of 1-2 micrometer spectral bands are consistent with a medium to fine-grained frost and/or frost-on-ice surface, based on comparison with laboratory spectra of various frost and ice samples (see Table 1 in Clark, 1980). Near-infrared spectroscopy by Clark and McCord (1980) indicated that the water absorption features are due to free water, not bound.

Clark (1980) suggested that non-ice surface impurities (only a few weight percent for Europa) were imbedded in and mixed with the ice. Weak absorption bands at 0.8-0.9 micrometers may be due to silicate materials (Clark, 1980). The non-icy components of Europa's spectra have some similarities to Ganymede's spectra, and the near-infrared spectra of Io and Ganymede have distinct similarities (Clark, 1980). This might suggest that the rocky components of the Galilean moons are similar, and that some sulfur or salt components (both reported on Io) might also be found on Europa. Unfortunately, no reliable compositional information on the darker surface component is available. See Clark (1980) for a more complete discussion.

Earth-based studies have also shown that Europa's trailing hemisphere (Europa is in synchronous rotation) is redder than the leading hemisphere (McFadden, Bell and McCord, 1980), and that it has bright polar 'caps' (Murray, 1975). Radar measurements have been made (Ostro et al., 1980) but reveal information only about the upper few centimeters of the surface.

Pollack and Reynolds (1974) modeled thermal and physical conditions near Jupiter at the time of its formation and concluded that water ice would form a significant portion of its satellites. Lower temperature condensates, e.g., ammonium clathrate, would not be stable. Thermal modeling in the early 1970's of Europa's interior, based on the accretion modeling of Pollack and Reynolds (1974) and the then known density, produced models of Europa dominated by a large silicate core overlain by a thick icy crust. Estimates of the crustal thickness varied between 75 km (Fanale *et al*., 1977), and 150 km (Consolmagno and Lewis, 1976). These early models were based on an assumed chondritic rocky component.

Fanale *et al*. (1977) and Cassen *et al*. (1979) suggested that the icy layer might presently be underlain by a liquid water layer. Subsequent revisions by Cassen *et al*. (1980) suggested that any thick water layer formed early in the moon's history would probably freeze. They assumed that the orbital resonance locks among Io, Europa, and Ganymede, which are responsible for tidal flexing and heating of both Io and Europa, are ancient. It is conceivable that this last condition was not met (Yoder, 1979). See Section 2.9 for further discussion.

In 1979, Voyager I imaged Europa from a distance, with best resolution of ~33 km/lp (Smith *et al*., 1979a). The images showed Europa to be a white and brown sphere crossed by a set of globe-girdling brown stripes, many along great circles. Three months later, Voyager II passed much closer and showed the stripes to be a complex network of intersecting lineaments and the white surface to be extremely smooth and nearly crater free (Smith *et al*., 1979b). Crater counts by Shoemaker and Wolfe (1982) give a surface age ranging from 30 to 200 m.y., based on calculated cratering rates near Jupiter. This age might be low if viscous relaxation is more dominant than thought or if there is an undetected population of 4 km wide craters. The failure to detect more than one possible relict impact scar on Europa, while these are abundant on Ganymede

(Smith et al., 1979b), argues against an older age, however.

Infrared observations by Voyager place the lit-side surface temperature at ~ 85° K (Hanal et al., 1979). No detectable atmosphere has been reported in the literature. Voyager radio observations led to a revised density value of 3.03 g/cc (Smith et al., 1979a), slightly lower than those of Earth's moon and Io (Table 1.1).

After the Voyager flybys, several major review articles on Europa's geology were published. Pieri (1981) analyzed the polygons formed by the intersecting lineaments in terms of possible stress fields. Finnerty et al. (1981) and Ransford et al. (1981) reevaluated the thermal modeling and proposed that much of Europa's water could be bound in subcrustal silicates as water of hydration. They also proposed a model by which some lineaments could form through upward fracture propagation. Lucchitta and Soderblom (1982) (L&S), and Lucchitta, Soderblom and Ferguson (1981) (LS&F) made a more complete descriptive evaluation and review of the global geology. The L&S paper is probably the most thorough review of Europa's geology to date. However, there are several points on which the present study differs with L&S and several aspects of the problem discussed here that are not in L&S, as will be seen later. Much of the terminology employed here is borrowed from the latter two sources.

1.4 Global Morphology

Voyager observations have given us our first clear view of Europa's surface (Smith et al., 1979a; 1979b). Even in long-range images, two basic terrain types, or crustal units, are apparent, one white and visible at most latitudes, and the other brown and restricted to low latitudes. The average global albedo (0.64) is the highest in the Galilean system, but the dark brown units differ from this by only 20% (L&S). Thus, even at 0.45 albedo, this terrain is still brighter than Ganymede (0.43), whose surface is 70-90% water ice (Clark, 1980). This implies that the brown terrain is also water rich, despite obvious contamination or discoloration by unknown agent(s).

The white terrain is crossed by abundant intersecting brown lineaments (Fig. 1.3). Long lineaments (triple bands) generally follow great circles, whereas short ones near the anti-jove point (simple lineaments, wedge-shaped bands) generally follow small circles (Smith et al., 1979a). The lineament materials generally have a color and albedo very similar to the brown terrain (McCord et al., 1982), suggesting similar compositions. At close range, white terrain appears quite smooth, whereas brown terrain has a hummocky but low relief topography, not exceeding hundreds of meters (Smith et al., 1979b).

For the purposes of this discussion, it is assumed that the white terrain represents the surface exposure of a global crustal layer, of uncertain thickness, composed dominantly of water ice with trace impurities. The brown units, including brown spots, mottled terrain and fracture fillings are assumed to be water rich, with substantial contamination from unknown agents, and derived from below the surface. These assumptions follow directly from the preceding discussion.

Various contaminating agents have been proposed for the brown units, including organic polymers (Schonfeld, 1982), hydrated silicates (Kieffer and Smythe, 1974; Finnerty et al., 1981), polysulfides (Lebovsky and Fegley, 1976), and salts (Cassen et al., 1979). The relative abundance of the later two as volatiles on Io leads to the suggestion that they may also be abundant on Europa, and were incorporated into the water layer during its formation. Saline discharges from glacier bases in Antarctica commonly have a reddish-yellow color (Black et al., 1965). The dominant salts there are halite and aragonite; however, Black et al. (1965) ascribed the color to iron-fixing bacteria, or to iron oxidation, something considered unlikely for Europa (Schonfeld, 1982).

In the case of fracture fillings, this material might have taken several possible forms, ranging from 'dirty' liquid water to water-rich ice slurries to relatively plastic, water-rich silicate magmas. In only a few cases will it be possible to differentiate among these. The term 'slurry,' defined here as a dilute watery mixture, will be used to refer to this material in subsequent discussions when it is not known which term is valid.

Europa has been called the smoothest object in the solar system

(Smith et al., 1979b), although some relief is visible along the terminator (Fig. 1.4). In addition to abundant ridges (q.v.), there are several crater-like features (L&S). Some small bright spots (Fig. 1.3) might also be interpreted as small craters. Also visible near the terminator are several elliptical or linear depressions of unknown origin. It is not certain if they are associated with dark lineaments. There is also irregular hummocky relief associated with brown mottled terrain (q.v.). This is composed of irregular flat-topped mesas and interspersed depressions, with some areas being more irregular. The plains are largely devoid of local relief; isolated mesas are visible in a few locations.

1.5 Europa in the Galilean System

Our current understanding of the Galilean moon system, based on Earth-based and Voyager data, suggests that the system is an orderly one, and that the formation and early history, and thus bulk composition of these bodies, was influenced by their proximity to the thermal effects of proto-Jupiter (Pollack and Reynolds, 1974). It has been known for some time that the densities of the moons decrease outward from Jupiter, and that bulk water content increases concomitantly (Table 1.1) (Pollack and Reynolds, 1974). An apparent contradiction emerged when it was discovered that surface water content and albedo decrease outward from Jupiter, except for Io which has no water. The Voyager flybys (Smith *et al.*, 1979a; 1979b) determined that relative surface age decreases dramatically inward toward Jupiter, apparently as a result of increasing tidal interactions within the system, and to a lesser extent, proximity to past or present Jovian thermal activity. It is now generally believed that Callisto has never been active geologically and preserves an ancient, mixed ice-silicate crust. Ganymede was more active, replacing some of its ancient crust several aeons ago with grooved terrain. Europa has experienced one or more global resurfacing events in its recent past, while Io is undergoing resurfacing at the present time (Smith et al., 1979a; 1979b). It appears that the evolution of these bodies was controlled by any combination of several factors: the thermal energy of proto-Jupiter, the resultant bulk compositions of the moons, and heating from tidal flexture and deformation.

CHAPTER II: LINEAMENT TYPES AND FRACTURE PATTERNS

2.1 Introduction

In this section, the morphology, structure and distribution of the various lineament types, first described by LS&F and Pieri (1981), are reviewed and reexamined. The lineaments are reclassified (Table 2.1) and in part redefined. They are also reinterpreted, although no models for their origin have conclusive observational support, except perhaps wedge-shaped bands.

Lineaments, which are narrow, elongate surface features, are interpreted as crustal fractures. Several lineament types may be interrelated, or may represent the same structural features under different lighting conditions. Complex age relationships between lineament types are also apparent. Histograms of lineament trends reveal distinct patterns whose meanings are interpreted below. Lineament widths quoted below are based on direct measurements from the Voyager images in Figs. 1.2 and 1.4 and may be slightly exaggerated by resolution effects in the Voyager cameras.

2.2 Simple Lineaments

Simple lineaments (Fig. 2.1; Plate 1) are defined here as dark, narrow, straight to locally arcuate lineaments. They are equivalent to Types 4 and 5 of Pieri (1981). They are the most abundant type, and are generally no wider than 8 km. Their edges are well defined,

Table 2.1 Lineament Classifications

Pieri (1981)	L&S	Schenk (this paper)*	
Type 1	Triple Bands	Triple Bands - (subdued)	Possible tensional features
Type 3		Triple Bands	
-	Light Bands	Bright Lineaments	
-	Gray Bands	Gray Bands	Possible compressional features
Type 7	Triple Bands	Bright Bands	
Type 6	Ridges	Ridges - cycloid	
		- linear	Probable tensional features
Type 2	Wedge-shaped Bands	Wedge-shaped Bands	
Type 4	-	Simple Lineaments	
Type 5	-		
Type 8 (scarps)	-	-	

*Tectonic classifications at extreme right are preliminary, based on discussions and interpretations in the text.

ORIGINAL PAGE IS
OF POOR QUALITY

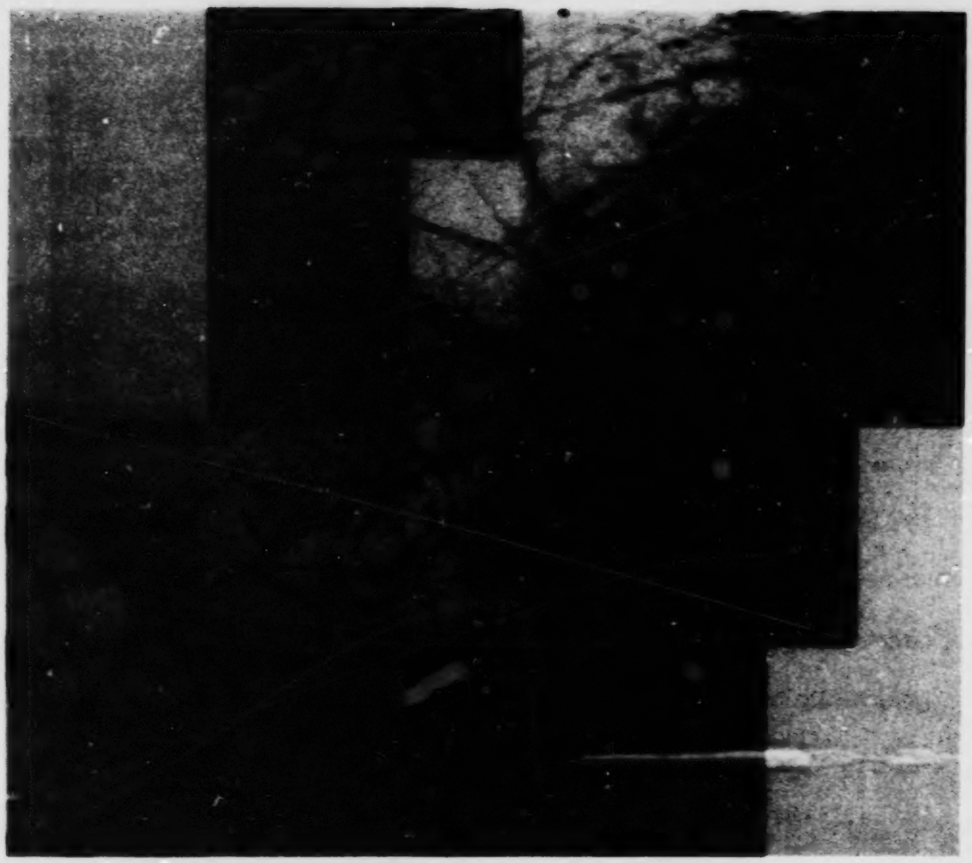

Fig. 2.1 Mosaic showing simple lineaments. Examples are indicated by symbols. Tyre Macula is the circular dark spot at upper right. See Fig. 1.2 for location.

at least down to the limit of resolution. They appear to be reticulate. A histogram of simple lineament trends in the mapped area (Fig. 2.2a) shows strong east-west and northeasterly peaks and a smaller, less well defined northwesterly peak. The northeast peak seems to reflect a strong northeasterly trend among simple lineaments south of the equator (Plate 1). LS&F did construct rosette diagrams for other lineament types but not for simple lineaments. Simple lineaments are observed to cut some triple bands (*q.v.*), but are more often cut by them or merge with them (Fig. 2.1). This suggests some overlap in the formation times of these lineament types, but that simple lineaments are generally older. This type of relationship is seen with other lineament types also (see below).

The origin of these lineaments cannot be determined directly, many being on the threshold of resolution. Their sharp edges and generally parallel sides argue for a simple crustal fracture model: *i.e.*, single fractures, opened without graben formation or tilting of fault blocks. The dark color suggests that we are seeing either a shadowing effect in deep crevasses, or more likely the filling of the fractures by dark material. The observation of simple lineaments under high solar incidence angle and their apparent lack of relief (Smith *et al.*, 1979b) tends to support the latter model.

An alternative interpretation is that they represent replacement features, involving the direct conversion of 'clean' white ice to dirty ice. A classic test of fracture vs. replacement is the dilation

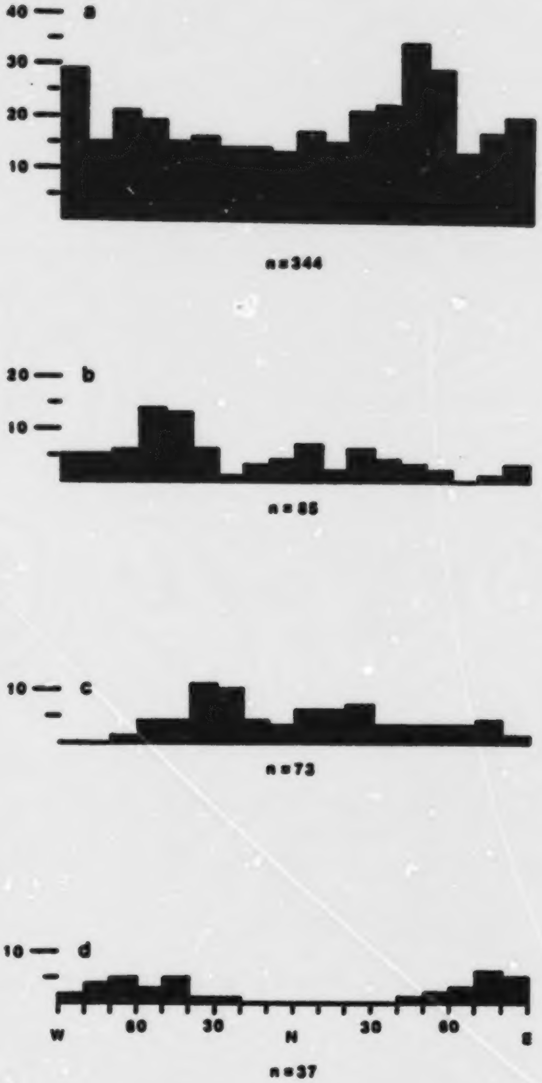

Fig. 2.2 Histograms of lineament trends: a) simple lineaments, b) wedge-shaped bands, c) linear ridges and d) triple bands. Vertical axis is frequency, (n) is the number of sampled lineaments.

(or lack thereof) of an older crosscut lineament. The simple lineaments are too narrow and too poorly resolved to apply this test satisfactorily, but it is directly applicable to wedge-shaped bands and may be to the triple bands. The apparent co-activity of simple lineaments and wedge-shaped bands, which are interpreted as opened fractures (see below), supports a simple fracture model.

2.3 Wedge-shaped Bands

Brown wedge-shaped bands (Type 2 of the Pieri classification) extend in a broad belt between 0 and 45° S latitude and 160 and 210° W longitude (Fig. 2.3, Plate 2). These bands are defined here as any dark, sharply defined, rectilinear lineament greater than 6 km wide, but generally no wider than 40 km, and ranging from 10 to 200 km long. They are generally straight, with some angular bends. The edges of these bands fit tightly together when the sides are rejoined (Fig. 2.4). In other words, for every indentation into the edge of a wedge-shaped band, there is a corresponding projection along the opposite edge (Fig. 2.5). This suggests the opening and subsequent filling of a simple crustal fracture, without graben formation or flooding. The classification wedge-shaped bands is used whether the sides of the lineament are parallel, or converge in a hinge-like manner (Fig. 2.5).

While wedge-shaped bands resemble open tensional rifts in the icy crust, there is still the possibility of a non-tensional origin. This will be substantially reduced if definitive evidence for a

ORIGINAL PAGE IS
OF POOR QUALITY

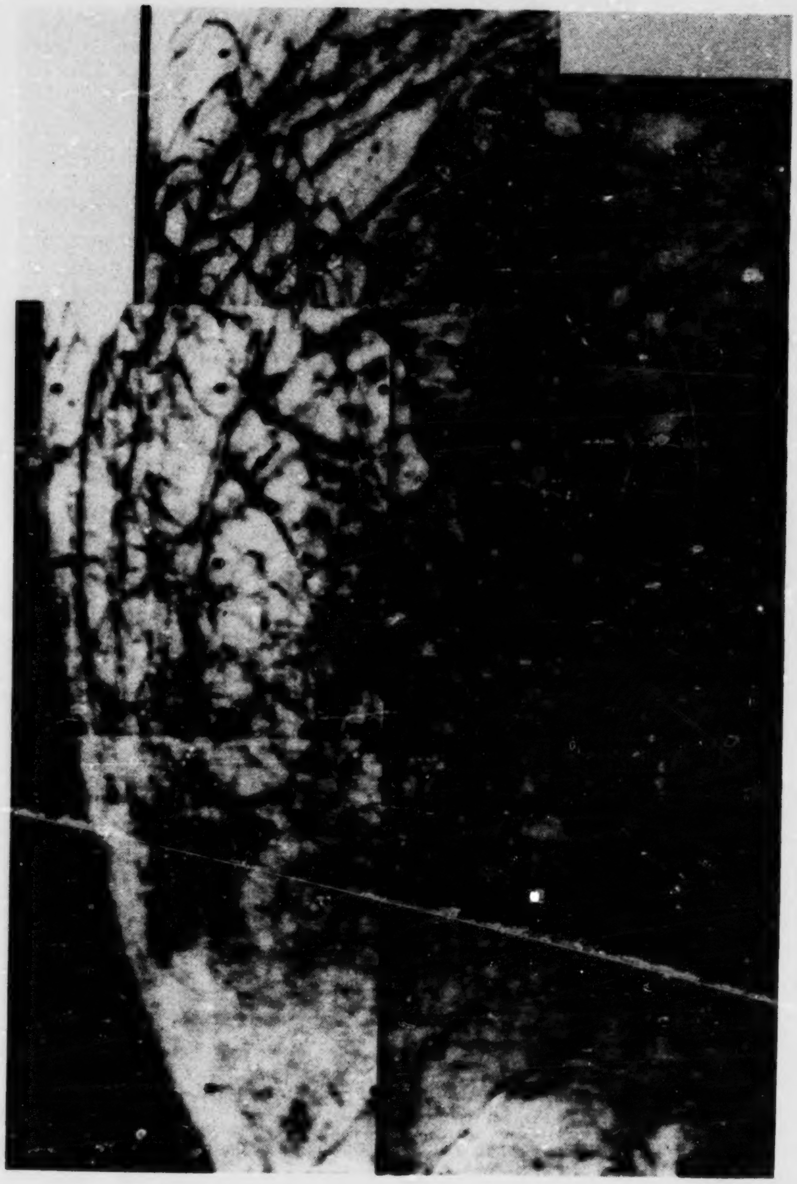

Fig. 2.3 Mosaic showing wedge-shaped bands. Small, irregular brown spots are also abundant. See Fig. 1.2 for location.

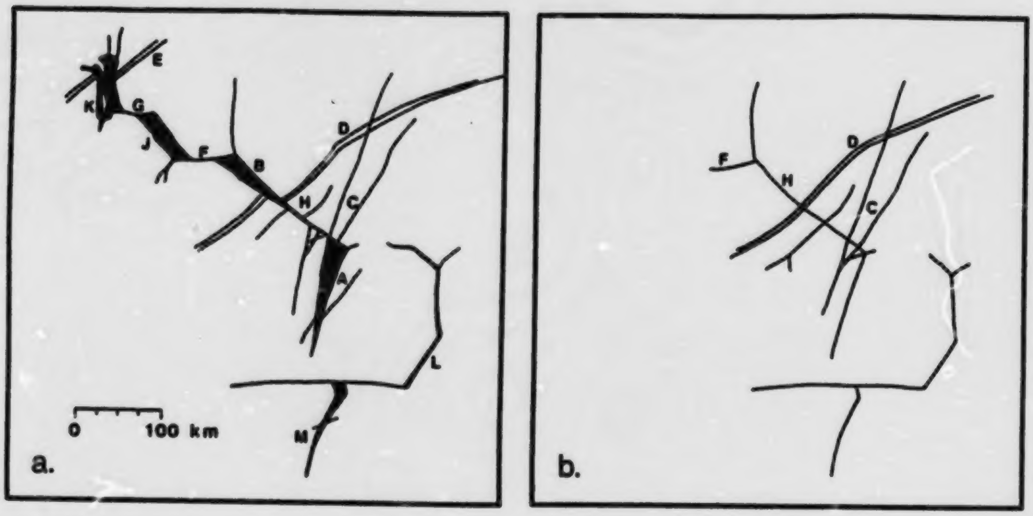
E
K
G
J
F
B
D
H
C
A
L
0
100 km
M
a.
F
H
D
C
b.

Fig. 2.4 Reconstruction of wedge-shaped bands. a) present configuration, b) proposed configuration prior to the opening of wedge-shaped bands. Letters refer to features descibed in the text. Maps are approximately 300 km across. See Fig. 1.2 for location.

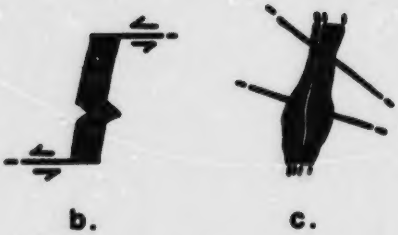

Fig. 2.5 a,b) typical wedge-shaped bands, c) a typical triple band.

tensional origin is found. Such evidence might take the form of simple structural offsets parallel to the direction of opening of fractures and along lineaments approximately perpendicular to them (Fig. 2.5). This would be analogous to mid-ocean ridge transform faults. Below is a set of observations that represents such evidence. All letters refer to locations in Fig. 2.4.

1. One set of narrow, simple lineaments (C), and one set of Type 1 triple bands (D), each on the south side of the east-west trending lineament (H), can be realigned with counterparts on the north side of (H) when the edges of the two wedge-shaped bands (A) and (B) are brought together as in the reconstruction in Fig. 2.4b. That lineaments (C) and (D) were continuous across (H) is supported by the constancy of their width, morphology and direction when reconstructed. Lineament (H) is interpreted as an extension of band (B) along which no dilation has occurred. The amount of displacement along (H) precisely matches the maximum width of bands (A) and (B), at 25 ± 2 km. It can be concluded, based on these observations, that both (C) and (D) have been offset and/or dilated by movement along lineament (H), resulting from rifting and rotational separation of crustal elements across fractures (A) and (B) (Fig. 2.4). Additional unlabeled lineaments also appear to be offset along lineament (H) (Fig. 2.4) but may be secondary fractures related to the initial fracturing event.

2. Lineaments (F) and (G) (Fig. 2.4a) strongly resemble transform type faults in that they appear to have undergone trans-

lational displacement. They appear to offset the two wedge-shaped bands (J) and (K) in the same direction (sense) and by approximately the same amount. Both (J) and (K) are thus interpreted as offset extensions of the wedge-shaped band (B). These features may be analogous to mid-ocean ridge transform faults in form, if not in origin.

3. Numerous additional wedge-shaped fractures, oriented almost exclusively northwest-southeast, are found in the region centered on 7° S, 195° W, near the anti-jove (Plate 2). The striking orientation of these fractures breaks down in the area of Fig. 2.3, an area rich in brown spots. These wedge-shaped bands are all intercepted by simple lineaments trending perpendicular to the strike of the bands and following small circles (Fig. 2.3). While offsets have not been conclusively recognized in this area, lateral motion along these perpendicular lineaments is inferred, generated by the hinge-like opening of the wedge-shaped bands.

4. These subparallel wedge-shaped bands are distributed in a linear, northwest-southeast trending belt ~1300 km long, just southwest of the anti-jove point (Plate 2). A less well defined belt extends southwest from the southern end of the main belt. Examination of medium range images with a resolution of ~12 km/lp (Fig. 1.1) reveals no obvious trace of this type of fracturing, at least on the leading hemisphere, despite sufficient resolution. In the mosaics, regions north and east of the main belt appear clear of wedge-shaped bands. Long range images (Voyager frame no. 0333J1-002)

show a region of brown terrain just west of the fractured zone, and just beyond the limb in the near-range mosaics. The paucity of wedge-shaped bands in such terrain and in areas to the north and east supports the idea that these bands are a localized phenomenon, limited to the white terrain near the anti-jove. It is for these reasons that a global mechanism, such as global expansion, is considered unlikely as an origin for the opening of these fractures.

5. The fractures in this zone appear to be simple; that is, single faults, perhaps sub-vertical, penetrating the crustal layer. This conclusion stems from the presence of dark allochthonous materials within the fractures and the match of offsets with fracture width, indicating that these are not flooded grabens, a model often proposed for Ganymede grooves (Allison et al., 1982; Parmentier et al., 1982). A comparable fracturing model is that of polar sea ice, particularily in the formation of open leads. In sea ice, open areas called leads develop due to differential ice movement. The fractures penetrate through the ice, allowing water to fill the fractures from beneath. This is the interpretation favored by the author for both wedge-shaped bands and simple lineaments.

These fractures appear to be the main part of a large scale rift zone that in many ways is reminiscent of terrestrial plate rifting and separation (Schenk and Seyfert, 1980), and can be analyzed and described in a similar manner. The nature of wedge-shaped bands suggests lateral motion of icy blocks has taken place. The demonstrated offsets and apparent filling from below leads to the conclusion that these fractures penetrate through the crustal layer, dividing the crust into discrete blocks, or plates, such as has occurred on Earth. The restricted belt-like nature of the wedge-shaped bands further leads to the suggestion that this marks a major rift zone, or divergent boundary, between two large crustal units, whose smaller components (called plates) appear to have a unified sense of motion that can be described.

The strikingly parallel orientation of wedge-shaped bands near the anti-jove and north of Thrace Macula (Fig. 2.6) implies the dilation of preexisting northwest-southeast fractures (i.e. simple lineaments) in a direction parallel to the simple lineaments that terminate the fractures. These perpendicular simple lineaments, inferred to be transform-type faults, trace small circles roughly concentric about a point to the southeast (Fig. 2.6). This configuration is directly analogous to transform faults along terrestrial rift zones (Morgan, 1968).

If these inferences are correct, the same geometric rules governing plate motions on Earth should be applicable here. Relative motion between two plates on a sphere can be expressed as a rotation of the plate about a pole of rotation (Morgan, 1968), which can be located by constructing perpendiculars to transform faults and pinpointing their intersection. Transform faults must, by definition, be concentric about the pole but rift or subduction zones need not be radial to it if spreading or subduction is oblique (Morgan, 1968). It should be remembered that the pole is merely a geometric construct

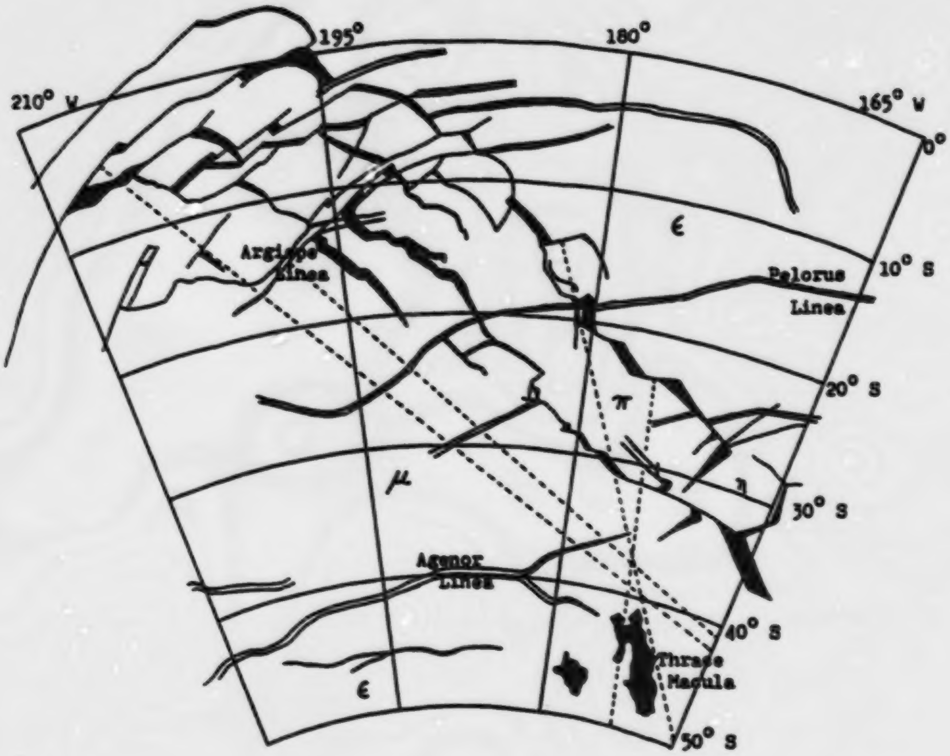
195°
180°
210° W
165° W
0°
ε
10° S
Argiope Linea
Pelorus Linea
20° S
π
μ
η
30° S
Agenor Linea
40° S
Thrace Macula
ε
50° S

Fig. 2.6 Wedge-shaped band fracture zone. Lambert conformal conic projection. Dashed lines are representative perpendiculars to inferred transform faults.

describing a motion, and does not bear directly on the location of the stress.

Perpendiculars to inferred transforms at the anti-jove converge in a poorly defined region north of Thrace Macula (Fig. 2.6). The low resolution limit and small angular spread of the perpendiculars result in a large error in the pole location. Wedge-shaped bands to the north of this area help refine the location by increasing the angular spread. It is assumed that the ice in this area has moved with the same sense as that near the anti-jove since no major breakup has occurred between. The addition of perpendiculars from this area gives a more accurate location for the pole, at ~ 38° S, 174° W, with a radial error of ~10 degrees (Fig. 2.6). The fact that a majority of the perpendiculars do converge further strengthens the model.

The maximum width of separation across the proposed rift zone is estimated at approximately 100 km. The angular separation between the plates can thus be derived, knowing the distance to the pole, and is estimated to be about 4 degrees. This is relatively minor compared to the 50-60 degree separation across the Atlantic Ocean. This implies that the rifting process on Europa either is proceeding very slowly, is very recent relative to the current terrestrial spreading cycle, or more likely, did not progress too far before ceasing.

In many ways, this fracture pattern is similar to that seen in continental rifting, in which a linear fracture zone, composed of subparallel tensional faults and often initiated by doming, splits continental masses, creating new crustal material between. The fracture style is different, however. The tilting of fault blocks and creation of graben associated with terrestrial rifting is characteristic of the rifting of brittle crustal blocks overlying a plastic medium undergoing stretching and necking (Tapponier and Francheteau, 1978; LePichon et al., 1982). This type of deformation would be expected if the fractures formed in an icy shell underlain by a warm, soft, icy layer, as suggested by L&S. The lack of this style of fracturing and the presence instead of a sea ice type fracturing (simple fracture without graben or tilt block formation) leads me to propose that the near-surface crustal ice layer floated over a liquid (watery) medium during the period of fracturing.

A histogram of wedge-shaped band trends reveals a distinct northwest-southeast trend (Fig. 2.2b). This reflects their subparallel character. Addition of wedge-shaped bands, interpreted as opened simple lineaments, to the simple lineament trend totals reveals a strikingly simple conjugate pattern, with peaks at approximately N85W, N55W and N45E (Fig. 2.7). This tends to strengthen arguments relating wedge-shaped bands to simple lineaments.

2.4 Triple Bands

Triple bands (Type 3 of Pieri, 1981; L&S) are perhaps the most enigmatic lineament type. They are so called because they commonly consist of a dark lineament with a narrow, white stripe

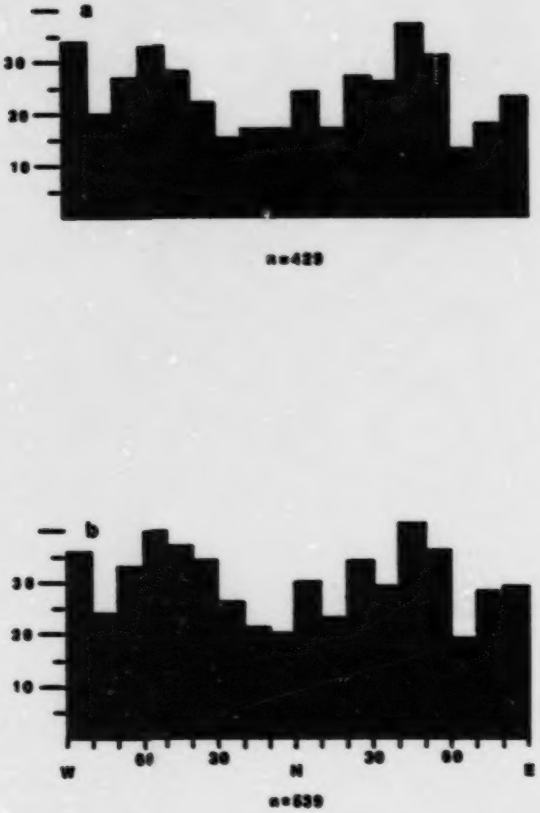

Fig. 2.7 Histograms of a) wedge-shaped bands and simple lineaments and b) wedge-shaped bands, simple lineaments, linear ridges and triple bands. Verticle axis is frequency, (n) is number of sampled lineaments.

along the center (Fig. 2.8). This medial stripe usually disappears if the lineament narrows. The medial stripes are often straighter than the main lineaments and do not regularly follow the center of the lineament. Occasionally triple bands merge with simple lineaments (LS&F), but in many cases they terminate by blending into brown mottled terrain. These bands vary in width from 5 to 30 km or so, and are usually very long, some being nearly global. They often trace great circles (Smith et al., 1979b) but can be locally irregular, one example appearing sinuous. Edges can be sharp but are generally ragged. Examples include Minos Linea, Pelorus Linea and Cadmus Linea (Plate 3). Agenor Linea is classified separately as a bright band (q.v.) for various reasons.

In the mapped area (Plate 3), triple bands are divided into two groups by the equator. North of the equator they trend northwest-southeast, but to the south they trend northeast-southwest. Each set intersects the equator at approximately 30-35 degrees (Helfenstein and Parmentier, 1980). The northern set is part of the group of dark bands that trace great circles (Smith et al., 1979b) and they arc back toward the equator west of the mapped area. The southern set does not appear to extend beyond the limits of the mapped area. In addition to this, there appears to be a subtle morphological difference between the two groups. The southern triple bands do not merge or appear related to simple lineaments. Their trace is generally more irregular, less arcuate. The contrast across the lineament is subdued slightly and the central stripe is less

ORIGINAL PAGE IS
OF POOR QUALITY

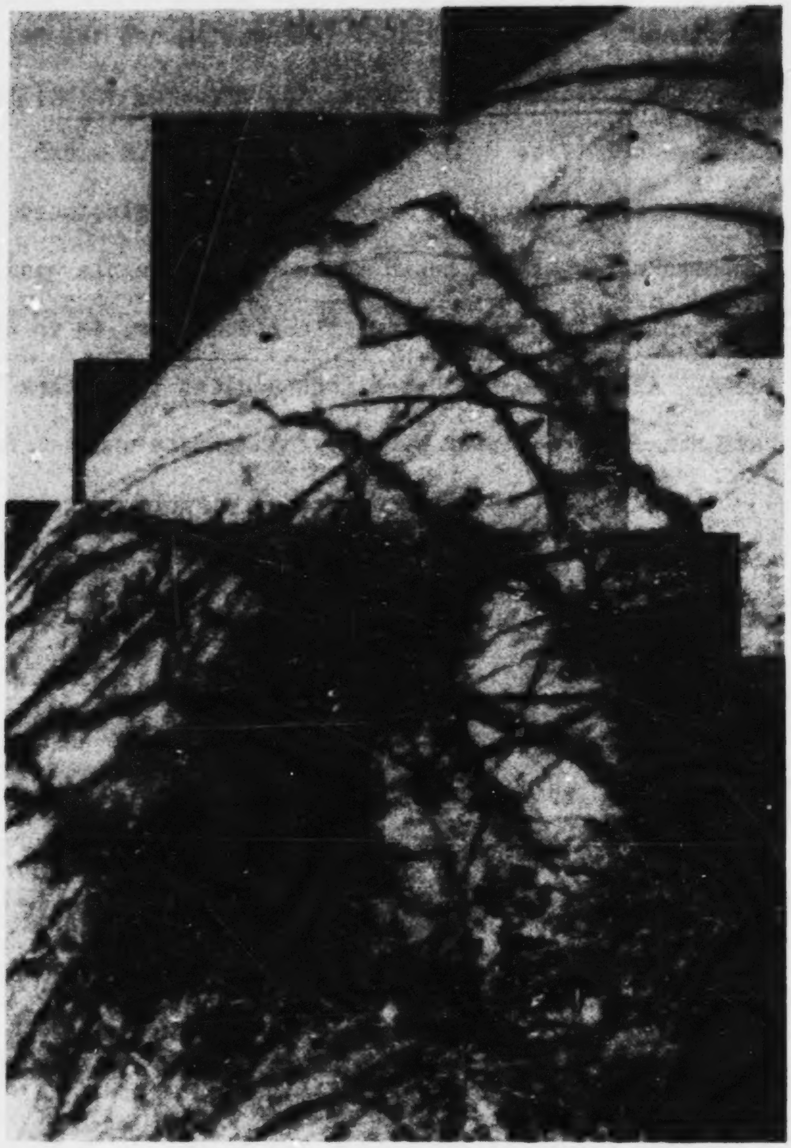

Fig. 2.8 Mosaic showing triple bands. Examples are indicated by the symbols. Bright lineaments are visible at the lower left of center. See Fig. 1.2 for location.

distinct and less linear. It is not clear what this might mean, but it could imply a subtle difference in how the bands are formed.

Unlike wedge-shaped bands, the sides of triple bands do not fit together (Fig. 2.5). Some are uniform in width, but most vary irregularly and may have the appearance of stretched boudins, as if composed of adjoining brown spots (L&S). Triple bands never terminate against perpendicular simple lineaments, as do wedge-shaped bands. All of these observations suggest that these lineaments have had a more complex history than simple crustal fracture.

LS&F suggest that ridges (q.v.) visible near the terminator are equivalent to the central stripes of triple bands, based on the contention by Malin (1980) that these central stripes can be traced to ridges along the terminator, a contention this author disputes. An examination of the region of the terminator ridges in low-phase-angle, medium-range imagery (Fig. 1.1) reveals no trace of otherwise very distinct triple bands. The region is well illuminated and triple bands should be visible if present. Thus I contend that while there may be a correlation between triple band medial stripes and some ridges, there is little or no evidence to support this, at least in the study area.

Several origins have been proposed for triple bands. Finnerty et al. (1981) proposed that they originate by rapid upward propagation of fluid-filled basal lithospheric fractures. The rapidly moving fluid would break off 'xenoliths' in a subcrustal layer, creating a breccia-rich 'slurry' that would penetrate to the surface.

They suggest CO_2-driven kimberlites as an analog. The violence of the event would presumably destroy some original crust. The medial stripe would result from secondary fracturing due to the refreezing of the fracture plug (Finnerty et al., 1981). Helfenstein and Parmentier (1980) suggest that they represent tidally induced conjugate shear zones. This tends to be supported by the distribution pattern (LS&F), but there is little other evidence for this.

The irregular morphology of these features is somewhat consistent with the Finnerty et al. (1981) model, in that their mechanism can act more or less vigorously in different locations, producing the bulbous appearance of some triple bands. However, their model predicts a median stripe along the center, and this is seldom observed. The straight nature of the central stripes might be more consistent with the conjugate shear model. It is also possible that the triple bands trace ancient, weakened shear zones, and the emplacement of new 'dirty' material allowed temporary reactivation of the shears.

Alternatively, the gradation of some triple bands into simple lineaments suggests that they may have had an origin as simple crustal fractures, i.e., simple lineaments, before evolving into their present form. Possibly, the material that filled the simple lineaments overflowed locally, especially in low spots. This would be consistent with the observed ragged edges and the observation of grading of triple bands into mottled terrain (q.v.), which could represent a similar, flood-type feature. It is also consistent with a sea ice model for wedge-shaped bands, which may be of similar age. The medial stripe may represent the trace of the original fracture, along which some component of shear, or lateral stress, was later reactivated.

It is interesting to note that triple bands do not cut or dilate each other at intersections. Central stripes always meet at the intersection, often in a manner reminiscent of simple lineament intersections. Sometimes the central stripes appear offset at intersections, but never consistently in the same direction.

Another alternative is similar to the Finnerty et al. (1981) model but is less violent. It involves the upwelling of a 'magma,' in a style similar to salt doming, along structurally controlled conduits, i.e., global shear planes. Again, medial stripes would require a secondary, post-emplacement event. Resolution is insufficient to differentiate among these models, although I tend to support an origin by overflow from simple lineaments. In any case, the semi-irregular morphology, medial stripes and failure of the sides of these lineaments to fit back together imply a more complex history than simple fracture, although they may have evolved from simple fractures.

2.5 Bright Bands

Prominent in the region south of the wedge-shaped bands (Figs. 1.3; 2.9) are two high-albedo, lobate lineaments (Type 7, Pieri, 1981), hundreds of kilometers long, with intermittent dark edges.

ORIGINAL PAGE IS
OF POOR QUALITY

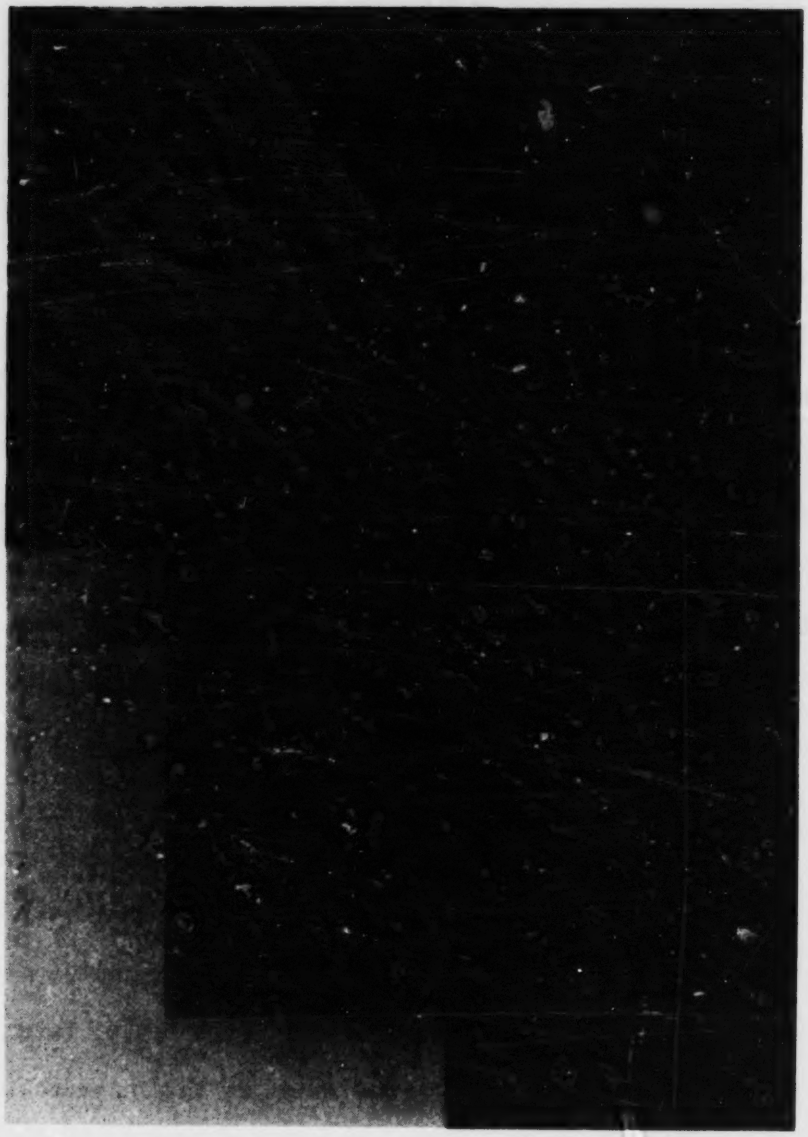

Fig. 2.9 Mosaic showing the bright band Agenor Linea. Brown spots Thera and Thrace Maculae are visible at upper right. See Fig. 1.2 for location.

They are young (Pieri, 1981) and are the only such features detected so far on the surface. L&S consider them to be Type 1 triple bands (Table 2.1), and Pieri (1981) considers them to be possible modifications of the same. I regard them as being distinct from triple bands, or any other type, in morphology, occurrence, and probably origin. Their trace is distinctly lobate and, on mercator projections (Plate 4), they parallel ridges (q.v.) more so than triple bands. They are the only features on the surface known to have an albedo distinctly higher than the surrounding terrain. The dark borders, while dominant in triple bands, are secondary here, being present along less than 25% of the total length of the bright core, which is fairly constant in width. Their edges are much less ragged and more parallel than triple bands. Agenor Linea (Fig. 2.9) is the more prominent of the two known examples, and is at least 900 km long, trending roughly east-west.

Both examples terminate by narrowing and fading into the surrounding plains, supporting the conclusion that they form by deformation of these plains. Agenor Linea terminates near Thrace Macula in a short, borderless segment (Fig. 2.9). This segment joins the main segment of Agenor Linea at the intersection with a short triple band. The bright core of Agenor Linea forks here and can be traced a very short distance into the triple band, where it changes into an ordinary central stripe. Thus Agenor Linea may have been formed by the partial reactivation of a triple band, or more likely, it may have formed along the trace of an older triple band.

If fracturing and 'plate' rotation is an accurate model for the development of wedge-shaped bands, then a compressional (subduction-type) zone might be expected subparallel to the wedge-shaped band rift zone, assuming no net planetary expansion. Since the rift zone is believed to be localized, an associated compressional zone is not unlikely. Several lines of circumstantial evidence suggest that Agenor Linea is this compressional zone. Its trace is lobate, reminiscent of some terrestrial subduction zones (e.g. Marianas and Peru-Chile trenches). Its morphology is not characteristic of tensional fractures, such as wedge-shaped bands or lunar rilles, and is certainly not characteristic of shear fractures. It does run sub-parallel to and for approximately the same length as the wedge-shaped rift zone (Fig. 2.6). Identifiable tensional fractures are absent near Agenor Linea. Since both features are believed to be unique, at least within the mapped area, an associated compressional zone is not unlikely.

The bright bands are tentatively interpreted as compressional features directly related to the opening of the wedge-shaped band rift zone to the north. The evidence is not conclusive, however, and does little to explain the generation of the observed high-albedo features. They may represent a form of pressure ridge, although there is no indication of negative or positive relief associated with it. Arctic pressure ridges do have high albedo when observed from high altitude, possibly due to the exposure of fresh, broken ice surfaces. The high albedo of Agenor Linea may be due to the recrystallization of the ice, causing impurities to migrate outward, thereby enhancing albedo. This might account for the observed dark borders, which generally cluster in pairs (Fig. 2.9). Anderson (1970) reports that dark borders on Arctic pressure ridges are due to the flooding of parallel depressions that result from the rafting of one ice floe onto the other. In the Agenor Linea model, the flooding would be by material forced out of the main ridge. Alternatively, they may represent the traces of mega-thrusts, much like the lobate scarps on Mercury (Dzurisin, 1978). Unfortunately, these ideas remain conjectural, and the question of how these lineaments are produced requires further study and images with improved resolution.

2.6 Ridges

Ridges (Type 6, Pieri 1981) are defined as narrow, continuous, topographically elevated rises. Their apparent width is generally constant, and ranges from 2 to 4 pixels (4 to 8 km). Lengths range from ~ 20 km to well over 1000 km. As reported by Smith et al. (1979b), they are distributed close to the terminator, being highlighted by shadow effects (Figs. 1.2; 1.4; 2.10). But some are found as far as 50 degrees west of the terminator and are abundant south of 50° S (Plate 5). Malin (1980) reports that ridge heights range in the hundreds of meters.

When ridges intersect other lineament types, they cut across, and are therefore younger than the other types. Ridges are not

ORIGINAL PAGE IS
OF POOR QUALITY

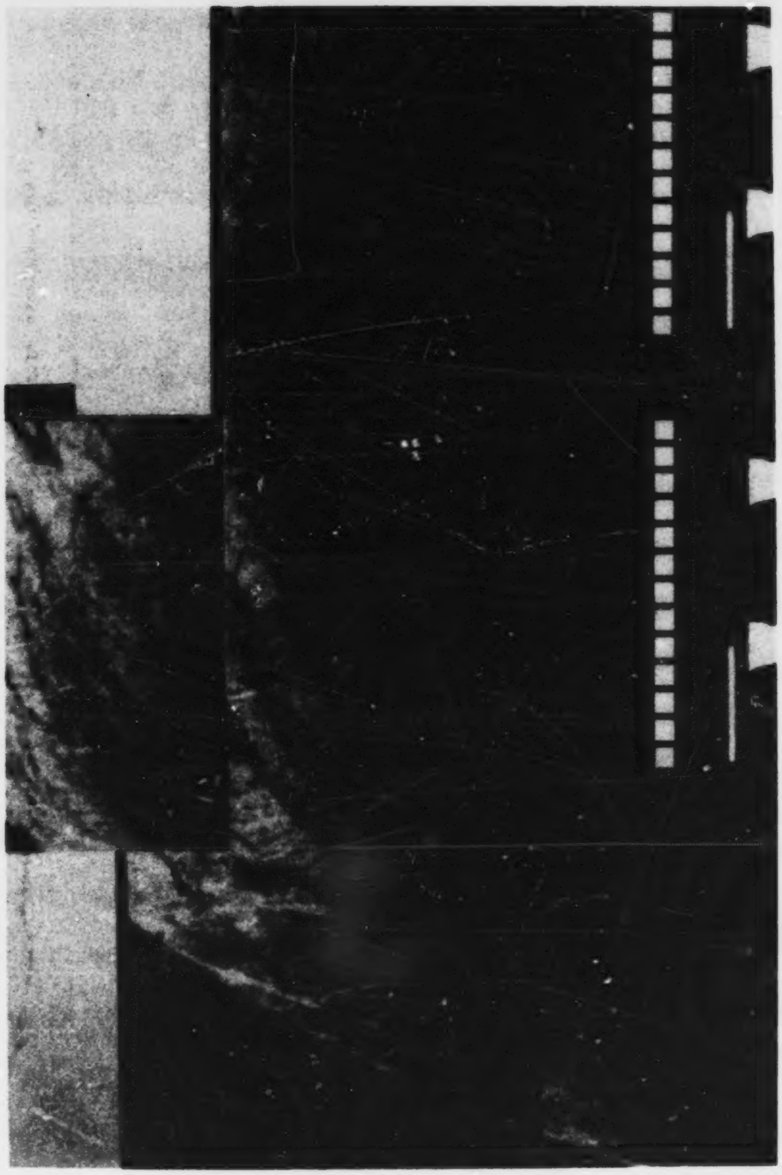

Fig. 2.10 Mosaic showing ridges (dominantly cycloid). Examples are indicated by symbols. Several gray bands are visible (G). See Fig. 1.2 for location.

observed to intersect the bright bands and most simple lineaments and triple bands. Resolution is insufficient to detect structural crosscutting relationships among ridges, but it does not appear that they overlap like twine on a ball, as suggested by Smith et al. (1979b).

Ridges are separable into two subclasses, based on morphology and probable origin. The linear ridges are generally straight and can be found from 30° S to at least 55° N (Plate 5). They are observed to trend into simple lineaments in areas north of the equator and north of Thrace Macula (See Fig. 2.11; Plates 1, 5). No instances were detected of ridges trending into triple bands, contrary to the report of L&S. Except for their observed color and apparent topography, linear ridges resemble simple lineaments, yet they are rarely observed in the same area. Simple lineaments fade away within 10 degrees of the terminator, and linear ridges generally disappear about 10-15 degrees beyond the terminator, although there are exceptions. Most lineaments near the terminator in the first mosaic mapped as simple lineaments are revealed as linear ridges in the second mosaic, when they are some 15 degrees closer to the terminator (Fig. 2.11). Thus most linear ridges are interpreted as simple lineaments under low-illumination conditions.

Extrapolating from previous discussions, it can be said that wedge-shaped bands are opened simple lineaments and thus the dark band that defines the simple lineament is a fracture fill analogous to a dike. My suggestion is that a dark 'slurry,' probably from the

ORIGINAL PAGE IS
OF POOR QUALITY

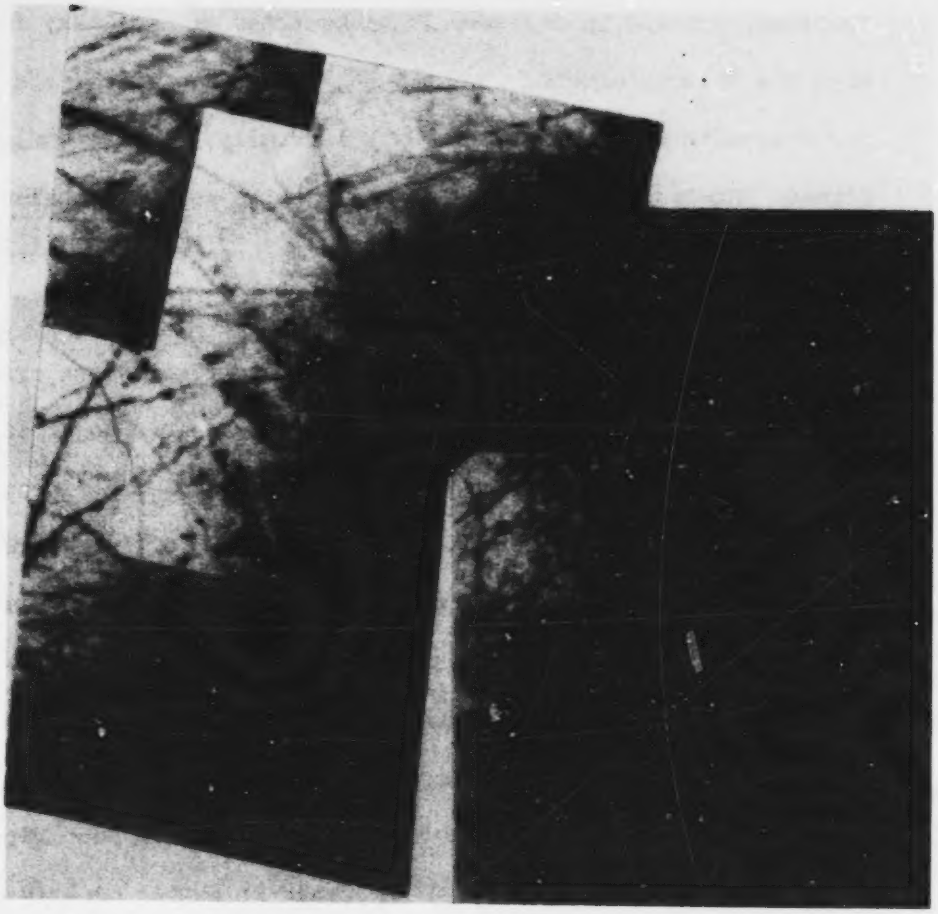

Fig. 2.11 Stereo pair of simple lineaments and ridges near the terminator. See Fig. 1.2 for location.

same source as wedge-shaped band fillings, intruded up along the fracture, perhaps in response to hydrostatic or capillary forces. When the 'slurry' froze, it expanded, being water rich. Unless the ice fragments were able to give way laterally, a ridge would have formed. However, unless the 'slurry' source was very shallow, the 'slurry' would probably have frozen before reaching the surface (Parmentier and Head, 1979).

Resolution is certainly insufficient to resolve the origin of the ridges. However, any other models must be able to explain the apparent correlation between linear ridges and simple lineaments. It is possible that linear ridges represent a sort of 'pressure ridge' similar to those found in arctic waters. In this model, similar to one discussed by LS&F, fractures were opened slightly in the crust, they were filled, and reclosed, thereby squeezing the fill up into a ridge. Another alternative suggests that the ridges involve some component of lateral shear. Such shear ridges have been reported in arctic sea ice (Anderson, 1970) but there is as yet no evidence to support such a model for Europa's ridges.

A fourth possibility for the generation of a linear topographic rise is to start with a filled fracture and etch it, through differential erosion. R. Johnson _et al._ (1981), using Voyager fields and particles data, estimated a charged particle sputtering erosion rate of ~100 meters/1000 m.y. Eviatar _et al._ (1981) and Purves and Pilcher (1980) report lower erosion rates. The eroding agent would be high energy particles trapped in the Jovian magnetosphere. Although not specifically addressed in the literature, implications are that dirty ice would be more resistant than clean ice, leaving anything composed of dirty ice, such as a ridge, standing high. Considering the surface age of 30-200 m.y., and relative youth of ridges, this erosion rate is insufficient to account for the observed relief of hundreds of meters.

A trend histogram of linear ridges (Fig. 2.2) shows a peak at approximately N30W, broadly consistent with the peak found by LS&F. However, rosettes from LS&F are length weighted, resulting in higher peaks. This peak is probably related to the northwesterly peak associated with simple lineaments, and tends to support the interpretation of linear ridges as highlighted simple lineaments.

In regions south of the equator, ridges are dominantly cycloidal, in that they consist of a series of connected arcs, the cusps oriented in the same direction along any one ridge system. Locally, some ridges are extremely irregular while maintaining their regionally arcuate shape (Fig. 2.10). These cycloid ridges, as well as can be determined, do not appear to trend into simple, or any other type lineaments. When traced away from the terminator, they generally have an albedo similar to that of the surrounding plains, suggesting the involvement and possible deformation of plains material. Sinuous ridges in the equatorial region are grouped in this subclass because of a similar color relationship and a lack of linearity.

The only cycloid pattern of similar type known to the author (after a preliminary search of planetary imagery) is along the western Pacific Ocean margin. There, arcuate island arc chains join in continuous sets of concave-west arcs, although not as orderly or abundant as those on Europa. The Pacific arcs, and the related subduction zones, were clearly formed in a compressional environment and seem to be controlled by the simple geometry of subducting a thin two-dimensional plate on a curved surface (Frank, 1968). Thus, cycloid ridges could represent the traces of connected, low-angle thrusts similar to lobate scarps on Mercury (Dzurisin, 1978). Whether any compressional model for cycloidal ridges can be successfully applied remains to be seen. Finnerty et al. (1981) make the assumption that they probably are of compressional origin, and this author has no objection to their model.

Those cycloid ridges that have been mapped are generally concentric about the anti-jove region, a region of proposed upwelling (Schenk and Seyfert, 1980; Finnerty et al., 1981). A region of compressional stress related to and concentric about a convective region is not unreasonable. This same convective system would also be responsible for the opening of the wedge-shaped bands, about which the cycloid ridges are also concentric.

2.7 Gray Bands

L&S described this lineament type as arcuate, light brown, elevated plateaus (Fig. 2.10; Plate 4). There are two known examples, both south of Thrace Macula. L&S suggest that these are concentric about a point near 65° S, 110° W, and are a separate class of lineaments. Their location among abundant cycloid ridges and their similar cycloid pattern suggests that they are a subclass of ridges. They appear cut, or overlain, by some ridges and so may be an older ridge pattern, but are too scarce for reliable age determination.

2.8 Bright Lineaments

Bright lineaments, distinct from bright bands, are the only lineament type restricted to the brown mottled terrain (q.v.). They are also restricted to the vicinity of the anti-jove point (Plate 4). They appear as fine whitish lines within the terrain, but do not have an abnormally high albedo (Fig. 2.8). There are an insufficient number to construct a reliable histogram.

These lineaments may be the equivalent of simple lineaments in the brown mottled terrain, but their limited distribution hampers interpretation. One area near the anti-jove appears to be crossed by abundant, very fine, discontinuous bright lineaments, partially masking the mottled terrain. This area is classified as bright lineated terrain (Lb) in Plate 6.

During the cooling of Alae Lava Lake, bright sublimate deposits were observed along the edges of some cracks on the crust (Peck and Kinoshita, 1976). These deposits included sulfur, anhydrite and gypsum (Peck and Kinoshita, 1976). Similarly, bright lineaments may represent some sort of sublimate deposits, most likely of water frost, that are otherwise invisible if deposited on a bright surface. They may instead be related to the central stripes of triple bands.

2.9 Fracturing Mechanisms and Origins

The global distribution of intersecting simple lineaments and triple bands requires a global mechanism for their formation. Simple lineaments have been opened an average of 2-6 km. Triple bands may or may not have involved major fracture dilation, depending on how they were formed. A 9% crustal volume expansion during the freezing of a 20 km thick global ocean (Smith et al., 1979b; using the Ransford et al., 1981 crustal model) would have dilated these fractures less than 0.1 km, assuming no crustal shortening elsewhere. The observed simple lineament dilation might be explained by a volume expansion of a subcrustal ocean during outgassing of volatiles from the interior, stretching a preexisting, overlying icy crustal layer. While this type of low-level, long-term stress would probably be relaxed viscously, rather than by brittle failure (Parmentier and Head, 1979), it may have been responsible for the dilation of fractures once they formed. However, a radius increase of at least 75 km is required to explain the observed dilation, a value inconsistent with thin-ice crustal models (Sect. 5.1). Both models are probably insufficient to explain the observed fracture dilation and require some crustal shortening elsewhere. Large-scale global expansion due to internal dehydration reactions (Ransford et al., 1981) is possible but has no supporting evidence.

An internal second-order convection cell beneath the anti-jove point may have been responsible for the opening of wedge-shaped bands and possibly the formation of bright bands and cycloid ridges in a zone around the anti-jove point (Schenk and Seyfert, 1980; Finnerty et al., 1981). In my crustal model (Sect. 5.1), this requires an aqueous plume in a subcrustal liquid-water layer, generated over a hot spot, or outgassing vent, on the rocky ocean 'floor' (Schenk and Seyfert, 1980). Until more complete photographic coverage is obtained, it cannot be determined whether convection cells ever operated within Europa, locally or globally. Confirmation of this model would strengthen arguments for continued outgassing during and shortly after crustal formation, and contamination of the subcrustal ocean with internally derived rocky materials.

Outward migration of Europa's orbit and consequent relaxation of a tidal bulge radial to Jupiter is predicted prior to the establishment of the present three-way tidal resonance lock among the inner Galilean satellites (Yoder, 1979). The relaxation of the bulge would induce low-level stresses over a period of several million years that would be relaxed viscously (Parmentier and Head, 1979). Also, the observed fracture patterns bear little resemblence to those predicted for such a collapse (Melosh, 1980).

Tidal deformation, if responsible for fracturing, resulted from the oscillation of Europa's tidal bulge across the sub- and anti-jove points due to a forced orbital eccentricity as Europa moved in its orbit (Yoder, 1979). These short-term flexural stresses may have been insufficient to rupture the icy crust at its present temperature (Finnerty et al., 1981). If Europa's crust was warmer (and thinner) in the past, tidal stresses may have exceeded the tensile strength of ice near its melting point (Cassen et al., 1979). It should be stressed that the mechanical behavior of ice, especially as a function of temperature, is not well understood. One study suggests that the tensile strength of ice may increase as temperature decreases (Parameswaran and Jones, 1975). The same study indicates that ice fractures at very low stress levels (1-5 bars), a result supported by observations of terrestrial sea ice (Coon and Pritchard, 1975). The bearing strength of ice is also dependent on such properties as grain size, crystallographic orientation, and fluid and solid inclusion concentrations (Kovacs and Mellor, 1975).

A histogram of wedge-shaped band and simple lineament trends (Fig. 2.7a) shows a simple conjugate pattern with three peaks that exceed 2σ, at N85W, N55W and N45E. This pattern supports suggestions of structural control (i.e. tidal stresses) during the formation of these lineaments, and that a relatively simple stress field prevailed during that time. A histogram of all lineament trends in the map area (Fig. 2.7b) is similar but the peaks are statistically less significant.

The preservation of a simple fracture pattern, especially near the anti-jove point where wedge-shaped bands and simple lineaments dominate, argues that Europa's present surface is not as highly evolved as other planets appear to be. A similar orthogonal lineament pattern has been reported for portions of the lunar farside (Casella, 1976), selected areas on Mercury (Dzurisin, 1978;

Melosh and Dzurisin, 1978), and for a few tectonically active areas on Earth (Corbett, 1978). This pattern has been extensively obscured or destroyed elsewhere on these bodies by volcanic, tectonic or impact events. The Moon's fracture pattern appears to have been at least partially controlled by major basin-forming impacts (Casella, 1976). Only one major impact structure (Tyre Macula; see Sect. 3.3) has been proposed for Europa within the mapped area. The only area on Europa that might have been subjected to secondary volcanism or tectonic disruption is brown mottled terrain (q.v.), where few lineaments are found. Thus, Europa's simple lineaments and wedge-shaped bands may represent a well-preserved example of the 'lunar grid' network (Strom, 1964). This lineament network may represent an ancient global fracture network common to the terrestrial planets. The origin, significance and even the reality of this network on the planets is still debated, however.

Models for sea ice fracturing (Coon and Pritchard, 1975) have not been applied to Europa. These models include: long-period waves (e.g. sea tides), isostatic imbalance (due to partial rafting of ice on the sea bed) and thermal fracturing. Thermal fracturing involves failure due to strong thermal contrast through the ice (Evans, 1971; Evans and Untersteiner, 1971). If Europa's subcrustal layer was ever liquid, as proposed earlier, the strong thermal contrast between liquid water and deep space could have been a powerful stress-inducing agent.

Fracturing on Europa may have been due to any combination of factors. In any case, tidal stresses probably were a controlling factor in their development. They may or may not have been sufficient to fracture the crust, but they were probably sufficient to enhance the lateral propagation of fractures along preferred trends. Also, some mechanism widened the fractures after their formation. At present, thermal fracturing, tidal deformation and internal convection are the most tenable models for the origin of Europa's fractures. More study needs to be done on the various models, however.

CHAPTER III: TERRAIN TYPES AND DISTRIBUTIONS

3.1 Introduction

In this section, I will examine the morphology and distribution of the three main terrain types and their subdivisions. Two of these, brown spots and mottled terrain, may be related, but are classed separately. The classification scheme developed here is similar to that developed by L&S, with some modification. The last section of this chapter will deal with possible origins for the terrains. However, the resolution problem limits the ability to differentiate among the various models. The terrain types are mapped on Plate 6, and are best seen in Fig. 1.3.

3.2 Plains

The plains units (Plate 6) are bright, orange-white, smooth regions crossed by abundant lineaments (Fig. 1.3). These units appear to dominate over others, and are found at all latitudes. The plains can be divided into four subunits: the smooth plains (Ps), fractured plains (Pf), lineated plains (Pl), and gray plains (Pg). These units are similar and appear to be subtle variations on each other.

The smooth plains are the brightest and most abundant, especially in moderate to high latitudes. Their color is off-white to pale orange-white. Along the terminator, very little relief is apparent. They are generally uniform in brightness and color, except for the ubiquitous lineaments. All lineament types are present in the smooth plains, except bright lineaments.

Fractured plains are smooth plains so highly fractured as to make mapping very difficult. It is possible that the density of fracturing in the fractured and smooth plains may be related to the thickness of the icy layer at the time of fracturing. Areas of denser fracturing would be areas of thinner crust in this model. A similar concept has been applied on Ganymede (Fink and Fletcher, 1981) (see Sect. 5.1). Lineated plains are found south of the fractured plains (Plate 6). They comprise abundant, very faint dark curvilinear and irregular lineaments that are not easily distinguished from the intervening plains. They may be related to the fractured plains, to Agenor Linea, which crosses this area, or to the ridges to the south. They are too poorly resolved to properly discuss their origin, however.

Gray plains are also similar to smooth plains except for a slightly lower albedo and a slight grayish-brown to greenish-brown tint. Their spectra are very similar to bright plains except for an increased absorption at ultraviolet wavelengths (L&S). It appears as though these plains may have been stained. This subunit is almost always associated with and darkest near brown mottled terrain, which may have acted as a source for the stain. The contacts between the plains units are extremely diffuse, but between any one of them and either brown spots or mottled terrain, it is very sharp.

3.3 Brown Spots

Brown spots (Sb) are irregular, well defined, low albedo markings within the plains units. Their color is similar to that found in fracture fillings. They vary in size from pixel size to 150 km (Thera, Thrace and Tyre Maculae; Plate 6). Some appear to be small dark rings, but are too poorly resolved to be certain. Unfortunately, no brown spots can be unambiguously identified near the terminator or correlated with topographic effects there.

Tyre Macula (Plate 6) has been proposed to be an impact scar, or palimpsest (L&S). It is roughly circular in shape, and under high enhancement, displays a set of narrow concentric rings, or lineaments (Fig. 2.1), supporting an impact interpretation. Also under high enhancement, the spot appears to have a serrated edge, similar to that observed around Mare Crisium. Although Minos Linea is tangential to Tyre Macula (L&S), others are not, and mapping (Plates 1-6) does not reveal any obvious structural control of fracturing by Tyre Macula, as proposed by LS&F.

Thrace and Thera Maculae are irregular and more sharply defined than Tyre Macula. Portions of the plains units around Thrace Macula appear to have 'calved' off from the surrounding plains and rotated partially into the brown spot, resembling tabular icebergs. In this model, the larger brown spots may represent frozen-over polynyas (irregular ice-free areas in polar ice packs). This is consistent with the floating icy crust model developed for wedge-shaped bands. The absence of any concentric structures within or outside these spots suggest that impact is not a likely origin for these spots.

Most spots appear isolated and not associated with linear or lineament trends. Local clustering does occur (Fig. 2.3; Sb in Plate 6), suggesting these may represent centers of 'volcanic' or diapiric activity analogous to the lunar Marius Hills, Martian Elysium volcanics, or terrestrial Hopi Buttes.

3.4 Mottled Terrain

Mottled terrain (patterned unit in Plate 6) is generally characterized by low albedo and an orange-brown color similar to brown spots and most fracture fillings. It has been associated with the hummocky or irregular topography along the terminator (Smith et al., 1979b; L&S). This unit is generally confined to equatorial areas between 40 degrees north and south, although small, subdued patches may occur as far south as 50° S. It is possible brown units are covered by polar frost deposits (Murray, 1975; Purves and Pilcher, 1981), an idea supported by the brightening of Minos Linea, a triple band at approximately 40° N (L&S). Medium-range images indicate that this terrain is distributed over most longitudes.

Albedo is highly variable within mottled terrain. The terrain appears to consist of partially coalesced brown spots, imbedded in gray plains. Along the contact with plains units, mottled terrain commonly breaks down into discrete brown spots (Fig. 2.8). For these reasons, brown spots and mottled terrain are considered to have similar or related origins.

Only three lineament types have been identified within the terrain: triple bands, ridges, and bright lineaments. Triple bands tend to blend into the terrain over a short distance, suggesting a possible relationship between the two; the few ridges present do not appear to be affected by the terrain. All other lineament types abut against the terrain. Occasionally mottled terrain will cluster around some triple bands, but not necessarily at triple band intersections as suggested by L&S.

Stereo views (Fig. 3.1) are suggestive of possible relief along the mottled terrain-plains contact northeast of Thrace Macula. The appearance is that of a narrow, plains-facing scarp. This apparent scarp correlates well with the observed contact. Some ridges appear to emanate from an elevated plateau of similar height, corresponding to the mottled terrain-plains contact. Some areas of plains material near the terminator are clearly surrounded by higher elevation, but contrast loss makes it difficult to locate the contact here. These features may be illusory, however, due to the limited resolution and poor illumination. Caution should be used in citing them as evidence.

3.5 Minor Terrain Units

Bright lineated terrain (Lb) consists of abundant bright lineaments (q.v.) in mottled terrain near the anti-jove point. These may represent frost deposits along fractures or a variety of simple lineaments, as discussed in Sect. 2.8. Irregular bright terrain (Ib) (Plate 6) is an area of irregular hills and depressions found

ORIGINAL PAGE IS
OF POOR QUALITY

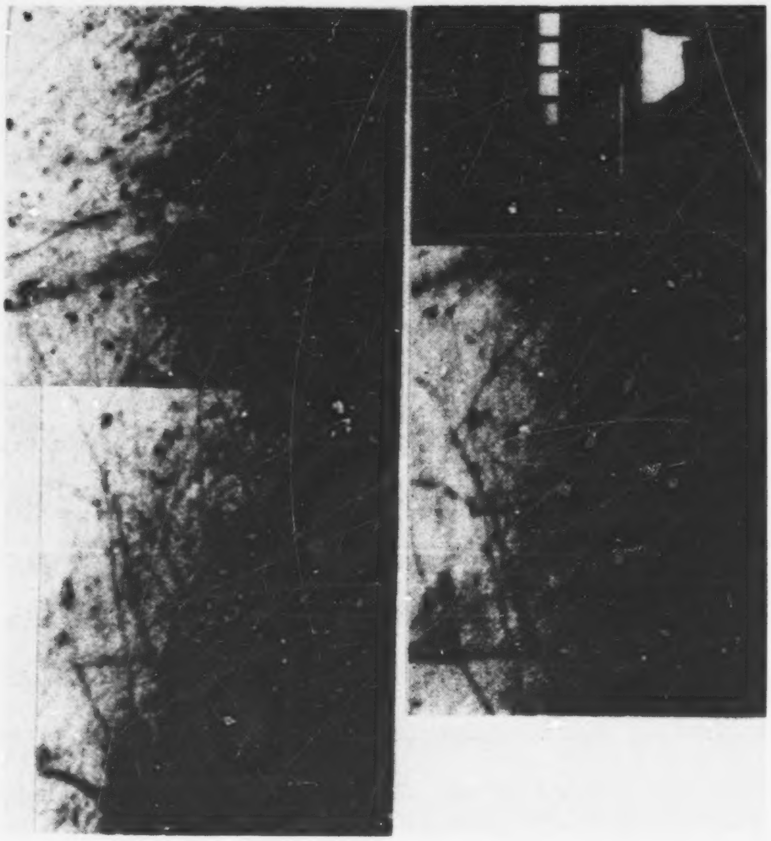

Fig. 3.1 Stereo pair of region north-northeast of Thrace Macula. The contact between the plains and mottled terrain runs from north to south approximately down the center of each image. See Fig. 1.2 for location.

immediately east of Tyre Macula along the terminator. It appears bright white in color photographs. The origin of this unit is unknown, due to its unknown distribution and relation to other features. It may be some form of ejecta deposit originating from Tyre Macula, but this is speculative.

3.6 Terrain Origins

Terrain origins can be divided into three possible classes: external, intrusive, or extrusive. Each model has implications regarding the relative ages of the various terrain units. Unfortunately, crater counts do not have enough statistical weight to constrain these ages.

It is conceivable that spots may represent craters, or puncture marks, in a thin, icy crust. This has been discussed for the large spots. The lack of concentric fractures or other potential impact-related features near other spots, and their generally polygonal shape tends to argue against an impact origin for most spots.

Extrusive models for brown terrain development include flooding of plains units materials onto mottled terrain and vice versa. There are two ways to model the former. The first is to flood low-lying mottled terrain areas with a relatively clean liquid, presumably water, and freeze it. This is equivalent to the 'silicate mountain' model outlined in Smith et al. (1979b). In areas of rifting, this would require ice to flow around fixed and rooted 'silicate' mountains, much like an ice sheet, but this is not observed. The maintenance of such relief on the ice-silicate core interface is considered unlikely for Europa (Smith et al., 1979b; L&S).

The second is to melt major portions of an original crust, allowing any impurities to settle, and then refreeze the layer, rafting any remaining portions of original crust (mottled terrain). Fracture patterns are not consistent with the freezing of a layer adjoining a fixed 'shoreline.' Observations of the freezing of fresh-water lakes suggests a pattern both radial and parallel to any confining shore (Zumberge and Watson, 1953). Rather, fracture patterns appear interrupted, or covered, by mottled terrain. Some lineaments are observed to disappear into mottled terrain, only to reappear on the other side along the same trend. This observation is more consistent with a third extrusive model.

The third model requires that mottled terrain be young, formed by material flooded out onto the plains units, presumably as 'lava' flows. This is consistent with most observations, including the apparent scarp along the contact, the sharpness of which does not unequivocally prove any model, however. The low viscosity of liquid water or a water-enriched slurry (two possible 'lavas') could account for the low relief. Small, individual intrusions from many discrete sites, including fractures, rather than massive eruptions from a few sites, could account for the mottled or spotty character. This would be especially true if eruptions occurred in several phases. This model is consistent with the overflow model for triple bands.

A modification of the latter model suggests that the brown units represent exposures of diapir-like intrusives, analogous to terrestrial salt domes. Although structurally controlled 'salt doming' along fracture traces is an intriguing idea for triple bands, it is unlikely they would form in stable crust; the 'dirty' material, most probably being denser than the ice, would resist ascent to the surface (Parmentier and Head, 1979).

The observation of possible 'calving' of fragments into Thrace Macula (Sect. 3.3) suggests that some spots may be sites of crustal foundering. Similar irregular spots, formed by the foundering of crustal blocks and exposure of fresh material, were seen in the formation of the Alae Lava Lake crust (Peck and Kinoshita, 1976).

The association of gray plains with spots and mottled terrain is at first glance difficult to reconcile with any of the models. However, ice (and silicate) particles sputtered from the surface by high-energy magnetospheric particles will follow a ballistic trajectory (Purves and Pilcher, 1980). It is possible that gray plains represent otherwise clean ice contaminated by particles or frost derived from sputtering off adjacent, recently formed mottled terrain. L&S report that spectral curves for gray plains are darker in the ultraviolet than other units. Perhaps certain components of the mottled areas were preferentially sputtered, thus biasing the contaminant composition and spectral character. L&S also suggest that the darkening of the gray plains may result from formation of a lag deposit through the selective sputtering of ice. However, this is not consistent with the sharp contact between the gray plains and the associated mottled terrain. Eviatar et al. (1981) report the detection of sulfurous particles (e.g. SO_2) on Europa's trailing hemisphere, apparently implanted by Jupiter's magnetosphere. This might explain the apparent darkening of the trailing hemisphere (T. Johnson et al., 1981) and the possible correlation of infrared spectroscopy with a polysulfide contaminant (Lebovsky and Fegley, 1976). It may also account for gray plains observed west of the anti-jove point, but does not explain their association with mottled terrain nor their presence east of the anti-jove point (Plate 6).

Observations of terrain units on Europa tend to support an extrusive model for the formation of brown mottled terrain, but not conclusively. In any case, the spectral and visual similarities between the brown terrain units and fracture fillings (L&S; McCord et al., 1982) suggests that they were derived from the same material and possibly the same source region. As will be shown later, this probably was a contaminated liquid-water layer immediately subjacent to the icy crust.

CHAPTER IV: COMPARISONS AND ANALOGS

4.1 Sea Ice

Comparisons and contrasts between Europa's fracturing and terrestrial sea ice features have been made throughout this thesis. Leads, shear and pressure ridges, and possibly polynyas (Fig. 4.1), all seem to be useful analogs to features on Europa. Further analogs might be found with higher resolution. The fact that these comparisions can be so abundantly made underscores the probability that these features formed in an icy crustal layer underlain by a liquid or quasi-liquid layer. This also supports suggestions that Europa may prove to be a unique natural laboratory for the study of the behavior of large scale ice covers.

According to the elastic-plastic theory of sea ice behavior (Coon and Pritchard, 1975), under typical terrestrial conditions sea ice cannot support tensile stress, and responds plastically over a broad pressure and temperature range to compressional stress before rupturing. In other words, leads (open fractures) and ridges form under tensile and compressional stress, respectively. This model is consistent with the observed abundance on Europa of simple lineaments and wedge-shaped bands, and of ridges, interpreted as tensional fractures and compressional features, respectively. While Europa's fracturing style resembles that of sea ice, fracture patterns on Europa are highly rectilinear in contrast to sea ice patterns (Fig.

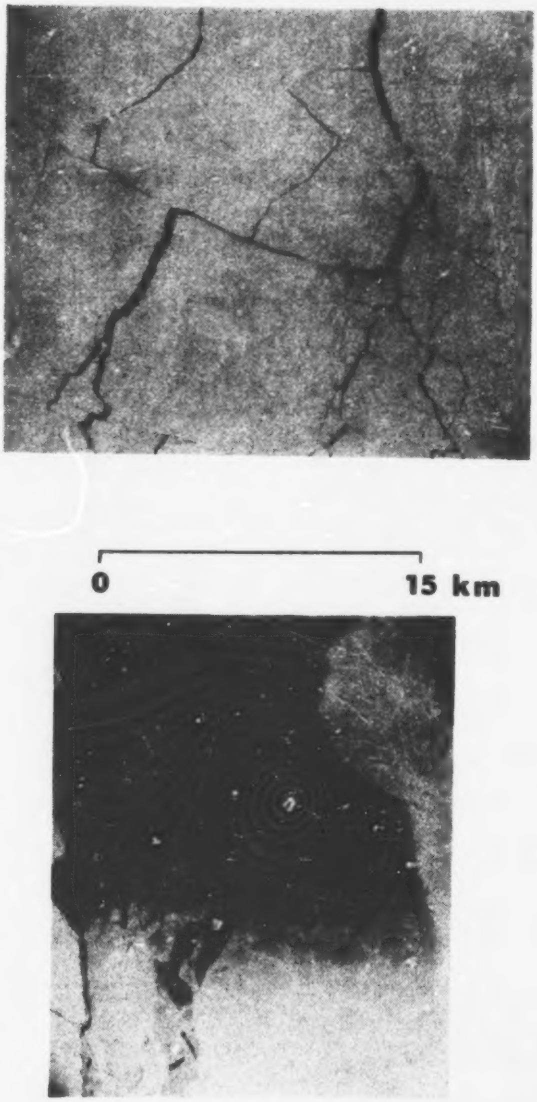

Fig. 4.1 Selected photographs of terrestrial arctic sea ice.

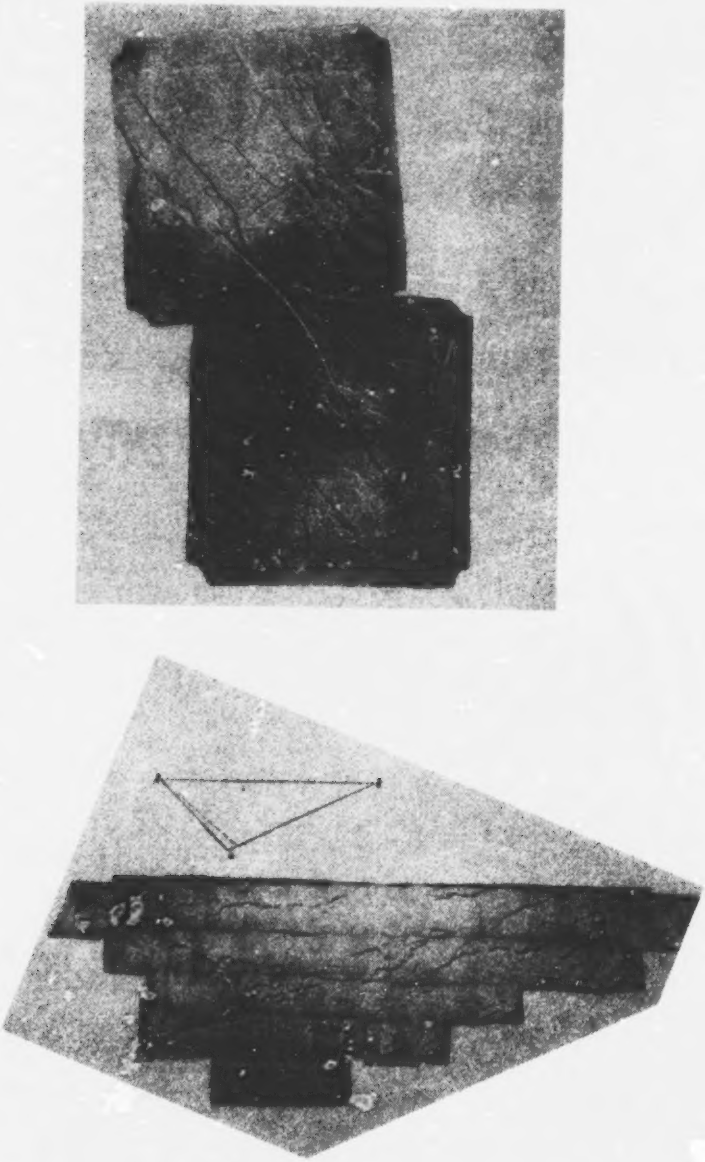

Fig. 4.1 (cont.)

ORIGINAL PAGE IS
OF POOR QUALITY

4.1), supporting suggestions of structural control during formation of Europa's fractures.

The present surface temperature of Europa is near 100° K, well below that encountered in terrestrial polar regions or typically employed in the laboratory. At this low temperature, ice behaves brittlely and plastic behavior is much more restricted (Parameswaran and Jones, 1975). Thus, very cold ice behaves much as silicate rocks do at room temperature. This suggests that Europa's icy crust would deform brittlely under present conditions and that the observed sea ice type features were more likely formed at a time when the crust was considerably warmer than at present. Thermodynamic considerations (Cassen et al., 1980) suggest that internal heat is quickly lost through the ice over geologic time. Therefore it is possible to imagine a scenario in which Europa's upper layer was warmer in the past and floated over a liquid water layer, much like sea ice. During this time the crust was deforming elastic-plastically, followed by a cooling period marked by refreezing of the liquid layer.

4.2 Lava Lakes

Terrestrial lava lakes display many features that may be analogous to some on Europa. Tension cracks in lava crusts (Fig. 4.2), revealing hot magma beneath, are common during Hawaiian eruptions (Peck and Kinoshita, 1976; Peck et al., 1979). These cracks strongly resemble wedge-shaped bands and simple lineaments. Irregular patches of subcrustal magma are also common near the intersections

Fig 4.2 Alae Lava Lake, Hawaii, during 1963 eruption. View is from crater rim. Bright curvilinear and irregular features are exposures of hot magma through fractured and foundered basaltic crust (Peck and Kinoshita, 1976).

of some cracks, where blocks of crust have foundered (Fig. 4.2). These bear a strong resemblance to brown spots. Other comparisons may be possible with higher resolution.

Studies of the Kilauea lava lakes by Peck and Kinoshita (1976) revealed several important rheological and thermodynamic differences between the freezing of sea ice and basaltic lava. The contact between lava crusts and the subjacent magma was found to be gradational, because of the heterogenous mineral composition of basalt. Sea water and sea ice have a sharp phase boundary. Thus basaltic lava lakes more easily transmit stress through the crustal layer, which acts as a recorder of that stress. Theoretically, dense basaltic crusts should be hydrostatically unstable, but Kilauean crusts were relatively buoyant due to incorporation of vesicles as they solidified. Foundering was less common than expected. As basaltic lava cools it forms suspended crystals and exsolves gas bubbles, both of which 'stiffen' the lava, giving it a more plastic-like viscosity than sea water (Peck et al., 1979).

The morphology of the filled lava crust fracture in Fig. 4.3 is reminiscent in some ways of triple bands; more so than wedge-shaped bands, which are better modeled by sea ice. Triple bands may reflect a fracturing episode during which the sub-crustal layer behaved in a more plastic manner. Differences in fracture style may reflect differences in the state of Europa's sub-crustal layer.

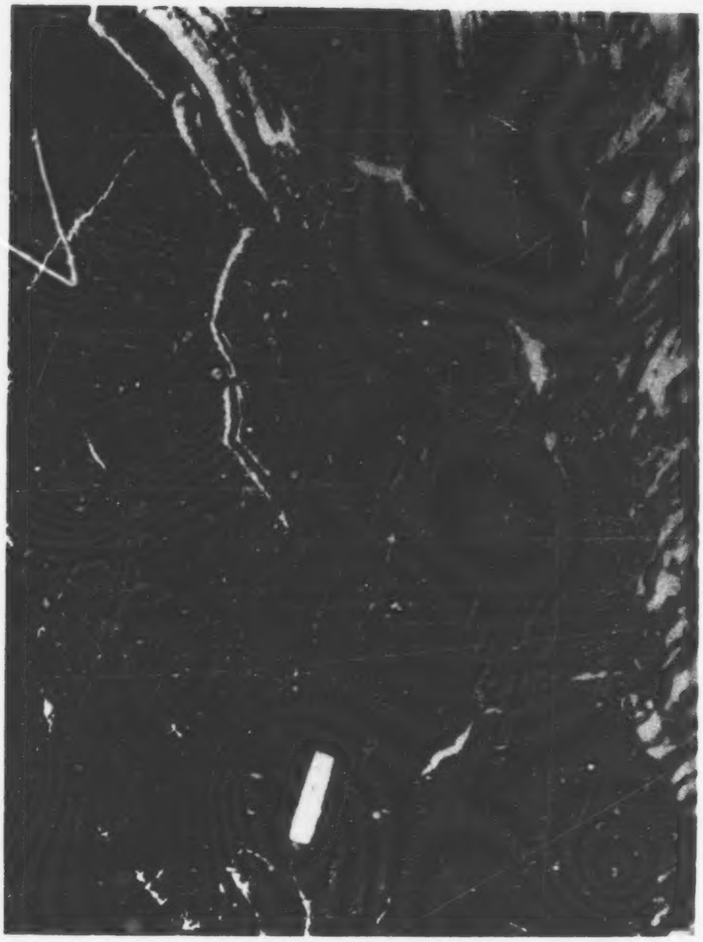

Fig. 4.3 Solidified crack in a Kilauea lava flow. Scale bar is 2 meters long.

4.3 Ganymede vs. Europa

Internally, Europa most closely resembles Io (Table 1.1), and may ultimately reflect this in its history. The surface materials on Europa, however, most closely resemble those of Ganymede and a comparison of surface features can be made.

Features on the two bodies bear no direct resemblance to each other. Formation of Ganymede's grooves is often ascribed to graben-style tensional fracturing (Lucchitta, 1980; Allison et al., 1982) and localized infilling (Parmentier et al., 1982). This deformation does not appear to involve crust-penetrating fracturing but rather in situ deformation of older terrain (Lucchitta, 1980), and intra-crustal extension and necking (Parmentier and Head, 1982), as described by Tapponier and Francheteau (1978) for continental and mid-ocean rifts.

Comparison of medium-range photographs of Ganymede (see Fig. 23 in Smith et al., 1979b) with the photograph of the Antarctic ice sheet in Fig. 4.4 shows a startling similarity. Fig. 4.4 shows an area near the edge of the West Antarctic ice sheet (vicinity Ross Sea) that is currently undergoing stretching as downslope portions accelerate. Within this area, blocks of relatively undeformed ice have been separated by deformed zones and partially rotated. The deformed zones contain discontinuous groove sets in curvilinear wedge-shaped belts, reminiscent of grooved terrain on Ganymede (Parmentier et al., 1982), and not to be confused with wedge-shaped

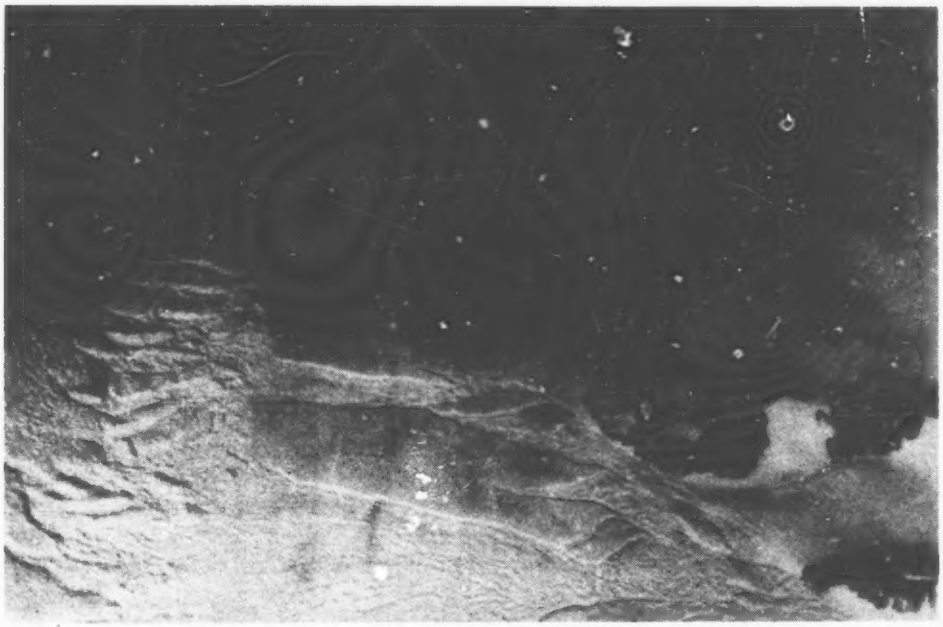

Fig. 4.4 Antarctic ice sheet, vicinity of Ross Sea and the Transantarctic Mtns. Photo approximately 5-10 miles wide. Courtesy of W. Burdelik.

is no suggestion

bands on Europa. There is no suggestion of flooding by any new material within these zones. In Antarctica and on Ganymede, 'new' crustal material appears to have been created by lateral stretching of the upper layer and intracrustal, or continental style, deformation (i.e. thick-skin tectonics). Europa, as discussed earlier, is characterized by sea ice style deformation (i.e. thin-skin tectonics).

Another important observation is the reversal in the albedo relationship between old and young crustal material. On Ganymede, older, darker, more silicate-rich crust has been replaced by brighter, relatively silicate-free material (grooved terrain). This is consistent with the thermodynamic models of Parmentier and Head (1979) in which Ganymede retains much of its primordial crust. This contrasts with the 'clean' older crust and darker, contaminated replacement material from the interior seen on Europa. This suggests a more complicated history for Europa involving total replacement of the outer layers, and minor subsequent replacement from a well-mixed subcrustal layer.

Although Io and Europa are grossly similar and appear to be or have been active internally, the differences in surface composition preclude direct comparison. If Io did possess water after formation, it has since been lost. No Europa- or Ganymede-style fracturing or deformation is apparent, despite the high resurfacing rate (Smith et al., 1979a). This may be due to the different mechanical properties of a sulfur-enriched crust on Io.

CHAPTER V: DISCUSSION AND CONCLUSIONS

5.1 Crustal Models

Two types of crustal models for Europa have been proposed in the literature (Fig. 5.1). The 'thick-ice' models propose that an ice shell to 150 km thick overlies a 'dry' silicate interior (Consolmagno and Lewis, 1976). Fanale et al. (1977) estimate the thickness of the icy crustal layer at ~75 km, the lower 35 km possibly being liquid. Both models assumed chondritic heat flux values. Cassen et al. (1980) suggested that any thick water layer would freeze within a few million years.

Thin-ice models developed after the Voyager missions proposed that a large portion of Europa's water was tied up as water of hydration in a 200-300 km thick zone of hydrated silicate material beneath a brittle, ~25 km thick icy crust (Ransford et al., 1981). Observation of abundant crust-penetrating fractures and other sea ice style features tend to support the thin-ice model of Ransford et al. (1981), a conclusion similar to that reached by L&S (q.v. for further discussion). Unfortunately, there is no evidence that the proposed hydrated silicate zone exists.

Crustal deformation, as described in the preceding chapters, suggests that a modification of thin-ice models might be necessary. A major conclusion of this work is that the icy crustal layer was underlain by a liquid-like layer, at least during fracture formation.

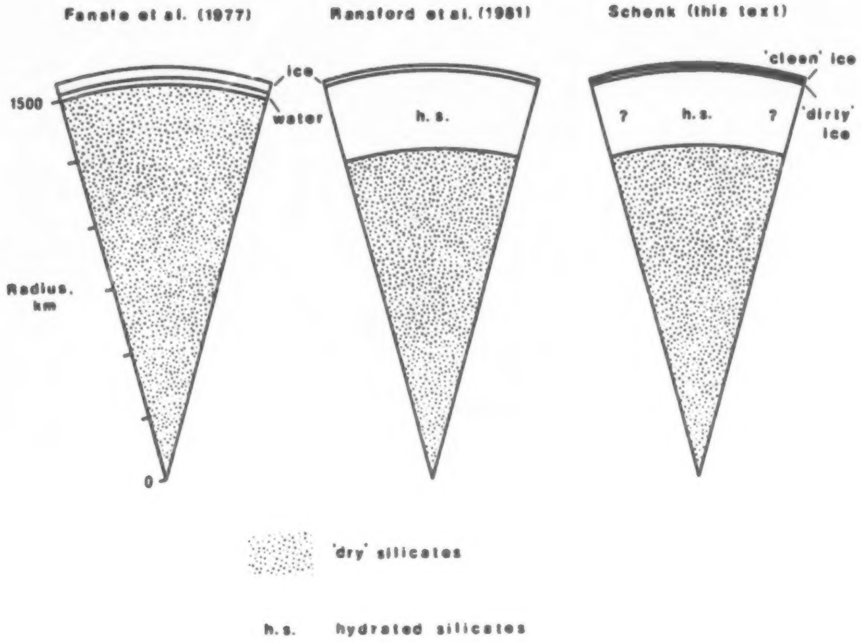
Fanale et al. (1977)
Ransford et al. (1981)
Schenk (this text)
ice
water
1500
Radius, km
0
h. s.
'clean' ice
?
h. s.
?
'dirty' ice
'dry' silicates
h. s. hydrated silicates

Fig. 5.1 Comparison of models of Europa's interior.

This subcrustal layer is presently exposed as brown fracture fillings, implying the existence of an intermediate layer (layer 2) between the icy crust and silicate interior. Plastic (thick-skin) style deformation would be expected if the hydrated silicate layer, as described by Ransford et al. (1981), was directly beneath the icy layer during fracture formation. The sea ice style of fracturing, relatively high albedo of the fracture fillings (~ 50%), and the dominance of water in Europa's spectra suggest that layer 2 was composed of liquid water, with a minor amount of orange-brown contaminant. The nature and source of this contaminant is unknown.

The thicknesses of these outer layers is a major question that cannot be answered directly. Price (1966) reported that joint spacing in subhorizontal rock layers was inversely proportional to their thickness. This relationship is dependent on several assumptions: no lateral lithologic variations, no major tectonic events, and no effective cohesion between the layers, assumptions that can be regarded as reasonably valid for the proposed crustal model. Visual inspection of smooth plains at mid-latitudes suggests an average spacing between lineaments of 30-40 km, and a corresponding maximum estimated thickness of 9-10 km for the outer icy layer. A ratio of between 3.4 and 4.0 between lineament spacing and crustal thickness was used. This is the same ratio used by Fink and Fletcher (1981) when they applied a similar concept to grooves on Ganymede. The 9-10 km estimate is half the value proposed by Ransford et al. (1981), but does not include layer 2, since the lineaments are interpreted as having been formed while layer 2 was liquid. The inferred thickness value will decrease if increased resolution reveals more fractures.

5.2 Origin and Evolution of Europa's Surface

My model for wedge-shaped bands and simple lineaments requires a sub-crustal liquid layer during their formation. Since a liquid layer is expected to freeze geologically quickly (Cassen et al., 1980), an energy source supplementary to radioactive decay and normal tidal energies is needed to maintain the liquid state throughout Europa's geologic history, or to initiate a recent remelting event. The proposed initiation of the three-way orbital resonance lock among the inner Galilean satellites at ~200 m.y. (Yoder, 1979) (corresponding to the maximum age estimate of Shoemaker and Wolfe, 1982), and the associated boost in tidal flexing due to forced eccentricities, may have been sufficient to melt any preexisting icy crustal layer, or stimulate extensive outgassing of watery materials from dehydration reactions in the interior, as described by Ransford et al. (1981).

Extensive outgassing may have had several effects in addition to creating a global ocean. If the outgassing was energetic enough, suspended silicates may have been introduced into the ocean, creating the observed coloration. Contamination of the ocean may have resulted from the concentration of dissolved 'salts' into a brine as the water layer continued to freeze (Reynolds and Cassen, 1979). Alternatively, primordial gases (CO_2 and CH_4), released from the interior, may have produced organic molecules by reacting with water in fracture fillings, as suggested by Schonfeld (1982). Outgassing would also provide a convenient mechanism for apparent planetary expansion and the opening of some fractures.

If an original outer layer were completely remelted, any original fracture patterns would be erased. The exposure of liquid water to deep space would result in violent boiling (Parmentier and Head, 1979), perhaps sufficient to generate a temporary atmosphere. The generation of this atmosphere would have released large quantities of heat into deep space, enhancing refreezing. With its source then removed, this atmosphere would both diffuse into space and condense out on the ice, possibly explaining the observed surface frosts.

If not totally remelted, fracture patterns, craters, spots, etc., would tend to anneal due to enhanced viscous relaxation and gravitational segregation of silicates (Parmentier and Head, 1979) in the warmed crust. This would result in an artifically young age, and the 200 m.y. date of Shoemaker and Wolfe (1982) would reflect the time of this event, not the original age.

In either case, a new fracture network would develop in the new crustal layer as it began refreezing, due to tidal flexing, thermal fracturing or some combination of these and other factors. Tidal flexing probably enhanced the lateral propagation of preferentially-oriented fractures. This is the probable origin for the 'grid'

C-2

pattern in Fig. 2.7a. Outgassing of volatiles into the subcrustal ocean may have caused the observed coloration and may have generated a localized convection cell or plume beneath the anti-jove point, explaining the opening of wedge-shaped bands. Most of the observed lineaments and brown terrain units were probably formed during this epoch, as the global ocean began refreezing. The spectral similarity and global distribution of brown fracture fillings and terrain units (McCord et al., 1982) suggests they are formed from similar materials, and perhaps from the same source region, i.e., a global subcrustal ocean.

Fracturing and deformation probably continued during the refreezing of the subcrustal ocean, accounting for the overlapping age relationships among the lineament types. Shortly after the icy crust first formed, the subjacent liquid-water layer became contaminated, probably as a result of continued outgassing. Whether the subcrustal ocean has since refrozen is a moot point. If the crust was remelted at ~ 200 m.y., calculations by Cassen et al. (1980) suggest refreezing within several million years. If refrozen to a depth below 10 km, the ice would be 'soft' (L&S), and probably behave plastically. Triple bands may reflect deformation of a crust in such a state, but this is uncertain.

Europa's features can be explained by a history involving a major reheating event several hundred million years ago, the creation of a global ocean, and subsequent refreezing. Any record of Europa's history prior to this event appears to have been erased. The history of this period is thus unknown, although if Yoder's (1979) model is correct, Europa may have been quiet during its first 4.4 b.y.

The evidence for the above scenario is not conclusive, although in some regards it is compelling. It is hoped that the following proposed outline will promote further discussion of Europa problems and their solutions. It is also hoped that these ideas will promote debate as to their merit and validity.

1. 4,600 to 200 m.y. ago. Presumably events during this epoch included accretion into a globe and subsequent differentiation, which may or may not have been completed. No record of these events appears to have been preserved.

2. ~200 m.y. ago. Creation of a three-way tidal resonance lock with Io and Ganymede may have been responsible for a sudden, large-scale increase in tidal heating, remelting major portions of the exterior, creating a global ocean, and perhaps stimulating outgassing from the interior. A temporary atmosphere may have been generated at this time.

3. ~200 m.y. to the present. Due to tremendous heat loss into space, the global ocean began refreezing. Tidal, thermal and mechanical stresses acted on the newly forming icy crustal layer, fracturing, and perhaps locally flooding it. Oscillating tidal stresses probably acted as a controlling factor on the orientation and growth of many of these fractures. Whether this fracturing has continued to the present or whether any liquid remains below the surface is not ascertainable from the present data, although

thermodynamic analysis suggests no liquid remains.

Europa's history is certainly more complex than the above discussion suggests. Minor contraction episodes due to the cooling of the near-surface layers to their present low temperature, cyclic remelting episodes and the recoupling of the icy crust to the silicate interior are possible processes that have not been discussed. Also, the 200 m.y. age, based on comparison with lunar crater curves, is poorly constrained (M. Gurnis, personal communication), although the relative youth of the surface is readily apparent from the images.

5.3 Conclusions

Several conclusions can be drawn from the preceding discussion of Voyager imaging and groundbased data. Despite resolution and coverage limitations, these conclusions, and the preceding tentative geologic history, can be advanced with some confidence.

1. Offsets of simple lineaments associated with wedge-shaped bands demonstrates that Europa's crust has been fractured and new, darker material emplaced from below. Although the exact mechanism(s) of fracturing is (are) uncertain, fracture development was probably controlled by tidal oscillations and stresses. The 'grid' pattern in Fig. 2.7 is evidence thereof. Other forces may have been responsible, including global expansion during outgassing, and thermal fracturing.

2. Geometrically, plate tectonics is useful in describing the motions associated with the opening of wedge-shaped bands and the wedge-shaped band rift zone and rotations of crustal blocks. A

compressional zone associated with this opening may exist in the form of the bright band Agenor Linea. The different crustal and subcrustal materials result in a distinctly different style of deformation compared to terrestrial rifting, however. Care must be taken in extending this comparison beyond the geometrical sense, although a convective cell may have been operating during wedge-shaped band formation.

3. A liquid or liquid-like subcrustal layer was present during the formation of wedge-shaped bands, simple lineaments, and possibly other lineament types. The sea ice style of fracturing supports this. The high albedo of fracture fillings and the ubiquitous water in Europa's spectra imply that this layer was dominantly water, with some orange-brown coloration.

4. Europa's crust appears to have two layers: a fractured, relatively 'clean' icy upper layer ~10 km thick, and a subjacent 'dirty' water-rich layer from which most fracture-filling material probably originated. The brown terrain units may have been formed by extrusions from or exposures of this dirty layer. Aside from this second layer, the evidence cited here tends to support thin-ice crustal models in which a relatively thin ice layer, here divided into two, is underlain by a 200-300 km thick hydrated silicate zone (Ransford et al., 1981), although there is no observational evidence for this hydrated silicate zone. Implicit in this conclusion is that Europa's crust was decoupled from the rocky interior during deforma-

tion, in contrast to the conclusions of Finnerty et al. (1981) and L&S.

5. The extremely smooth and relatively 'clean' icy surface and low crater density imply a recent resurfacing event on Europa. This may have been linked to the inception of a tidal lock among the inner satellites and a forced eccentricity (Yoder, 1979), which possibly resulted in the formation of the subcrustal ocean. Many, if not most, of Europa's surface features were probably formed during this time and the subsequent refreezing of the ocean.

6. Several of the lineament types appear to be related. Wedge-shaped bands are probably simple lineaments that have been opened more than a few kilometers, linear ridges are probably simple lineaments under low sun angles, and triple bands may have evolved from simple lineaments.

7. Sea ice and lava lake crustal behavior are both valuable models for the fracturing and mechanical properties of Europa's crust during deformation. I encourage further comparison of Europa with these terrestrial analogs.

Future investigations are limited because of the quality of the data. New breakthroughs will probably have to await the arrival of the Galileo orbiter in the late 1980's. This mission is designed to perform the first in-depth, long-term investigation of the Jupiter system. A solid-state imaging system is expected to provide highest resolution in the 10's of meters on the four Galilean satellites, and the near-infrared mapping spectrometer should be able to determine the composition of the orange-brown material on Europa's surface, thus answering many questions (it is hoped). More accurate crater counts, and relative ages, should also result. Whether fractures are visible down to Galileo's resolution limit and whether there is any relief along the plains-mottled terrain contact may also be determined.

REFERENCES CITED

Allison, M., Head, J., and Parmentier, E., 1982, Grooved terrain on Ganymede: origin as flooded graben, in Morrison, D., ed., Satellites of Jupiter: Tuscon, Univ. Arizona Press.

Anderson, V., 1970, Sea ice pressure ridge study: an airphoto analysis: Photogrammetria, v. 26, p. 201-228.

Black, R., Jackson, M., and Berg, T., 1965, Saline discharge from Taylor Glacier, Victoria Land, Antarctica: Jour. Geology, v. 73, p. 175-180.

Casella, C., 1976, Evolution of the lunar fracture network: Geol. Soc. Am. Bull., v. 87, p. 226-234.

Cassen, P., Peale, S. J., and Reynolds, R. T., 1980, Tidal dissipation in Europa: a correction: Geophys. Res. Lett., v. 7, p. 987-988.

Cassen, P., Reynolds, R. T., and Peale, S. J., 1979, Is there liquid water on Europa? Geophys. Res. Lett., v. 6, p. 731-734.

Clark, R., 1980, Ganymede, Europa, Callisto and Saturn's rings: compositional analysis from reflectance spectroscopy: Icarus, v. 44, p. 388-409.

Clark, R., and McCord, T., 1980, The Galilean satellites: new near-infrared spectral reflectance measurements (0.65-2.5 μm) and a 0.325-5 μm summary: Icarus, v. 41, p. 323-339.

Coon, M., and Pritchard, R., 1975, Application of an elastic-plastic model of arctic pack ice, in Reed, J., and Sater, J., eds., The coast and shelf of the Beaufort Sea: Arlington, Arctic Inst. of No. America, p. 173-194.

Consolmagno, G., and Lewis, J., 1976, Structural and thermal models of icy Galilean satellites, in Gehrels, T., ed., Jupiter: Tuscon, Univ. Arizona Press, p. 1035-1051.

Corbett, M., 1979, Origin of pervasive orthogonal fracturing of the Earth's crust, in Podwysocki, M., and Earle, J., eds., Proc. second intl. conf. on basement tectonics: Denver, Basement Tectonics Committee, Inc., p. 319-325.

Davies, M., and Katayama, F., 1981, Coordinates of features on the

Galilean satellites: Jour. Geophys. Res., v. 86, p. 8635-8657.

Dzurisin, D., 1978, The tectonic and volcanic history of Mercury as inferred from studies of scarps, ridges, troughs, and other lineaments: Jour. Geophys. Res., v. 83, p. 4883-4906.

Evans, R., 1971, Cracks in perrenial sea ice due to thermally induced stress: Jour. Geophys. Res., v. 76, p. 8153-8155.

Evans, R., and Untersteiner, N., 1971, Thermal cracks in floating ice sheets: Jour. Geophys. Res., v. 76, p. 694-703.

Eviatar, A., Siscoe, G., Johnson, T. V., and Matson, D., 1981, Effects of Io ejecta on Europa: Icarus, v. 47, p. 75-83.

Fanale, F., Johnson, T. V., and Matson, D., 1977, Io's surface and the histories of the Galilean satellites, in Burns, J. A., ed., Planetary satellites: Tuscon, Univ. Arizona Press, p. 379-405.

Fink, J., and Fletcher, R., 1981, Variations in thickness of Ganymede's lithosphere determined by spacing in lineations (abs.): Lunar Planet. Sci. XII, p. 277-278.

Finnerty A., Ransford, G., Pieri, D., and Collerson, K., 1981, Is Europa's surface cracking due to thermal evolution? Nature, v. 289, p. 24-27.

Frank, F. C., 1968, Curvature of island arcs: Nature, v. 220, p. 363.

Hanal, R., Conrath, B., Flasar, M., Herath, L., Kunde, V., Lowman, P., Maguire, W., Pearl, J., Pirraglia, J., Samuelson, R., Gautier, D., Gierasch, P., Horn, L., Kumar, S., Ponnamperuma, C., 1979, Infrared observations of the Jovian system from Voyager 2: Science, v. 206, p. 952-956.

Helfenstein, P., and Parmentier, E., 1980, Fractures on Europa: possible response of an ice crust to tidal deformation: Proc. Lunar Planet. Sci. Conf. 11th, p. 1987-1998.

Johnson, R. E., Lanzerotti, L., Brown, W., Armstrong, T., 1981, Erosion of Galilean satellite surfaces by Jovian magnetospheric particles: Science, v. 212, p. 1027-1030.

Johnson, T. V., Soderblom, L., Mosher, J., Danielson, G., Kupfermar, P., 1981, Multispectral mosaics of the Galilean satellites (abs.): Lunar Planet. Sci. XII, p. 509-510.

Kieffer, H., and Smythe, W., 1974, Frost spectra: comparison with Jupiter's satellites: Icarus, v. 21, p. 506-512.

Kovacs, A., and Mellor, M., 1975, Sea ice morphology and ice as a geologic agent in the Southern Beaufort Sea, in Reed, J., and Sater, J., eds., The coast and shelf of the Beaufort Sea: Arlington, Arctic Inst. of No. America, p. 113-161.

Lebovsky, L., and Fegley, M., 1976, Laboratory reflection spectra for the determination of chemical composition of icy bodies: Icarus, v. 28, p. 379-387.

LePichon, X., Angelier, J., and Sibuet, J-C., 1982, Plate boundaries and extensional tectonics: Tectonophysics, v. 81, p. 239-256.

Lucchitta, B., 1980, Grooved terrain on Ganymede: Icarus, v. 44, p. 481-501.

Lucchitta, B., and Soderblom, L., 1982, The geology of Europa, in Morrison, D., ed., Satellites of Jupiter: Tuscon, Univ. Arizona Press.

Lucchitta, B., Soderblom, L., and Ferguson, H., 1981, Structures on Europa: Proc. Lunar Planet. Sci. Conf. 12th, Oxford, Pergamon Press.

Malin, M., 1980, Morphology of lineaments on Europa: Intl. Astron. Union Coll. 57, The satellites of Jupiter (Abs. 7-2).

McCord, T., Clark, R., Meloy, A., Nelson, M., Johnson, T. V., Matson, D., Mosher, J., and Soderblom, L., 1982, Spectral unit maps of Europa (abs.): Lunar Planet. Sci. XIII, p. 485-486.

McFadden, L., Bell, J., and McCord, T., 1980, Visible spectral reflectance measurements (0.33-1.1 m) of the Galilean satellites at many orbital phase angles: Icarus, v. 44, p. 410-430.

Melosh, H., 1980, Tectonic patterns on a tidally distorted planet: Icarus, v. 43, p. 334-337.

Melosh, H., and Dzurisin, D., 1978, Mercurian global tectonics: a consequence of tidal despinning? Icarus, v. 35, p. 227-236.

Morgan, W., 1968, Rises, trenches, great faults, and crustal blocks: Jour. Geophys. Res., v. 73, p. 1959-1982.

Murray, J., 1975, New observations of surface marking on Jupiter's satellites: Icarus, v. 25, p. 397-404.

Ostro, S., Campbell, D., Pettengill, G., and Shapiro, I., 1980, Radar observations of the icy Galilean satellites: Icarus, v. 44, p. 431-440.

Parameswaran, U., and Jones, S., 1975, Brittle fracture of ice at 77° K: Jour. Glaciology, v. 14, p. 305-315.

Parmentier, E., and Head, J., 1979, Internal processes affecting surfaces of low-density satellites: Ganymede and Callisto: Jour. Geophys. Res., v. 84, p. 6263-6276.

Parmentier, E., and Head, J., 1982, Emplacement of bright terrain on Ganymede in response to lithospheric extension (abs.): Lunar Planet. Sci. XIII, p. 615-616.

Parmentier, E., Squyres, S., Head, J., and Allison, M., 1982, The tectonics of Ganymede: Nature, v. 295, p. 290-293.

Peck, D., and Kinoshita, W., 1976, The eruption of August 1963 and the formation of Alae Lava Lake, Hawaii (Solidification of Alae Lava Lake, Hawaii): U. S. Geol. Survey Prof. Paper 935-A, 33 p.

Peck, D., Wright, T., and Decker, R., 1979, The lava lakes of Kilauea: Sci. Am., v. 241, no. 4, p. 114-129.

Pieri, D., 1981, Lineament and polygon patterns on Europa: Nature v. 289, p. 17-21.

Pilcher, C., Ridgway, S., McCord, T., 1972, Galilean satellites: identification of water frost: Science, v. 178, p. 1087-1089.

Pollack, J., and Reynolds, R., 1974, Implications of Jupiter's early contraction history for the composition of the Galilean satellites: Icarus, v. 21, p. 248-253.

Price, N., 1966, Fault and joint development in brittle and semi-brittle rock: Oxford, Pergamon Press, Ch. 3.

Purves, N., and Pilcher, C., 1980, Thermal migration of water on the Galilean satellites: Icarus, v. 43, p. 51-55.

Ransford, G., Finnerty, A., and Collerson, K., 1981, Europa's petrological thermal history: Nature, v. 289, p. 21-24.

Reynolds, R., and Cassen, P., 1979, On the internal structure of the major satellites of the outer planets: Geophys. Res. Lett., v. 6, p. 121-124.

Schenk, P., and Seyfert, C., 1980, Fault offsets and proposed plate motions for Europa (abs.): EOS (Am. Geophys. Union Trans.), v. 61, p. 286.

Schonfeld, E., 1982, Organic chemistry on Europa? (abs.): Lunar Planet. Sci. XIII, p. 691.

Shoemaker, E., and Wolfe, R., 1982, Cratering timescales for the Galilean satellites, in Morrison, D., ed., Satellites of Jupiter: Tuscon, Univ. Arizona Press.

Smith, B., Soderblom, L., Johnson, T. V., Ingersoll, A., Collins, S., Shoemaker, E., Hunt, G., Masursky, H., Carr, M., Davies, M., Cook, A., Boyce, J., Danielson, G., Owen, T., Sagan, C., Beebe, R., Veverka, J., Strom, R., McCauley, J., Morrison, D., Briggs, G., Suomi, V., 1979a, The Jupiter system through the eyes of Voyager 1: Science, v. 204, p. 951-972.

Smith, B., Soderblom, L., Beebe, R., Boyce, J., Briggs, G., Carr, M., Collins, S., Cook, A., Danielson, G., Davies, M., Hunt, G., Ingersoll, A., Johnson, T. V., Masursky, H., McCauley, J., Morrison, D., Owen, T., Sagan, C., Shoemaker, E., Strom, R., Suomi, V., Veverka, J., 1979b, The Galilean satellites and Jupiter: Voyager 2 imaging science results: Science, v. 206, p. 927-950.

Strom, R., 1964, Analysis of lunar lineaments: I-tectonic maps of the Moon: Univ. Arizona Lunar and Planet. Lab. Communs., v. 2, no. 39, p. 205-221.

Tapponier, P., and Francheteau, J., 1978, Necking of the lithosphere and the mechanics of slowly accreting plate boundaries: Jour. Geophys. Res., v. 83, p. 3955-3970.

Yoder, C., 1979, How tidal heating in Io drives the Galilean orbital resonance locks: Nature, v. 279, p. 767-770.

Zumberge, J., and Wilson, J., 1953, Quantitative studies on thermal expansion and contraction of lake ice: Jour. Geology, v. 61, p. 374-383.

CAPTIONS FOR PLATES 1-6

The plates are mercator maps of lineament and terrain distributions, as described in the text. The map edges extend from 55° N to 68° S latitude and from 130° to 230° W longitude. The anti-jove point is marked by a dot inside a circle. The scale is accurate at the equator, and the curved dashed line in the upper left-hand corner represents the approximate limit of highest-resolution imaging. Proper names are those adopted by the IAU.

Plate 4:

Bright bands are the two subparallel lineaments at approximately 40° S latitude; bright lineaments are the short lineaments clustered near the anti-jove point; gray bands are the two cycloid lineament sets toward the bottom of the map.

Plate 6:

EXPLANATION

Ps - Smooth plains
Pg - Gray plains
Pf - Fractured plains
Pl - Lineated plains
Lb - Bright lineated terrain
Ib - Irregular bright terrain
c - Crater
¢ - Inferred crater
Sb or irregular
dark spots - Brown spots
Patterned unit - Mottled terrain

Contacts are dashed where approximated.

ORIGINAL PAGE IS
OF POOR QUALITY

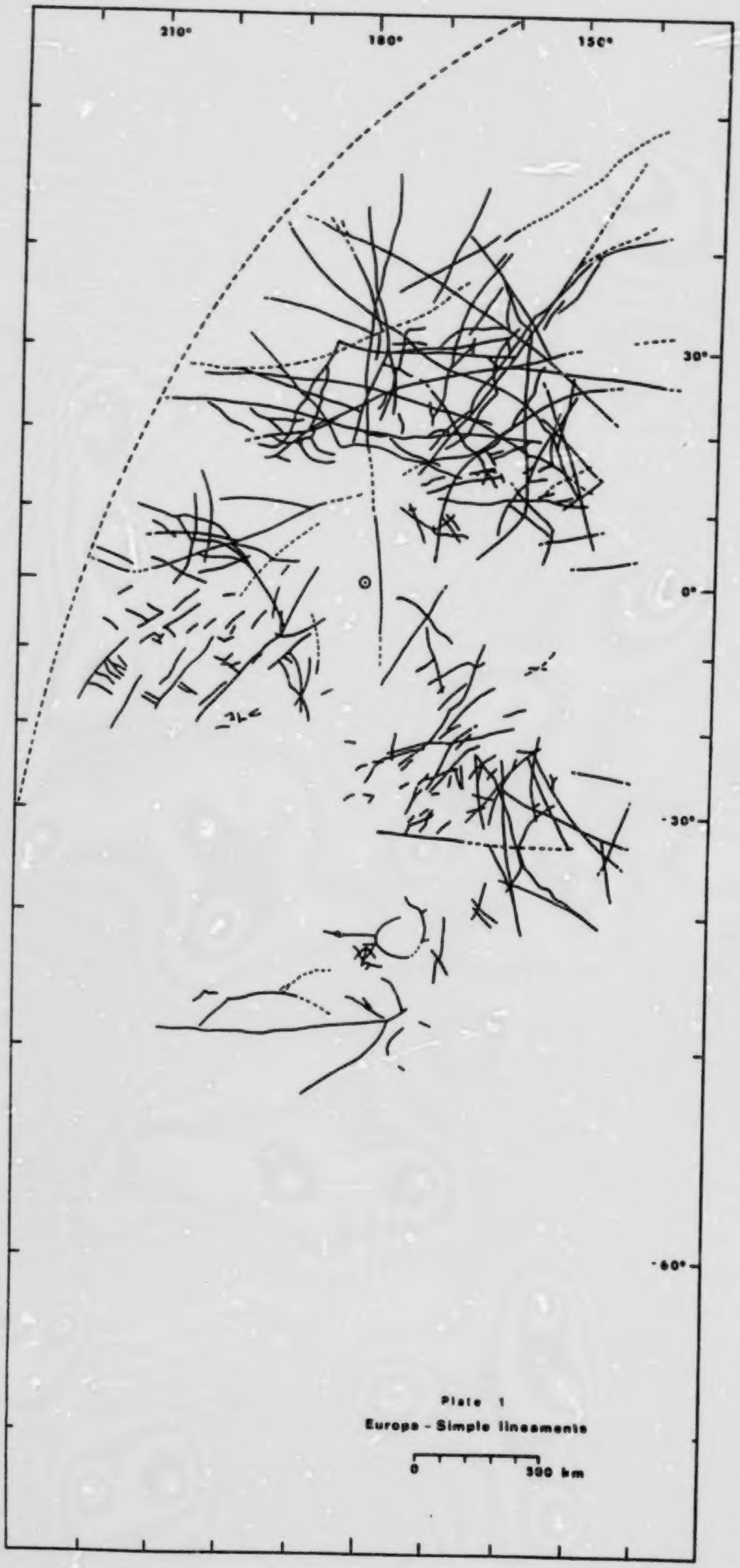
210°
180°
150°
30°
0°
-30°
-60°
0
300 km

Plate 1

Europa - Simple lineaments

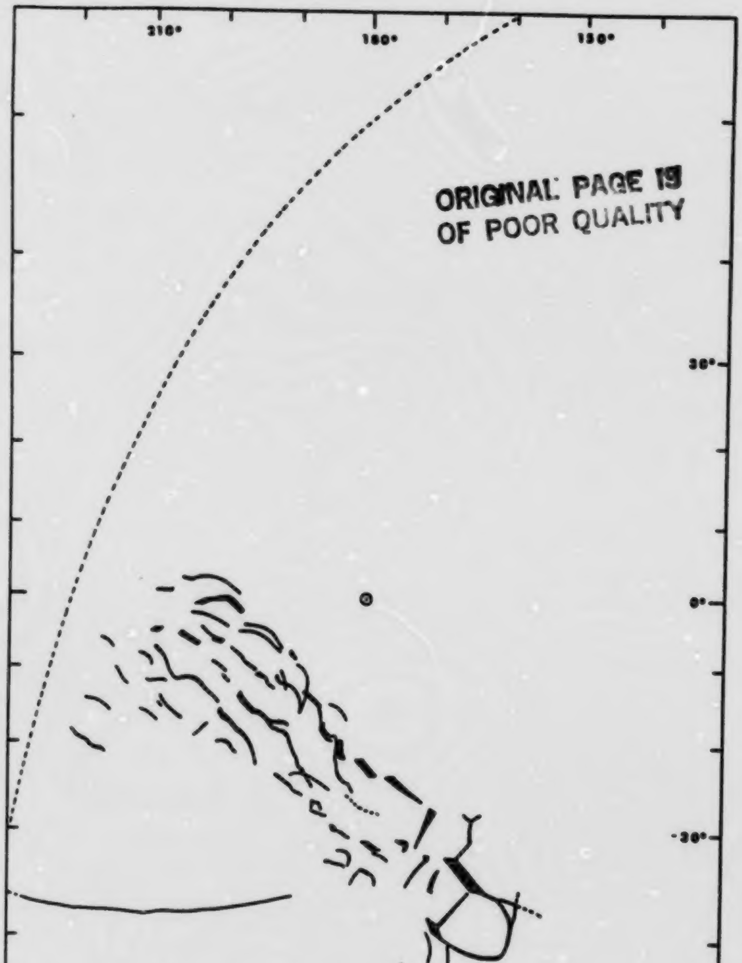
210°
180°
150°
30°
0°
-30°
-60°
0
500 km

Plate 2
Europa - Wedge-shaped bands

ORIGINAL PAGE IS
OF POOR QUALITY

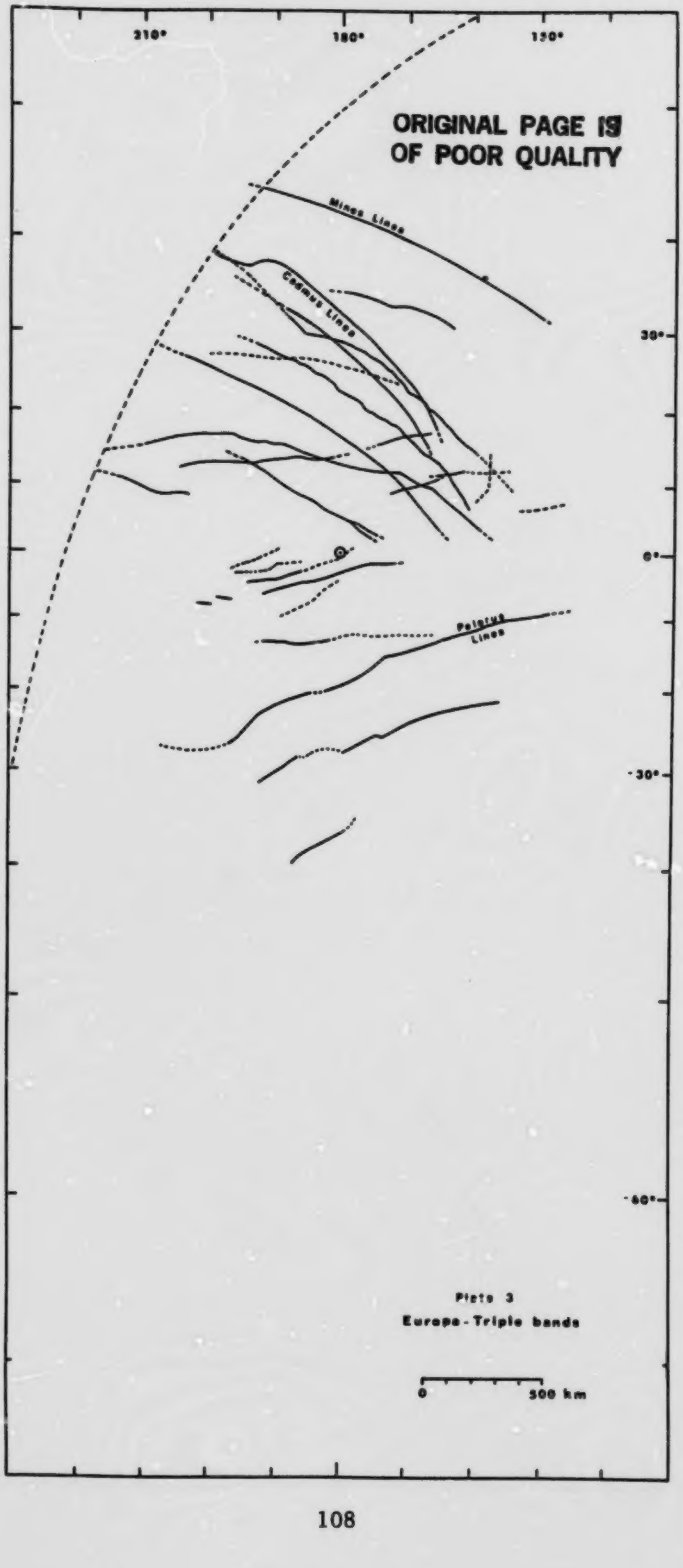
210°
180°
150°
30°
0°
-30°
-60°
Minos Linea
Cadmus Linea
Pelagus Linea
0
500 km

Plate 3
Europa - Triple bands

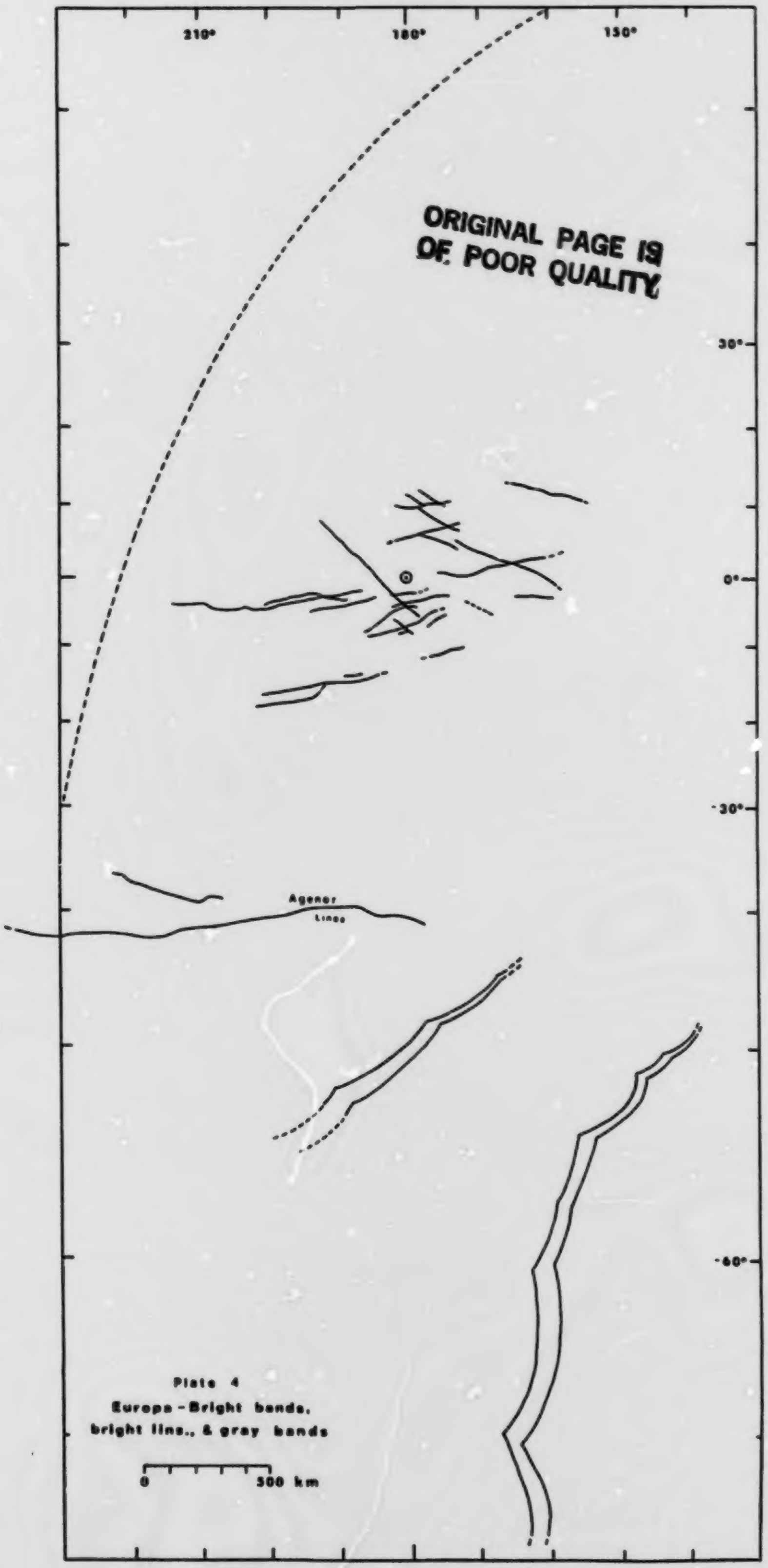
210°
180°
150°
30°
0°
-30°
-60°
Agenor
Linea
0
300 km

Plate 4
Europa - Bright bands,
bright lins., & gray bands

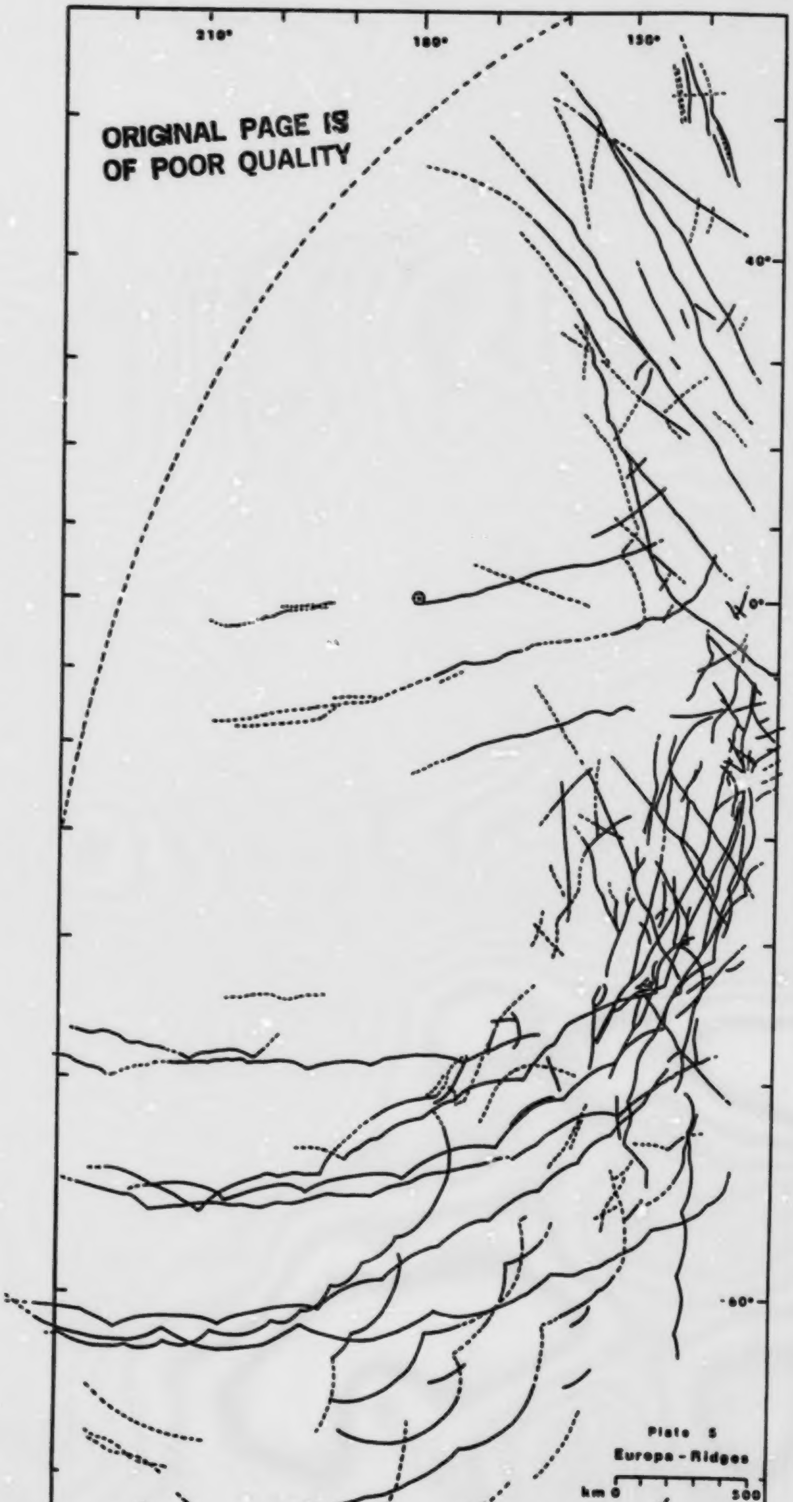
210°
180°
150°
40°
0°
-60°

Plate 5

Europa - Ridges

km 0 500

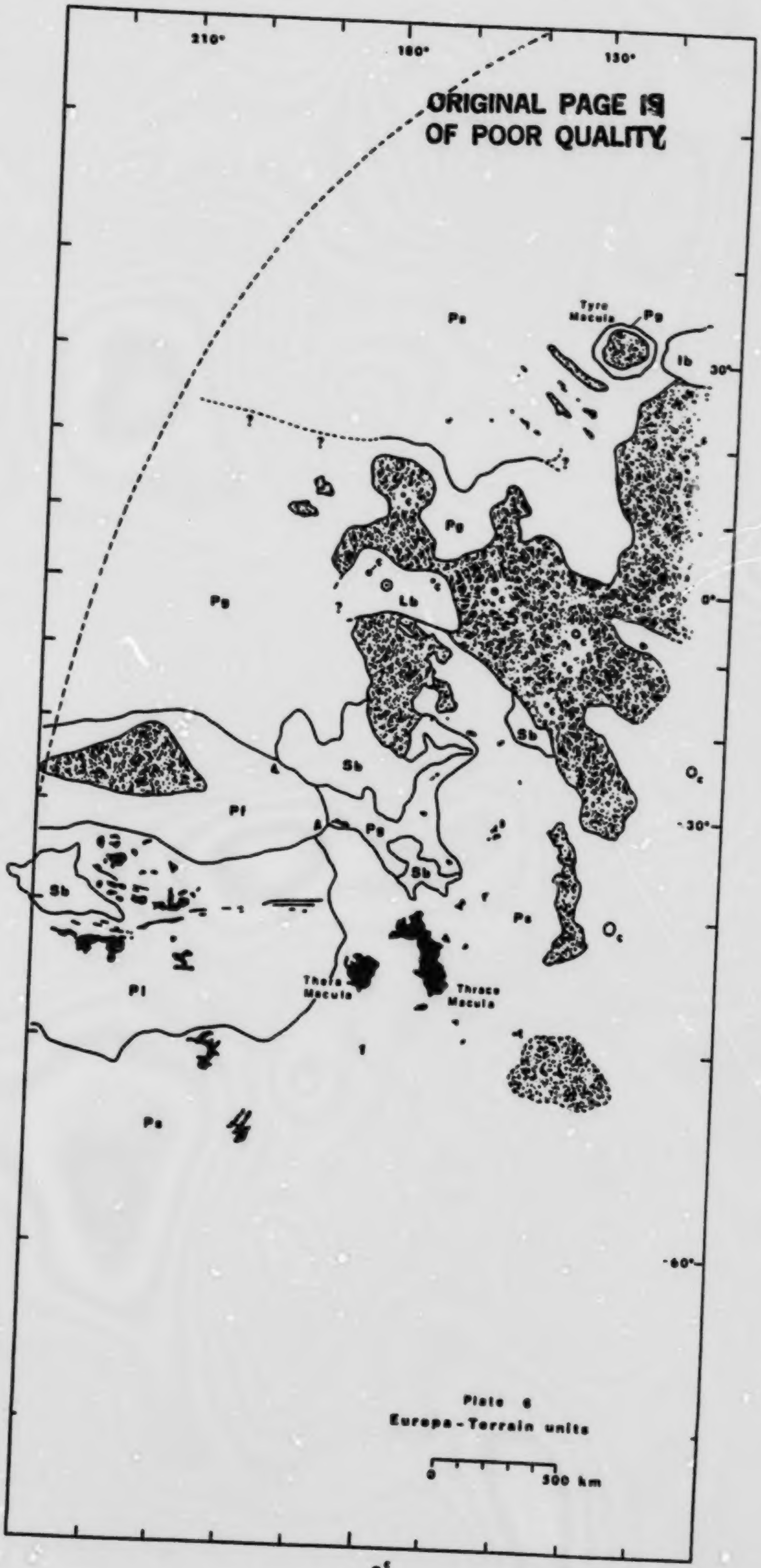
210°
180°
150°
30°
0°
-30°
-60°
Ps
Tyre Macula
Pg
Ib
?
Pg
Lb
Pg
Sb
Sb
Oc
Pf
Pg
Sb
Sb
Ps
Oc
Pl
Thera Macula
Thrace Macula
Ps
0
300 km
0°

Plate 6
Europa-Terrain units

SECTION II

PRECEDING PAGE BLANK NOT FILMED

N84 25569

Analysis of Permafrost Depths on Mars

Gennaro H. Crescenti, Southern Connecticut State College, Planetary Geology Intern, Summer 1982, Conducted at the State University of New York at Buffalo.

Permafrost is defined as any soil or rock material, regardless of the amount of moisture content, that has remained below 273°K (0°C) for more than two years (D.M. Anderson et al. 1973). It is defined solely on the basis of temperature without reference to ice content, soil texture, or lithology. It is therefore expected and has been generally agreed upon that much of the Martian surface is underlaid with permafrost. However, the thickness of such layers and percentage of ice content within the permafrost zone (cryosphere) has been subject to much debate.

Rossbacher and Judson (1981) modeled thicknesses of permafrost at latitudes of 10° increments using the average temperature data obtained from Fanale (1976), surface heat flow of 0.035 W m^{-2} (Toksoz & Hsui, 1978), and a thermal conductivity value of hard frozen limonitic soil with a 60% ice content of 0.8 W m^{-1} $°K^{-1}$ (Clark, 1966). Solving for the geothermal gradient, g:

$$g = Q/K \tag{1}$$

where Q is the heat flow and K is the thermal conductivity, and their value of g was 0.044° K m^{-1}. The following equation was used to solve for the depth or thickness of the permafrost, Z:

$$Z = T_c/-g \tag{2}$$

PRECEDING PAGE BLANK NOT FILMED

where T_C is the mean annual temperature in degrees celcius and g is the geothermal gradient. Rossbacher & Judson (1981) obtained depths in the range of 1.1 km at the equator to 2.6 - 3.0 km at the South and North Poles respectively.

However, serious error may be associated with their thicknesses due to the thermal conductivity value. The thermal conductivity used by Rossbacher & Judson is for hard frozen limonite, which is present throughout the entire surface of Mars but only exists as a mask (Mutch et al. 1976). Mutch et al., also go on to suggest that the crust may be, for the most part, basaltic in nature. This paper, therefore, reexamines the approach used by Rossbacher and Judson in analyzing the Martian thermal regime and extends the analysis. Using basaltic thermal values, the same technique is used.

Temperature data for the Martian surface was derived from Kieffer's et al. (1977) thermal model for the mean, maximum, and minimum temperatures. In their model, diurnal temperatures were plotted as isotherms for the entire Martian globe (90°N to 90°S), and for the duration of the entire Martian year. I picked four temperature points at 90° intervals of the Martian year (areocentric longitude intervals, 360° = 1 year) and then were averaged together for a given latitude. Latitudes of 10° intervals were chosen from 90°N to 90°S and this was done for each of the three charts (a minimum, mean, and maximum) from Kieffer's et al. (1977) paper. The temperature data can be seen in Table 3. Since the temperatures were extrapolated from the charts, they may be subject to an error of plus or minus several degrees.

ORIGINAL PAGE IS
OF POOR QUALITY

The next step was to obtain a heat flow value of the Martian surface. There are currently two theorical values, $Q = 0.035$ and $0.040\ W\ m^{-2}$ from Toksoz & Hsui (1978) and Davies & Arvidson (1981), respectively.

Not to be biased to any one set of thermal values for basalt, two sets are presented here. From Wyllie (1971):

$K = 2.5\ W\ m^{-1}\ {}^{o}K^{-1}$

$\rho = 2.9 \times 10^{6}\ g\ m^{-3}$

$C = 0.959\ J\ g^{-1}\ {}^{o}K^{-1}$

$D = 9.0 \times 10^{-7}\ m^{2}\ sec^{-1}$

And from Kieffer et al. (1977):

$K = 2.09\ W\ m^{-1}\ {}^{o}K^{-1}$

$\rho = 2.8 \times 10^{6}\ g\ m^{-3}$

$C = 0.8\ J\ g^{-1}\ {}^{o}K^{-1}$

$D = 9.3 \times 10^{-7}\ m^{2}\ sec^{-1}$

where K is the thermal conductivity, ρ is the density, C is the heat capacity, and D, which is equal to $K/\rho C$, is the thermal diffusivity of basalt. Using equation (1), a total of four geothermal gradients were derived for the Martian crust (see Table 2). The depths were then solved by using equation (2) and can be seen for various latitudes with the different geothermal gradients (Table 3, see also fig. 1).

The next objective was to determine the depth of zero temperature change of the surface temperature amplitude. The following equation was obtained from Hillel (1980):

$$d = (2D/\omega)^{1/2} \tag{3}$$

where d is the damping depth, D is the thermal diffusivity, and ω is the radial frequency. At the depth d, the temperature amplitude decreases to the fraction of 1/e or approximately 0.37 of the amplitude at the surface, A_o (Hillel, 1980). By extrapolation the depth of zero temperature change can be determined graphically (see figs. 2-6). The damping depth is directly related to the thermal properties of the soil or rock and to the frequency of the temperature fluctuation. The depth of zero temperature amplitude is dependent in part by the surface amplitude, generally the larger the amplitude the greater the depth of zero temperature fluctuation.

Using equation (3), the values shown in Table 4 were obtained. They give the damping depths for Earth and Mars (both are based on basaltic crusts) for three cycles — diurnal, annual, and the obliquity cycle of each planet.

Discussion:

From the results in Table 3 of this paper, it appears that the thicknesses of the permafrost on Mars are on the order of two to three times the values obtained by Rossbacher & Judson (1981). This paper does not take into account such items as thermal inertias and albedo features and how they have an affect upon the surface temperatures, the effect on the freezing point of water by influence of dissolved salts, the thickness of loose regolith (which has lower conductivity values), and other variables. Nor at the point can this paper offer an exact percentage of ice content within the cryosphere. Rossbacher & Judson (1981) suggest that 7.9 x 10^6 Km^3 of ice is present within the given parameters of their cryosphere. Should that value of water content hold true, a similar argument may be applied by having the same amount of ice distributed over a larger volume such as this paper suggests. Thus, if all assumptions do hold true, the cryosphere presented here is much drier than Rossbacher & Judson had originally conceived. The percentage of ice in their model is 3.7% where as 1.1% is now suggested in this paper. Also juvenile water, if any at all does exist, must be taken into consideration when figuring the total sink of water present on Mars.

The surface heat flow values of both the Earth and Mars are quite comparable. Harlan & Nixon (1978) give an average heat flow value for the earth of 0.046 W m^{-2}, and report extremes 0.025 to 0.084 W m^{-2}. No doubt Mars' values of Q also vary considerably from place to place, being higher in areas of suspected volcanic activity and lower near the polar caps. Further studies are necessary to place extreme limits on the heat flow values given by Toksoz & Hsui (1978) and Davies & Arvidson (1981). Harlan & Nixon (1978) also give a normal geothermal gradient of 0.015° C m^{-1} for Earth which is very comparible to this paper's findings for Mars. Knowing that Mars is much colder than Earth, it is natural to expect a much thicker and more extensive cryosphere. On Earth maximum reported thicknesses of permafrost are 1400 - 1450 m in the vicinity of the upper Markha River in Siberia and about 1000 m near Alert, Ellesmere Island in the Canadian Arctic (Washburn, 1980). With all things taken into consideration, the depths of the permafrost on Mars does not seem to be overly brash.

When looking at the damping depths of Mars, we are primarily interested in looking at the annual cycles first. In fig. 2, the top 18 meters of the Martian crust vary with the surface temperature changes. In fig. 3 it is approximately 15 meters and in fig. 4, the top 14 meters. These layers explained above here should not be confused with the active layer, which freezes and thaws in a periodic fashion. In figs. 2-4 the ground remains frozen from the top down to the bottom of permafrost, several kilometers below. After the designated zero temperature change points on the graphs does the temperature in the ground follow the geothermal gradient in a linear fashion. In figs. 5 and 6, diurnal temperatures were extrapolated from Kieffer's et al. (1977) thermal chart for the most extreme temperature variations possible to show the maximum depth of the active layer. Washburn (1980) defines the active layer as the layer of ground above the permafrost which thaws in the summer and freezes again in the winter. From figures 5 & 6, the active layer on Mars has been determined to be about 6 to 7 cm.

Damping depths were determined for the cycle of obliquity changes of both Earth and Mars. However, Mars cannot be graphically displayed because the temperature extremes for such a cycle are not known. Interestingly enough, Coradini & Flamini (1979) suggested of an active layer of 100 m for a large scale cycle, which would imply significant temperature extremes for such a situation to exist.

Acknowledgements

The author wishes to acknowledge and thank Dr. Duwayne M. Anderson, my host and supervisor of my internship, who had guided, taught, and possessed an unlimited amount of patience with me and had led me to valuable insights on writing this paper. Special mention to Professor M. N. Toksoz who readily sent me his journal article that I could not obtain. To Martha K. Howe for typing this report and tables and to the office Xerox machine, which made journal articles more accessible for my use.

References

Anderson, D. M., L. W. Gatto, and F. Ugolini, 1973. An examination of Mariner 6 and 7 Imagery for Evidence of Permafrost Terrain on Mars in Permafrost: The North American Contribution to the Second International Conference, National Academy of Sciences, Washington D.C., 499-508.

Clark, S.P., Jr., 1966. Handbook of Physical Constants, Geol. Soc. Amer. Mem. 97, Geological Society of America, New York, 459-482.

Coradini, M. and E. Flamini, 1979. A Thermodynamical Study of the Martian Permafrost, Journal of Geophysical Research, 84, 8115-8130.

Davies, G.F. and R.E. Arvidson, 1981. Martian Thermal History, Core Segregation, and Tectonics, Icarus, 45, 339-346.

Harlan, R.L. and J.F. Nixon, 1978. Ground Thermal Regime, 103-163, in Andersland, O.B. and D.M. Anderson, 1978. Geotechnical Engineering for Cold Regions, McGraw-Hill, New York.

Hillel, D., 1980. Fundamentals of Soil Physics, Academic Press, New York, pp. 305-306.

Kieffer, H.H., T.Z. Martin, A.R. Peterfreund, B.M. Jakosky, E.D. Miner, F.D. Palluconi, 1977. Thermal and Albedo Mapping of Mars During the Viking Primary Mission, Journal of Geophysical Research, 84, 4249-4291.

Mutch, T.A., R.E. Arvidson, J.W. Head, K.L. Jones, and R.S. Saunders, 1976. The Geology of Mars, Princeton University Press, New Jersey, pp. 4, 6, 20, 198, 199, 273.

Rossbacher, L.A. and J. Judson, 1981. Ground Ice on Mars: Inventory, Distribution, and Resulting Landforms, Icarus, 45, 39-59.

Toksoz, M.N. and A.T. Hsui, 1978. Thermal History and Evolution of Mars, Icarus, 34, 537-547.

Washburn, A.L., 1980. Geocryology, John Wiley & Sons, New York, pp. 35, 36, 57.

Wyllie, P.J., 1971. The Dynamic Earth: Textbook in Geosciences, John Wiley & Sons, New York, p. 240.

TABLE 1

Definitions of Symbols

A_o - Surface temperature amplitude, difference between the average mean and average minimum or maximum temperatures.

C - Heat capacity ($J\ g^{-1}\ {}^{o}K^{-1}$)

d - Damping depth, temperature amplitude equal to (1/e) A_o at d.

D - Thermal diffusivity = $K/\rho C$ ($m^{2}\ sec^{-1}$)

g - Geothermal gradient (${}^{o}K\ m^{-1}$, ${}^{o}C\ m^{-1}$) both are equivalent

K - Thermal conductivity ($W\ m^{-1}\ {}^{o}K^{-1}$)

Q - Heat flow ($W\ m^{-2}$)

T_C - Mean average annual temperature (${}^{o}C$)

T_K - Mean average annual temperature (${}^{o}K$)

T_H - Maximum average annual temperature (${}^{o}K$)

T_L - Minimum average annual temperature (${}^{o}K$)

Z - Depth or thickness of permafrost (m)

ρ - Density ($g\ m^{-3}$)

ω - Radial frequency (2π/# of seconds of given period)

TABLE 2

Derivation of Geothermal Gradients

$Q_1 = 0.035 \text{ W m}^{-2}$ Toksoz & Hsui (1978)

$Q_2 = 0.040 \text{ W m}^{-2}$ Davies & Arvidson (1981)

$K_1 = 2.5 \text{ W m}^{-1}\ {}^{o}\text{K}^{-1}$ Kieffer et al. (1977)

$K_2 = 2.09 \text{ W m}^{-1}\ {}^{o}\text{K}^{-1}$ Wyllie (1971)

$g_1 = Q_1/K_1 = 0.014\ {}^{o}\text{K m}^{-1}$

$g_2 = Q_2/K_1 = 0.016\ {}^{o}\text{K m}^{-1}$

$g_3 = Q_1/K_2 = 0.017\ {}^{o}\text{K m}^{-1}$

$g_4 = Q_2/K_2 = 0.019\ {}^{o}\text{K m}^{-1}$

TABLE 3

LAT	Average Annual Temperatures (^oK) Min	Mean	Max	Temperature Amplitude (^oK) T_K-T_L	T_H-T_K	T_C (^oC)	$Z = T_C/-g_x$ Z/1000 (m) x=1	x=2	x=3	x=4	Z avg
90	144	144	144	0	0	-129	9.2	8.1	7.6	6.8	7.9
80	146	147	148	1	1	-126	9.0	7.9	7.4	6.6	7.7
70	151	157	164	6	7	-116	8.3	7.3	6.8	6.1	7.1
60	161	177	195	16	18	-96	6.9	6.0	5.6	5.1	5.9
50	165	187	216	22	29	-86	6.1	5.4	5.1	4.5	5.3
40	170	202	251	32	49	-71	5.1	4.4	4.2	3.7	4.4
30	172	208	261	36	53	-65	4.6	4.1	3.8	3.4	4.0
20	174	212	269	38	57	-61	4.4	3.8	3.6	3.2	3.8
10	176	215	273	39	58	-58	4.1	3.6	3.4	3.1	3.6
0	177	216	274	39	58	-57	4.1	3.6	3.4	3.0	3.5
-10	175	215	275	40	60	-58	4.1	3.6	3.4	3.1	3.6
-20	174	213	271	39	58	-60	4.3	3.8	3.5	3.2	3.7
-30	173	209	262	36	53	-64	4.6	4.0	3.8	3.4	4.0
-40	170	201	246	31	45	-72	5.1	4.5	4.2	3.8	4.4
-50	164	183	207	19	24	-90	6.4	5.6	5.3	4.7	5.5
-60	161	180	199	19	19	-93	6.6	5.8	5.5	4.9	5.7
-70	148	153	160	5	7	-120	8.6	7.5	7.1	6.3	7.4
-80	145	147	148	2	1	-126	9.0	7.9	7.4	6.6	7.7
-90	144	144	144	0	0	-129	9.2	8.1	7.6	6.8	7.9

Note: The average temperature must first be converted to °C before it is to be divided by the geothermal gradient, this can be easily illustrated on a graph of temperature vs. depth, the geothermal gradient as the slope of the line. Where the line interests the 273°K isotherm (0°C) is the bottom of the permafrost.

TABLE 4

Damping Depths for Various Cycles

$$d = (2D/\omega)^{1/2}$$

Cycle	Earth Period (secs)	Frequency (2π/Period)	d (Meters)	Mars Period (secs)	Frequency (2π/Period)	d (Meters)
Diurnal	86400	7.27×10^{-5}	0.160	88776	7.08×10^{-5}	0.162
Annual	3.15×10^{7}	1.99×10^{-7}	3.06	6.10×10^{7}	1.03×10^{-7}	4.25
Solar Obliquity	1.29×10^{12}	4.9×10^{-12}	6.2×10^{2}	*5.2×10^{12}	1.2×10^{-12}	1.2×10^{3}
				**3.9×10^{13}	1.6×10^{-13}	3.4×10^{3}

Notes:

$D = 9.3 \times 10^{-7}\ m^2\ sec^{-1}$, from Kieffer, et al. (1977)

*Smaller period, 1° change in axial tilt

**Larger period, 5° change in axial tilt

All periodic data from Mutch, et al. (1976)

ORIGINAL PAGE IS OF POOR QUALITY

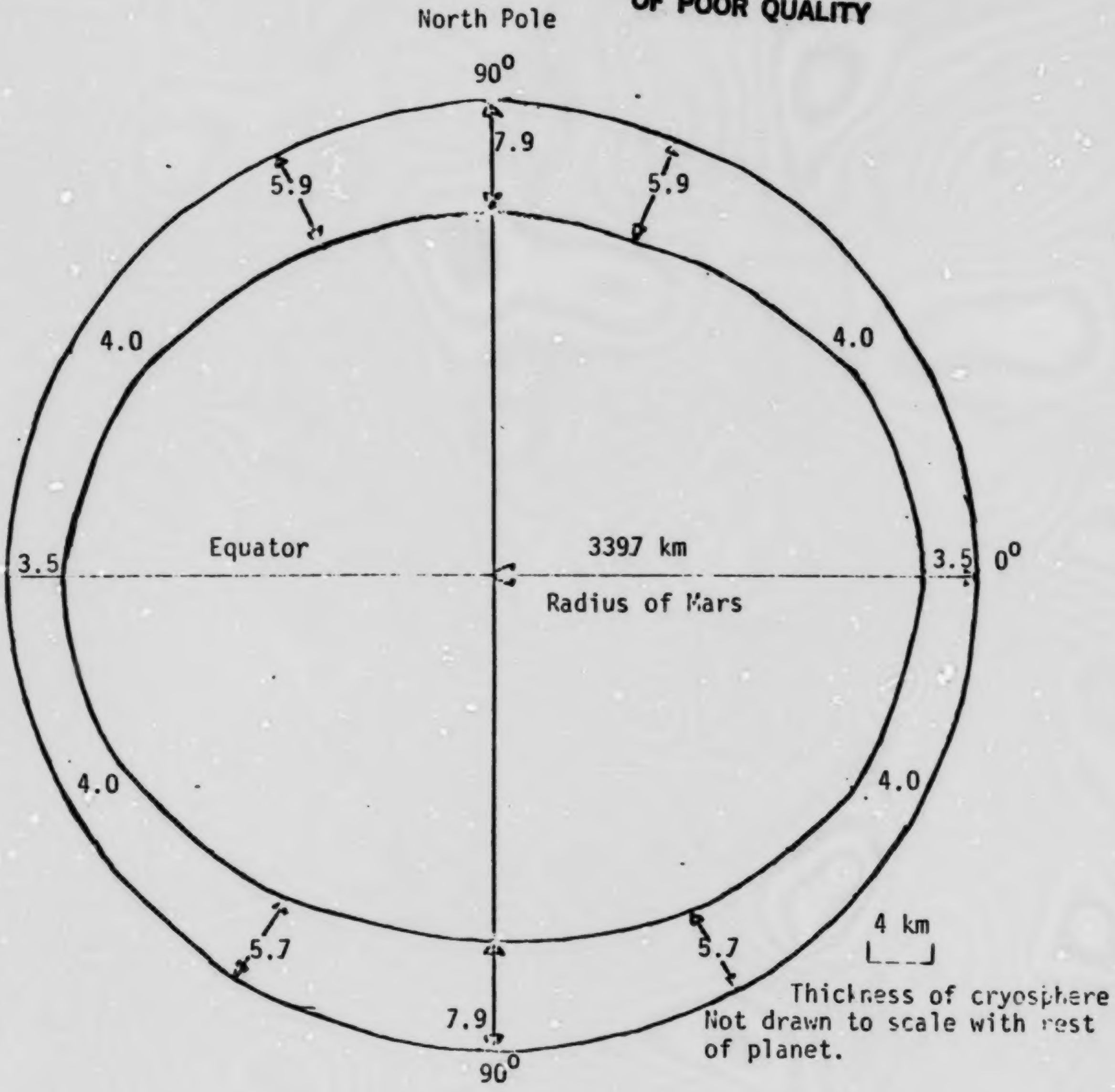
North Pole
90°
7.9
5.9
5.9
4.0
4.0
Equator
3397 km
3.5
3.5
0°
Radius of Mars
4.0
4.0
5.7
5.7
4 km
7.9
90°
Thickness of cryosphere
Not drawn to scale with rest
of planet.

Fig. 1

Cross section of Martian cryosphere, adopted and modified version from Rossbacher and Judson (1981). Inner circle represents 273°K isotherm, point at which any frozen ground ice becomes liquid water. Total average volume of cryosphere is 7.2×10^8 km^3.

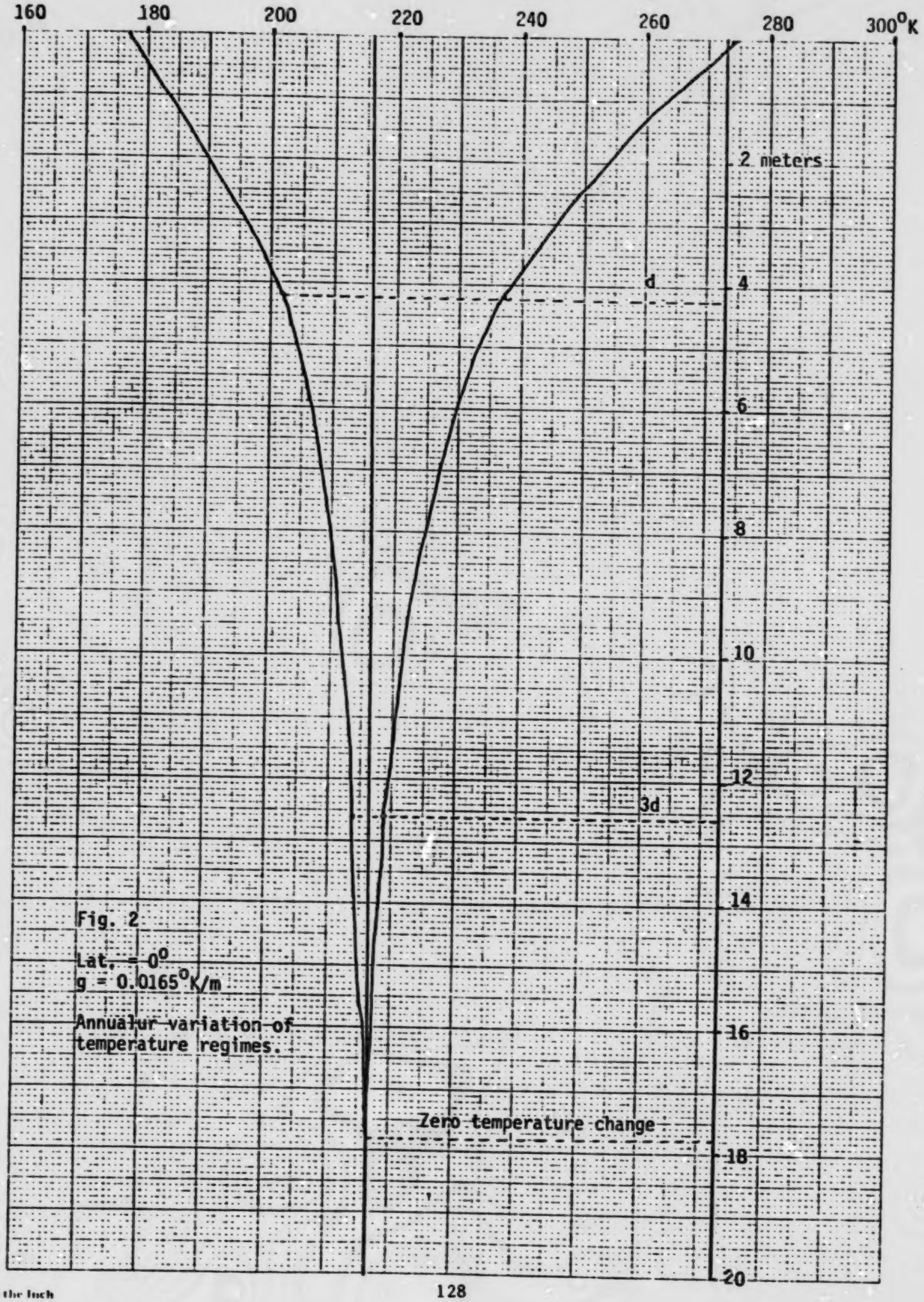

Fig. 2

Lat. = 0°
g = 0.0165°K/m

Annualur variation of temperature regimes.

ares to the inch

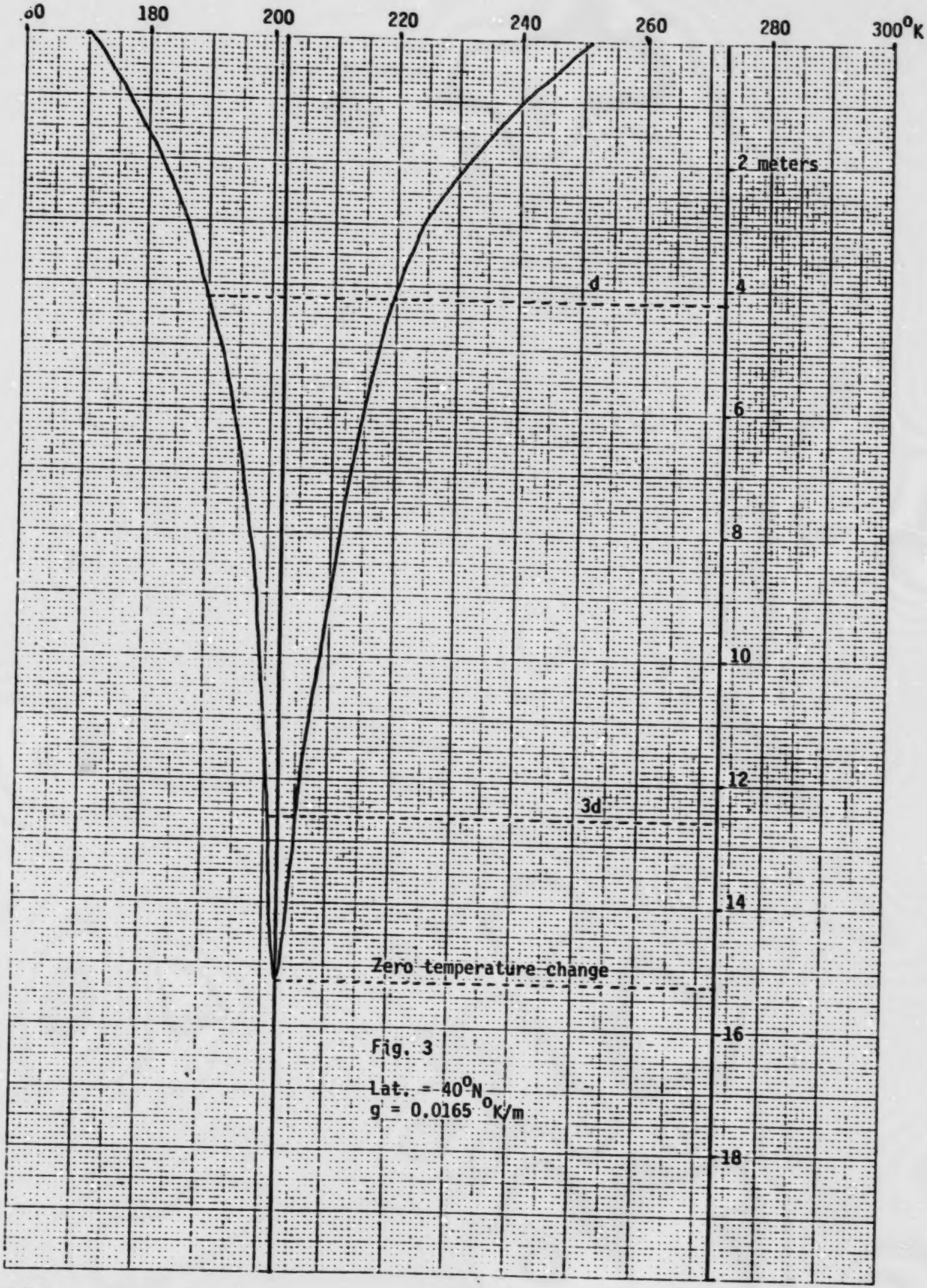

Fig. 3

Lat. = 40°N
g = 0.0165 °K/m

...s to the inch

ORIGINAL PAGE IS
OF POOR QUALITY

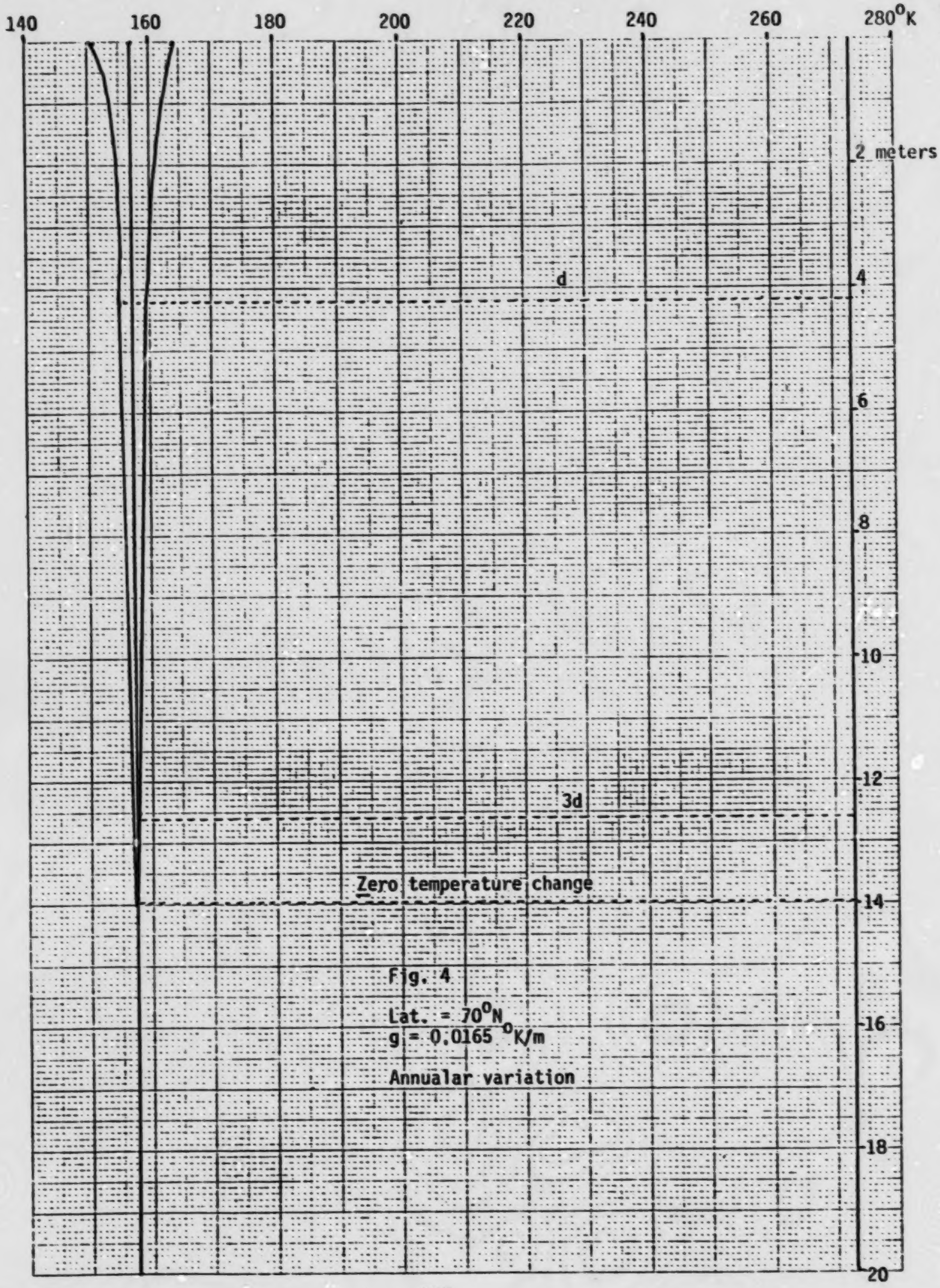

Fig. 4

Lat. = 70°N
g = 0.0165 °K/m

Annualar variation

5 Squares to the Inch

ORIGINAL PAGE IS
OF POOR QUALITY

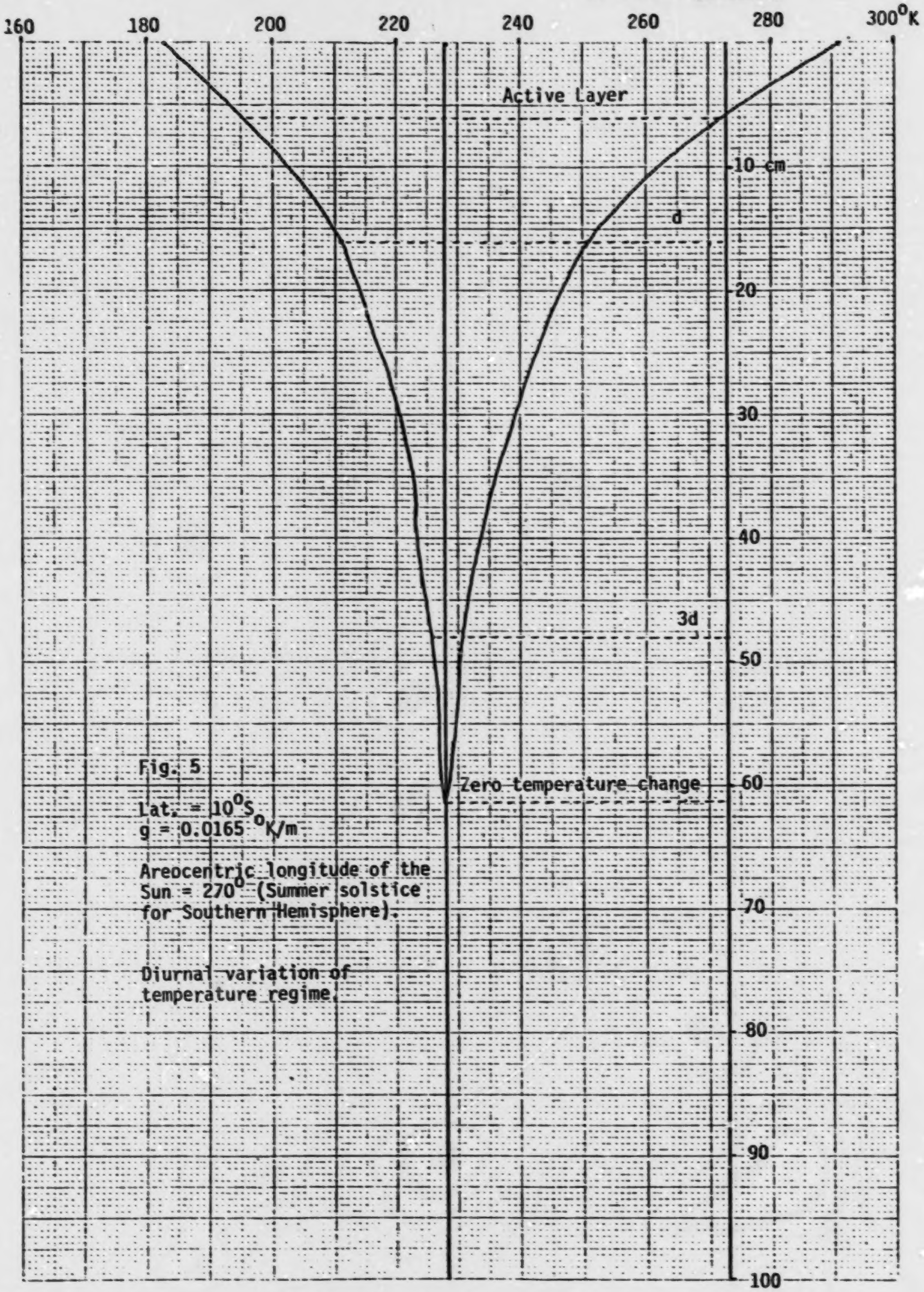

Fig. 5

Lat. = 10°S
g = 0.0165 °K/m

Areocentric longitude of the Sun = 270° (Summer solstice for Southern Hemisphere).

Diurnal variation of temperature regime.

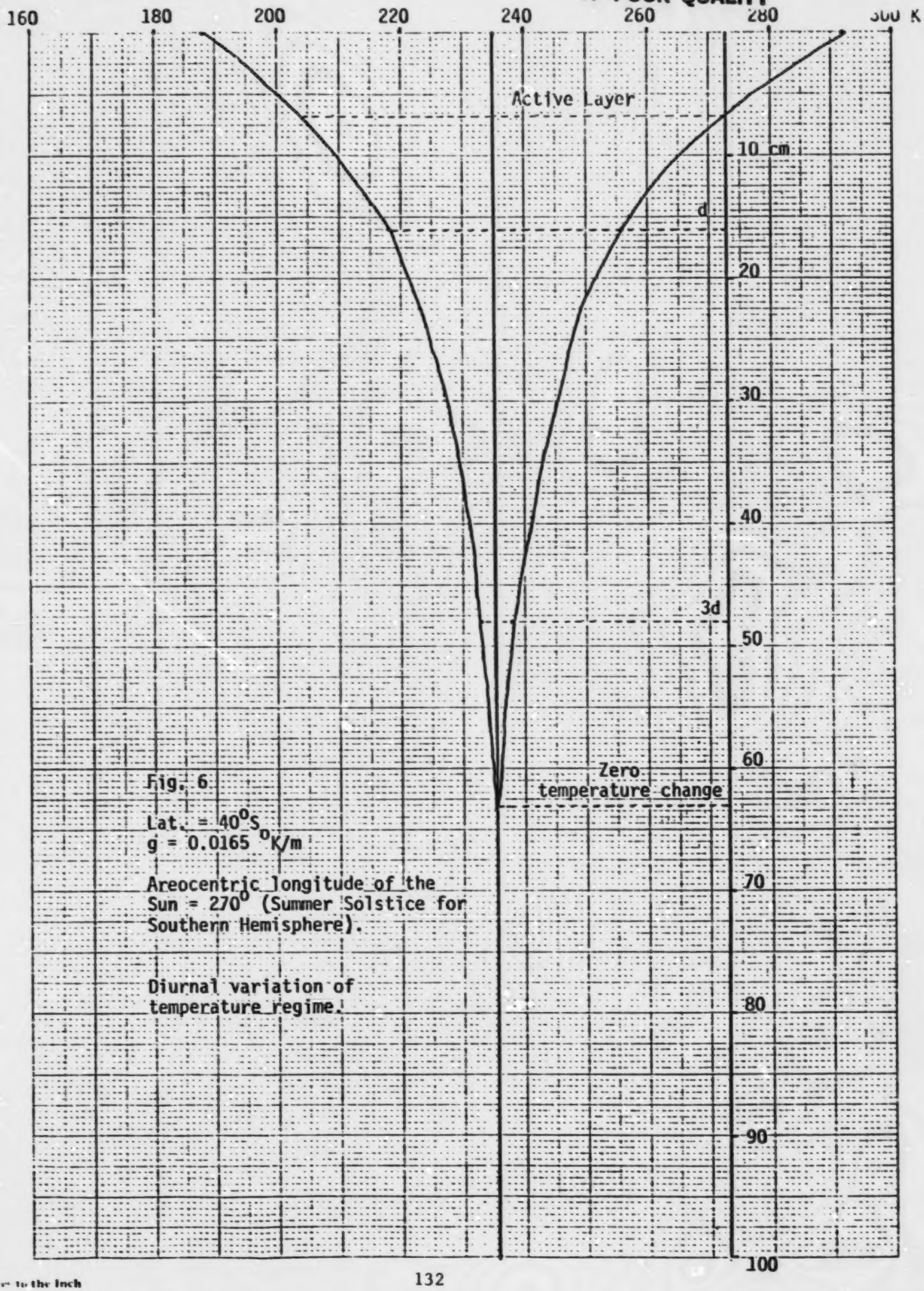

Fig. 6

Lat. = 40°S
g = 0.0165 °K/m

Areocentric longitude of the Sun = 270° (Summer Solstice for Southern Hemisphere).

Diurnal variation of temperature regime.

20 Squares to the Inch

N84 25570

SPECTRAL ANALYSIS OF GROOVE SPACING ON GANYMEDE

Robert E. Grimm,
Dept. of Geological Sciences, University of Tennessee, Knoxville, TN 37996

Origin of grooved terrain and the significance of groove spacing: Ganymede's bright "grooved" terrain is thought to have been formed as the result of global extension (Smith et. al., 1979), probably caused by phase transitions during differentiation (Squyres, 1980). Parmentier et. al. (1982) have argued that graben formation is the overall tectonic style of this extension. However, it is not clear whether individual grooves represent actual graben, extension fractures, or ductile necking features. Regular groove spacing is observed and could result from extension of a brittle lithosphere, causing a necking instability which undergoes normal faulting at regular intervals (Fink and Fletcher, 1981). Squyres (1982) argues that grooves are extension fractures, with spacing depending on a necking instability or the formation of a cooled, strengthened zone around a fracture where no further extension can take place. The geothermal gradient at the time of fracturing, and hence the thickness of the layer in which fracturing occurs, controls all models of extensional tectonic features on Ganymede. Quantitative estimates of groove spacing can therefore be used to constrain this important indicator of planetary evolution.

Here only the technique used to analyze groove spacing is discussed, complete results and interpretation will follow in future reports.

Criteria for data selection: Approximately 160 tracks perpendicular to the trend of grooved terrains from 28 Voyager images were selected for study. Groove sets selected had to satisfy a uniqueness criterion; that is, no grooves could be traced unbroken into adjacent sets. Grooves that were not nearly parallel were avoided, as were those that were extensively cratered. In addition, features of less than a few wavelengths were not used, e.g., single grooves and groove pairs. Because of the lack of stereo coverage and the unsuitability of most images for detailed photoclinometric analysis, digital photometric intensities as recorded by Voyager cameras through clear filters were considered to correlate with the relative amplitudes and wavelengths of surface topography. Hence anomalous contrasts in reflectivity had to be avoided, such as those due to bright ejecta or the planet's terminator. Similarly, those groove sets judged not to have adequate contrast to be resolved from noise were not used.

Determination of scale along cross-groove tracks: The relative distance per pixel along a given track depends on the angle (*a* in Fig. 1) between the subspacecraft position and the target center, and the angle (*b* in Fig. 1) *in image plane projection* between the track and the spacecraft line-of-sight:

$$\Delta d = \frac{cr}{\cos(a \cdot \cos b)} \qquad (1)$$

where r is the range from planet center to the spacecraft and c is a constant depending on the camera field of view and the number of pixels per image. Solution of equation (1) also requires knowledge of the subspacecraft latitude and longitude, the image north azimuth, the latitude and longitude of a control point in the image (Davies and Katayama, 1981), and the line and sample numbers of the control point as well as both endpoints of the cross-groove track. The latitude and longitude of the track center can also be calculated from this information.

Power spectral estimates of groove spacing: For each desired cross-groove track, a set of 5 closely spaced tracks are summed, bandpass filtered, and tapered in the spatial domain in order to reduce the effects of regional trends, noise, aliasing, and side lobes in the wavenumber domain. The power in a given spatial frequency is proportional to the square of the modulus of its Fourier transform:

$$\hat{A}(k) = \int_{-\infty}^{\infty} A(r) e^{i2\pi kr} dr \qquad (2)$$

$$P(k) \sim \mathrm{Re}^2[\hat{A}(k)] + \mathrm{Im}^2[\hat{A}(k)] \qquad (3)$$

A sample cross-groove track and its power spectrum are shown in Figs. 2-3. This spectrum shows a peak at approximately 0.3 km^{-1} (about 3 km wavelength), although much of the power is dispersed at higher frequencies. Since groove spacing may depend on latitude (Squyres, 1982), power spectra in a given latitude band are averaged and compared with other latitudes. The spectra are also statistically analyzed with respect to the viewing geometry parameters in order to reveal any hidden systematic errors. When completed, this work will provide a global picture of the variation of groove spacing on Ganymede.

**ORIGINAL PAGE IS
OF POOR QUALITY**

Ganymede groove spacing

Grimm, R. E.

Acknowledgement: This work was supported in part by the Planetary Geology Undergraduate Research Program, and was carried out at the NASA Ames Research Center under the direction of Dr. Steven W. Squyres.

References:
Davies, M.E., and F.V. Katayama (1981), Jour. Geophys. Res. 86, 8635-8677.
Fink, J.H, and R.C. Fletcher (1981), in Reports of Planetary Geology Program, NASA TM-84211.
Parmentier, E.M., S.W. Squyres, J.W. Head, and M.L. Allison (1982), Nature 295, 290-293.
Smith, B.A., and the Voyager Imaging Team (1979), Science 206, 504-537.
Squyres, S.W. (1980), Geophys. Res. Let. 7, 593-596.
Squyres, S.W. (1982), in press.

FIG.1 Schematic Ganymede Viewing Geometry. Angles 'a' and 'b' defined in text.

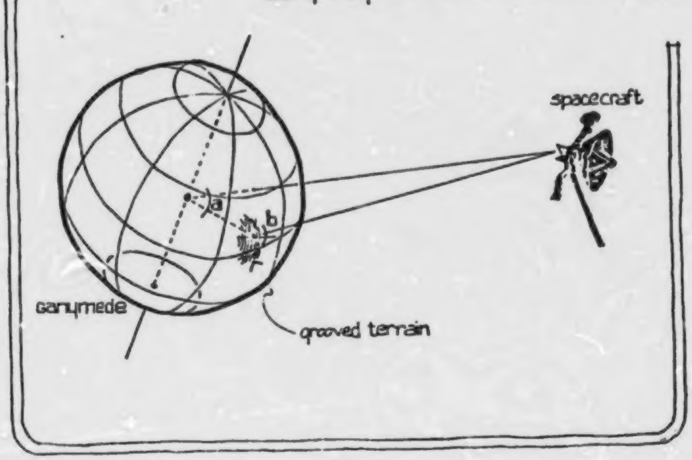

FIG.2 Sample Ganymede Surface Scan:

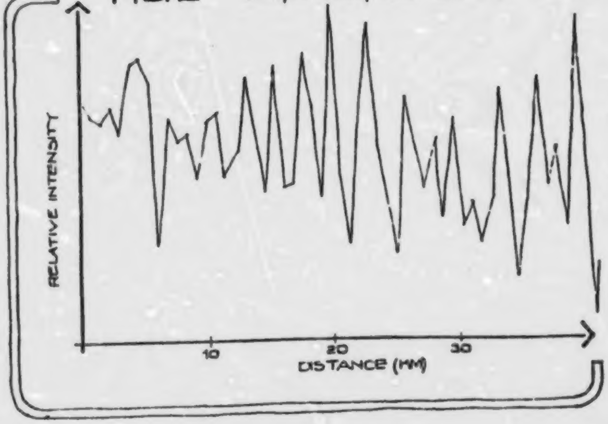

FIG.3. Sample Ganymede Power Spectrum:

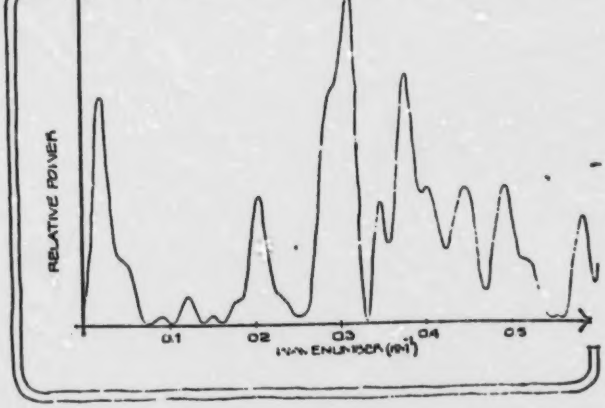

STRATIGRAPHY OF THE CRATER COPERNICUS

Rita Paquette
NASA Undergraduate Summer Intern, 1982
Brown University
Providence, RI 02912

Advisor: Carlé M. Pieters
Assistant Professor (Research)
Department of Geological Sciences

N84 25571

INTRODUCTION:

Copernicus is a large, bright-rayed crater located in Oceanus Procellarum at 9.5°N, 20°W. Its unique character is due to the presence of a significant amount of olivine in its central peak region (Pieters, 1982), a mineral which is widely distributed but not abundant on the lunar surface. Of the 11 large craters for which spectral data is available, only Copernicus conclusively shows olivine absorption bands. The focus of this report is on postulating the Copernicus stratigraphy such that it is in agreement with this observation and known stratigraphic units. This will be accomplished primarily through cratering mechanics and available Earth-based spectral data. Diagrams of four postulated stratigraphic sections of Copernicus are given with accompanying discussion in the text.

GEOLOGIC SETTING:

The large (485 km diameter) mare-filled basin centered approximately 840 km north of Copernicus is the Imbrium basin. Its outer ring structures, the Apenninus and Carpatus mountains, lie a crater diameter north of Copernicus, while a substantial amount of basin ejecta underlie the mare near Copernicus.

Though the Imbrium cavity may have ejected material from as deep as 60 km (Grieve, 1979), no major amounts of mantle material have been observed in the mountain ridges during the Apollo missions. Thus it is very unlikely that olivine-rich mantle would have been deposited near Copernicus prior to its formation and re-excavated to form the peak material. Also, the central peaks of Copernicus are comprised of material excavated from up to 10 km depth, which is much deeper than ejecta emplacement could occur. This 10 km depth follows from (Dence et al., 1977) relation for bright craters that the maximum depth of excavation is approximately 1/8 the diameter, which is 95 km in the case of Copernicus.

SPECTRAL INFORMATION:

A single telescopic near infrared spectral reading encompasses an area of 5 to 15 km in diameter in the Copernicus region (Pieters, 1982). The locations of these areas are shown on the map of Figure 1. The telescopic spectra of the Apollo 16 site are very similar to the spectra of the soil samples measured in the laboratory (McCord et al., 1981), and is a useful aid in calibrating the spectral data. The dominant mineral in the breccias of the Apollo 16 is plagioclase feldspar (An_{95-97}), with low-Ca orthopyroxene present in less abundant though significant amounts. Olivine and clinopyroxene occur in only minor proportions.

The pyroxene absorption band tends to dominate spectra, obliterating many of the effects of the nonmafic minerals. These pyroxene bands are symmetric and narrow at 1 μm, becoming broader and asymmetric at the 2 μm absorption band (McCord et al., 1981). Olivine spectra differs from this in that it displays a multiple band near 1 μm (see Figure 2).

Agglutinates, or glass-welded aggregates of material reworked by numerous small impact events, will weaken the mineral absorption bands, as in the case of the Apollo 16 soils. Fresh craters do not yet display large changes due to the effects of agglutinates. An area with a high albedo generally has not been affected, which is the situation with the high albedo peaks and walls of Copernicus (Pieters, 1982). The wall spectra indicate orthopyroxene absorption in combination with other absorption bands of indeterminate composition centered near 1 μm. Orthopyroxenes are associated with feldspathic lunar crustal material, so the wall deposits as well as the rim deposits appear to be of the same composition as the lunar terra material sampled by the Apollo missions. Slightly more distant from the crater (e.g., point 13 on map), though still in the continuous ejecta deposits, clinopyroxenes become sometimes more abundant than the orthopyroxenes, indicating more mafic rocks. This could be due to the influence of local mare material on the more feldspathic ejecta, or it may be a function of changing pyroxene composition with depth. In general, ejecta from deeper in the crater is deposited closer to the rim (Rehfuss et al., 1977). This is shown in the accompanying cross sections.

The floor of Copernicus has been interpreted by Howard (1975) to be pooled and/or veneered with impact melt. An alternative explanation (S. R. Taylor, 1982) which is consistent with the Apollo 17 infrared scanning radiometer data is that fine-grained debris flows were deposited on the floor. The spectra of the floor indicate the presence of orthopyroxenes and other minerals which skew the absorption band complex to a shorter wavelength. The undetermined mineral bands could be a result of the highly shocked debris, which is also present in "pools" on the crater walls and on the rim deposits. It is difficult to establish the presence of feldspar in shocked material, as it will not retain its crystalline structure as will shocked mafic minerals (Adams et al., 1979).

Three peaks in Copernicus have been spectrally analyzed by Pieters (1982) and inferred to contain a mineral assemblage of olivine and feldspar. Another large, fresh crater near Copernicus -- Eratosthenes -- does not display a similar assemblage in its central peak but instead includes clinopyroxene. From this one can infer that clinopyroxenes predominate over orthopyroxenes at the depth of excavation of this crater, which could be as much as 7 km. A few kilometers deeper, another major compositional horizon was encountered during the Copernicus excavation, causing an olivine assemblage to be emplaced in the central peaks.

UPPER STRATIGRAPHIC UNITS:

The upper units for the Copernicus area include deposits from the Copernicus impact, the mare basalts, and the Imbrium ejecta. Using Pike's relation (1980) the rim height of Copernicus is 1.4 km, with the rim deposits thinning very quickly within the distance of one crater radius from the rim. A sheet of highly shocked debris or impact melt covers the crater floor. All four stratigraphic models are uniform in displaying these units.

Values for the thickness of the Imbrium ejecta at Copernicus range from 430 m (McGetchin et al., 1973) to 3.08 km (Pike, 1974), depending on the ring designated as the crater rim and the choice of transient crater models. Copernicus stratigraphic model 1 is consistent with McGetchin et al., while model 2 is consistent with one of Pike's ejecta thickness relations. The average thickness of the basalt overlying the Imbrium ejecta in the Copernicus area was calculated by DeHon (1979) to be 250 m, which all four models display.

LOWER STRATIGRAPHIC UNITS:

Another observation made by DeHon (1979) is a localized thickening of the basaltic crust, possibly filling an old basin centered at 12°N, 13°W. Gravity data supports this idea, as well as the presence of a disconnected, arcuate trend of old ridges in a circular and concentric formation (Wilhelms and McCauley, 1971). This basin has been referred to as South Imbrium and it predates the Imbrium event. During the South Imbrium impact event, substantial uplift of the mantle may have occurred, forming a plug which was later uplifted by the Copernicus impact to its present position in the central peaks. The proximity of the two crater centers (Copernicus and South Imbrium) strengthen the case for such a scenario. Both models 1 and 2 indicate a prior basinal impact event.

As mentioned earlier, Eratosthenes displays a clinopyroxene assemblage in its crater peak, suggesting a substantial clinopyroxene-bearing unit at the depth of excavation. Though both Copernicus and Eratosthenes lie within the South Imbrium basin, Copernicus does not display this mineralogy, but instead is feldspathic and contains significant amounts of orthopyroxene. This suggests that a more mafic layer which underlies Eratosthenes either thins westward as it approaches Copernicus or some other distontinuity occurs between these two craters.

Cadogan (1974) proposes an older, much larger basin on the lunar nearside centered at 26°N, 15°W with ring diameters of 1700, 2400 and 3200 km. The existence of Gargantuan basin, as it is called, has not been established. Though there is some photogeologic evidence for the existence of this basin, geophysical data does not support the idea of such a large, ancient impact (Hawke and Head, 1977). A separate stratigraphic model is not necessary to display this event, since the same sequence as in models 1 and 2 of mantle uplift and re-excavation by Copernicus applies to this as well.

An interesting distribution of the olivine in the three central peaks is observable in the spectra. A narrower, generally stronger, olivine absorption curve describes the smaller and more central of the three peaks (point 2 on the map). This is possible evidence for the presence of a very localized concentration of olivine, such as a dunite plug or dike beneath the Copernicus crater. A similar situation exists on Annette Island in southeastern Alaska where 98% of the plug is serpentinized olivine with only monor amounts of clinopyroxene and chromite (H. Taylor, 1967). This model (model 3) doesn't require a previous, larger, impact event.

One final model is inconsistent with the lunar geophysical data, and is supported only by the original observation that olivine occurs in the central peaks. Model 4 is of a mantle not at 60 km depth (as the geophysical data suggests), but at 10 km, and thus is within excavation depth of the Copernicus impact event. This model is highly unlikely due to its unreasonable mantle depth. However, this doesn't preclude a geochemical differentiation sequence whereby a troctolite layer is formed at a 10-km depth.

CONCLUSION:

A table follows summarizing the advantages and disadvantages of each model discussed in the text. Despite the points made concerning the disadvantages of model 1, which postulates an early impact basin centered near Copernicus with only a thin layer of Imbrium ejecta, this model is most consistent with the data. There are points concerning the stratigraphic units which are not yet understood, but which don't refute the model, either. The thick layer of feldspathic material above the olivine layer and below the Imbrium ejecta may be fallback ejecta from the South Imbrium cratering event, though the origin is left open to speculation.

More extensive spectral data collecting, combined with the more refined techniques and interpretations that are presently being worked on, will perhaps provide a means to identify the unknown stratigraphic units.

	ADVANTAGES	DISADVANTAGES
Model 1 430 m of Imbrium ejecta over early impact basin centered near Copernicus	(1) Remnant ring structure suggests a previous basin subsequently filled by mare (2) Depth of early basin is sufficient to excavate mantle at 60 km (3) Gravity data consistent with early basin (4) Basaltic crust thickens near center of proposed early basin, thinning outward	(1) Origin of feldspar-pyroxene unit above the early basin excavation and below the Imbrium ejecta is unaccounted for (2) No conclusive evidence that major basins excavate mantle material
Model 2 3.08 km of Imbrium ejecta over early impact basin centered near Copernicus	(1) Remnant ring structure a previous basin, subsequently filled by mare (2) Depth of early basin sufficient to excavate mantle at 60 km (3) Gravity data consistent with early basin (4) Basaltic crust thickens near center of proposed early basin, thinning outward	(1) Unlikely ejecta thickness extrapolated from small-scale cratering mechanics (2) Origin of thinner feldspar-pyroxene unit above the early basin excavation and below the Imbrium ejecta is unaccounted for (3) No conclusive evidence that major basins excavate mantle material
Model 3 Dunite plug/dike beneath the Copernicus crater	(1) A small plug/dike is consistent with the higher concentration of olivine in one peak over the others (2) Monomineralic quality of a plug accounts for this same quality in the Copernicus peaks	(1) The Copernicus impact, by necessity, had to occur directly over the plug/dike

Model 4 Mantle at 10 km depth	(1) Simple model, dependent on no prior event	(1) Geophysical data inconsistent with 10 km mantle depth (2) No other evidence for a shallow mantle

REFERENCES

Adams, J. B. (1975) Interpretation of visible and near infrared diffuse reflectance spectra of pyroxenes and other rock-forming minerals, Infrared and Raman Spectroscopy of Lunar and Terrestrial Minerals, Academic Press, NY, p. 91-116.

Adams, J. B., F. Hörz, R. V. Gibbons (1979) Effects of shock-loading on the reflectance spectra of plagioclase, pyroxene and glass, Lunar and Planet. Sci., v. 10, p. 1-3.

Cadogan, P. H. (1974) Oldest and largest lunar basin? Nature, v. 250, 315-316.

DeHon, R. (1979) Thickness of the western mare basalts, Proc. Lunar Planet. Sci. Conf. 10th, p. 2935-2955.

Dence, M. R., R. A. F. Grieve, and P. B. Robertson (1977) Terrestrial impact structures: principal characteristics and energy considerations, Impact and Explosion Cratering, Pergamon Press, NY, p. 247-275.

Grieve, R. A. F. (1979) Cratering in the lunar highlands: some problems with the process, records, and effects, Proc. Conf. on Lunar Highland Crust, Supp. 12, p. 173-196.

Hawke, B. R., and J. W. Head (1977) Pre-Imbrium history of the Fra Mauro region and Apollo 14 sample provenance, Proc. Lunar Sci. Conf. 8th, p. 2741-2761.

Head, J. W., M. Settle, and R. S. Stein (1975) Volume of material ejected from major lunar basins and implications for the depth of excavation of lunar samples, Proc. Lunar Sci. Conf. 6th, p. 2805-2829.

Hodges, C. A. and D. E. Wilhelms (1978) Formation of lunar basin rings, Icarus, v. 34, p. 294-323.

Howard, K. A. (1975) Geologic map of the crater Copernicus, USGS Map I-840.

Lunar Orbiter photos, mission IV (121, 126)
mission V (150-157).

McCord, T. B., R. N. Clark, B. R. Hawke, L. A. McFadden, P. D. Owensby, C. M. Pieters, and J. B. Adams (1981) Moon: Near infrared spectral reflectance, a first good look, Jour. Geophys. Res., v. 86, no. 1311, p. 10883-10892.

McGetchin, T. R., M. Settle, and J. W. Head (1973) Radial thickness variation in impact crater ejecta: implications for lunar basin deposits, Earth and Planet. Sci. Let., 20, p. 226-236.

Oberbeck, V. R. (1975) The role of ballistic erosion and sedimentation in lunar stratigraphy, Reviews of Geophys. and Space Phys., v. 13, no. 2, p. 337-362.

Pieters, C. M. (1982) Copernicus crater central peak: lunar mountain of unique composition, *Science*, v. 215, p. 59-61.

Pieters, C. M. and S. Smrekar (1982) Atlas of lunar spectral reflectance (.7 to 2.5 μm), Brown University planetary geology document.

Pike, R. J. (1974) Ejecta from large craters on the moon: Comments on the geometric model of McGetchin *et al.*, *Earth and Planet. Sci. Let.*, 23, p. 265-271.

Pike, R. J. (1980) Geometric interpretation of lunar craters, *USGS Prof. Paper* 1046-C, 77 pp.

Rehfuss, D. E., D. Michael, J. C. Anselmo, N. K. Kincheloe, and S. A. Wolfe (1977) Hyper-ballistic transport models of Copernicus ejecta, *Proc. Lunar Sci. Conf. 8th*, p. 3375-3388.

Schmitt, H. H., N. J. Trask, E. M. Shoemaker (1967) Geologic map of the Copernicus quadrangle of the Moon, *USGS Geol. Atlas of the Moon*, Map I-515 (LAC-58).

Settle, M., J. W. Head, T. R. McGetchin (1974) Ejecta from large craters on the moon: Discussion, *Earth and Planet. Sci. Let.*, *23*, p. 271-274.

Stöffler, D., D. E. Gault, J. Wedekind, and G. Polkowski (1975) Experimental hypervelocity impact into quartz sand: Distribution and shock metamorphism of ejecta, *Jour. Geophys. Res.*, v. 80, no. 29, p. 4062-4077.

Taylor, H. P. (1967) The Duke Island ultramafic complex, SE Alaska, *Ultramafic and Related Rocks*, R. J. Wyllie (ed.), John Wiley and Sons, NY, p. 97-121.

Taylor, S. R. (1982) *Planetary Science: A Lunar Perspective*, Lunar and Planetary Institute, 481 pp.

Whitaker, E. A., G. P. Kuiper, W. K. Hartmann, and L. H. Spradley (1963) *Rectified Lunar Atlas*, supplement #2 to the Photographic Lunar Atlas, Univ. of Arizona, Tucson, photo #12.

Wilhelms, D. E. (1970) Summary of lunar stratigraphy - Telescopic observations, *USGS Prof. Paper* 599-F, 47 pp.

Wilhelms, D. E. and J. F. McCauley (1971) Geologic map of the near side of the Moon, USGS Map I-703.

Wood, C. A. and J. W. Head (1976) Comparison of impact basins on Mercury, Mars, and the Moon, *Proc. Lunar Sci. Conf. 7th*, p. 3629-3651.

FIGURE 1: BASE MAPS

A - base map of Copernicus ares, showing spectral points, names of important geographical areas

B - view of entire moon, showing basins mentioned in text

FIGURE 2: SPECTRAL DATA

A - graphs of typical spectra of olivine, px, feldspar

B - graphs of continuum for Copernicus wall, peak, Eratosthenes peak, and Apollo 16 sample (offset, on same graph)

FIGURE 3 - All 4 models

ORIGINAL PAGE IS
OF POOR QUALITY

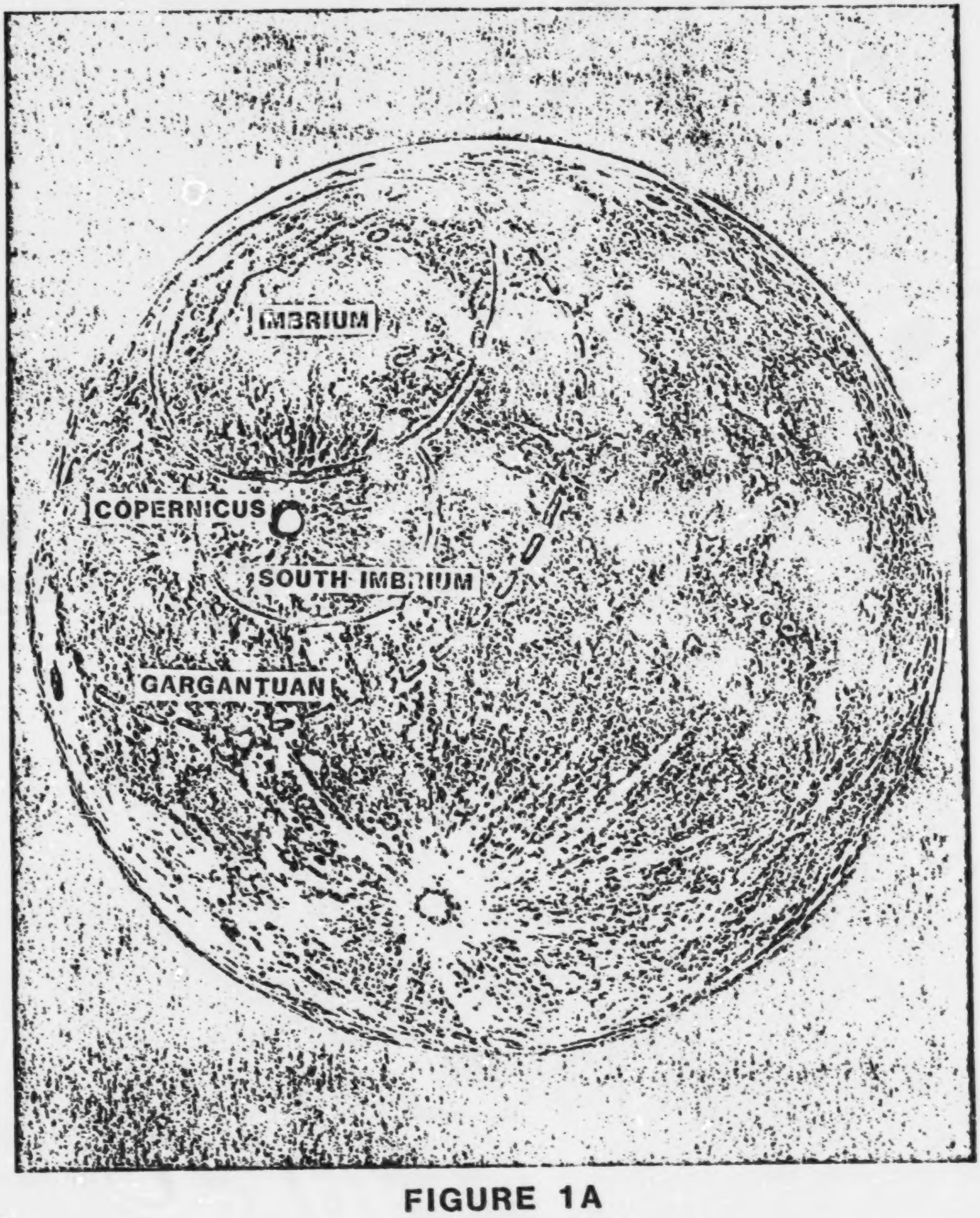
IMBRIUM
COPERNICUS
SOUTH IMBRIUM
GARGANTUAN

FIGURE 1A
Lunar nearside

ORIGINAL PAGE IS
OF POOR QUALITY

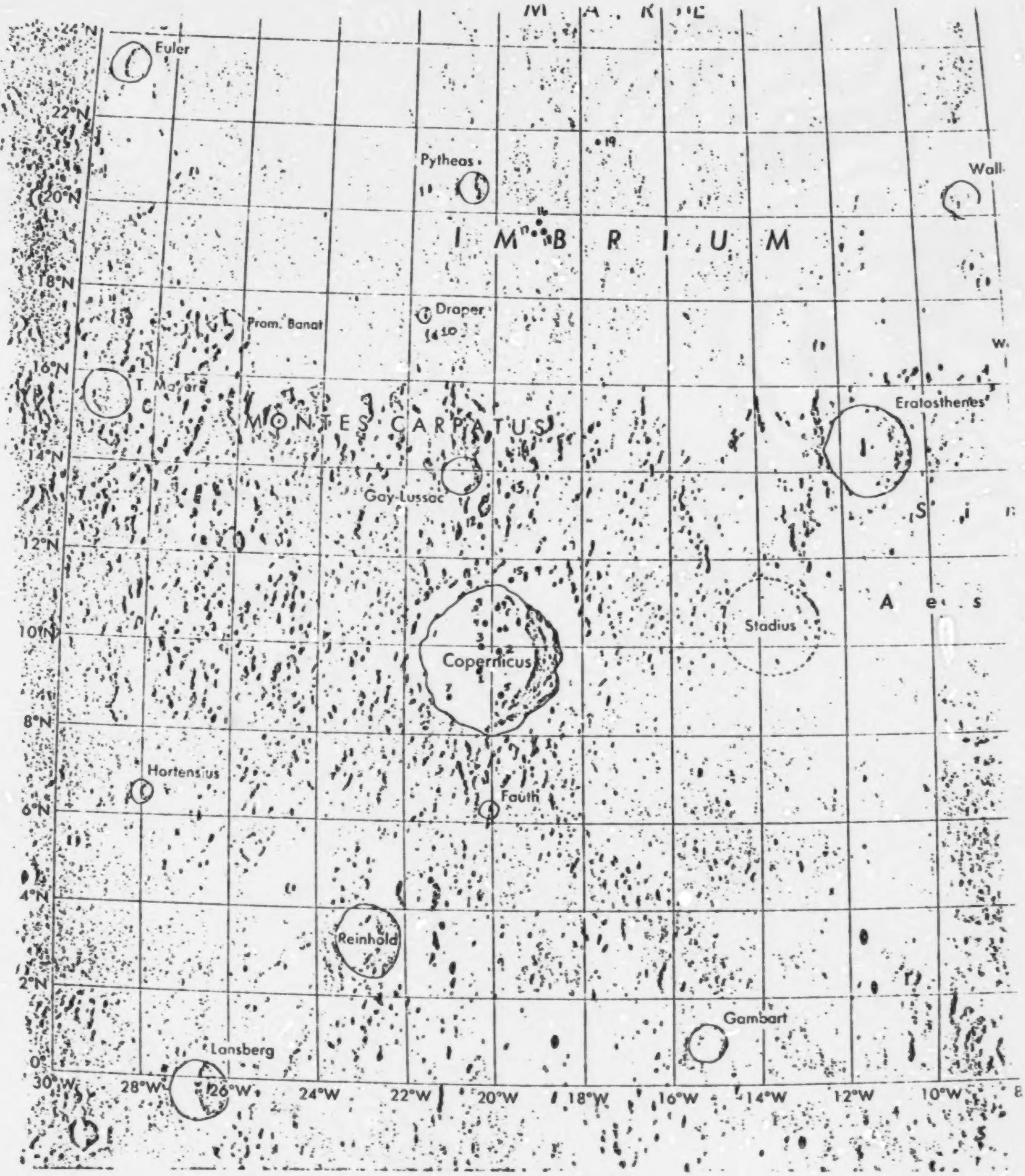
M A R E
24°N
Euler
22°N
Pytheas
Wall
20°N
I M B R I U M
18°N
Prom. Banat
Draper
16°N
T. Mayer
MONTES CARPATUS
Eratosthenes
14°N
Gay-Lussac
S i n
12°N
A e s
10°N
Stadius
Copernicus
8°N
Hortensius
6°N
Fauth
4°N
Reinhold
2°N
Gambart
0°
Lansberg
30°W
28°W
26°W
24°W
22°W
20°W
18°W
16°W
14°W
12°W
10°W

Scale 1:3,500,000 approximate
3.5 kilometers per millimeter 55 miles per inch

FIGURE 1B

Spectral data points

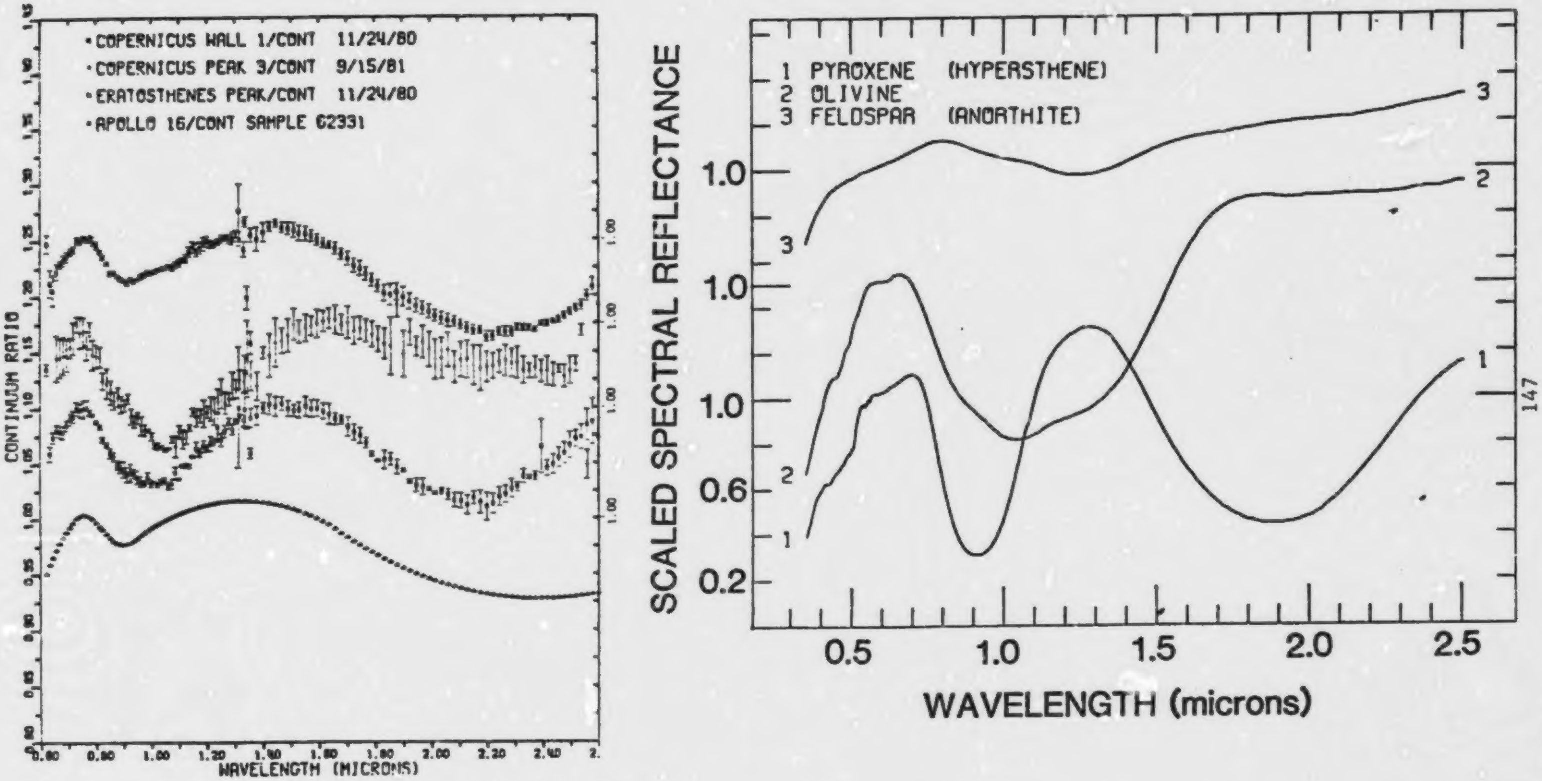
• COPERNICUS WALL 1/CONT 11/24/80
• COPERNICUS PEAK 3/CONT 9/15/81
• ERATOSTHENES PEAK/CONT 11/24/80
• APOLLO 16/CONT SAMPLE 62331
CONTINUUM RATIO
1.25
1.20
1.15
1.10
1.05
1.00
0.95
WAVELENGTH (MICRONS)
0.60
0.80
1.00
1.20
2.00
2.20
2.40
1.00
1.00
1.00
1.00
SCALED SPECTRAL REFLECTANCE
1 PYROXENE (HYPERSTHENE)
2 OLIVINE
3 FELDSPAR (ANORTHITE)
1.0
1.0
1.0
0.6
0.2
1
2
3
0.5
1.0
1.5
2.0
2.5
WAVELENGTH (microns)

FIGURE 2

ORIGINAL PAGE IS
OF POOR QUALITY

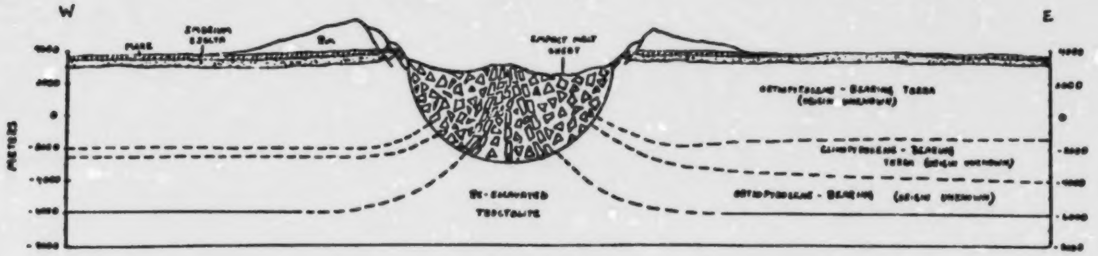
W
E
MARE
IMBRIUM EJECTA
RIM
IMPACT MELT SHEET
ORTHOPYROXENE - BEARING TERRA (ORIGIN UNKNOWN)
CLINOPYROXENE - BEARING TERRA (ORIGIN UNKNOWN)
ORTHOPYROXENE - BEARING (ORIGIN UNKNOWN)
RE-EXCAVATED TROCTOLITE
METERS
4000
2000
0
-2000
-4000
-6000
-8000

MODEL I

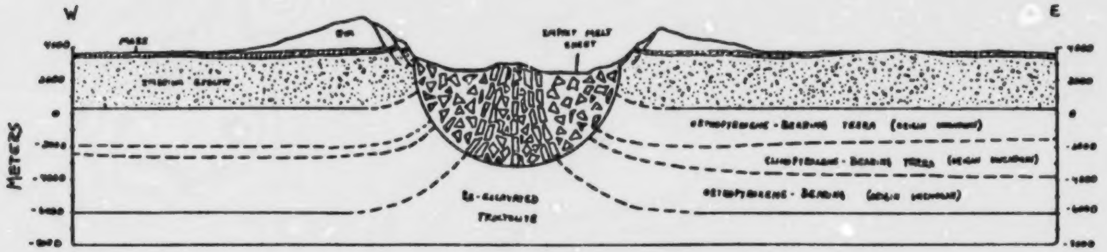
W
E
MARE
RIM
IMPACT MELT SHEET
IMBRIUM GROUP
ORTHOPYROXENE - BEARING TERRA (ORIGIN UNKNOWN)
CLINOPYROXENE - BEARING TERRA (ORIGIN UNKNOWN)
ORTHOPYROXENE - BEARING (ORIGIN UNKNOWN)
RE-EXCAVATED TROCTOLITE
METERS
4000
2000
0
-2000
-4000
-6000
-8000

MODEL 2

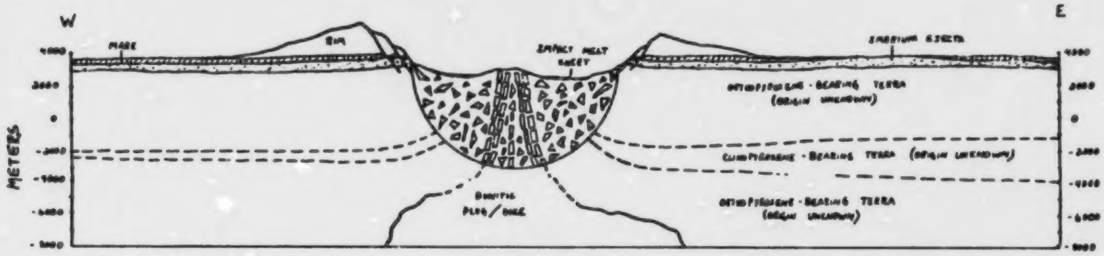
W
E
MARE
RIM
IMPACT MELT SHEET
IMBRIUM EJECTA
ORTHOPYROXENE - BEARING TERRA (ORIGIN UNKNOWN)
CLINOPYROXENE - BEARING TERRA (ORIGIN UNKNOWN)
ORTHOPYROXENE - BEARING TERRA (ORIGIN UNKNOWN)
DUNITIC PLUG/DIKE
METERS
4000
2000
0
-2000
-4000
-6000
-8000

MODEL 3

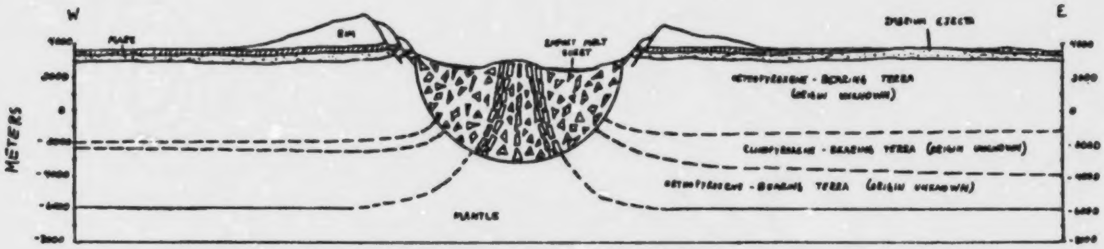
W
E
MARE
RIM
IMPACT MELT SHEET
IMBRIUM EJECTA
ORTHOPYROXENE - BEARING TERRA (ORIGIN UNKNOWN)
CLINOPYROXENE - BEARING TERRA (ORIGIN UNKNOWN)
ORTHOPYROXENE - BEARING TERRA (ORIGIN UNKNOWN)
MANTLE
METERS
4000
2000
0
-2000
-4000
-6000
-8000

MODEL 4

0 10 20 30 40 50 km

VERTICAL EXAGGERATION 5X

FIGURE 3

N84 25572

GEOLOGIC OBSERVATIONS OF THE MARTIAN HIGHLAND BOUNDARY IN THE MAMERS VALLES REGION

James H. Persky, Department of Geology, Boston University, Boston, MA 02215

During my internship at the U.S.G.S. Branch of Astrogeologic Studies in Flagstaff, Arizona, I completed a geologic map of the Ismenius Lacus (MC-5) SW subquadrangle of Mars, using the 1:2,000,000 photomosaic as a base. The mapping, and a limited study of the surrounding areas, was done under the supervision of Baerbel K. Lucchitta, and is part of an effort to determine the nature and origin of fretted terrain, fretted channels, and the northern highland scarp. Some highlights resulting from the mapping and accompanying topical investigations are listed below.

1) The cratered highlands of Mars, in the vicinity of Mamers Valles and Deuteronilus Mensae, appear to consist of ice-cemented material 1-2 km thick, similar to what has been suggested by Sharp (1973). However, the percentage of ice appears to be far greater than previously thought. Fully-enclosed, steep-walled, debris-floored depressions such as the one located at 38.5° N, 332° W (Viking Orbiter image 567A09) suggest an origin by collapse (Carr and Schaber, 1977) rather than by deflation, because the enclosed debris has not been removed. Also, in several places, surface layers are inclined toward troughs or along scarp edges, suggesting withdrawal of material from the subsurface. The removed material may have flowed away in places (Squyres, 1978), but more likely sublimated in those areas where no external exits existed, such as in closed depressions. Furthermore, flows appear to result in headward expansion of valley tributaries by sapping, which would require removal of appreciable amounts of highland material, yet the flow materials do not extend more than about 20 km into the main valleys. This suggests a sizeable difference in mass between material removed and material deposited, a difference which sublimation of ground ice may account for.

2) To the west of Deuteronilus Mensae, a unit of material darker and topographically lower than the majority of the regional highland surface is visible. These two highland units will hereafter be referred to as the dark and light highlands, respectively. The scarps along the dark highlands are

lower than those along the light highlands, and, on a few mesas in the northwestern Deuteronilus Mensae, the dark unit is seen to underlie the light highland material. The dark highlands appear to be stratigraphically lower, and exposed by erosion of the light highlands. Similar layering is seen along the Mamers Valles near 33° N, 343° W (Viking Orbiter image 637A16), where three discrete layers are visible along a channel wall. The two layers of highland material may be of contemporaneous origin, the difference between them the result of diagenesis below the interface of ice-rich and liquid-water-rich materials (Soderblom and Wenner, 1978). The additional layering seen along the southern Mamers Valles could be caused by progressive lowering of the position of the ice-water interface as the Martian climate cooled.

Crater counts on the dark and light highland units are similar, with the dark unit apparently being slightly younger (Table 1). This observation is consistent with the dark unit being an erosional surface that has been exposed to cratering more recently than the light highland surface. Based on crater densities, both highland surfaces are much more recent than highland surfaces in the interior of the highlands elsewhere (Scott and Tanaka, 1981).

Table 1. Crater densities of highland units (values given are numbers of craters equal to or larger than the given diameter per 10^6 km^2).

Superposed Craters	Light Highlands	Dark Highlands
1 km	1080	547
3 km	400	250

3) In Deuteronilus Mensae, the fretted terrain is floored by smooth, flat-lying material darker than either of the highland units. Farther north and west of Deuteronilus Mensae, the floor material and several mesas of dark highland material are buried by two other units. The first is a dark material similar to that found along much of the southern extent of Vastitas Borealis, and has a density of 398 craters greater than or equal to 1 km per 10^6 km^2. The other unit is a material of lesser areal extent which exhibits abundant polygonal and curvilinear features of unknown origin. The features do not resemble the patterned ground of probable ice-wedging origin common in the Mare Acidalium (MC-4) quadrangle. This unit has a density of 456 craters greater

than or equal to 1 km per 10^6 km^2. The burying material is apparently quite young. It appears to have invaded the fretted terrain from the north and west, and may well represent young lava flows.

Overall, ground ice and its removal seem to play an important role in the formation of the fretted terrain. The processes have been active relatively late in Martian history. This implies that either the formation of the fretted terrain is young, or, if it is old, that the processes acted extremely slowly or interruptedly from ancient into relatively recent times.

REFERENCES

Carr, Michael H. and Schaber, Gerald G., 1977, Martian permafrost features, Journal of Geophysical Research, 82, 28, pp. 4039-4054.

Scott, David H., and Tanaka, Kenneth L., 1981, Mars : Paleostratigraphic restoration of buried surfaces in Tharsis Montes, Icarus, 45, pp. 304-319.

Sharp, Robert P., 1973, Mars : Fretted and chaotic terrains, Journal of Geophysical Research, 78, 20, pp. 4073-4083.

Soderblom, Laurence A. and Wenner, David B., 1978, Possible fossil H_2O liquid-ice interfaces in the Martian crust, Icarus, 34, pp. 622-637.

Squyres, Steven W., 1978, Martian fretted terrain : Flow of erosional debris, Icarus, 34, pp. 600-613.

The Source of Mangalla Vales

Pfau, Gerchard Edmund
Wayne State University
Detroit, MI

Saunders, R. Stevens
Jet Propulsion Laboratory
California Institute of Technology
Pasadena, CA

N84 25573

Mangalla Vales is a huge network of channels in the Memnonia Quadrangle of Mars. It appears to have been produced by a single catastrophic flood. There are at least three examples of catastrophic floods known on earth. They are the Channeled Scablands in East Washington (Bretz, 1969; Baker, 1973, 1974), the Snake River Plain in Idaho (Malde, 1968), and the Wright Valley in Antartica (Smith, 1965; Warren, 1965). The catastrophic flows on earth involved millions of cubic meters per second of water (Baker and Milton, 1974). On earth the volume is usually supplied by the breaching of ponded water (such as the collapse of glacial dams).

Catastrophic flows on Mars could not have had the same source as those on earth. Liquid water could not exist on Mars' surface for long without freezing and subliming. Carr (1981) lists several sources for the formation of catastrophic flows on Mars. They are retrogressive flow slides, liquefaction, geothermal melting of ice, decomposition of hydrated minerals, and the breakout of water from confined aquifers.

Breadout of water from the subsurface is the source of Mangalla Vales (Carr, 1981). At the south end of Mangalla is a graben that has been breached (639A11). The faults that formed the graben released subsurface water. The fluid escaped to the surface via the fault and breached the graben wall. From there it flowed north for approximatly 750 kilometers. Evidence from high resolution pictures produced by Viking, tend to support Carr's conclusions.

As the water escaped into the graben it eroded the rock walls, doubling the original width of the graben near the breach. Several remnant portions of the wall appear in the middle of the graben (312A03). They stand upright and are rounded. Before the graben was breached the fluid overflowed, filling a crater located to the southeast of the graben breach (312A04, 690A01). A channel line can be seen within the crater. Later, as the fluid flowed north through the breach, the water probably drained from the crater, because the breach outlet is at a lower level then the crater.

Topographic data suggest a source of the water to the east of the breach, on the other side of a ridge of highland terrain east of Mangella. The source of water is probably ice lenses within the regolith. To the east of the ridge, lava flows cover the entire terrain. These lava flows erupted from Arsia Mons. We are suggesting that as the lava flows extended further from the caldera they heated the graound and melted the trapped ice. The lava cover acted as a cap preventing escape. This area is along the southwest margin of the Tharsis highland. Ground water flowed down the slope from Arsia Mons and collected along the east side of the ridge near Mangalla Vales. The pore pressure would have gradually increased at this location.

A contour map was made using radar topography data to determine the topography of the Memnonia Quadrangle. Along the graben there is a low point that surrounds the graben breach. As the fault, that produced the graben, broke into the aquifer the water flowed along the fault erupting into the graben. The fluid could not have continued flowing west past the present graben breach because the elevation increases in that direction. The fluid collected in this portion of the graben and then followed the path already outlined earlier.

With the release of the fluid from the aquifer, the terrain possibly collapsed. There is no direct evidence for the collapse area because it has been filled by lava. However, there are features that suggest collapse. There appears to be an oval area to the west of the ridge that has no ancient terrain protruding from the lava flows (646A03). On the west, it is bounded by the ridge. To the north, the ridge and crater protrude. To the east, several orld craters and remnant hills appear. To the southeast, a remnant crater and crater peak can be seen. In addition, the graben that broke through to the aquifer, can not be traced across the area but appears at either side.

The source of the lava flows immediatly to the east of the ridge near the graben, is different than the other lava flows in the area. The crests of the lava flows were traced out from high resolution Viking pictures (034A55; 034A53, 034A54; 312A03, 312A04; 639A11 to 14). Throughout the area to the east of the ridge, the lava appear to have flowed east to west. But near the ridge graben intersection the lava flowed to the north, east, and south in an arc. The source for these flows can not be Arsia Mons.

Magma tends to flow along natural paths of weakness within rock strata. Magma would flow along faults and erupt at the lowest points along the faults. The graben passed through the collapse area, which formed when the water was released. This spot was the low point along the graben. Lava erupted from the collapse area along the graben. The rising lava along the fault, may even have helped to melt the ice in the regolith. This would have increased the pore pressure in the aquifer and aided the fluid in bursting out to form the channel.

For this series of events to have occurred, the lava flows must have covered the collapse feature soon after it formed. Evidence exists for this. Within the partially flooded crater southwest of the breach is a fault. This fault is recorded in the portion of the crater remaining free of the flow. The flow obviously buried the fault when it flooded the crater (637A82). The fault passes east through the crater but disappears as it enters the lava flows. Therefore the lava and the catastrophic flows both occured after the formation of the fault. The burial of the fault lend credence to the events discussed earlier in the paper.

References

Baker, V. R., 1973, Paleohydrology and Sedimentology of Lake Missoula Flooding in E. Washington: Geol. Soc. of Am. Spec. Paper 144, 79pp.

——— 1974, Erosional Forms and Processies for the Catastrophic Pleistocene Missoula Floods in E. Washington *In* Marie Marisawa, ed., Proceedings of the fourth Annual Geomorphology Symposium, Binghampton, N.Y. Publication of Geomorphology, State University, N.Y. Binghampton, N.Y.

——— and Milton, D. J., 1974, Erosion by Catastrophic Floods on Mars and Earth: Icarus 23, pp. 27-41.

Bretz, J. A., 1969, The Lake Missoula Floods and the Channeled Scabland: J. Geol., 77, pp. 505-543.

Carr, M. H., 1981, The Surface of Mars: New Haven and London, Yale University Press. 232 p.

Malden, H. E. 1968, The Catastrophic Late Pleistocene Bonneville Flood in the Snake R. Plain, Idaho, USGS Prof. Paper, 596, 52 pp.

Smith, H. T. U., 1965, Anomalous Erosional Topography in Victorialand, Antartica: Science, 148, pp. 941-942.

Warren, C. R., 1965, Wright Valley: Conjectural Volcanoes, Science, 149, p. 658.

N84 25574

Spatial Distribution of Craters on the Moon and Callisto

Alex Ruzicka and Robert G. Strom, Lunar and Planetary Laboratory,
University of Arizona, Tucson, AZ 85721

The crater size/frequency distribution on Callisto (and Ganymede) has a marked deficiency of craters greater than about 30 km diameter relative to the heavily cratered regions on the terrestrial planets (Mercury, Moon and Mars). This deficiency has been attributed to either (a) an obliteration of large craters by viscous relaxation when the crust of Callisto was more thermally active (1, 2,), or (b) the impact of a population of objects which was intrinsicilly deficient in large objects (3, 4).

To distinguish between these two explanations, Woronow and Strom (4) conducted a Monte Carlo computer simulation in which a lunar highland size/frequency distribution was imprinted on a surface and craters eliminated in such a way as to produce the observed Callisto size/frequency distribution. The simulation was completely independent of any assumptions concerning the thermal history, crustal-thickness history or ice rheology of Callisto. The simulated surface (Fig. 2d) showed a crater spatial distribution markedly different from that observed on Callisto (Fig 2c). On the simulated surface, extensive uncratered areas were produced by the obliteration of large craters; a condition not observed on Callisto. Gurnis (5) carried this approach farther by using a variety of size distributions in the Monte Carlo simulation and comparing the resulting spatial distributions with that observed on Callisto by "nearest neighbor" statistical methods. This more rigorous study confirmed the previous results and set more accurate limits on the amount of large-crater obliteration on Callisto. Both studies indicate that the observed crater size/frequency distribution on Callisto is essentially a production population which differs significantly from that on the terrestial planets.

In order to further test these Monte Carlo computer results, an actual surface of the lunar farside highlands was selected to perform a somewhat similar simulation for comparison with Callisto. Although two lunar areas were initally chosen for their apparent lack of plains and secondary craters, one of these areas has a super-abundance of smaller craters relative to other regions of the lunar highlands. Until we understand the reason for this anomaly (possibly clusters of secondaries from Orientale and another nearby basin), only the more typical region will be considered in this preliminary report.

The goal of this study was to compare the spatial distribution of craters 8 km diameter on an area of Callisto with that of a lunar highlands area from which craters had been removed to produce the Callisto size/frequency distribution. The region on Callisto was one used earlier by Woronow and Strom (4) for their comparison with the Monte Carlo simulation, and comprises an area of 6.4×10^5 km^2 (Fig 2c). The similar-sized lunar area (6.2×10^5 km^2) is centered at 160°W, 65°N in the farside north polar region (Fig. 2a).

Craters in the lunar area were mapped and classified according to degradational type using the five-fold LPL scheme where Class 1 is the freshest and Class 5 the most degraded. The size/frequency distribution was then determined and compared with that for the Callisto area (Fig. 1).

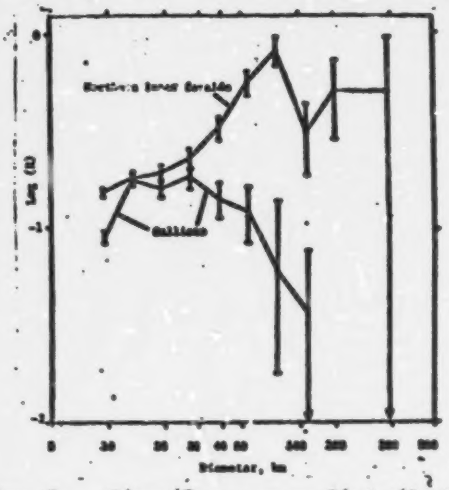

Fig. 1. Size/frequency distributions for the lunar and Callisto areas shown in Fig. 2a and c.

Craters were removed from the lunar area so that the size/frequency distribution matched that of the Callisto area. The obliteration sequence was determined by the degradational state of the craters; the older degraded craters were removed first followed by progressively fresher craters. At the larger size even some of the relatively fresh craters had to be removed to reproduce the Callisto curve.

Figure 2a, shows the spatial distribution of craters in the lunar area while Fig. 2b shows the distribution after the appropriate number of craters were removed to produce the observed Callisto size/frequency distribution (Fig. 1). A visual comparison of Figures 2b and 2c shows that the spatial distributions of the two areas are very different despite the similarities in the overall crater density and size/frequency distribution. On the lunar area there are large relatively crater-free regions not observed on Callisto, because of the necessity of removing substantial numbers of large, relatively fresh craters in order to derive the Callisto size distribution. On the other hand, the derived spatial distribution of the lunar area (Fig. 2b) is similar to Figure 2d, which is the spatial distribution derived from the Monte Carlo computer simulation of a lunar-like impact history done by Woronow and Strom (4). This confirms the validity of the earlier Monte Carlo simulations.

The results of this study, together with those of the Monte Carlo computer simulations, strongly suggest that the Callisto (and Ganymede) crater population is basically a production population deficient in large craters relative to that of the terrestrial planets. This indicates that the population of impacting objects responsible for the period of heavy bombardment in the inner Solar System was different from that at Jupiter, and probably had a different origin as well.

References

(1) Parmentier, E.M. and Head, J.W., Internal Processes Affecting Surfaces of Low-density Satellites: Ganymede and Callisto, J. Geophs. Res., 84, 6263-6276, 1979.

(2) Shoemaker, E.M. and Wolfe, R.F., Cratering Time Scales for the Galilean Satellites, The Galilean Satellites, (Morrison, ed.), Chapter 10, Univ. of Ariz. Press, 1982.

(3) Strom, R.G., Woronow, A., and Gurnis, M., Crater Populations on Ganymede and Callisto, Jour. Geophys. Res., 85, 8659-8674, 1981.

(4) Woronow, A. and Strom, R.G., Limits on Large-Crater Production and Obliteration on Callisto, Geophys. Res. Lett., 8, 891-894, 1981.

(5) Gurnis, M., Spatial Distribution of Craters on Callisto and Limits on the Crater Production Population of the Jovian System, Icarus, in Press, 1982.

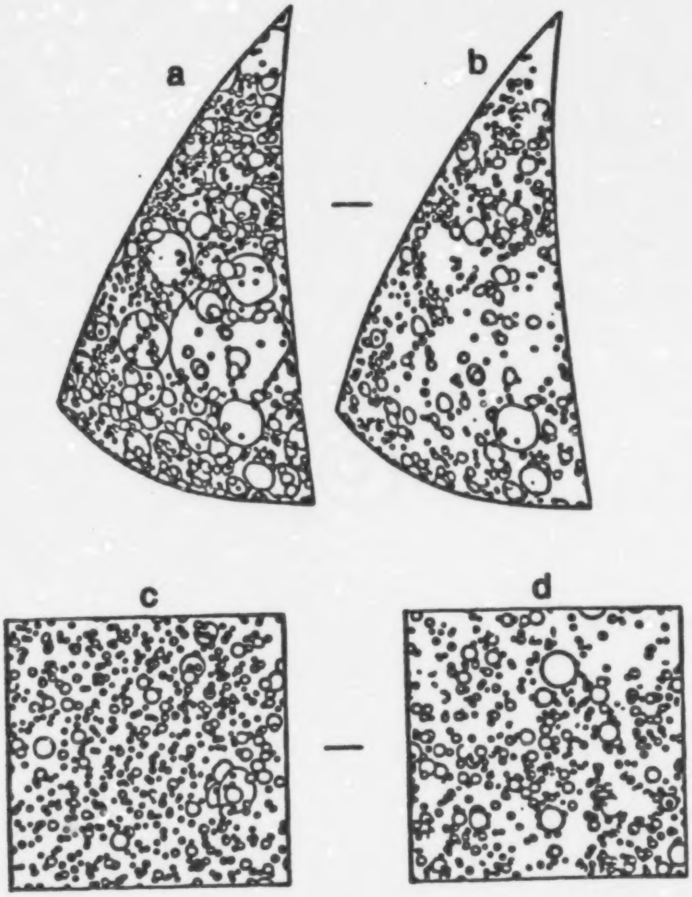

Fig. 2. Spatial distributions of craters observed on the lunar area (a) the Callisto area (c), after crater removal from lunar area to produce Callisto size/frequency distribution (b) and from Monte Carlo computer simulation (d). Scale bars represent 100 km. Fig. 2c and d are from Woronow and Strom (4).

D8 N84 25575

Callisto: A Lunar-like Bombardment?

Alex Ruzicka, Lunar and Planetary Lab, Tucson, Arizona, 85721

Voyager spacecraft imagery of the Galilean satellites in 1979 revealed Callisto and portions of Ganymede to be densely cratered, but nonetheless deficient in craters larger than 30 km relative to the cratered highlands of the moon, Mars, and Mercury (Strom et al., 1981; Woronow and Strom, 1981; Woronow et al., 1981). This relative deficiency of large craters could have been due to the complete obliteration of large craters through viscous relaxation in the icy surfaces of Ganymede and Callisto at a time when their surfaces were presumably warmer and more mobile (Parmentier and Head, 1979; Parmentier et al., 1980; Parmentier and Head, 1981; Shoemaker and Wolfe, 1981), or the deficiency could have stemmed from a relative depletion of large impacting bodies in the Jupiter system, compared with the terrestial planets (Strom et al., 1981; Woronow and Strom, 1981; Woronow et al., 1981).

To test which alternative is correct, and, specifically, to see whether Callisto could have been subjected to a lunar-like bombardment, two areas on the heavily cratered lunar farside were compared with an area on Callisto. The two farside regions are representative of the heavily cratered terranes on the moon uncontaminated with plains or basin secondaries. While they appear typical of the rugged farside terra, they have a visually apparent difference in the density of large craters. The area on Callisto is typical of Callisto, and was seen at approximately 4 km resolution near the terminator by Voyager 2 (Woronow and Strom, 1981).

Relative size-frequency plots for craters 8 km in diameter and larger show that both farside areas have a greater density of craters of all sizes than Callisto (Fig. 1), although for craters between 10 and 30 km in diameter, the northern farside is statistically indistinguishable from Callisto (the error bars for each region overlap). Also apparent from Figure 1 is the great difference between the size-frequency distributions of each farside area—a disparity that is most striking for craters with diameters below about 40 km. The equatorial farside distribution (Fig. 1a) strongly resembles Hartmann's "pure uplands" plot (Basaltic Volcanism Study Project, 1981, p. 1118) for roughly the same region, while the northern farside (Fig. 1b) resembles Strom's (1977) nearside highlands distribution. The relatively lower density of craters in the smallest size bin on Callisto could be due to the incomplete recognition of craters less than 10 km across, even with 4-km-resolution photography (Strom _et al._, 1981; Woronow and Strom, 1981; Woronow _et al._, 1981).

Figures 2a and 2b show the areal distribution of craters 8 km and larger for the northern and equatorial farside, respectively, while Figure 3a, reproduced from Woronow and Strom (1981), shows craters 8 km and greater in diameter on Callisto. Comparison of these figures illustrates the dearth of large craters on Callisto relative to the moon (especially relative to the northern farside), and the extremely high density of craters in the equatorial farside.

All lunar craters 8 km and larger were classified according to degradation state, using the five-part Lunar and Planetary Laboratory scheme developed by Arthur _et al._ (1963), where 1= a fresh crater with a little-modified rim, 2= a somewhat more degraded crater with a modified rim, etc. The density of lunar craters in each size bin was then adjusted— by removing the most degraded craters in succession— until the observed density of Callisto was reached (Fig. 2c and 2d). In other words, Figures 2c and 2d have the same size-frequency distribution as Figure 3a. In the case of the equatorial area, many small as well as large craters were removed (including all class 5 and 4 craters and most class 3 craters). In the northern area, most of the craters removed were less than 10 and greater than 30 km in diameter; only some of the class 5 craters in the 10-30 km range were removed.

The crater removal from the moon simulates the destruction of craters by any process that could have converted an original lunar size-frequency distribution to the observed distribution of Callisto. In Figures 2c, 2d and 3a, the more uniformly cratered appearance of Callisto compared with the lunar regions following crater removal can be seen. That both lunar regions, which have a visually apparent difference in the number of large craters (Fig. 2a and 2b), and drastically different size-frequency distributions, should yield the same patchy areal distribution following reduction to the Callisto size-frequency distribution, can hardly be coincidence. The moon and Callisto are so dissimilar that it is impossible to "force" the moon to look like Callisto, even with a process that can effectively remove any number of craters of any size from the moon. The moon and Callisto must have been bombarded by two different populations, and though viscous relaxation could have modified, or even completely obliterated, craters on Callisto's surface, it could not have been solely responsible for the observed deficiency of large craters on Callisto relative to the moon.

The same conclusion was reached by Woronow and Strom (1981), who used Monte Carlo simulations of the moon that sought to match the nearside highlands size-frequency curve to that of Callisto. They included the effects of completely relaxed craters in portraying the areal distribution of craters, and their result (Fig. 3b), shows "gaps" of low crater density where large craters have been relaxed— yielding a patchy distribution.

Acknowledgements-- Special thanks to John Spencer, who verified the equatorial size-frequency distribution; to Bob Strom, for his guidance; and to Martha Leake, for her valued help.

References

Arthur, D.W.G., A.P. Agnieray, R.A. Horvath, C.A. Wood and C.R. Chapman (1963), The System of Lunar Craters, Quadrant I, in Communications of the Lunar and Planetary Laboratory, 2, 30, 71-78, The University of Arizona.

Basaltic Volcanism Study Project (1981), Basaltic Volcanism on the Terrestial Planets, Pergamon Press, Inc., New York, 1286 pp.

Parmentier, E.M. and J.W. Head (1979), Internal Processes Affecting Surfaces of Low-density Satellites: Ganymede and Callisto, Journal of Geophysical Research, 84, 6263-6276.

Parmentier, E.M., M.L. Allison, M.J. Cintala and J.W. Head (1980), Viscous Degradation of Impact Craters on Icy Satellite Surfaces (abstract), Lunar and Planetary Science Conference XII, 857-859.

Parmentier, E.M. and J.W. Head (1981), Viscous Relaxation of Impact Craters on Icy Planetary Surfaces: Determination of Viscosity Variation with Depth, Icarus, 47, 100-111.

Shoemaker, E.M. and R.F. Wolfe (1981), Cratering Time Scales for the Galilean Satellites, The Galilean Satellites (Morrison,ed.), Chapt. 10, University of Arizona Press, in press.

Strom, R.G. (1977), Origin and Relative Age of Lunar and Mercurian Intercrater Plains, Physics of the Earth and Planetary Interiors, 15, 156, 1977.

Strom, R.G. , A. Woronow and M.C. Gurnis (1981), Crater Populations on Ganymede and Callisto, Journal of Geophysical Research, 86, 8659-8674.

Woronow, A. and R.G. Strom (1981), Limits on Large-crater Production and Obliteration on Callisto, Geophysical Research Letters, 8, 8, 891-894.

Woronow, A., R.G. Strom and M.C. Gurnis (1981), Interpreting the Cratering Record: From Mercury to Ganymede and Callisto, The Galilean Satellites (Morrison, ed.), Chapt. 9, University of Arizona Press, in press.

ORIGINAL PAGE IS OF POOR QUALITY

Figure 1. Relative size-frequency plots for craters in the equatorial lunar farside (a) and the northern lunar farside (b) compared with Callisto. The Callisto data is from Woronow and Strom (1981).

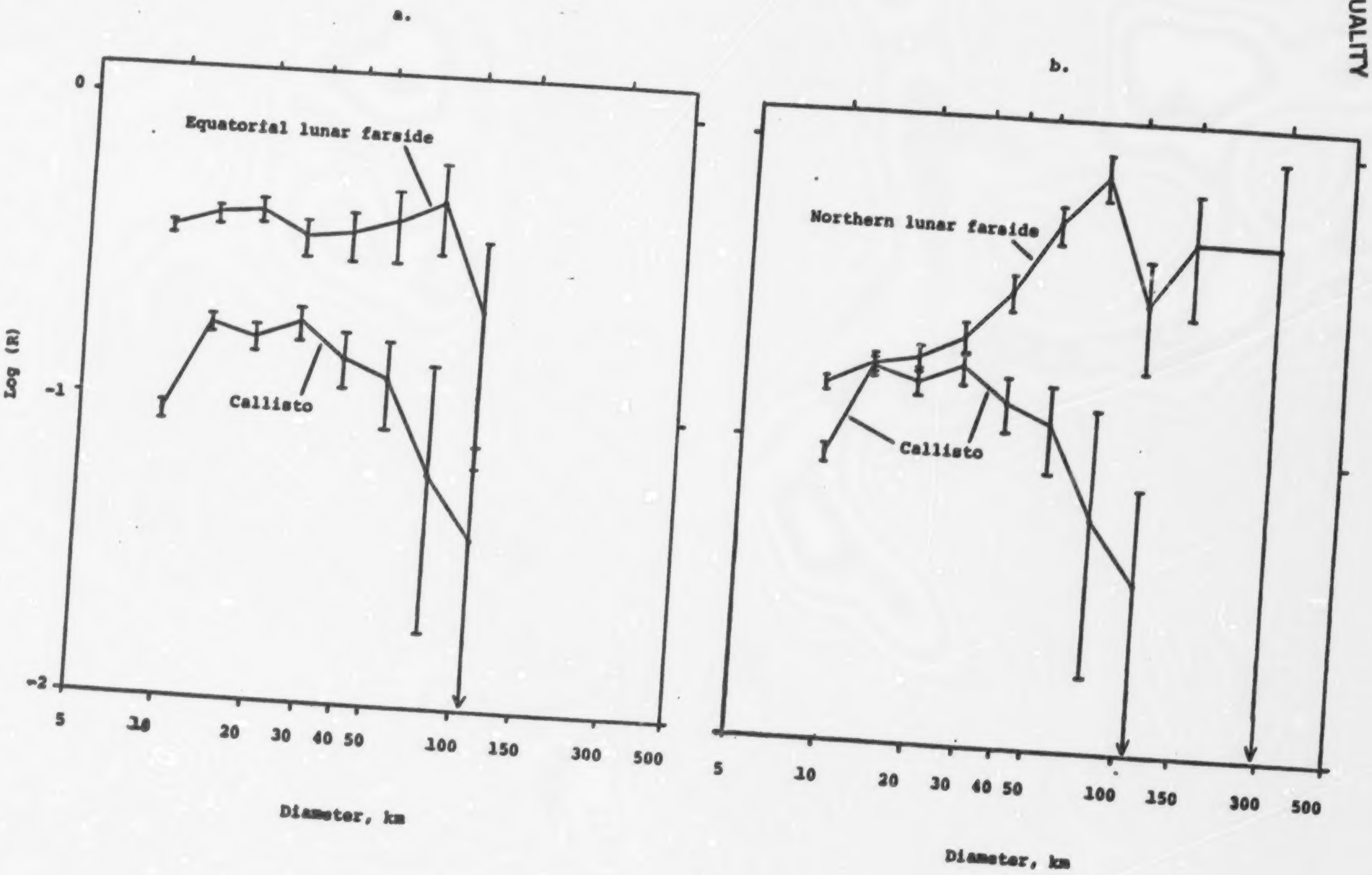

ORIGINAL PAGE IS
OF POOR QUALITY

Figure 2. Areal distribution of craters prior to, and following, removal of craters from: the northern lunar farside (a and c, respectively); the equatorial lunar farside (b and d, respectively). Scale bars represent 100 kilometers.

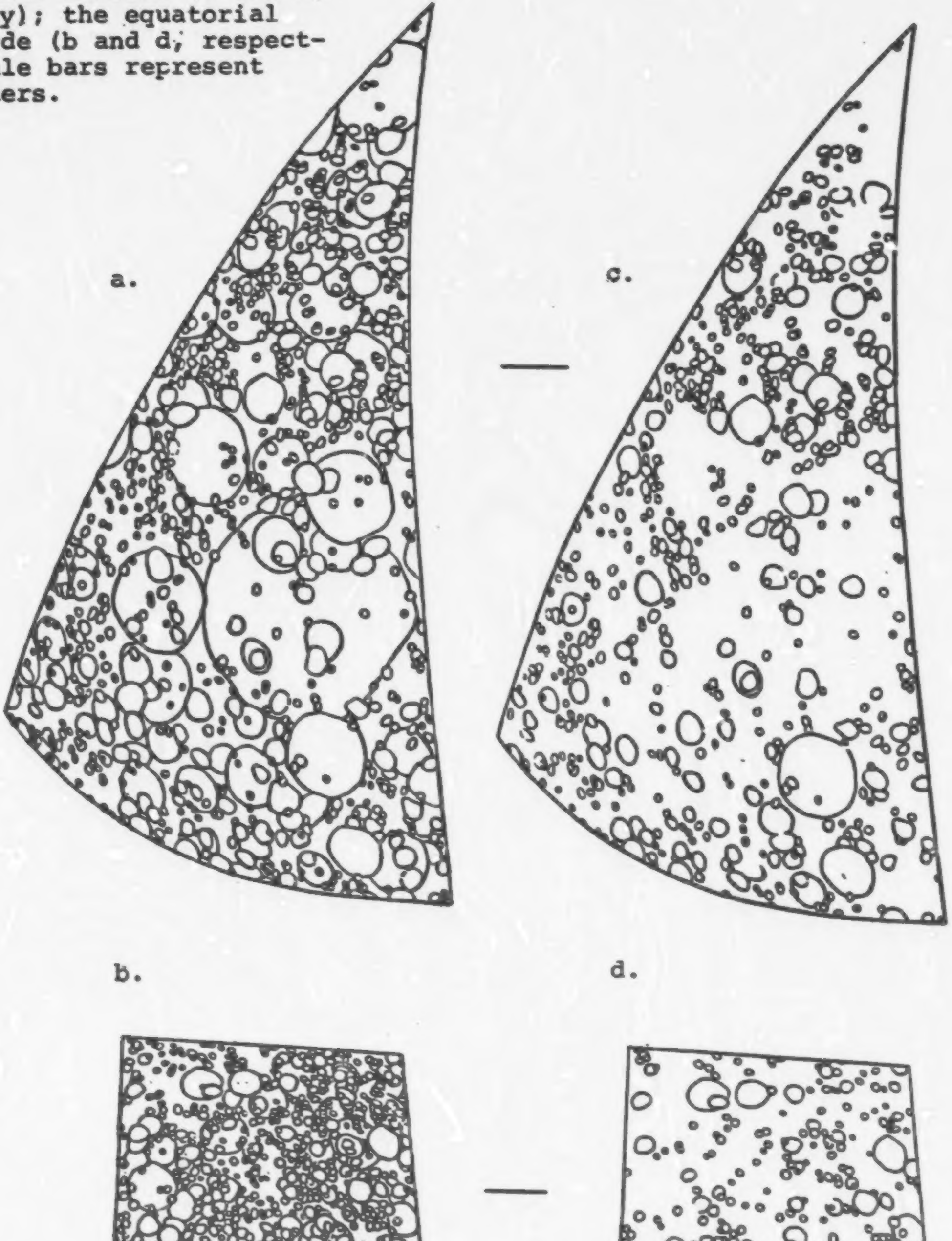

Figure 3. Areal distribution of craters 8 km and larger in the area on Callisto mapped by Woronow and Strom (1981) (a); and (b), a computer simulation of the moon following relaxation to match the size-frequency distribution of Callisto in (a), from Woronow and Strom (1981). Scale bar represents 100 kilometers.

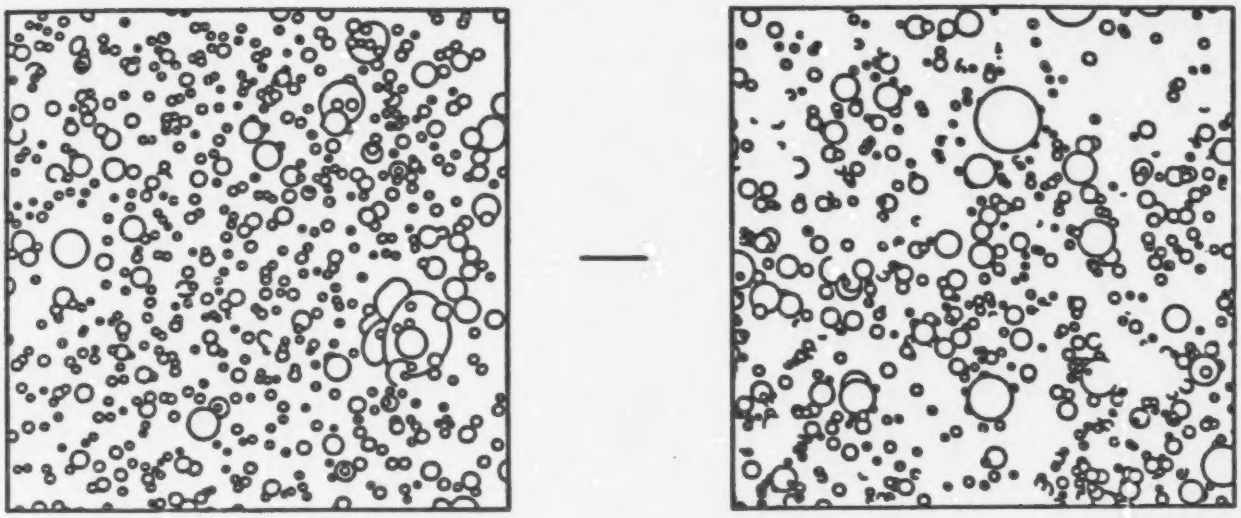

a.

b.

N84 25576 D9

L CHONDRITE METEORITES: A COMPILATION AND PRELIMINARY ANALYSES.

Alan Silliman, Planetary Geology Intern, Johnson Space Center, Houston, TX.

A compilation of those meteorites currently recognized as being L chondrites, exclusive of the numerous Antarctica finds, has been made and is known as the L Chondrite Register. Data for these 576 meteorites has been collected from a variety of sources, primarily the British Museum's Catalogue of Meteorites (Hey, 1966) and the Appendix to the Catalogue of Meteorites (Hutchison et. al., 1977). Also used was the Revised Cambridge Chondrite Compendium (Motylewski, 1978), which provided a convenient listing of L chondrites; other sources include Chinese Meteorites (Depei, 1981), Meteorites, by Wasson (1974), and the Meteoritical Bulletin of Meteoritics. This last source provided data for most recent falls and was referenced through March of 1982. All such data were recorded on a computer data file with an HP 2647A terminal, so that information could easily be retrieved and manipulated. For each meteorite, the petrographic class, location of find, fall date and hour, mass, mole per cent fayalite, weight per cent Fe, SiO2/MgO ratio, shock class, metal class, 4He abundance, UTh-He gas retention age, K-Ar gas retention age, and 21Ne cosmic ray exposure age, was recorded when known (figure 1).

Upon completion of the L Chondrite Register certain of the data could be graphically represented with the aid of the HP 2647A terminal. A histogram of the UTh-He gas retention ages of 189 meteorites (figure 2) was produced to search for possible shock events in a postulated L Chondrite parent body. This histogram suggested natural diviisions of time: <0.6 B.y.; =>0.6, <1.4 B.y.; =>1.4, <2.1 B.y.; =>2.1, <3.2 B.y.; =>3.2 B.y. Most available data of the L Chondrite Register was plotted in histogram form against these UTh-He gas retention age intervals by producing a sorted listing of all L chondrites with UTh-He data, and then plotting the appropriate meteorite datum in a histogram of the appropriate gas retention age interval. Thus each interval defines its own histogram and a series of five histograms must be produced for each variable studied, covering the entire range of UTh-He gas retention age for L chondrite meteorites. From numerous histograms with these intervals, several plots may be derived which exhibit interesting trends in the variable concerned. A histogram series of mole per cent fayalite with these time intervals shows a subtle shift in the distribution toward higher iron content in olivine with increasing UTh-He gas retention age (figure 3). This shift in distribution is presented in tabular form in table 1. With a correlation of unknown significance established between mole per cent fayalite and UTh-He gas retention age, I sought to further examine chemical parameters vs. gas retention age by producing histogram plots of the total weight per cent iron of the meteorite and the SiO2/MgO ratio of the meteorite with these time intervals. An approximate relationship was established between the weight per cent iron and gas retention age; however, there is no apparent trend between the SiO2/MgO ratio and the gas retention age (table 1).

In a 1979 paper, Dodd and Jarosewich establish shock facies criteria by which L chondrites may further be classified and they have done so for 52 L chondrites. I have constructed a plot of shock facies vs. UTh-He gas retention age for 47 of these 52 meteorites, and have confirmed a definite trend toward weaker shock intensity with greater gas retention age, as previously reported by Taylor and Heymann (1969) (table 1).

A hypothesis to account for these chemical and petrographic trends is that all L chondritic material is a sample of a singular parent body. Presumably, as early impacts with this parent body excavated its surface only, those meteorites with greatest gas retention ages are chemically representative of the outermost material of the parent. As impacts continued to occur an increasing proportion of the parent body's surface which originally existed at some depth, was exposed by repeated collisions. Thus, it is reasonable to expect that meteorites with successively earlier gas retention ages have been sampled fron interior portions of successively greater depth within the parent body, and that their chemical characteristics are then representative of the parent body at that depth. Accordingly, this body possesses a chemical gradient in which the amount of iron in olivine in the bulk rock decreases with depth and the total weight per cent of iron in the bulk rock increases with depth. I can only note that there exists no discernable trend in the SiO2/MgO ratio with gas retention age and thus depth within the parent body. 21Ne cosmic ray exposure age averaged for the meteorites of any particular gas retention age interval is interpreted simply as that amount of time the meteorite mass spent in passage from the parent body to the Earth. The 21Ne cosmic ray exposure age of the most recent gas retention age interval is a factor of two less than in the remaining intervals. Perhaps the L chondrite parent body suffered a shock event some 0.6 B.y. which modified the orbit of ejecta from its previous path, thereby reducing the amount of time of passage for the ejecta.

The correlation between the shock facies of a meteorite and its UTh-He gas retention age perhaps indicates a variation in the nature of collisions suffered by the parent body through time. Since L chondrite meteorites tend to exhibit evidence of greater shock intensity as their gas retention age decreases, one may speculate that in general the energy of impacts in the universe has increased through time.

I wish to thank Dr. Charles A. Wood for his guidance on this project, and James Gooding, Richard Lee-Berman, and Thomas See for their contributions and suggestions.

REFERENCES:

Dodd, R.T. and Jarosewich, E., 1979, Incipient melting in and shock classification of L-group chondrites; Earth and Planetary Science Letters, vol. 44, pp. 335-340.

Taylor, G.J. and Heymann, D., 1969, Shock, reheating, and the gas retention ages of chondrites; Earth and Planetary Science Letters, vol. 7, pp. 151-161.

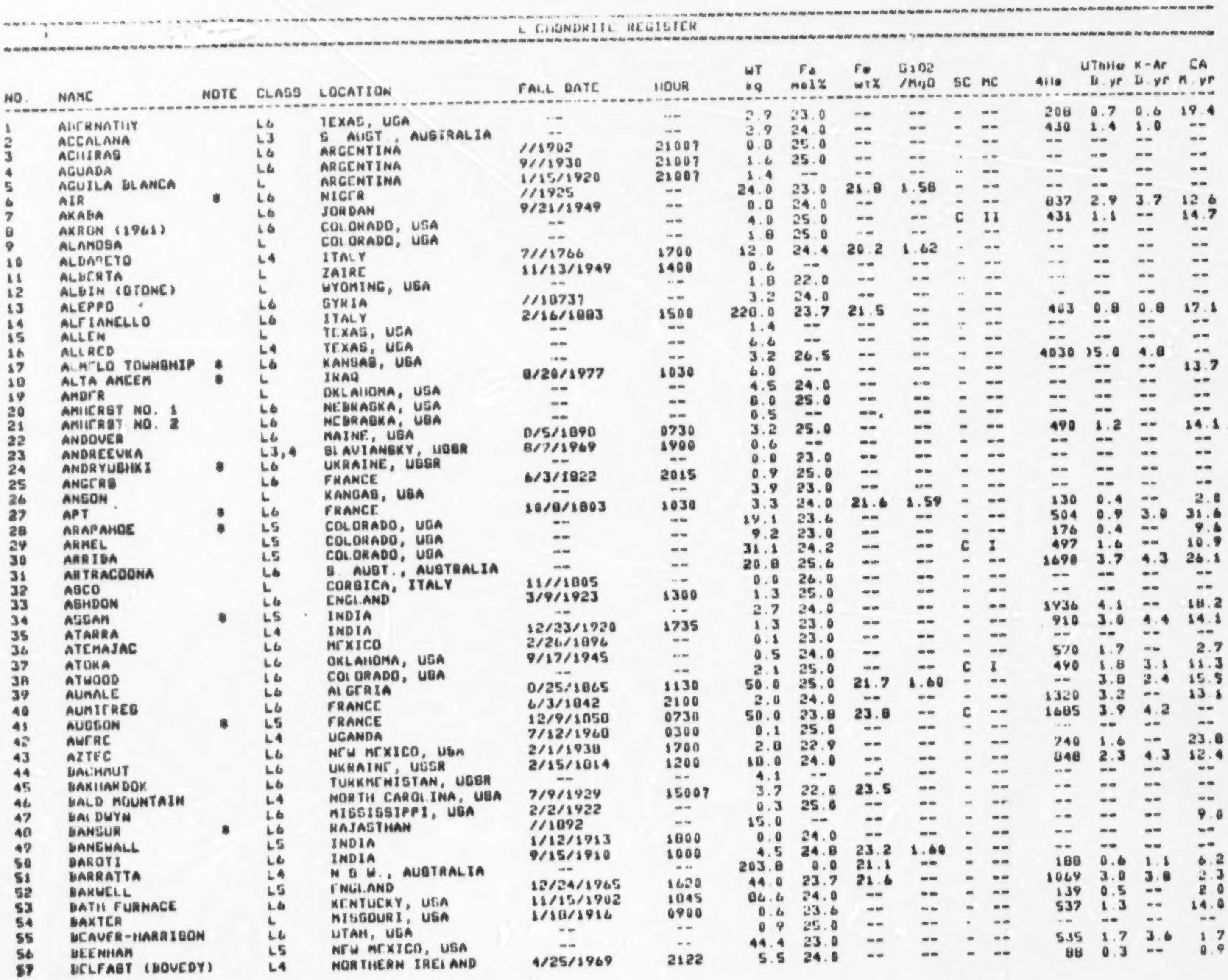

L CHONDRITE REGISTER

NO.	NAME	NOTE	CLASS	LOCATION	FALL DATE	HOUR	WT kg	Fa mol%	Fe wt%	SiO2 /MgO	SC	MC	4He	UThHe B.yr	K-Ar B.yr	CA M.yr
1	ABERNATHY		L6	TEXAS, USA	--	--	2.9	23.0	--	--	-	--	208	0.7	0.6	19.4
2	ACCALANA		L3	S. AUST., AUSTRALIA	--	--	2.9	24.0	--	--	-	--	430	1.4	1.0	--
3	ACHIRAS		L6	ARGENTINA	//1902	2100?	0.8	25.0	--	--	-	--	--	--	--	--
4	AGUADA		L6	ARGENTINA	9//1930	2100?	1.6	25.0	--	--	-	--	--	--	--	--
5	AGUILA BLANCA		L	ARGENTINA	1/15/1920	2100?	1.4	--	--	--	-	--	--	--	--	--
6	AIR	*	L6	NIGER	//1925	--	24.0	23.0	21.8	1.58	-	--	--	--	--	--
7	AKABA		L6	JORDAN	9/21/1949	--	0.8	24.0	--	--	-	--	837	2.9	3.7	12.6
8	AKRON (1961)		L6	COLORADO, USA	--	--	4.0	25.0	--	--	C	II	431	1.1	--	14.7
9	ALAMOSA		L	COLORADO, USA	--	--	1.8	25.0	--	--	-	--	--	--	--	--
10	ALBARETO		L4	ITALY	7//1766	1700	12.0	24.4	20.2	1.62	-	--	--	--	--	--
11	ALBERTA		L	ZAIRE	11/13/1949	1400	0.6	--	--	--	-	--	--	--	--	--
12	ALBIN (STONE)		L	WYOMING, USA	--	--	1.8	22.0	--	--	-	--	--	--	--	--
13	ALEPPO		L6	SYRIA	//1873?	--	3.2	24.0	--	--	-	--	-	--	--	--
14	ALFIANELLO		L6	ITALY	2/16/1883	1500	220.0	23.7	21.5	--	-	--	403	0.8	0.8	17.1
15	ALLEN		L	TEXAS, USA	--	--	1.4	--	--	--	-	--	--	--	--	--
16	ALLRED		L4	TEXAS, USA	--	--	6.6	--	--	--	-	--	--	--	--	--
17	ALMELO TOWNSHIP	*	L6	KANSAS, USA	--	--	3.2	26.5	--	--	-	--	4030	>5.0	4.8	--
18	ALTA AMEEM	*	L	IRAQ	8/28/1977	1030	6.0	--	--	--	-	--	--	--	--	13.7
19	AMBER		L	OKLAHOMA, USA	--	--	4.5	24.0	--	--	-	--	--	--	--	--
20	AMHERST NO. 1		L6	NEBRASKA, USA	--	--	8.0	25.0	--	--	-	--	--	--	--	--
21	AMHERST NO. 2		L6	NEBRASKA, USA	--	--	0.5	--	--	--	-	--	--	--	--	--
22	ANDOVER		L6	MAINE, USA	8/5/1898	0730	3.2	25.0	--	--	-	--	490	1.2	--	14.1
23	ANDREEVKA		L3,4	SLAVIANSKY, USSR	8/7/1969	1900	0.6	--	--	--	-	--	--	--	--	--
24	ANDRYUSHKI	*	L6	UKRAINE, USSR	--	--	0.0	23.0	--	--	-	--	--	--	--	--
25	ANGERS		L6	FRANCE	6/3/1822	2015	0.9	25.0	--	--	-	--	--	--	--	--
26	ANSON		L	KANSAS, USA	--	--	3.9	23.0	--	--	-	--	--	--	--	--
27	APT	*	L6	FRANCE	10/8/1803	1030	3.3	24.0	21.6	1.59	-	--	130	0.4	--	2.8
28	ARAPAHOE	*	L5	COLORADO, USA	--	--	19.1	23.6	--	--	-	--	504	0.9	3.0	31.6
29	ARMEL		L5	COLORADO, USA	--	--	9.2	23.0	--	--	-	--	176	0.4	--	9.6
30	ARRIBA		L5	COLORADO, USA	--	--	31.1	24.2	--	--	C	I	497	1.6	--	10.9
31	ARTRACOONA		L6	S. AUST., AUSTRALIA	--	--	20.8	25.6	--	--	-	--	1690	3.7	4.3	26.1
32	ASCO		L	CORSICA, ITALY	11//1805	--	0.8	26.0	--	--	-	--	--	--	--	--
33	ASHDON		L6	ENGLAND	3/9/1923	1300	1.3	25.0	--	--	-	--	--	--	--	--
34	ASSAM	*	L5	INDIA	--	--	2.7	24.0	--	--	-	--	1936	4.1	--	18.2
35	ATARRA		L4	INDIA	12/23/1920	1735	1.3	23.0	--	--	-	--	910	3.0	4.4	14.1
36	ATEMAJAC		L6	MEXICO	2/26/1896	--	0.1	23.0	--	--	-	--	--	--	--	--
37	ATOKA		L6	OKLAHOMA, USA	9/17/1945	--	0.5	24.0	--	--	-	--	570	1.7	--	2.7
38	ATWOOD		L6	COLORADO, USA	--	--	2.1	25.0	--	--	C	I	490	1.8	3.1	11.3
39	AUMALE		L6	ALGERIA	8/25/1865	1130	50.0	25.0	21.7	1.60	-	--	--	3.8	2.4	15.5
40	AUMIERES		L6	FRANCE	6/3/1842	2100	2.0	24.0	--	--	-	--	1320	3.2	--	13.1
41	AUSSON	*	L5	FRANCE	12/9/1858	0730	50.0	23.8	23.8	--	C	--	1605	3.9	4.2	--
42	AWERE		L4	UGANDA	7/12/1968	0300	0.1	25.0	--	--	-	--	--	--	--	--
43	AZTEC		L6	NEW MEXICO, USA	2/1/1938	1700	2.8	22.9	--	--	-	--	740	1.6	--	23.8
44	BACHMUT		L6	UKRAINE, USSR	2/15/1814	1200	18.0	24.0	--	--	-	--	848	2.3	4.3	12.4
45	BAKHARDOK		L6	TURKMENISTAN, USSR	--	--	4.1	--	--	--	-	--	--	--	--	--
46	BALD MOUNTAIN		L4	NORTH CAROLINA, USA	7/9/1929	1500?	3.7	22.0	23.5	--	-	--	--	--	--	--
47	BALDWYN		L6	MISSISSIPPI, USA	2/2/1922	--	0.3	25.0	--	--	-	--	--	--	--	--
48	BANSUR	*	L6	RAJASTHAN	//1892	--	15.0	--	--	--	-	--	--	--	--	9.0
49	BANSWAL		L5	INDIA	1/12/1913	1800	0.0	24.0	--	--	-	--	--	--	--	--
50	BAROTI		L6	INDIA	9/15/1910	1000	4.5	24.8	23.2	1.60	-	--	--	--	--	--
51	BARRATTA		L4	N.S.W., AUSTRALIA	--	--	203.8	0.0	21.1	--	-	--	188	0.6	1.1	6.2
52	BARWELL		L5	ENGLAND	12/24/1965	1620	44.0	23.7	21.6	--	-	--	1069	3.0	3.8	2.3
53	BATH FURNACE		L6	KENTUCKY, USA	11/15/1902	1045	86.6	24.0	--	--	-	--	139	0.5	--	2.0
54	BAXTER		L	MISSOURI, USA	1/18/1916	0900	0.6	23.6	--	--	-	--	537	1.3	--	14.8
55	BEAVER-HARRISON		L6	UTAH, USA	--	--	0.9	25.0	--	--	-	--	--	--	--	--
56	BEENHAM		L5	NEW MEXICO, USA	--	--	44.4	23.0	--	--	-	--	535	1.7	3.6	1.7
57	BELFAST (BOVEDY)		L4	NORTHERN IRELAND	4/25/1969	2122	5.5	24.8	--	--	-	--	88	0.3	--	0.9

Figure 1. Sample page from the L Chondrite Register.

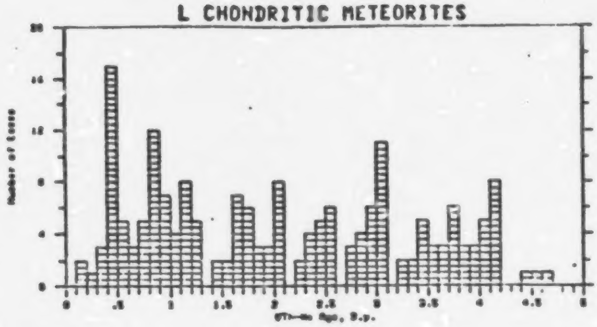

Figure 2. Histogram of UTh-He gas retention age for 189 L chondrites.

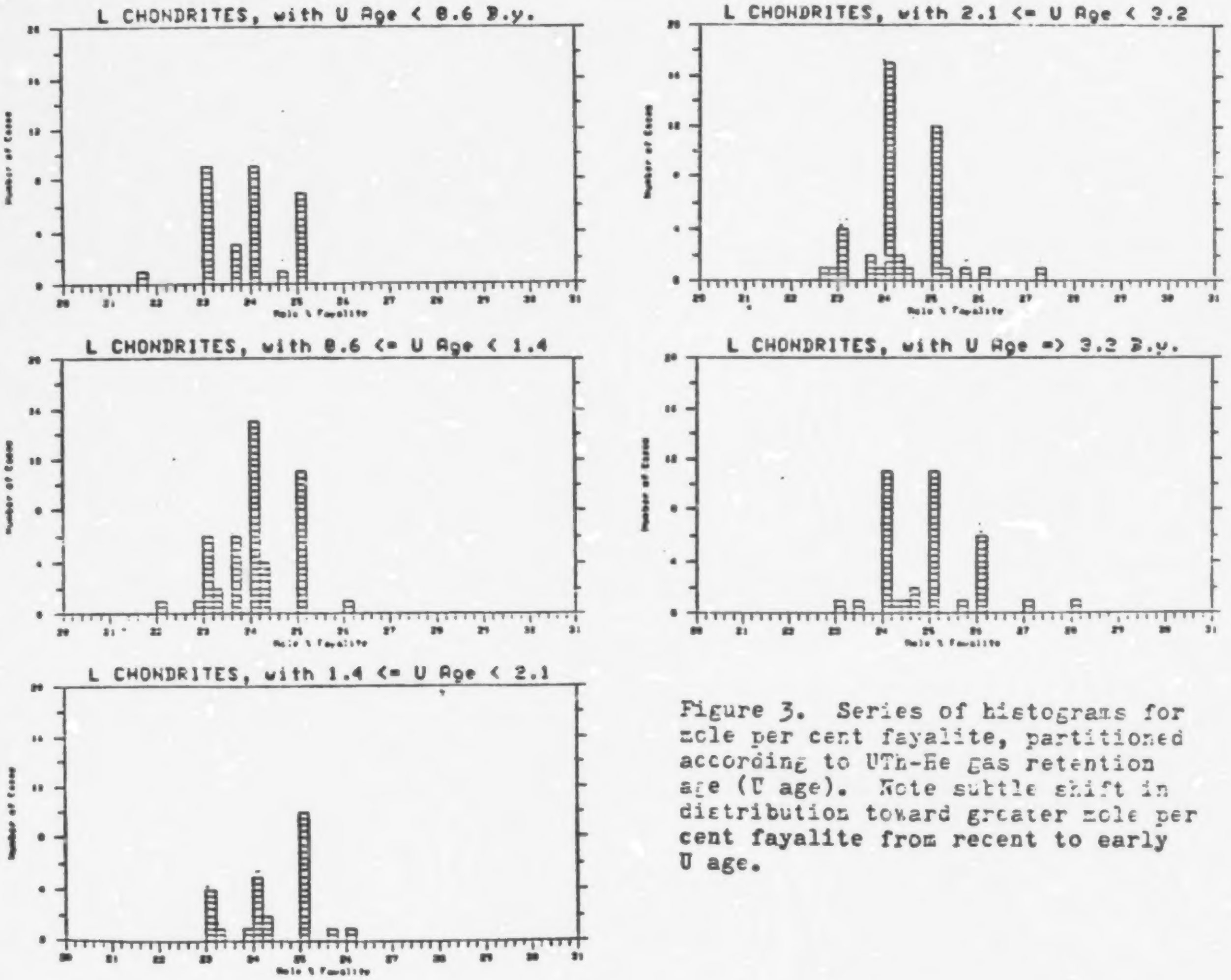

Figure 3. Series of histograms for mole per cent fayalite, partitioned according to UTh-He gas retention age (U age). Note subtle shift in distribution toward greater mole per cent fayalite from recent to early U age.

TABLE 1: UTh-He Gas Retention Age (U) Interval, B.y.

PARAMETER	U<0.6	0.6<=U<1.4	1.4<=U<2.1	2.1<=U<3.2	U>=3.2
Fa, mole % average	23.98	23.96	24.25	24.38	24.76
Fe, wt.% average	22.42	22.01	21.79	22.34	21.58
SiO_2/MgO average	1.60	1.63	1.57	1.59	1.64
^{21}Ne exposure age M.y. average	7.71	13.69	16.49	15.88	16.67
Shock facies average	4.79	4.27	4.25-4.50	3.13	1.90-2.00
number of counts	14	11	4	8	10

Tabulation of preliminary analyses of L chondrite data. Shock facies data from Dodd and Jarosewich (1979); their alphabetic scale was converted to a numeric one to allow averaging of values for each UTh-He gas retention age interval. Scale is from 1 to 5 with greater numbers representing increasing shocking of the meteorite. Number of counts refers to shock facies average, and records the number of meteorites averaged for each interval.

D10

N84 25577

ORIGINAL PAGE IS
OF POOR QUALITY

THE CRATER DENSITY OF A LINEAR FEATURE

Lawrence Spong, Department of Geology, The University of Toledo,
2801 West Bancroft Street, Toledo, Ohio 43606

The standard method of crater counting presently employed permits determination of the relative ages of areal geologic features on cratered planets and satellites. A new method is presented here which calculates the areal density of the craters superposed upon linear features.

The method produces an effective "synthetic" area around the linear feature for each crater bin size, permitting the line counts to be compared directly with standard area counts. The shape of the synthetic area produced by the method is an oval, with the calculation of this area for each bin being dependent on the median crater size for that bin, as well as the length and width of the linear feature (See Figure 1). Incorporated into the method's equation is a factor to normalize the count to 10^6 square kilometers for each bin. Because of the dependence of the method on the crater sizes, the largest possible number of bins should be counted for the method to be the most effective.

We introduce the method's equation

$$C_D = \frac{N_d \times 10^6}{A} \pm \frac{\sqrt{N_d} \times 10^6}{A} \qquad \text{with}$$

$$A = (D_m + W)L + \pi (D_m/2)^2 + D_m W$$

where C_D is the crater density of the crater diameter bin, N_d is the number

ORIGINAL PAGE IS
OF POOR QUALITY

of craters counted in that particular bin, D_m is the median crater diameter for that bin (in kilometers), W and L are the width and length of the linear feature (in kilometers), respectively. The equation provides the crater density for a particular crater diameter size of the number of superposed craters divided by the effective area for that diameter (see Figure 1). The equation, and method, is unlike conventional crater counts in that the cumulative counts and errors of the crater size bins are summed discreetly,

i.e.:
$$C_i = \sum_d^i C_d \pm \sum_d^i \text{error}_d$$

and not directly calculated. As can be seen from Figure 1, when we proceed from the larger crater diameters to the smaller crater diameters, the effective area oval approaches the actual area of the linear feature. This decrease in effective area size, when applied to the equation, produces a statistically larger crater density for the line in the small size bins that approximates the crater density for the area for the small size bins.

The method is prone to several error producing situations. First, often crater diameter sizes found in the area counts are not represented in the line counts. This is especially true with regard to the larger diameter craters which chance not to superpose the linear feature. Second, the number of craters in any particular bin on the line is much less than the number of craters in the corresponding bin in the area count. This tends to produce unusually large error bars in the larger size diameter (small crater population) bins. Third, as with the standard count, the crater density of the linear feature is applicable to a specific geologic province. If the linear feature occupies a number of geologic provinces, a crater density for each province is needed. Considering the above in the method's test region, the errors encountered are acceptable if the linear features length is sufficiently long (several hundred kilometers or longer) and the number of crater bin sizes great enough to provide good statistics.

A test of the method was conducted in the Lunae Palus region of Mars using a 1:2,000,000 quadrangle photomasaic (U. S. Geological Survey, 1980). The geology of the region consists of moderately to heavily cratered plateau material and heavily cratered plains and hilly materials. Both rimless and partially buried impact craters exist, the rimless craters were completely buried but have since reappeared when material filling the craters were removed by an undetermined erosional process (Miltor, 1974). Our test consisted of determining the crater densities of the various geologic provinces on the photomosaic, then drawing a random line through the region and determining the line's crater density by the method (see Figure 2). The length of the line was approximately 4900 kilometers and the smallest crater size counted corresponded to 2 kilometers. The graphical results are shown in Figure 3. Additional preliminary tests were conducted with grabens in the Tharsis region where we found that a significantly shorter line (in the range of several hundred kilometers) with a small number of bins and smaller crater density will still reflect the crater density of the surrounding plain.

Future research projects that utilize this method fall into three catagories. First, this method provides us with the opportunity to date the relative ages of major tectonic and geomorphic events and features on cratered planets and satellites. Examples include the rate of retreat of the escarpments of the fretted terrain and a more accurate appraisal of the age of major stream channels. Second, research in the direction to refine this method to produce a more accurate estimate of the true age of the linear feature, rather than presenting the youngest possible age of the feature, as the method new provides. Third, and most practical, when wishing to determine the crater density of a large areal province, using this method, we now have evidence that the crater density of a random line drawn over a representative portion of the area would provide a reasonably accurate representation of the crater density of that province. This promises to save countless hours in future research projects requiring crater counting.

Acknowledgements

I wish to extend my gratitude to Laurence Soderblom for his originating and suggesting this idea as a possible research project, and for his numerous suggestions and comments concerning this problem. As well I wish to thank Kenneth Tanaka for his help in the development of both the method and principal equation, and with the computer support. This project was funded as an internship in the NASA Planetary Geology Undergraduate Research Program and the work conducted at the U. S. Geological Survey's Branch of Astrogeologic Studies in Flagstaff, Arizona during the summer of 1982.

References

Miltor, D. J., 1974, Geologic Map Of The Lunae Palus Quadrangle Of Mars: U. S. Geological Survey Miscellaneous Investigations Series Map I-894.

U. S. Geological Survey, 1980, Controlled Photomosaic Of The Lunae Palus Southeast Quadrange Of Mars: U. S. Geological Survey Miscellaneous Investigations Series Map I-1307.

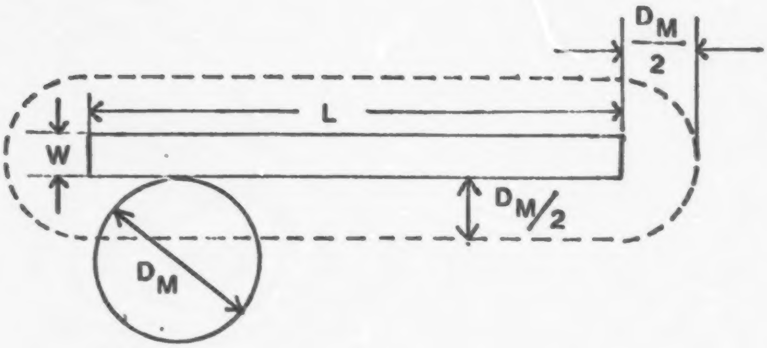

D_M = median diameter of crater size range being counted

L = length of linear feature

W = width of linear feature

Figure 1. Effective "synthetic" area for a line count.

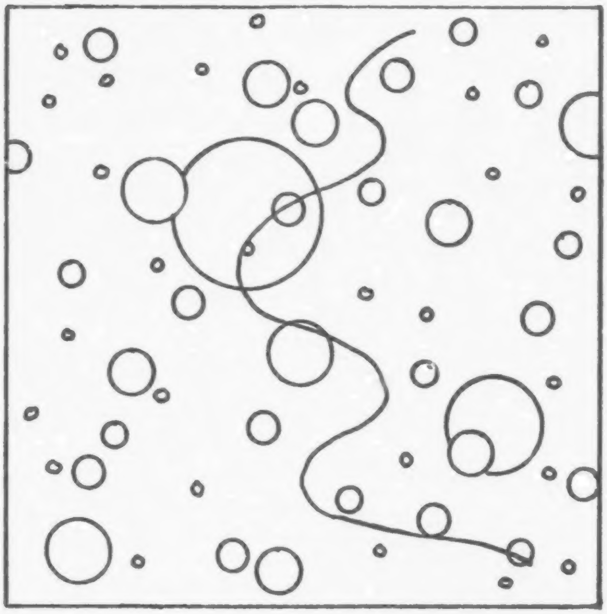

Figure 2. Representation of Lunae Palus test line count.

ORIGINAL PAGE IS
OF POOR QUALITY

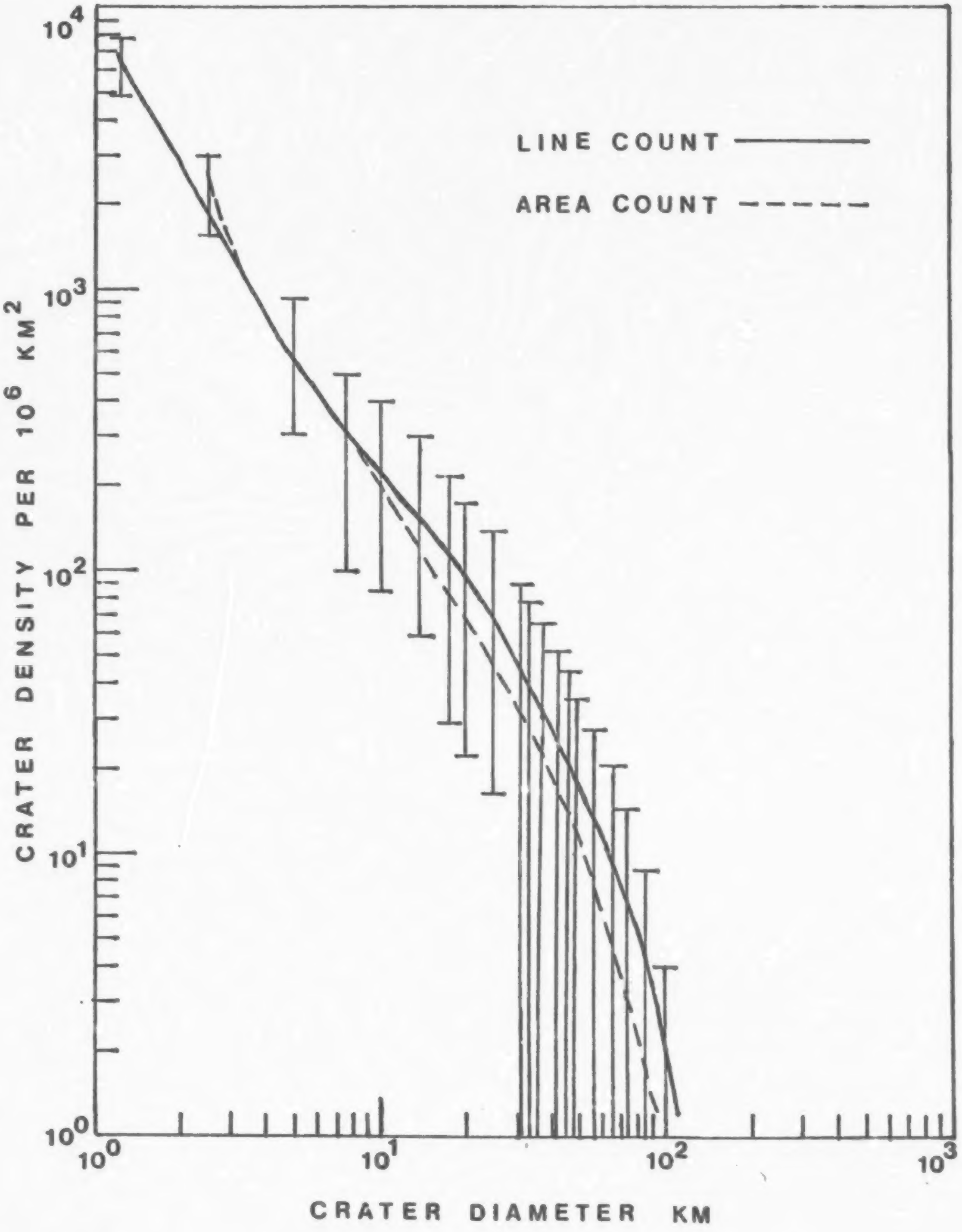

Figure 3. Crater density data for Lunae Palus Test

TABLE 1.

Median Crater Diameter of Bin (km)	Number of Craters in Bin	Cumulative Number of Crater	Crater Density (Per 10^6 km^2)	Error
185	1	1	0.57	0.57
100	1	2	1.14	0.81
85	1	3	1.72	0.99
75	1	4	2.29	1.14
71.25	2	6	3.43	1.4
68.75	1	7	4.01	1.51
65	1	8	4.58	1.62
60	2	10	5.72	1.81
56.25	1	11	6.3	1.9
53.75	1	12	6.87	1.98
51.25	2	14	8.01	2.14
48.75	3	17	9.73	2.36
46.25	2	19	10.87	2.49
43.75	2	21	12.02	2.62
41.25	9	30	17.17	3.13
38.75	2	32	18.31	3.24
36.25	5	37	21.18	3.48
33.75	3	40	22.89	3.62
31.25	10	50	28.62	4.05
28.75	9	59	33.77	4.4
26.25	10	69	39.49	4.75
23.75	11	80	45.78	5.12
22.5	14	94	53.8	5.55
20	22	116	66.39	6.16
17.5	18	124	76.69	6.62
15	16	150	85.85	7.01
12.5	64	214	122.47	8.37
10	113	327	187.15	10.35
7.5	180	507	290.16	12.89
5	378	885	506.49	17.03
2.5	2673	3558	2036.28	34.14

The graph shows the crater density curves for the Lunae Palus test. The error bars are associated with the line data points. Table 1 shows the crater density data of the Lunae Palus test area described in the text. The area was approximately 1,747,300 km^2. Table 2 is the data for the Lunae Palus test line where the line's length was 4905 km and the width was 0 km. The bin sizes were arbitrarily choosen (size of bin varies from 2-10 km).

TABLE 2.

Median Crater Diameter of Bin (km)	Number of Craters in Bin	Cumulative Number of Craters	Crater Density (Per 10^6 km^2)	Error
100	1	1	2.01	2.01
85	1	2	4.37	4.37
73.75	1	3	7.11	7.11
66.25	1	4	10.15	10.15
56.25	1	5	13.74	13.74
48.75	1	6	17.89	17.89
46.25	1	7	22.27	22.27
42.5	1	8	27.03	27.03
37.5	1	9	32.44	32.44
33.75	1	10	38.44	38.44
31.25	1	11	44.94	44.94
25	4	15	77.43	61.18
20	2	17	97.75	75.55
17.5	2	19	120.98	91.98
13.75	4	23	180.16	121.57
10	3	26	241.23	156.83
7.5	2	28	295.53	195.22
5	8	36	621.46	310.46
2.5	20	56	2251.8	675.01
1.25	25	81	6328.46	1490.34

D11

N84 25578

NITROGEN THRESHOLD
EXPERIMENT

Cheryl L. Treat

Summer 1982

TABLE OF CONTENTS

Introduction Pages 183-186

Theoretical Basis Pages 187-190

Apparatus Pages 191-192

Defining threshold Pages 193-194

Experimental Procedure Pages 195-197

Results Pages 198-201

Conclusions Pages 202-204

Appendix

TABLE OF GRAPHS, FIGURES, AND TABLES

Report

Graph 1 pressure(carbon dioxide) vs. pressure(nitrogen)
Table 1 equivalent pressures
Graph 3 viscosity vs. pressure
Figure 1 Venus wind tunnel
Figure 2 operator/camera set-up
Graph 5 threshold vs. pressure
Graph 6 pressure vs. threshold
Graph 7 particle size vs. Reynold's number (30 psi)
Graph 8 particle size vs. Reynold's number (760 psi)
Graph 9 C_f' vs. pressure
Graph 10 u_{*t} vs. particle size (CO_2)
Graph 11 u_{*t} vs. particle size (N_2)

ORIGINAL PAGE IS
OF POOR QUALITY

Geology is the study of the Earth, it's composition, origin, and history. Evidence of our origin is difficult to find. The surface is tectonically active and therefore it is hard to find an extended past record. The Earth is also covered by three quarters water. The erosional effect of this water destroys existing surface features and makes it further difficult to study our past. Geologists, and other scientists, are therefore forced to rely on small clues and experimental data to piece together a historical scenario.

Studies on the Earth have concentrated on erosion by water. Fluid studies have been able to accurately predict the effects of water erosion today. Using this information and working backwards we can establish the existing features of the past. But there are other agents of erosion, such as wind and ice. Because of the smaller effect of wind on our surface, aeolian processes are much less understood than water erosion. Bagnold was the pioneer for analysis of wind blown sand. His studies of terrestrial environments provided a basis for future experimental work. Studying the Earth alone does not provide enough information for a universal theory on aeolian processes.

Looking to the other planets in our solar system for answers to questions about the Earth and the universe affords a better geologic record of its origin. Galileo first saw the moon through a telescope and prepared a detailed map of its features. He recognized the use of information from other bodies and how it can be related to the Earth. Through this type of observation, Planetary Geology evolved.

The first studies in Planetary Geology included observations of the Moon and Mars. The Moon, being the closest body, is the easiest to observe through a telescope and became the target for space exploration. Scientists found a preserved past on the Moon's surface. They were able to study this surface, and the rocks found there, and relate this information back to the Earth. The Moon has no atmosphere or gravity and therefore, little erosion. It is necessary to look elsewhere for comparative studies of aeolian processes on the Earth.

Mars is the closest planet and the logical choice for studies on wind erosion. From a practical point of view, Mars is readily accessible. From telescopic observations, Mars is believed to have extensive aeolian activity, Mariner 9 returned conclusive evidence of this in 1971. Aeolian processes such as those found on Mars, are capable of moving enormous amounts of sand over its surface. Large landforms may be seen from orbit. A process that effects these changes can give an understanding to the geologic environment of a whole planet. Studying aeolian processes on Earth only gives a small scale understanding, studying aeolian processes on Mars gives a much larger scale understanding of the planet as a whole and in turn gives feedback on terrestrial environments.

Being smaller than Earth, Mars has little gravity. Its atmospheric pressure is much less than that of Earth also. In order to study aeolian processes on Mars, it is necessary to simulate the Martian environment. The Martian Wind Tunnel was constructed for this purpose. It is placed in a specially designed chamber suitable for achieving Martian pressures. Experiments are designed to observe the effect of pressure, gravity, and density on sand movement. Mars has a lower temperature, lower pressure and lower gravity than does the Earth. Since temperature and pressure effect gas density they are only important in attaining the correct gas density for a Martian environment. Gravity is assumed to be independent. By studying the results a theory is formulated which fits for data on Mars as well as on the Earth.

To test the assumptions made in setting up the Martian Wind Tunnel experiments, a control is needed. Venus provides just such a control. On Venus, the pressures are much higher than on the Earth. Temperatures are also higher, and because the sizes are similar, the gravity on Venus is very near the Earth's gravity. Mars and Venus form the two extremes for studying aeolian processes with the Earth falling the middle.

If a Theory for Mars and Earth is able to predict the data for Venus, then gravity may be assumed an independent variable, and a universal explanation for grain saltation as related to density can be defined. Following this line of thought, a Venus wind tunnel was constructed.

Venus, being on the other end of the spectrum in the Mars-Earth-Venus experiments, required a different set of conditions for its simulation. Because density is assumed to be the controling factor in grain saltation, the experiment is designed to simulate Venusian density rather than the actual pressures and temperatures of Venus. Temperature, as in the case of Mars, is important only in achieving these densities. Carbon dioxide is used to pressurize the wind tunnel and experiments are performed to determine the exact wind speed at saltation threshold. The conclusions of this experiment agreed with the Martian and terrestrial studies. To gain further control over the effect of fluid density, it was necessary to establish the effect of fluid viscosity on grain saltation. This was done by design of the nitrogen experiments.

ORIGINAL PAGE IS
OF POOR QUALITY

Theoretical Basis

Both Mars and Venus contain mostly carbon dioxide in their atmospheres, therefore all of the experiments thus far have utilized carbon dioxide for the wind tunnel. This gas is pressurized to attain densities similar to Venus. As a control to these experiments and to test the effects of fluid viscosity, nitrogen tests are also run. It is assumed that fluid density is the major contributing factor in predicting grain saltation. By designing an experiment to test fluid viscosity it is hoped that viscosity will have little or no effect on grain saltation. If this can be shown, then our theory for grain saltation may be extended to other surfaces and the wind tunnel, which was built on the premise that density is the controling factor, can be used to simulate these surfaces.

Nitrogen gas has a much lower molecular weight than carbon dioxide, therefore its viscosity is lower. With the experimental parameters the same as the carbon dioxide threshold experiment, only the gas and therefore the viscosity differs. Similar densities are achieved by changing the pressures of nitrogen.

Before the experiment is run it is necessary to make some preliminary calculations:

First, equivalent pressures for nitrogen to simulate the densities of the carbon dioxide runs are calculated using:

$$P = \frac{\rho Z R T}{m}$$

Where P is pressure in atmospheres, ρ is the density of carbon dioxide that is to be simulated, z is a compressibility constant, R is the universal gas constant, T is the temperature in degrees kelvin, and m is the molecular weight of nitrogen.

This calculation can be found in the appendix Table 2. Graph 1 shows pressure of carbon dioxide in psi versus equivalent pressure of nitrogen in psi. (Data is taken from Table 2 in the appendix.) Along the line shown in Graph 1 carbon dioxide and nitrogen have similar densities. This line is nearly straight with a slope of approximately 1/2. The pressures used for this experiment w ere read off the graph and are as follows, 760, 650, 545, 440, 345, 255, 165, and 80 psi. They appear in Table 1.

Second, expected Δ p, or the difference in dynamic pressure and static pressure, which is a function of velocity, is calculated for each grain size and pressure using data from carbon dioxide runs. The formula used is:

$$\Delta P = \frac{V^2 H}{2}$$

Where v is the velocity of the wind at threshold for the carbon dioxide runs, H is the pressure of nitrogen, and Δ p is the number of counts expected. (Using velocities obtained in the carbon dioxide runs is valid based on the assumption that velocity at threshold is the same for two gases at the same density. This calculation was done only as a rough guide.) Values for expected Δ p appear in the appendix Table 3.

Third, viscosities for nitrogen and carbon dioxide are calculated using Graph 2. To use this diagram, first calculate T_r where

$$T_r = \frac{T}{T_c}$$

T is the temperature in degrees kelvin, T_c is the temperature constant for nitrogen or carbon dioxide. Then calculate P_r where

$$P_r = \frac{P}{P_c}$$

P is the pressure in atmospheres, P_c is the pressure constant for nitrogen or carbon dioxide. Locating the intersection of T_r and P_r on the graph gives a value for μ_r . μ_r is a viscosity constant for nitrogen or carbon dioxide. Using

$$\mu_r = \frac{\mu}{\mu_c}$$

μ can be calculated for nitrogen and carbon dioxide. Calculations of viscosities appear in the appendix Table 4 and Table 5. This particular method was used to take into account the effect of pressure. A plot of carbon dioxide versus nitrogen viscosities at similar densities(Graph 3) shows the differences in the two gases.

Graph 3 is a plot of viscosity of nitrogen and carbon dioxide versus pressure of the gas. (Data is from the appendix Table 6) This graph shows that for equivalent densities, there is a larger difference in viscosity at the lower pressures. If there is any variance in our theory for grain movement caused by viscosity, this variance will appear at the low densities. However, since the viscosities of the two gases do not differ markedly, even at low pressures, it is doubtful whether this experiment will be conclusive in its attempt to isolate the effect of viscosity as a variable. Rather, it will gain better control over the movement of grain saltation and establish a good working definition of saltation threshold.

Using the calculated viscosities for selective pressures, and calculations of densities for these same pressures, Reynold's numbers for the tunnel can be found using:

$$R_e = \frac{v l \rho}{\mu}$$

Where v is the velocity of the gas at threshold, l is the length of the bed of sand, ρ is the density of the gas, and μ is the viscosity of the gas. Calculated values of Reynold's numbers appear in the appedix Tables 7 through 14. These calculations were done as a basic framework for the experiment and to gather data so that a graph of Reynold's number versus coefficient of friction, C_f', could be prepared. Graph 4 in the appendix is a plot of coefficient of friction and Reynold's number for each particle size. This graph is used in the calculation of u_{*t}. Table 15 in the appendix is a flow diagram of all the variables in the experiment and their relationship to each other.

Apparatus

The Venus wind tunnel is a closed circuit wind tunnel housed at the NASA Ames Research Facility. (See Figure 1) It is approximately 6 meters long and 3 meters wide and allows a gas to be circulated around by use of a fan. It has been tested to 1000 psi pressure. A one meter section of the tunnel is able to roll out which can then be loaded with a bed of sand. This test section contains four viewing ports. Two input systems allow carbon dioxide and nitrogen to enter the tunnel. The carbon dioxide is stored in a tank outside of the building and is brought in through a pipe line. It is then pumped into two tanks which can be individually heated and then bled off to let the carbon dioxide gas into the tunnel through a valve. Nitrogen gas is stored in a truck outside the building and is piped directly into the tunnel through a separate valve. The instrumentation includes a velocity guage which measures differences in dynamic and static pressure(ΔP), and gives an electrical signal which registeres on a chart recorder. This recorder can display tunnel pressure through use of a pressure guage. A temperature guage records tunnel temperature and is digitally displayed. The tunnel control box, controls the motor speed of the tunnel fan. The operator set up is shown in Figure 2B and C.

Because this experiment required operating at high pressures, a remote observation system was installed. This system consists of a closed circuit television camera mounted on a tripod over a port hole of the test section, viewing down on the bed. (See figure 2A) The television screen is placed on a table in the operator area. The camera mount allows free but stable movement of the camera. The next step involves calibrating the monitor with the unaided eye. A test to compare the CCTV with visual observation was designed as follows:

The tunnel was loaded with 710-833 micron sand and then pressurized at 400psi. The camera was set up viewing the bed at the lower end down through the top port window. The observer viewed the bed at the lower end from the side port window. The operator increased the fan speed until saltation threshold was reached. Both the observer and the camera system viewed grain saltation at precisely the same time. This test was repeated several times and results conclude that the camera system viewed the same as the observer. This test was done so that the carbon dioxide runs could be compared with the nitrogen runs without any inconsistancy in opertor viewing of grain saltation.

Defining Threshold

While conducting the calibration test, several thresholds were noted. 1) No movement at all 2) Slight wobling and rocking 3) Creeping or rolling 4) Intermittent grain saltation 5) Continuous saltation. In order to perform the nitrogen tests a good working definition of threshold has to be defined. The tunnel is loaded with sand which contains a range of sizes. When nearing threshold the smaller grains that are exposed will be carried away by the wind leaving the larger grains. Saltation will then cease. If the wind velocity is raised, the wind will carry away the larger grains exposing the smaller ones underneath and once again saltation will stop when only the largest particles are left. The velocity required to lift the largest grain sizes corresponds to Bagnold's idea of "Ultimate Threshold", and at this velocity saltation will be continuous. Our definition of threshold includes continuous saltation, however this is not enough to completely define threshold. There are two types of threshold, 1) fluid and 2) saltation. Fluid threshold is the point at which the fluid alone lifts the particles which begin to saltate. These particles may strike others further down the plate and cause other particles to move, this is saltation threshold. We are interested in determining fluid threshold for our studies. Fluid threshold is difficult to establish. Sand grains are needed on the front end of the bed in order to ensure turbulant flow at the end of the bed. One alternative would be to fix sand grains to the front end so that they can not cause saltation on grains further down the bed and yet still trip the boundry layer to turbulent flow.

Finally, our definition of threshold includes a precise way in which to measure it. Using the CCTV, and larger particle sizes, fluid threshold is defined as when saltation is continuous and striking grains from the front end of the plate leave small craters or streaks when they hit in the viewing area. The effect is seen as dark bands on the TV monitor. For smaller grain sizes motion is sudden and continuous thus making threshold easier to define. The advantages of using this definition is that we are able to define threshold precisely for both small and large grain sizes with consistency.

Experimental Procedure

The sand grains in this experiment are well rounded quartz grains which have been sieved by a Ro-Tap to a distribution of size ranges listed below:

23-38, 38-45, 45-53, 53-63, 63-75, 75-90, 90-125, 125-175, 250-354, 354-500, 500-600, 600-710, 710-833.

For each run the sand size is picked and loaded into the tunnel. to load the tunnel, the test section is rolled out, the plate that's held inside is checked to ensure a level bed. The sand is introduced in a wooden frame placed on the plate by means of a funnel. This frame is then pulled across the plate, it leaves a uniform layer of sand approximately ½ cm. thick. The test section is then rolled back and sealed to the tunnel by means of two clamps. The camera may then be rotated and lowered onto the port window. After the light has been set up, the TV monitor is turned on and the camera is focused for a sharp image. All valves are then checked to isolate the carbon dioxide system. The motor is off and the pressure reading is zeroed at 14.7 psi. At this point the nitrogen truck valves are opened and the line to the tunnel is pressurized. The valve to the tunnel is opened and the tunnel is filled to approximately 760 psi. When pressure and temperature are stabilized at 760 psi, the motor may then be turned up until the bed is "pre-saltated". This ensures uniform size distribution on top of the bed. Threshold is accurately determined by increasing the motor slowly and noting creep, intermittent saltation, and continuous saltation. True threshold is noted when impinging grains leave dark streaks across the TV screen. This is repeated two times for threshold values. Temperature , the number of counts and pressure are all recorded in the log book. The motor is turned off and the outside valve is opened. The tunnel is drained until the next pressure is reached. The procedure is repeated for each pressure to determine threshold. After 80 psi the tunnel may be completely drained and unloaded. All data for this experiment is recorded in the log book. The average values, along with calculations of velocity, Reynold's number, coefficient of friction, and wind sheer velocity, are found in Tables 16 through 29 in the appendix.

The second experiment run is a calibration experiment designed to test how well data from the carbon dioxide runs can be compared with data from the nitrogen runs. The procedure for this experiment is as follows:

Using 500-600 micron sand the tunnel is loaded. The tunnel is then filled with carbon dioxide gas. As the tunnel is filling the top valve is left open so that the air occupying the tunnel is pushed out as carbon dioxide enters. In this way, we are confident that the tunnel contains mostly carbon dioxide. A gas detector is used to determine the percentage carbon dioxide in the tunnel, this is significant because at lower pressures the relative percentage of air to carbon dioxide is higher. When the tunnel is pumped up and then bled down, as in the original carbon dioxide experiments, air is released to the atmosphere as gas is let out, so that at low pressure the relative percentage of air to gas is low. After closing the valve, the motor for the fan is turned up to full. The tunnel continues to fill at a slow rate until threshold is observed. At this pressure, measurements are taken for ΔP, pressure, and temperature. Several runs are taken and recorded in the log book. The tunnel is drained of carbon dioxide and filled with nitrogen without reloading the bed of sand. Again, carbon dioxide is bled out of the top valve as nitrogen enters. A gas detector is used to measure the percentage of nitrogen gas. Runs are made the same as the carbon dioxide runs and recorded. During this experiment, little bed erosion was observed.

All data and calculations appear in the appendix Table 30 and Table 31.

Results

Graph 5- pressure versus threshold velocity. Data is from Tables 16-29 in the appendix.

Some preliminary results are plotted on Graph 5. Threshold velocity in meters per second versus pressure of nitrogen in psi is plotted for a few of the grain sizes. The graph shows how velocity needed to attain grain saltation decreases with increasing pressure. With large particle sizes at low pressure there is not enough wind movement to induce grain saltation. For particles around 90 microns, threshold velocity is approximately the same as for particles 45-75 microns. However, for particles 23-38 microns, threshold velocity is higher. Particles in the 710-833 micron range require the largest threshold velocity for grain saltation. All curves seem to trend and parallel each other.

Graph 6- pressure versus threshold velocity. Data is from Tables 16-29 in the appendix.

The graph of pressure of nitrogen in psi versus threshold velocity in meters per second, shows all data for particle sizes 23-833 microns. Only four curves are drawn because of the amount of overlapping of points. Other curves may be inferred to be parallel and between curves drawn. This graph shows that with decreasing pressure, threshold velocity must increase to lift the same particle size. Threshold velocity increases with an increase in particle size for the same pressure. Particle sizes between 125 and 45 microns are all clustered around the same line, they require similar threshold velocities for the same pressure. Particles less than 45 microns(silt sizes) show a slight increase in threshold velocity for each pressure. They require a larger velocity to cause them to saltate.

Graph 7- particle size versus Reynold's number for 80 psi nitrogen. Data is from Tables 16-29 in the appendix. This graph shows that for particle sizes 100 to 500 microns, Reynold's number increases for increasing particle size. For particle sizes 23-100 microns, Reynold's number decreases with increasing size. The optimum particle size (or turning point in the curve) is about 100 micron sand. Grain sizes larger than 500 microns do not show on the graph because there was no sand movement at 80 psi for these particles therefore, no Reynold's number was recorded.

Graph 8- particle size versus Reynold's number for 760 psi nitrogen. Data is from Tables 16-29 in the appendix.

The curve of this graph is similar to Graph 7. For particle sizes 100-500 microns, Reynold's number increases for increasing particle size. At larger grain sizes, 500-833 microns, Reynold's number remains nearly the same and the graph of the line becomes a straight verticle line. For particles 23-100 microns, Reynold's number decreases with increasing particle size. Optimum particle size is about 100 microns.

Graph 9- coefficient of friction versus pressure. Data is taken from Tables 16-29 in the appendix.

This graph plots the coefficient of friction against pressure for all particle sizes. At low particle sizes, less than 125 microns, coefficient of friction decreases for increased pressure. All curves for particles less than 175 microns converge for 80 psi and diverge towards 760 psi. For particles whose size is 250-833 microns, coefficient of friction remains constant for increased pressure, for constant grain size. Coefficient of friction increases with increase in grain size for constant pressure.

Graph 10- wind shear speed of carbon dioxide versus particle size. Data is taken from Tables 32-45 in the appendix. This graph has been designed to facilitate comparisons with the nitrogen data by placing the graph between the transparencies of the nitrogen graph. All curves seem to follow the same trend and parallel each other. There is very little overlaping. There is an optimum particle size of about 75 microns. For particles less than 75 microns, U_{*t} decreases for increasing particle size. For particles greater than 75 microns, U_{*t} increases for increasing particle size. There is an optimum range of 40-125 microns where wind shear speed doesn't vary much with particle size. U_{*t} versus particle size for particles greater than 175 microns, seem to have a linear relationship with a steep slope for 50 psi and a shallow slope for 400 psi. U_{*t} increases for decreasing pressure for a constant particle size.

Graph 11- wind shear speed of nitrogen versus particle size. Data is taken from Tables 16-29 in the appendix.

As in the previous graph, all curves seem to follow the same trend and parallel each other. There is an optimum size range of about 75 microns. For particles less than 75 microns, U_{*t} decreases with increasing particle size. For particles greater than 75 microns, U_{*t} increases with increasing particle size. There is an optimum range of about 40-125 microns where U_{*t} doesn't vary much with particle size. U_{*t} versus particle size for particles greater than 175 microns, seem to have a linear relationship with a steep slope for 80 psi and a shallow slope for 760 psi. U_{*t} increases for decreasing pressure for constant particle size.

Note- When comparing Graphs 10 and 11, there seems to be an inconsistency in the 53-63 micron particle range. For both of these curves, the data for this range lies just above the curves drawn. This size range was sifted on the sonic sifter and a size distribution curve was drawn. (Graphs 12 and 13) These graphs show that 80% of the grains fell within 10 microns of the range. The slight offset of the mode is not enough to cause a change in the values for U_{*t}. Since the size distribution is good, other explanations must be saught to explain the inconsistency, like moisture in the sand or operator variance.

Conclusions

As seen from Graph 11, there is an optimum size range for particle movement. This range corresponds to about 75 microns but extends to as much as 40-125 microns. Particles in this size range are about equally easy to lift into saltation at similar pressures. The slight upturn in the curve to the left (less than 40 microns) shows that these particles are more difficult to move. On the Earth this upturn is more pronounced and therefore silt sized particles are rarely found in suspension. The sharp rise in the curve to the right (710 microns) shows that these particles are also difficult to lift, this is true for Earth as well as Venus. With this information, one would expect to find a larger size distribution of particles (40-100 microns) in suspension at the same time on Venus, or a greater amount of fines in suspension as that seen on the Earth.

This experiment was designed to test the effect of fluid viscosity on grain saltation. The data for the nitrogen runs is therefore compared with data from the carbon dioxide runs in two similar plots (Graphs 10 and 11). The curves for the two sets of data follow the same trends. At the smaller particle sizes (less than 175 microns) the curves vary. The curves for nitrogen are slightly higher. Small particles in nitrogen gas seem to be more difficult to move as compared to the carbon dioxide curves. With the larger particles, movement seems to be similar for both carbon dioxide and nitrogen. There are many reasons for these similarities and differences.

The definition of threshold used for the nitrogen runs is a good working definition in that we are able to view saltation threshold in a precise manner. Our definition has been tested by numerous runs and is shown to be consistent. The definition of threshold used for the carbon dioxide runs is ambiguous. It is believed that threshold was defined as first movement, for this reason thrshold values are consistently lower for carbon dioxide than for nitrogen.

The CCTV was not utilized in the carbon dioxide runs. However, calibration tests show CCTV to view the same as the unaided eye.

The experiment designed to test the operator variance was a comparative test between nitrogen and carbon dioxide. Pressure and therefore density was increased until threshold was noted. Using the CCTV and our definition of threshold, threshold was determined at precisely the same densities of the two gases. If viscosity were a contributing factor in grain saltation the effect would be noted at low pressures. Our experiment showed no such variance between carbon dioxide and nitrogen runs for low pressure (density).

The largest difference in viscosity between carbon dioxide and nitrogen occurs, at low pressures (densities). For 50 psi carbon dioxide (80 psi nitrogen), viscosity differs by only 2.05×10^{-5} gm/cmx sec. It is not certain whether this difference

ORIGINAL PAGE IS
OF POOR QUALITY

is large enough to have an effect on grain movement and/or be registered by our instrumentation.

It is not feasible to compare the carbon dioxide data with the nitrogen data because of the opertor variance. However, the nitrogen experiment did furnish a good working procedure and definition for threshold studies. The data gathered is accurate and precise. Also, the nitrogen and carbon dioxide experiment for low pressures showed no differences due to viscosity. At similar densities, the velocity needed for movement is the same.

Because of the problems stated above, the effect of viscosity is not clearly understood. Initial investigation seems to nullify the effect of viscosity as a controling factor to grain saltation. However, for a conclusive theory it is suggested that a further experiment be run, using a gas which shows considerable variance in viscosity with nitrogen. Because a definition of threshold has been accurately defined, a new operator should have no problem in estimating comparative threshold values consistent with the nitrogen operator definition of threshold. The two sets of data can then be compared to give a more accurate account of the difference in viscosities.

D12

THE GEOLOGY OF THAUMASIA-NORTHEAST QUADRANT

Marlene F. Tuesink
NASA Intern
U.S.G.S., Flagstaff, Arizona

N84 25579

July, 1982

INTRODUCTION

The northeastern section of Thaumasia is located in the heavily cratered southern highlands of Mars between 30° S and 47.5° S and 67.5° W and 90° W. To the northwest lies the Tharis bulge and to the southeast is the Argyre Basin.

Previous mapping in Thaumasia have included a geologic map of the entire quadrangle by McGill (1978) at a 1:5,000,000 scale and a map of lava flows in the northwest quadrant by Scott and Tanaka (1981). Most investigations have been concentrated west of 90°W long. in conjunction with the Tharis volcanics.

PURPOSE

This investigation was designed to examine the overall geology of this section of Thaumasia. After distinguishing various geomorphical units, a geologic map was made at a scale of 1:2,000,000. Lastly, a general sequence of events was developed for the area.

METHODS

Mapping was done from individual low, medium, and high resolution images from the Viking missions, as well as using a 1:2,000,000 scale photo mosaic of the northeast quadrant of Thaumasia. Amount of cratering and faulting, superposition, differences in morphology, and albedo were used to separate out geomorphologically distinct units.

Due to the higher resolution images produced by these two missions, more detailed mapping was possible. Low resolution images were used to determine local relief variations as specific radar mapping has not been done in this area. Medium to high resolution images were used in unit mapping. Crater counts were used to determine relative ages of units and to corroborate similar ages between units.

The geological history was worked out using superposition, crater counts, and taking into account the overall sequence of events for Mars as established by other investigations.

RESULTS

Extending SW-NE across the center of the area is an old cratered highlands, parts of which are heavily faulted. In this area, it was especially hard to distinguish individual units because of the re-surfacing affects of the aeolian deposits or volcanic flow material. Here units were separated by the amount of faulting that was present.

The highlands seem to be an area that once was volcanically active. One possible volcanic structure was located within the map area and another on its western boundary. At least three other sites are possible volcanic structures. Their degraded nature and/or the lack of high resolution images prevented a positive identification.

North and south of this central region are extensive, low-lying areas covered with smooth plains material which have buried most of the pre-existing faults. High resolution images show wrinkle ridges in some areas of this unit. This seems to suggest that the material is possibly lava and not aeolian deposits as suggested by McGill (1978). One smooth plains area contains some widely spaced faulting, but this may be due to thinner lava flows failing to cover entirely the faults or post lava-flooding tectonic activity.

South of the highlands is a cratered plateau unit. This stands about as high as the highlands and is enbayed by the smooth plains unit. It contains large craters similar to the highlands, but has no evidence of faulting. The intercrater area appears to be relatively smooth, unlike the highlands, and this could be do to the re-surfacing effects mentioned previously.

The oldest units appear to be the cratered plateaus and the highlands. These are part of the ancient highland crust and have been called the "cratered plains unit" by others. At the same time these units formed, so did the Argyre Basin. Because the highlands form an arcuate pattern around Syria Planun, along with furrowed massifs and scarps, Schultz and Glicken (1979) speculate that this is the remains of an ancient impact basin. Others feel that there might have been a pre-Tharis doming at 40° S and 90° W that developed the N-S fault patterns. Probably associated with this rise, or a bit later, volcanic structures would have developed on the highlands and spread volcanic material into the lower lying areas of the highlands.

As the Tharis region began its doming, the NW-SE fault system developed across the area. Later, in the lower lying areas outside of the highlands, lava flows came in and covered over most of the pre-exsisting faults.

ACKNOWLEDGMENTS

I would like to thank the staff at the Flagstaff Center for their help and support during my project. Special thanks goes to my advisor David Scott for all the time and help that he has given me.

REFERENCES

Frey, H., Thaumasia: A fossilized early-forming Tharis uplift. J. Geophys. Res., 84, 1009-1023, 1979.

Greeley, R., and P. D. Spudis, Volcanism in the cratered terrain hemisphere of Mars, Geophys. Res. Lett., 5, 453-455, 1978.

McGill, G. E., 1978, Geologic map of the Thaumasia quadrangle of Mars, U.S. Geol. Survey Misc. Geol. Inv. Map I-1083, scale 1:25,000,000.

McGill, G. E., Geologic history of Thaumasia quadrangle, Mars, NASA Tech. Memo., X-3364, 224-228, 1975-1976.

Saunders, R. S., Geologic constraints on the evolution of the Tharis region, Inter. Colloquim on Mars (3rd), 1981.

Schultz, P. H. and Glicken, H., Impact craters and basin control of igneous processes on Mars. J. Geophys. Res. - Second Mars Colloquim, 84, No. 14, 8033-8047, 1979.

Scott, D. H. and Carr, M. H., 1978, Geologic map of Mars, U.S. Geol. Survey Misc. Geol. Inv. Map I-1077, scale 1:5,000,000.

Scott, D. H. and Tanaka, K. L., Mars: A large highland volcanic province revealed by Viking images., Proc. Lunar Sci. Conf. 12th, 1449-1458, 1981.

D13

N84 25580

PLANET-CROSSING ASTEROID SURVEY

Peter D. Wilder
NASA Planetary Geology Undergraduate
Research Program
Division of Geological and Planetary Sciences
Jet Propulsion Laboratory
California Institute of Technology

Address:

Department of Geological Sciences
State University College at Geneseo
Geneseo, New York 14454

PLANET-CROSSING ASTEROID SURVEY

INTRODUCTION:

The planet-crossing asteroid survey was begun in 1973 by Eugene M. Shoemaker and Eleanor F. Helin of the California Institute of Technology in order to study those asteroids which may intersect the orbits of the inner planets. Throughout the history of the survey, many of the various classes of asteroids have been investigated. The near-Earth objects, including the Apollo, Amor, and Aten families, have usually received the most attention. However, asteroids whose orbits cross that of Mars, and some objects which are generally confined to the main belt have also been studied. Improved population estimates of the different asteroid classes will lead to refinements in the estimated cratering rates of the planets, and provide a fuller understanding of the processes which are operative in the solar system.

TECHNIQUES:

Asteroids are most easily discovered when they are brightest, during periods of opposition with the sun. Therefore, by observing at or near the region of opposition, one would hopefully be able to find the maximum number of asteroids detectable. Since the study began, observing has been done on the 18 inch Schmidt telescope at the Palomar Mtn. Observatory. This telescope is well-suited to survey work because its field width is quite large, covering more than 8 degrees of arc. Typically, two consecutive photographs of a favorable field are taken. The exposure times of the films are usually twenty minutes and ten minutes, respectively. The telescope is guided at sidereal rate, so that asteroids will leave short trailed images. The films are then scanned for trails. By comparing the two films, the direction and approximate rate of motion of an asteroid may be determined. Those trails which are longer represent the closer asteroids. Attempts are then made to obtain recovery films of any faster moving objects. Using this technique, an average of about two Earth-crossing asteroids has been discovered annually.

Recently, two other techniques have also been used in the survey. The first makes use of the 48 inch Schmidt telescope at the Palomar Mtn. Observatory. The field width of this telescope is less than that of the 18 inch telescope, but the greater size of the instrument allows much fainter objects to be detected. Using the larger telescope some asteroids that are only 20th magnitude in brightness have been detected, whereas the detectability limits of the 18 inch telescope are near the 18th magnitude. A typical photographic plate taken at opposition on the 48 inch telescope may yield several hundred asteroids. Most of these are main belt asteroids, but occasionally other types are discovered.

The second technique which has been initiated is being conducted on the 18 inch Schmidt telescope. In this method, film pairs of four minute exposures are taken with approximately 30 minutes separating the two halves of each pair. The short exposure time is only long enough for asteroids to leave a star-like image. The objects are detected by viewing the film pairs in a specially designed stereoptic binocular microscope. A small displacement in an asteroid's position will occur during the 30 minute gap, and a parallax effect will be produced. Therefore, the asteroids may be found by a stereopsis technique. Objects which have moved will appear to be above or below the apparent plane of the stars. One of the benefits of this method is that the shorter exposure time allows more films to be taken.

RESEARCH:

Using photographic plates taken on the 48 inch Schmidt telescope, I measured the positions of 112 objects as they moved throughout a four day period. The right ascensions and declinations of the Comet Schwassmann-Wachmann II, 8 previously known asteroids, and 103 new asteroids were determined. The apparent photographic magnitudes of the asteroids were visually estimated by comparison with the magnitudes of known objects. The data on all objects measured have been forwarded to Brian Marsden of the Smithsonian Astrophysical Observatory, where they will be kept on file for future reference.

By measuring films obtained from the 18 inch Schmidt telescope, Caroline S. Schoemaker was able to provide follow-up positions for 6 of the brighter, newly discovered asteroids. These films were taken 4 to 5 days after those on the 48 inch telescope, and the extended arcs which these positions provide will allow for the determination of more accurate preliminary orbits. A three to four month arc is necessary to be able to calculate an object's definitive orbit.

One asteroid discovered on the plates which were taken on the 48 inch telescope had an apparent motion that was about twice that of the other asteroids, and was given a designation of 1982JD. After its positions were determined, Brian Marsden calculated a preliminary orbit for the asteroid. He concluded that the object is probably an inner main belt asteroid of fairly high inclination, belonging to either the Hungaria or Phocaea families. When follow-up positions for 1982JD become available, they will increase the accuracy of the orbit determined.

ACKNOWLEDGMENTS:

I would like to thank Eleanor Helin for providing the opportunity to participate in this research. I am also very grateful to Scott Dunbar for the assistance which he gave in many of the theoretical aspects of the project, and to 'Bobby' Bus for his time in explaining the practical side of the study.

D14

N84 25581

Preliminary Results of Albedo Correlation Between Europa and Ganymede

Sandra E.Yuter
NASA Intern
U.S. Geologic Survey,Branch of Astrogeologic Studies
Flagstaff,Arizona

Building on the work of Johnson et al (1982) on the multispectral properties of the icy Galilean satelites, Voyager images of Europa and Ganymede were analyzed to determine values for the exponent k of the Minnaert photometric function and preliminary spectra for various regions on the two satellites.

To compare multispectral albedo between satelites three basic sets of problems with the raw digital images must be corrected. First, corrections must be made for variations in camera sensitivity and dark current over the field of view. Next, images acquired in different spectral bandpasses must be registered. Finally, the photometric function, whose most dramatic effect is darkening of the image away from the subsolar point, causing the brightness of a single material to vary over an image as the solar incidence angle varies, must be compensated for.

Corrections for the first set of problems, sensitivity and dark current, have been well established using pre-,in- and post-flight camera calibration corrections and dark current frames (Danielson et al.,1981). Dark current errors which vary with scan rate and exposure time were corrected empirically so that the brightness value of dark space is as close as possible to zero. After this correction, the remaining dark current correction is less than + 0.005. The photometric function is primarily dependent on phase angle (Figure 1), wavelength, surface material and texture (Veverka et al.,1978). Full representations of the function with its many parameters are in the early stages of development (Squyres,1981). For the purpose of this paper, a simplified photometric correction in the form of the Minnaert function was applied following (Johnson et al.,1982).

The Minnaert function is:

$$B=B_o \cos^k i \cos^{k-1} e$$

where B=apparent albedo, B_o=normal albedo, i=solar incidence angle, e=viewing angle (Figure 1) and coefficient k varying with phase angle, and wavelength. The Minnaert function has been shown to describe the scattering behavior of various silicate materials at low phase angles (Veverka,1978).

To determine an average value of k for each planet and filter, two sets of color filtered images for each planet were choosen from the available low phase angle images. The image sets for each planet were chosen to have approximately the same phase angle, and provide overlappping coverage under different viewing and illumination conditons. These criteria were required by the method used to solve for k (A.McEwen, personal communication). Table 1 lists the images used.

To process the images, known camera distortions were removed (Soderblom et al.,1978;Danielson et al.,1981). The images were then geometrically transformed into simple cylindrical projections and the camera calibration factors applied (Danielson et al.,1981). The two cylindrical projections for each planet and filter were then registered with each other and their area of overlap processed to yield the k variable of the Minnaert function for each image. The mean values of k for the Europa images were found to be equal to

0.63 for the blue filter; and equal to 0.61 for the ultraviolet filter. Buratti and Veverka (1981) found the orange filter at phase angle of 2.94° to have a k equal to 0.7. The decreasing k with decreasing wavelength agrees with work by Veverka et al.(1978). For the Ganymede images the mean value of k was found to be equal to 0.50 for the blue filter.

The Minnaert function was then applied to the images to produce maps of normal albedo. Selected points from these images were used to produce the preliminary spectra in Figure 2. The most noticeable characteristic of the spectra is that the slope of the curves for Europa is steeper than that for Ganymede, making Europa brighter and redder than Ganymede. This is in agreement with spectra derived from other Voyager images (Johnson et al.,1982).

This study has shown that the k values for the Minnaert function for Ganymede and Europa are different and thus that the photometric behavior of the two bodies is different. This lends evidence to the idea that the physical nature of the surfaces of Ganymede and Europa are dissimiliar. It should be noted the many factors such as texture and roughness, not taken into account in the Minnaert equation have an effect on the photometric function. Thus, while the spectra do not rule out similar materials occurring on Europa and Ganymede, they do not contribute any evidence to that possibility. Much more work needs to be done with the photometric function, the parameters effecting it and its application to Voyager images before strong evidence for similarity or lack thereof between Galilean satellite materials can be established.

Acknowledgements

The author would like to extend her gratitude to Alfred McEwen for his invaluable assistance in understanding the theory behind the photometric corrections and the practice of using the U.S.G.S. Flagstaff Image Processing System. Special thanks also to Laurence Soderblom for directing the course of my research and to Kenneth Tanaka for his encouragement and help with various aspects of the project. This work was performed under the Planetary Geology Undergraduate Research Program from 7/19/82 to 9/9/82.

References

Buratti,B. and J.Veverka, 1981. Voyager photometry of Europa, Reports of the Planetary Geology Program 1981, pp.44-46.

Danielson,G.E.,P.N.Kuperman,T.V.Johnson and L.A.Soderblom, 1981. Radiometric performance of the Voyager cameras, J.Geophy.Res, 86:8683-8689.

Johnson,T.V.,L.A.Soderblom,J.A.Mosher,G.E.Danielson,A.F.Cook, and P.N.Kuperman, 1982. Global multispectral mosaics of icy Galilean satellites, J.Geophy.Res., in press .

Soderblom,L.A.,K.Edwards,E.M.Eliason,E.M.Sanchez and M.P.Charette, 1978. Global color variations of the Martian surface, Icarus, 34:446-464.

Squyres,S. 1981. The morphology and evolution of Ganymede and Callisto, Advances in Planetary Geology November 1981, pp.365-718.

Veverka,J.,J.Goguen,S.Yang and J.L.Elliot, 1978. Near-opposition limb darkening of solids of planetary interest, Icarus, 33:368-379.

Table 1

Image Pairs Used

Planet	PICNO	filter	phase angle
Europa	0578J1-001	V	3.09
Europa	1432J2-003	V	3.77
Europa	0580J1-001	B	2.97
Europa	1434J2-003	B	3.77
Europa	0582J1-001	OR	2.94
Europa	1436J2-003	OR	3.76
Europa	0584J1-001	G	2.94
Europa	1438J2-003	G	3.76
Europa	0586J1-001	UV	2.84
Europa	1440J2-003	UV	3.76
Ganymede	1273J2-004	V	4.87
Ganymede	1758J2-004	V	4.81
Ganymede	1275J2-004	B	4.88
Ganymede	1760J2-004	B	4.83
Ganymede	1277J2-004	OR	4.88
Ganymede	1762J2-004	OR	4.85
Ganymede	1279J2-004	G	4.87
Ganymede	1764J2-004	G	4.85
Ganymede	1281J2-004	UV	4.86
Ganymede	1766J2-004	UV	4.82

Figure Captions

Figure 1 Graphical depiction of solar incidence angle i, viewing angle e, and phase angle a (from Squyres, 1981).

Figure 2 Generalized spectra of normal albedo for relative dark, medium and light terrains on Ganymede and Europa.

ORIGINAL PAGE IS
OF POOR QUALITY

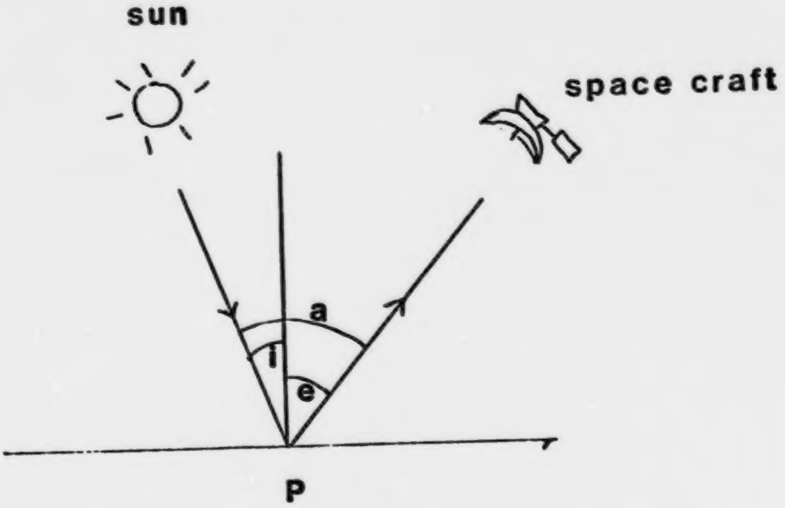
sun
space craft
a
i
e
P

Figure 1

ORIGINAL PAGE IS
OF POOR QUALITY

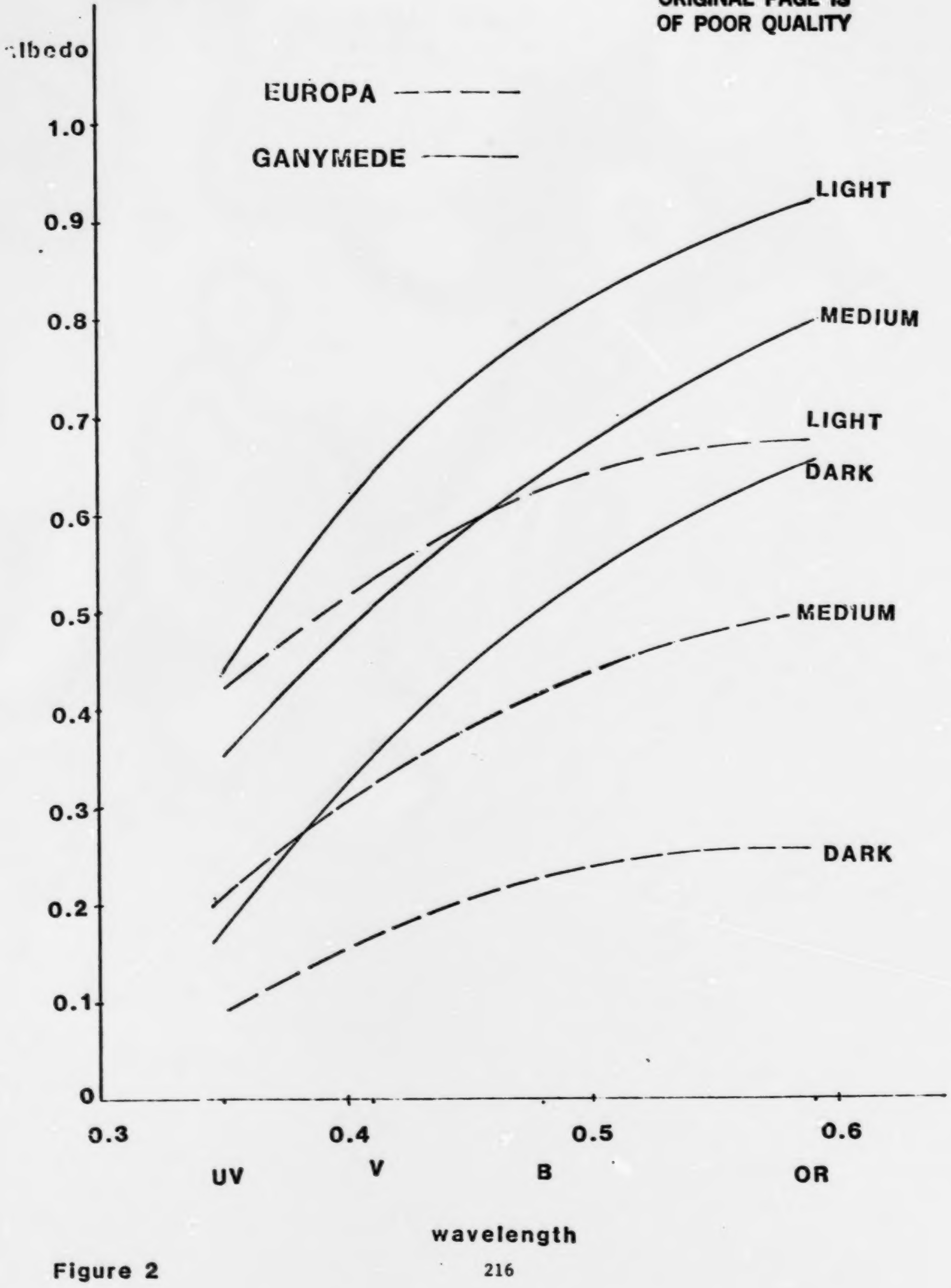

Figure 2

SECTION III

D15

N84 25582

THE GEOLOGY OF MARE ACIDALIUM QUADRANGLE MARS

by

NANCI E. WITBECK

B.S., Northern Arizona University, 1978

A MASTER'S THESIS

submitted in partial fulfillment of the

requirements for the degree

MASTER OF SCIENCE

Department of Geology

KANSAS STATE UNIVERSITY
Manhattan, Kansas

1982

PRECEDING PAGE BLANK NOT FILMED

ABSTRACT

Mare Acidalium quadrangle lies between 30° - 60°N latitude and 0° - 60°W longitude. Materials that were used in mapping the quadrangle include Mariner and Viking single-frame images and photomosaics. Preliminary geologic mapping was done on five 1:2,000,000-scale photomosaics and selected higher resolution photomosaics. The data were then compiled on one sheet at a scale of 1:5,000,000.

The Mariner 9 mission revealed a striking planetary dichotomy; high-standing, heavily-cratered terrain in the south that contrasts with low-lying, lightly-cratered terrain in the north. Both of these terrain types occur in Mare Acidalium quadrangle. The boundary separating the elevated cratered plateau from the lower plains is, in many places, an escarpment 1-2 km-high, however, in a few places where there is no escarpment, plains materials embay and overlap the heavily-cratered plateau material.

Plateau materials cover approximately 20 percent of the quadrangle and occur in three areas in the southern region. The plateau province consists of six units: (1) cratered plateau material (302,000 km^2). (2) dissected and fractured plateau material (25,000 km^2), (3) rugged plateau material (270,000 km^2), (4) ridged plateau material (95,000 km^2), (5) fractured plateau material (46,000 km^2), and (6) lower plateau material (small patches).

The cratered plateau and rugged plateau materials, believed to be the oldest in the quadrangle, are characterized by many ancient flat-floored, degraded and partially buried impact craters. The

younger ridged plateau and fractured plateau materials contain mare-type ridges and NE-trending grabens, respectively. The dissected and fractured plateau material is characterized by many N-S trending fractures and ghost craters and occurs near the center of the quadrangle. Lower plateau material occurs in small patches along the plateau-plains boundary in the southwest region. The unit may represent resistant material underlying the older plateau units and is exhumed, or material that was deposited on top of the smooth plains.

Lowland plains materials cover the remaining 80 percent of the quadrangle. The plains province consists of ten units: (1) mottled plains material - undivided (991,000 km^2), (2) hummocky mottled plains material (386,000 km^2), (3) patterned mottled plains material (458,000 km^2), (4) subdued patterned mottled plains material (37,000 km^2), (5) fractured plains material (23,000 km^2), (6) knobby plains material (193,000 km^2), (7) smooth plains material (1,162,000 km^2), (8) patterned smooth plains material (60,000 km^2), (9) variegated plains material (128,000 km^2), and (10) knobby terrain material (small patches).

The mottled plains units are characterized by high-albedo zones around impact craters that are surrounded by low-albedo intercrater plains. To the north, crater floors are commonly filled with light material, and there is a distinct NE-SE eolian grain. Gradiational boundaries exist between all mottled plains units. Boundaries between mottled plains units and other plains units commonly have distinct morphologic and albedo contrasts. The NW-SE eolian grain is most apparent on the mottled plains material - undivided. The hummocky mottled plains and the higher-albedo knobby plains are characterized by numerous, randomly distributed, small, dark hills or hummocks that may be volcanic. The patterned mottled plains, subdued patterned mottled plains, fractured plains, and patterned smooth plains are characterized by a polygonal pattern of troughs that may be the result of permafrost, desiccation, or tectonic activity. Lava flows partially obscure the trough pattern on the subdued patterned mottled plains. The troughs on the fractured plains are much larger than those on other plains units. Troughs on the patterned smooth plains may be slightly smaller than those on other plains units.

The vast smooth plains and variegated plains have few impact craters. Streamlined landforms and channels on the smooth plains indicate fluvial erosion and deposition. The variegated plains contain features that may be volcanic. Knobby terrain material occurs in patches throughout the lowland plains and may represent erosional remnants of plateau material, more resistant remnants of an underlying cratered surface, igneous intrusions, or volcanic constructs.

The heavily-cratered plateau materials in the southern region record an early period when the impact of large bodies was common. Later, these regions were partially or completely buried by younger volcanic and eolian materials and disrupted by faulting. The central region may have subsided and plateau material that once covered a large portion of the quadrangle began to break down and erode, leaving only erosional remnants of the higher surface scattered throughout the lowland region. Volcanic, eolian, and alluvial materials resurfaced a large portion of the lower plains. The distinctive and varied surface textures in Mare Acidalium quadrangle have been created by impact, tectonic, fluvial, eolian, periglacial activity and mass movement processes.

CONTENTS

Page

INTRODUCTION 230

Area of Study 232

Purpose of Study 232

Methods of Investigation 235

Data Base 237

Mariner 9 237

Viking 237

Previous Mapping 239

GEOLOGY OF MARS 242

Planetary Dichotomy 242

Impact Craters 247

Permafrost 250

Meteorology and the Atmosphere 254

Wind Features 256

Channels 257

Volcanism and Ice 259

GEOLOGY OF MARE ACIDALIUM QUADRANGLE 260

Impact Craters 260

Plateau Province 261

Cratered Plateau 261

Dissected and Fractured Plateau Material 269

Rugged Plateau Material 274

Ridged Plateau Material 280

Fractured Plateau Material 286

Lower Plateau Material 287

Page

Plains Province 293

Mottled Plains Region 296

Mottled Plains Material - Undivided 297

Hummocky Mottled Plains Material 303

Patterned Mottled Plains Material 309

Subdued Patterned Mottled Plains Material 315

Fractured Plains Material 320

Knobby Plains Material 328

Smooth Plains Material 329

Patterned Smooth Plains Material 337

Variegated Plains Material 344

Other Material 348

Dark Material 348

Light Material 348

Channel Material 349

Knobby Terrain Material 349

GEOLOGIC HISTORY 355

Early Cratering 355

Outgassing 356

Early Volcanism 356

Scarp Formation 357

Scarp Retreat and Formation of Plains Units 357

Tectonism 360

Late Volcanism 362

Recent Processes 362

Page

SUMMARY AND CONCLUSIONS 363

REFERENCES 365

ACKNOWLEDGMENTS 375

APPENDIX 376

APPENDIX I - TEMPE PLATEAU REGION 379

  Crater Material 382

APPENDIX II - CENTRAL PLATEAU REGION 385

  Crater Material 387

APPENDIX III - CYDONIA REGION 390

  Crater Material 397

  Bamberg Deposits 398

APPENDIX IV - GEOLOGIC MAP OF MARE ACIDALIUM QUADRANGLE 400

  Plateau Materials 400

  Plains Materials 404

  Other Materials 409

  Crater Materials 410

ILLUSTRATIONS

Figure Page

1. Generalized geologic map of Mars 233
2. Topographic map of Mare Acidalium quadrangle 234
3. Location of terrains on which crater counts were made 238
4. Location of Viking images and photomosaics shown in text 240
5. All craters greater than 15 km in diameter 243
6. Impact crater material 248
7. Mean annual surface temperature for each latitude of Mars 252
8. Cummulative crater size-frequency distributions for the plateau units 262
9. Small channels on cratered plateau 264
10. Floor-fractured crater on cratered plateau 266
11. Cratered plateau - smooth plains boundary 270
12. Dissected and fractured plateau materials 272
13. Rugged plateau material 276
14. Relative-height profiles of crater forms shown in Figure 13 278
15. Ridged plateau material 282
16. Flow fronts on ridged plateau 284
17. Fractured plateau material 288
18. Lower plateau material 290
19. Streamlined remnants of lower plateau material 294

Page

20. Cummulative crater size-frequency distributions for the mottled plains units and knobby plains 299

21. Mottled plains material - undivided, example 1 300

22. Mottled plains material - undivided, example 2 304

23. Hummocky mottled plains material 306

24. Patterned mottled plains material 312

25. Patterned mottled plains - variegated plains boundary 316

26. Lava flows on subdued patterned mottled plains 318

27. Subdued patterned mottled plains material 322

28. Patterned mottled plains - subdued patterned mottled plains boundary 324

29. Fractured plains material 326

30. Knobby plains material 330

31. Smooth plains material 332

32. Cummulative crater size - frequency distributions for the variegated plains, smooth plains, and mottled plains - undivided 334

33. Ridges on the smooth plains, example 1 338

34. Ridges on the smooth plains, example 2 340

35. Patterned smooth plains material 342

36. Variegated plains material 346

37. Dark, light, and channel material 350

38. Knobby terrain material 352

Page

39. Photomosaic of the Tempe Plateau region 377

40. Geologic map of the Tempe Plateau region 378

41. Photomosaic of the Central Plateau region 383

42. Geologic map of the Central Plateau region 384

43. Photomosaic of the Cydonia region 388

44. Geologic map of the Cydonia region 389

45. Geologic map of Mare Acidalium Quadrangle - NE 412

46. Geologic map of Mare Acidalium Quadrangle - NW 413

47. Geologic map of Mare Acidalium Quadrangle - SE 414

48. Geologic map of Mare Acidalium Quadrangle - SC 415

49. Geologic map of Mare Acidalium Quadrangle - SW 416

50. Correlation of Map Units 417

51. Schematic Cross Section from NW to SE 419

INTRODUCTION

Galileo, in 1610, was the first to observe Mars through a telescope. In 1659, Christian Huygens produced the first drawings of Mars showing the dark markings, maria, that early workers believed represented bodies of water. Father Secchi, in 1869, introduced the Italian word, "canali," which means channels, to describe some of the dark, streak-like martian markings. Unfortunately, the English language press translated the Italian word "canali" not as "channels," which has no necessary implication of intelligent design, but as "canals," (Hoyt, 1976). In 1877, Schiaparelli strengthened the idea that these streak-like features were canals by mapping their distribution. Percival Lowell, who established Lowell Observatory at Flagstaff in 1894 specifically to study Mars, suggested that Schiaparelli's channels were irrigation canals constructed by intelligent beings to bring water from the poles to the dry equatorial region (Hoyt, 1976). On the other hand, several scientists suggested that the polar caps were made up of frozen carbon dioxide, and therefore, subfreezing temperatures would make Mars uninhabitable. It was not until 1965 that some of these arguments began to be resolved.

In July, 1965, Mariner 4 flew by the southern hemisphere of Mars and sent back 22 close-up images that revealed a cratered, lunar-like surface. Four years later, in 1969, the Mariners 6 and 7 fly-by missions returned a total of 202 images from the southern hemisphere of Mars, confirming that relatively uninteresting lunar-like craters were indeed scattered over the martian surface. These later images also revealed that the craters were modified by erosion.

The atmosphere around Mars permits geologic processes that cannot occur on other planetary bodies such as the Moon and Mercury, e.g., wind erosion and deposition. It was not until the Mariner 9 orbital mission in 1971 that the scientists were able to see evidence of the diversity of geologic processes that have shaped martian geologic history. Processes that have been identified are impact, volcanic, tectonic, fluvial periglacial, and eolian.

Mariner 9 data revealed striking differences between the northern and southern hemispheres of Mars. This hemispheric dichotomy is expressed by an abrupt change from the high-standing, densely cratered terrain in the south, to low-lying, lightly cratered terrain in the north. The boundary separating these two terrain types is commonly expressed as a 1-2 km high, irregular scarp (Carr, 1980b), north of which the plains slope downward to elevations 5-6 km or more below the southern highlands.

The area involved in this investigation occurs along the boundary between the southern highlands and the northern plains. Several areas in the northern plains were selected on the basis of Mariner 9 data as potential landing sites for the Viking landers because the areas appeared to be relatively smooth. The 40° - 50°N latitude band was of special scientific interest because of the high atmospheric water content, moderate surface temperature, and the possibility of near-surface permafrost (Masursky and Cradbill, 1976).

When the Viking 1 orbiter arrived at Mars in June 1976, these areas were photographed in great detail in order to determine the safest landing site, and eventually the Utopia Planitia site (48°N, 226°W) was selected. One of the alternative landing sites, Cydonia (44°N, 10°W), occurs within the area of this investigation. The Cydonia site was originally considered for the Viking 2 lander because the atmospheric pressure in this region was high enough to permit water to exist in a liquid state. The Cydonia site was rejected because it appeared to be too rough.

Area of Study

Mare Acidalium was one of the dark areas that appeared on Schiaparelli's map of Mars in the late 1800's (Schiaparelli, 1878). The area of this investigation is Mare Acidalium quadrangle (MC-4); Acidalia Planitia, the largest area of low albedo in the northern hemisphere, constitutes much of the Mare Acidalium quadrangle. This quadrangle lies between 30° - 65°N latitude and 0° - 60°W longitude (Fig. 1). Occultation data from Mariner 9 indicate that the elevation in the central area of Acidalia Planitia is more than 3 km below the 6.1 millibar datum, the elevation reference surface established for Mars corresponding to the pressure at the triple point of water (Fig. 2).

Purpose of Study

Mariner 9 data from Mars revealed the striking planetary dichotomy, i.e., southern highlands and northern lowlands. The low-resolution Mariner 9 images depicted the northern plains as flat to gently rolling hills with few topographic irregularities (Scott, 1978). A few scattered

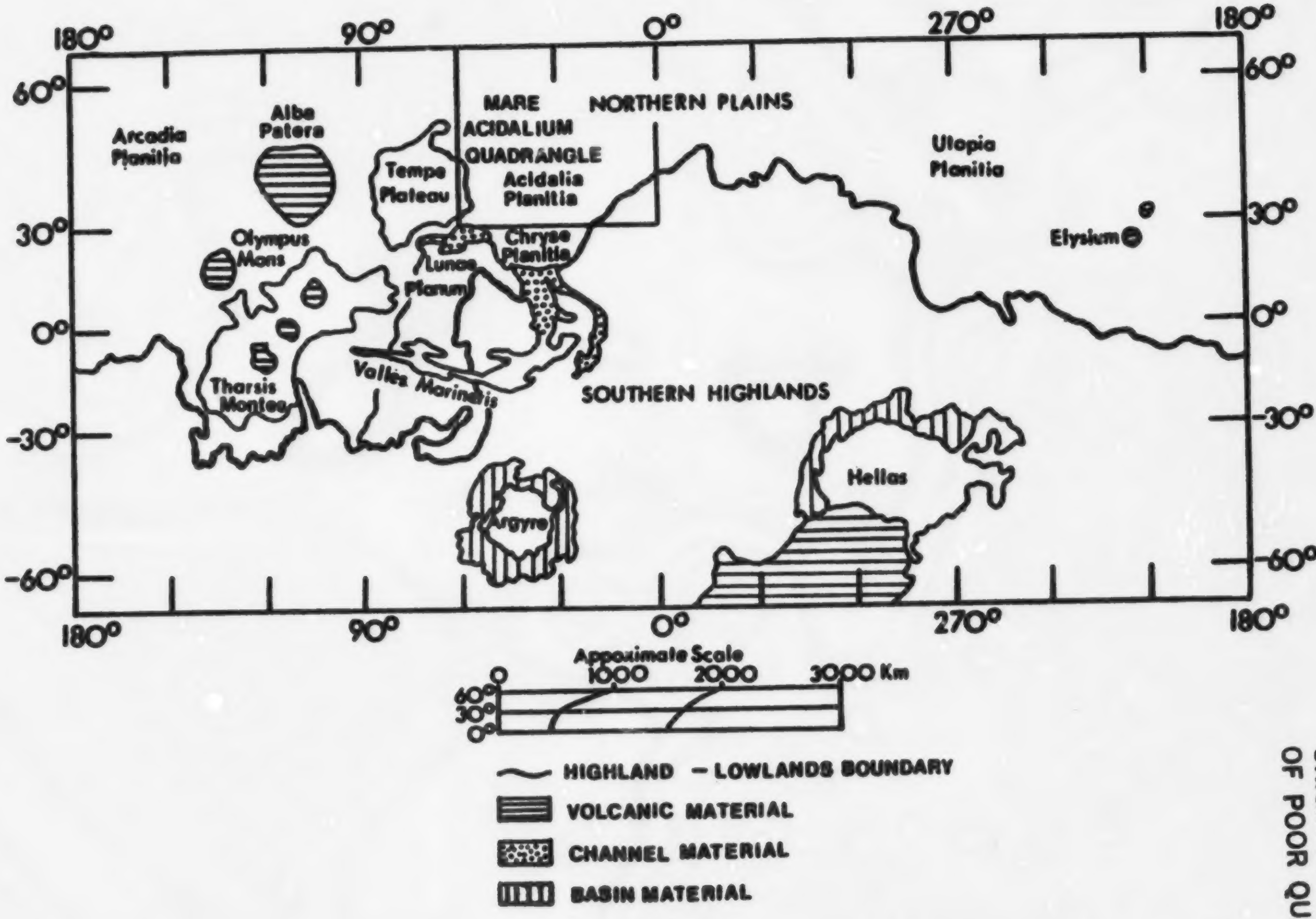
180°
90°
0°
270°
180°
60°
30°
0°
-30°
-60°
MARE ACIDALIUM QUADRANGLE
NORTHERN PLAINS
Arcadia Planitia
Alba Patera
Tempe Plateau
Acidalia Planitia
Utopia Planitia
Olympus Mons
Chryse Planitia
Lunae Planum
Elysium
Tharsis Montes
Valles Marineris
SOUTHERN HIGHLANDS
Hellas
Argyre
Appoximate Scale
0
1000
2000
3000 Km
60°
30°
0°
HIGHLAND - LOWLANDS BOUNDARY
VOLCANIC MATERIAL
CHANNEL MATERIAL
BASIN MATERIAL

Figure 1. Generalized geologic map of Mars. Mare Acidalium quadrangle is indicated by the box; terrain units are based on Scott and Carr (1978).

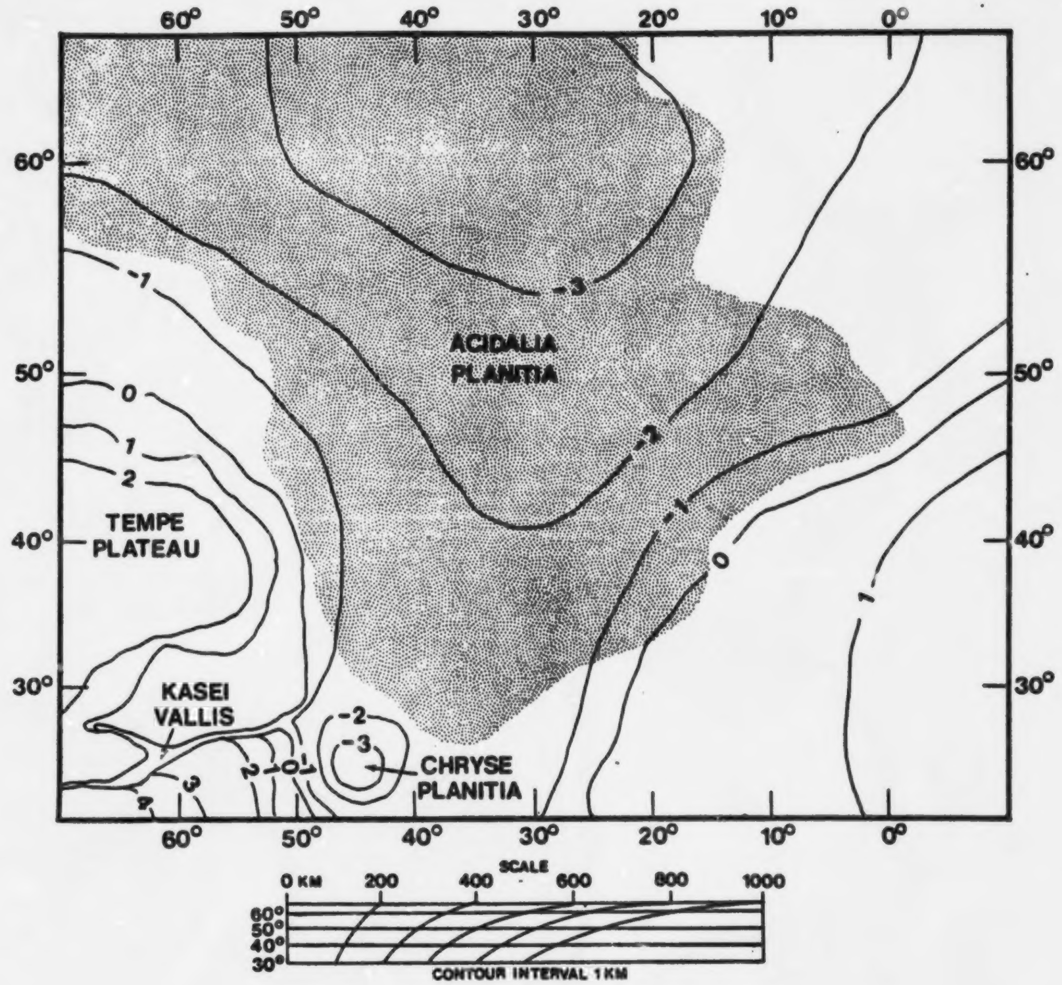
60°
50°
40°
30°
20°
10°
0°
ACIDALIA
PLANITIA
TEMPE
PLATEAU
KASEI
VALLIS
CHRYSE
PLANITIA
-3
-2
-1
0
1
2
3
4
SCALE
0 KM
200
400
600
800
1000
CONTOUR INTERVAL 1 KM

Figure 2. Topographic map of Mare Acidalium quadrangle. Stipple pattern indicates area of extremely low albedo; scale from the 1:25,000,000-scale Topographic Map of Mars (U.S. Geol. Survey, 1976).

ORIGINAL PAGE IS
OF POOR QUALITY

high-resolution Mariner 9 images in this northern region hinted that the geology was more complex. The higher-resolution Viking orbiter images have revealed a variety of surface features that confirm the complexity of the geology in the area. Few detailed studies of this area have been done utilizing the high-resolution Viking orbiter data.

This investigation incorporates data from both the Mariner and Viking missions in an effort of identify the materials in, and to infer the most reasonable geologic history of, the Mare Acidalium region of Mars.

Methods of Investigation

Photogeology is defined as: "The identification, recording, and study of geologic features and structures by means of photography, specifically the geologic interpretation of aerial and space photographs and images and the presentation of the information so obtained" (Bates and Jackson, 1980).

On Earth, aerial photographs commonly reveal details of the geology that are not detectable on the ground. Both fieldwork and photogeology are often incorporated into making a geologic map. Because geologic maps of Mars are based only on photographic observations and other remote sensing techniques rather than on ground surveys, the various definable geologic units must be characterized by geomorphic and albedo features. Ideally, the geologic terrains that are delineated have stratigraphic significance; however, the surface processes have been intermittently active such that surfaces of many ages are exposed in many different geographic areas. It is often difficult to distinguish between the age of a depositional or an erosional surface and the age of the material that immediately underlies it. The occurrence of surface features such as volcanoes, lava flows, impact craters, channels, dunes, and fractures are useful when interpreting the origin and geologic history of an area.

Mars has been divided into thirty quadrangles by the U.S. Geological Survey. The present investigation involves geologic mapping and interpretation of the plains and adjacent highlands in one of these quadrangles of the northern mid-latitudes. Materials that were used include Mariner and Viking single-frame images, stereopairs where available, and photomosaics. Preliminary geologic mapping was done on five 1:2,000,000-scale photomosaics and selected higher-resolution photomosaics. The data were then compiled on one sheet at a scale of 1:5,000.000 for presentation in this thesis. Also, included in the thesis are larger-scale maps and photomosaics of particularly relevant regions.

Early lunar workers developed a method based on statistics of impact crater populations to determine the relative ages of surfaces on the Moon and planets other than Earth. This method is based on the simple relationship between crater abundance and age, i.e., old surfaces are more densely cratered than young surfaces. The technique used for analysis of crater populations is to plot the crater diameter versus the abundance or frequency of craters. The early investigators found that the number of craters increases geometrically as the size of the crater decreases because the interplanetary debris is dominated by smaller-sized particles (Mutch et al., 1976).

To determine possible age relationships between surfaces with distinctive geomorphic and geologic characteristics, statistical analyses of crater frequencies were performed in accordance with the methods outlined by the Crater Analysis Techniques Working Group (Arvidson et al., 1978). These data are presented in cumulative size-frequency distribution plots. The locations of the crater counts are shown on Figure 3.

If every crater on a surface is younger than the surface material, this method will provide a minimum age of the surface material, as well as the exposure age of the surface itself (McGill, 1977). Caution must be used with this method of dating surfaces, because, as McGill (1977) pointed out, large craters have higher walls and deeper pits than small craters. Thin surface deposits such as lava flows, eolian materials, and air-fall materials, could completely obliterate the small craters, partially bury the intermediate size craters, but have little effect on the large craters.

Data Base

Mariner 9.--In 1971-1972, nearly 100 percent of the martian surface was photographed by Mariner 9. The vast majority of the 7,300 images returned by Mariner 9 have a resolution of 1-3 km (A-frames), whereas approximately 1-2 percent of the images have a resolution of 100-300 m (B-frames). Within the Mare Acidalium quadrangle, Mariner 9 transmitted to Earth 26 A-frames and 33 B-frames.

Viking.--Following their arrival at Mars in 1976, the two Viking orbiters acquired approximately 65,000 images of the martian surface. The

ORIGINAL PAGE IS
OF POOR QUALITY

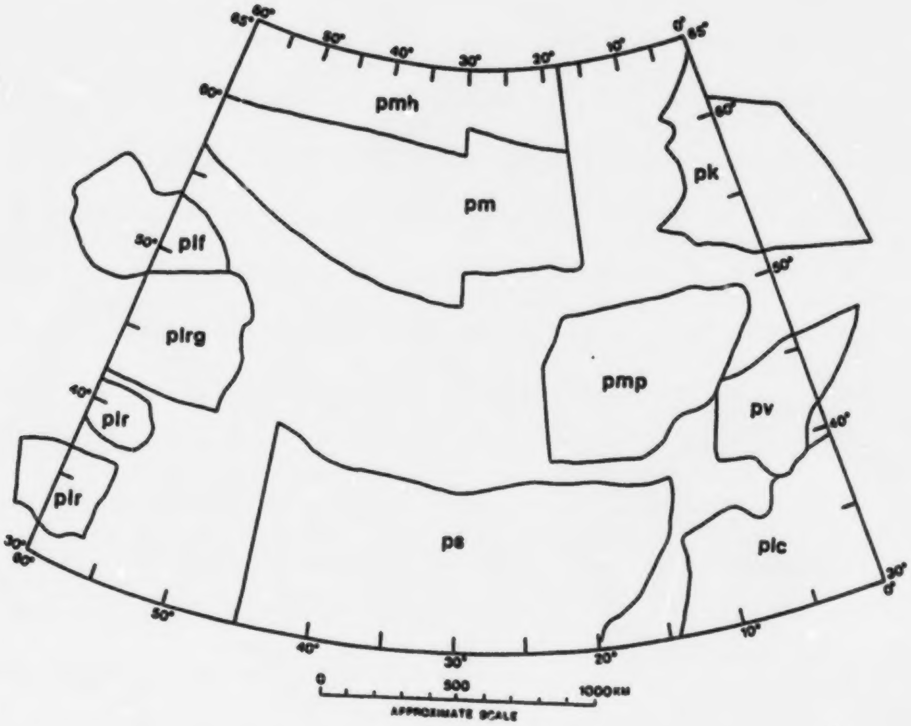

65°
60°
50°
40°
30°
20°
10°
0°
65°
60°
pmh
pm
pk
60°
50°
plf
plrg
50°
pmp
pv
40°
40°
plr
plr
ps
plc
30°
60°
30°
0°
50°
40°
30°
20°
10°
0
500
1000KM
APPROXIMATE SCALE

Figure 3. Location of terrains on which crater counts were made. Some areas extend into adjacent quadrangles; plateau units include: cratered plateau (plc), rugged plateau (plrg), ridged plateau (plr), and fractured plateau (plf), plains units include: mottled plains - undivided (pm), hummocky mottled plains (pmh), knobby plains (pk), patterned mottled plains (pmp), variegated plains (pv), and smooth plains (ps).

images are categorized into four groups:

(1) low resolution (average 70,000 km^2 per image, > 180 meters/pixel)

(2) medium resolution (average 40,000 km^2 per image, 130-180 meters/pixel),

(3) high resolution (average 10,000 km^2 per image, 35-130 meters/pixel), and

(4) very high resolution (average 2,500 km^2 per image, < 35 meters/pixel).

In Mare Acidalium quadrangle approximately 1,600 images of varied resolutions were acquired. Figure 4 shows the locations of the high-resolution strips within the quadrangle. Most of the high-resolution data were obtained from the Cydonia region, the area that was designated as a potential Viking landing site.

Previous Mapping

On the basis of Mariner 9 data, Underwood and Trask (1978) mapped the geology of Mare Acidalium quadrangle at a scale of 1:5,000,000. Mariner 9 images in the northern latitudes were of poor quality because of atmospheric dust and the high sun angle at which many of the images were acquired, and, as a result, only a few geologic subdivisions could be recognized within the lowland plains of the quadrangle. These divisions included: mottled plains material, plains material, plains and dissected plateau material, and channel material. The adjacent quadrangles were mapped by Wise (1979), Lucchitta (1978), Milton (1976), Wilhelms (1976), and Dial (1982) at a scale of 1:5,000,000. The Cydonia region of MC-4 was designated as a possible landing site for the Viking lander (Masursky and Cradbill, 1976), resulting in more detailed geologic mapping in this region (Scott, 1976).

Other cartographic products published by the U.S. Geological Survey

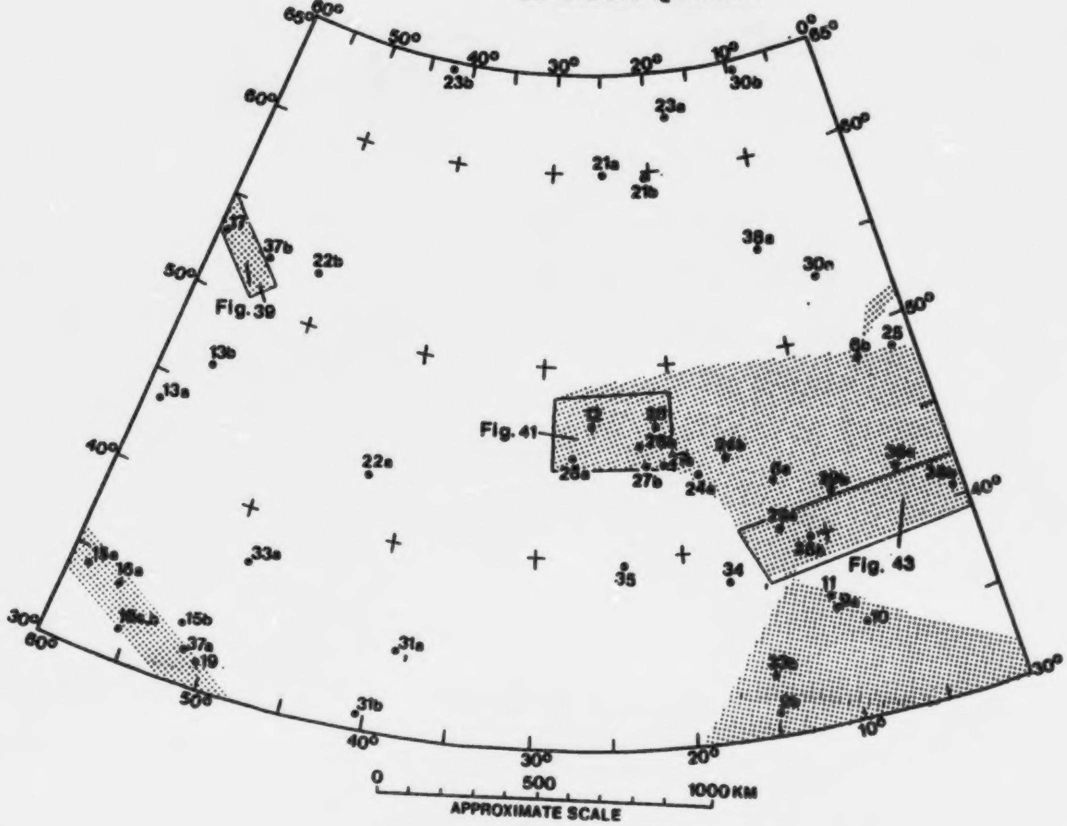
65°
60°
50°
40°
30°
20°
10°
0°
65°
60°
50°
40°
30°
60°
50°
40°
30°
20°
10°
30°
Fig. 39
Fig. 41
Fig. 43
23b
23a
30b
21a
21b
38a
30a
37
37b
22b
13b
13a
22a
6b
25
26a
27b
24a
24b
33a
35
34
15a
16a
16a,b
15b
37a
19
31a
31b
11
10
0
500
1000 KM
APPROXIMATE SCALE

Figure 4. Location of Viking images and photomosaics shown in text. Numbers correspond to figure numbers in this report; dots locate center of images; boxes show locations of high-resolution photomosaics and geologic maps included in Appendix I-III; shaded areas are regions of high-resolution data.

include: 1:5,000,000 topographic map of MC-4 (1976); 1:5,000,000 shaded relief map of MC-4 (1975); 1:1,000,000 topographic map of the Cydonia region (1976); 1:250,000 high-resolution map of the Cydonia region (1976); and 1:2,000,000 controlled photomosaics of the northeast, northwest, southeast, south-central, and southwest sub-quadrangles (1981).

GEOLOGY OF MARS

A general overview of the planet Mars and martian geology is important for understanding the processes that affect the geologic development of a particular region. Several review papers and books have been published (Masursky, 1973; Mutch et al., 1976; Carr, 1980b, 1981). Scott and Carr (1978) published a geologic map of Mars that shows 24 geologic units. Also included on the map are tectonic features, the majority of which are extensional. A number of geologic features on Mars indicate a long period of horizontal tensional stresses acting on the lithosphere. Solomon and Chaiken (1976) and Toksoz and Hsui (1978) presented thermal history models suggesting that Mars has undergone a period of expansion that resulted in extensive systems of tensional fractures and volcanism.

Planetary Dichotomy

One of the most interesting discoveries of the Mariner 9 mission was the striking difference between the northern and southern hemispheres of Mars. There is an abrupt change from the high-standing, heavily-cratered terrain in the south, to the low-lying, lightly-cratered terrain in the north (Fig. 1,5). The boundary between the two hemispheres is approximately a great circle inclined 35° to the equator (Mutch et al., 1976). The northern plains slope to elevations > 3 km below the mean datum, that level where the atmospheric pressure is 6.1 millibars. The southern highlands generally stand 2-3 km above the mean datum.

The heavily-cratered terrain in the southern hemisphere includes the planet's oldest exposed surfaces. Superficially, these old surfaces

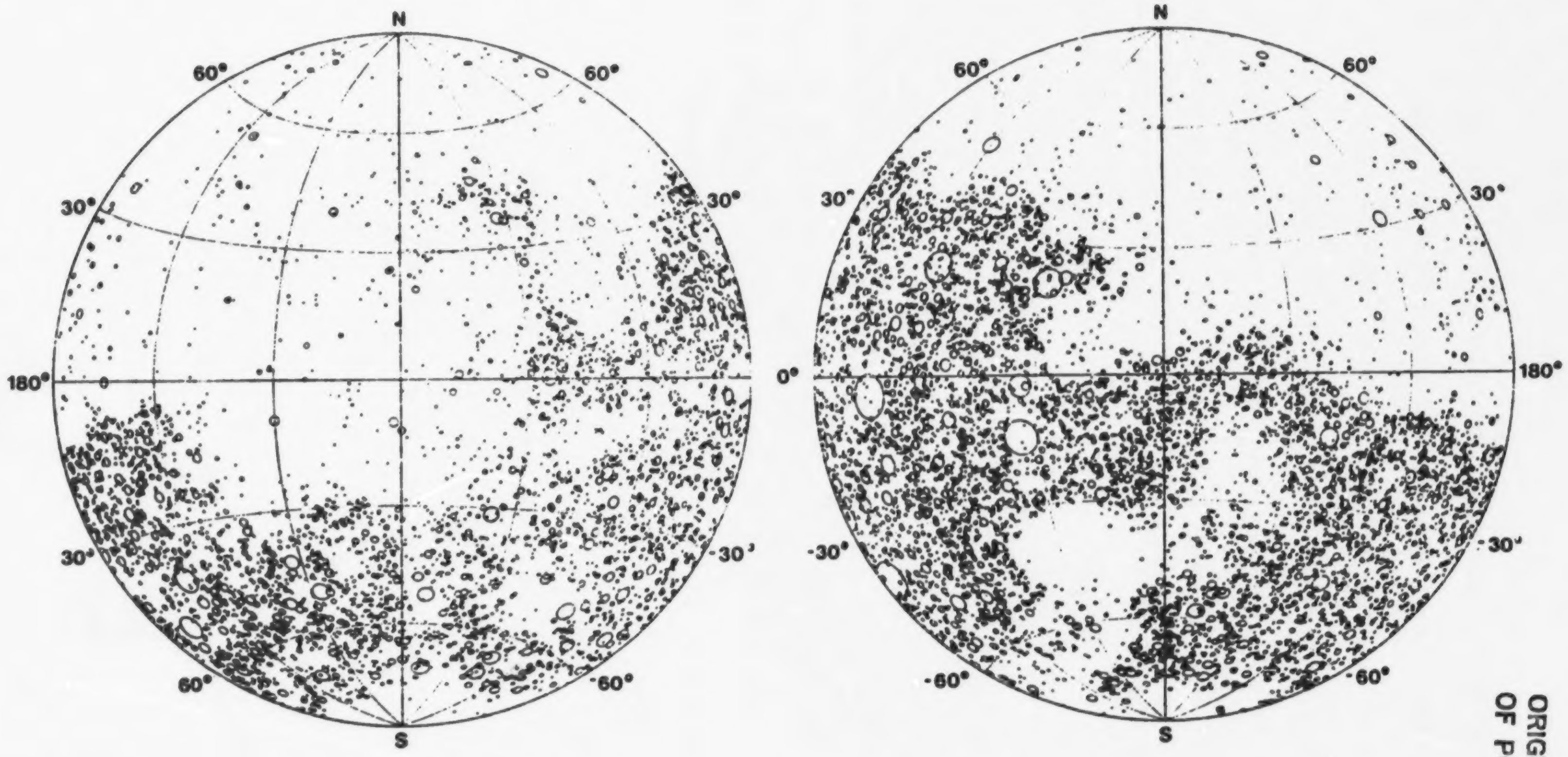
N
60°
60°
30°
30°
180°
0°
30°
-30°
60°
-60°
S
N
60°
60°
30°
30°
0°
180°
-30°
-30°
-60°
-60°
S

Figure 5. All craters greater than 15 km in diameter. Note the distinct difference in crater density between the northern and southern hemispheres. From Mutch et al. (1976).

resemble the lunar highlands. The two units are thought to be similar in age because of the abundance of large (> 30 km) craters on both units (Soderblom et al., 1974; Neukum and Wise, 1976). The ancient cratered terrain on Mars, however, records a far more complex history of depositional and erosional events. The larger martian craters tend to be highly degraded, and many of these large craters are channeled and gullied, indicating erosion by running water. Volcanic activity (Greeley and Spudis, 1978) and eolian activity (Carr, 1981) were important modifying agents. The old cratered terrain appears to represent a complex mixture of impact debris, volcanic rocks, and eolian and fluvial sediments.

In contrast, the northern plains include some of the youngest surfaces exposed on the planet. Some of the plains material in the Tharsis volcanic regions are almost devoid of impact craters (Scott and Carr, 1978). The low-latitude northern plains contain a number of overlapping volcanic units that have been modified to various degrees by fluvial and eolian processes (Carr, 1981).

The high-latitude northern plains are not as simple to understand as the low-latitide plains. The high-latitude northern plains appear to represent a complex history of erosion and deposition. The surface contains a wide array of topographic and albedo features such as polygonal fractures, pedestal and flow-ejecta craters, irregular depressions and hills of varied origin, and light and dark streaks.

Soderblom et al. (1973a) reported that many craters in the high northern latitudes were filled or partially filled with light material, suggesting the presence of an old debris mantle that has been stripped away from the intercrater regions. Carr and Schaber (1977), Rossbacher and Judson (1981), and Lucchitta (1981) have indicated the possible importance of ice in shaping the northern terrain. To complicate things further, the northern plains are probably sites of accumulation of fluvial debris derived from the large outflow channels to the south (Carr, 1980b). The complex characteristics of the northern plains most likely result from the interaction of impact, volcanic, eolian, fluvial, mass wasting, and periglacial processes.

The boundary separating the heavily-cratered highlands and the sparsely-cratered lowlands varies. In some places the relationship is simple; the younger plains overlap the older, cratered surface. In these areas, islands of older, cratered terrain can be seen protruding through the plains material (Carr, 1981). In other areas, the boundary is expressed by a steep escarpment 1-2 km high. In many areas along the escarpment there are flat-topped mesas and rounded, equidimensional hills that have been interpreted as erosional remnants of highlands material left by scarp retreat (Scott 1978, 1979; Scott and Carr, 1978).

The origin of the planetary dichotomy is controversial. Soderblom and Wenner (1978) pointed out that extensive areas throughout the northern equatorial region appear to have been uniformly stripped to depths 1-2 km below the pre-existing surface. These areas vary in age and in absolute elevation. Soderblom and Wenner suggested that the southern highlands are underlain by an ice-laden zone and sections of this layer were removed from the region by such processes as eolian deflation, gravitational slump, collapse, and fluvial transport. Erosion stopped at the liquid-ice interface because rocks below the zone of permafrost were cemented and much more resistant. Head et al. (1977) also concluded that the boundary between the cratered terrain and plains was the result of collapse and erosion at the north-facing escarpment.

Carr (1980a, 1981) and Wise et al. (1979) have argued that erosion by surface processes cannot fully explain the disappearance of the ancient crust from the northern hemisphere because there is no sink of sufficient size to accommodate the debris. Carr (1980a) and Mutch et al. (1976) suggested that differentiation produced a crust of varied thickness. The crust was thinner in the north and thicker in the south. The lack of a gravity anomaly along the plains-highlands boundary lends support to this view (Carr, 1980a).

Wise et al. (1979) discussed the possibility of subcrustal erosion by a convection cell operating beneath the northern plains region. The cell, rising beneath the northern plains, eroded the base of the crust and disrupted the remaining crust by fracturing. Subsequently, the northern region sank to maintain isostatic equilibrium (Phillips and Saunders, 1975) and was covered by volcanic material. The eroded basal-crustal material was eventually transported to the Tharsis region where slow transfer of heat from zones deep in the mantle produced an extremely long volcanic phase (Wise et al., 1979).

Impact Craters

Circular depressions are a common landform on the surface of nearly every solid planetary body in the solar system. Most workers have interpreted these features as impact craters. Impact craters can be very important indicators of such things as surface material, erosional and depositional events, and relative ages of exposed surfaces (Carr, 1981).

The morphology of ejecta around most of the martian craters is different from that around lunar and mercurian craters. Lunar and mercurian craters are surrounded by a continuous ejecta blanket that commonly extends outward as bright rays and fields of secondary craters. Ballistic emplacement is the mode of deposition of ejecta around these craters. In contrast, many of the martian ejecta blankets appear to have been emplaced by surface flow (Fig. 6a). These craters have been identified by a variety of names such as rampart, fluidized, splosh, flower, flow-ejecta, and so on. They shall be referred to either as rampart or flow-ejecta craters in this study.

Craters having ejecta blankets with a distinct outer ridge or rampart were first recognized on Mariner 9 B-frames and are designated as rampart craters. McCauley (1973) and Arvidson et al. (1976) attributed their unusual morphology to wind erosion. Further investigation revealed fine details of the ejecta blankets that were primary features and not the result of subsequent modification (Head and Roth, 1976). Most workers presently believe that the presence of liquid water, water ice, or other volatile material in the ejecta was the cause of its fluid properties (Carr, 1981). These fluidized or rampart craters occur on almost every geologic unit on Mars, and they apparently formed thoughout a considerable span of time

Figure 6. Impact crater material. (a) Ejecta lobes of Arandas crater (30 km diameter); concentric flow-ejecta deposits are indicated by the arrows; the inner ejecta deposit was interpreted as part of the crater's overturned rim flap that was subsequently overridden by the more extensive outer ejecta deposit (Carr et al., 1977); shadow length estimates indicate that the inner ejecta unit rises 40-100 m above the surrounding material, and the outer ejecta unit rises 80 m above the surrounding plains (Mouginis-Mark and Carey, 1980); fine radial structure occurs on the lobes; Viking frame 9A42 (43°N, 14.5°W). (b) Small pedestal crater (< 2 km diameter); compare the pedestal crater (p) to the other non-pedestal impact crater (c) of similar size; note that the pedestal crater has a low platform that extends outward approximately three crater diameters; the surrounding unit is patterned mottled plains material (pmp); the small arrows indicate troughs; the larger arrow indicates a ridge; faint lines at eastern and western side are image artifacts; Viking frame 26A56 (47.5°N, 5.2°W).

a.

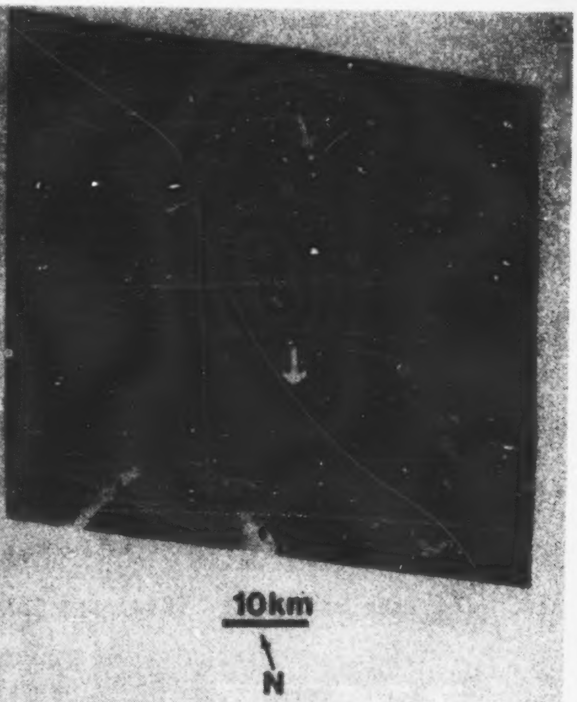

b.

(Allen, 1979a).

Another type of martian crater with unusual morphology is the pedestal crater (Fig. 6b). These kinds of craters are common in the northern hemisphere between latitudes 30°N and 70°N (Carr, 1981) and are craters situated in the center of a low platform or pedestal that extends outward more than three crater diameters. McCauley (1973) suggested that ejecta from the impact armored the surface adjacent to the crater and subsequent deflation of the intercrater region resulted in the crater and its surrounding ejecta remaining as a platform or pedestal overlooking the lower intercrater area. Mutch and Woronow (1980) suggested that the pedestal craters represent viscous ejecta, i.e., too viscous to flow into lobes.

Permafrost

The presence of permafrost on Mars has long been suspected based on observations of the annual surface temperatures and the assumed outgassing history of the planet (Sharp, 1973, 1974; Anderson et al., 1967; Farmer and Doms, 1979; Fanale, 1976). Water vapor or water ice is indicated from infrared and water-vapor measurements over the polar caps (Kieffer et al., 1977; Farmer and Doms, 1979) and from soil analysis by the Viking landers (Biemann et al., 1977). Mariner and Viking orbiter data have reinforced the suspicion that permafrost has played an important role in the development of the martian landscape (Carr and Schaber, 1977).

Probably the most important consideration is that Mars is cold. The present mean annual temperature is approximately -60°C (Leighton and Murray, 1966) well below the triple point of water. The cold temperature favors development of a zone of frozen ground everywhere beneath the surface of the planet (Carr and Schaber, 1977). Only between latitudes 70°S and 30°N do the summer, daytime temperatures exceed 0°C (Fig. 7) (Anderson et al., 1973).

Fanale (1976) showed that at latitudes > 40°, the mean annual surface temperature is low enough for subsurface ice to be in equilibrium with current levels of water vapor in the atmosphere. Below 40° latitude, water ice is unstable and could sublime and dissipate if exposed to the atmosphere. Observations of the atmospheric water vapor are consistent with the presence of a permanent reservoir of water ice buried at a depth of 10 cm to 1 m at all latitudes poleward of 40° (Farmer and Doms, 1979).

Approximately two-thirds of the study area lies north of 40° latitude. Fanale (1976) suggested that a regolith of unconsolidated material as much as two km thick may exist on Mars, and that within this regolith, permafrost could occur anywhere above the 273° K isotherm (ice-liquid water temperature boundary).

There have been a number of estimates made of the amount of water outgassed from Mars based on the elemental and isotopic composition of the atmosphere and on assumptions regarding the initial composition of Mars. These estimates include the use of the abundances of ^{36}Ar, ^{40}Ar (Anders and Owen, 1977; Owen and Biemann, 1976; Fanale, 1976), and N_2 (McElroy et al., 1977). These estimates predict that the thickness of a layer of water that could cover the entire surface of Mars ranges from 9 m (Anders and Owen, 1977) to 80-160 m (Pollack and Black, 1979). Presently, we observe water only as frost or ice of the polar caps and as water vapor in the atmosphere.

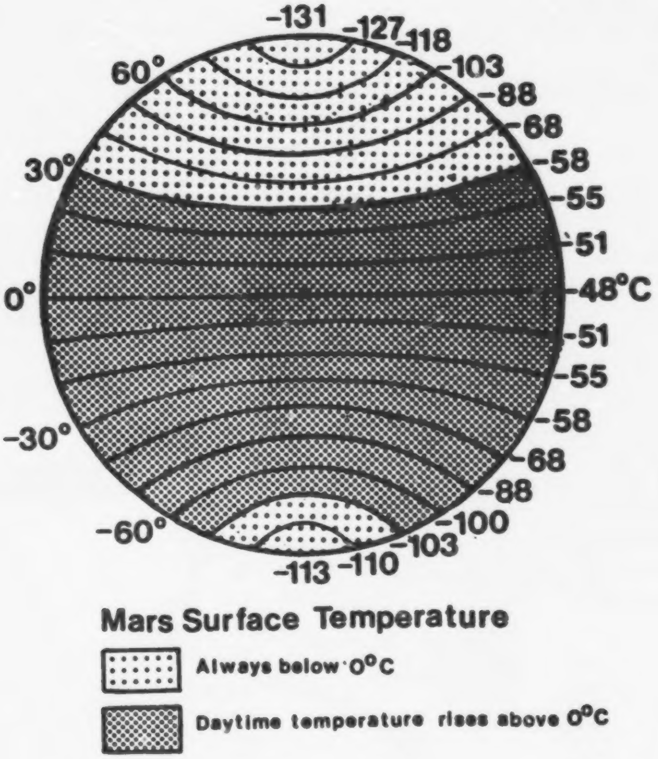
-131
-127
-118
-103
-88
-68
-58
-55
-51
-48°C
-51
-55
-58
-68
-88
-100
-103
-110
-113
60°
30°
0°
-30°
-60°
Mars Surface Temperature
Always below 0°C
Daytime temperature rises above 0°C

Figure 7. Mean annual surface temperature for each latitude of Mars. Temperatures are derived from the model of Leighton and Murray (1966); adapted from Fanale (1976) and Sharp (1974).

For the last two centuries, astronomers have observed the annual advance and retreat of the bright polar caps. Initially, these caps were regarded as comparable to a terrestrial polar ice sheet. Later it was realized that these masses could be little more than thin frost blankets (Sharp, 1974). Viking orbiter data indicate that frozen carbon dioxide advances and recedes from the polar caps seasonally, but the residual cap left in the summer is composed of water ice (Kieffer et al., 1977).

Estimates on the amount of water contained in the atmosphere, polar caps and surface frost, and the water lost through exospheric escape have been compared to the estimates of the amount of water originally outgassed (Rossbacher and Judson, 1981). These calculations indicate that much water is still unaccounted for and may be trapped as subsurface permafrost or chemically bound in the soil (Owen and Biemann, 1976).

A number of features have been interpreted by photogeologists as evidence for the presence of permafrost on Mars. Sharp et al. (1974) and Carr and Schaber (1977) suggested that permafrost may have been important in the formation of chaotic and fretted terrains and some channel features. Rampart or flow-ejecta depostis that surround many craters may be the result of impact into ice-laden regolith (Carr et al., 1977; Gault and Greeley, 1978). Patterned ground, similar to that seen in periglacial regions on Earth, characterizes extensive areas of plains in the 40° - 50°N latitude belt. Carr and Schaber (1977) and Gatto and Anderson (1975) interpreted scalloped scarps and irregular shallow depressions as thermokarst features, structures resulting from disturbances of the subsurface ice layers.

In summary, the conditions necessary for the formation of permafrost appear to exist on Mars. The mean annual temperature is well below freezing. Theoretical calculations on the outgassing history of the planet and current water-vapor measurements indicate the presence on Mars today of large volumes of water vapor or water ice, some of which may be stored in the subsurface. Geomorphological studies of Mars show many landforms that further reinforce the importance of permafrost on the planet.

Meteorology and the Atmosphere

An important factor in controlling martian surface conditions is the nature and activity of the atmosphere. Similar to Earth, the axis of Mars is tilted approximately 23° with respect to its orbital plane. As a result, the martian atmosphere undergoes seasonal changes analogous to those on Earth. The eccentricity of the martian orbit results in the southern hemisphere having a shorter but hotter summer than the northern hemisphere.

From Mariner 4 observations, scientists learned that the thin atmosphere of Mars was composed primarily of carbon dioxide and that the atmospheric pressure was much lower than had been previously assumed; Martian atmospheric pressure is an average of 7 millibars (Earth's average atmospheric pressure is 1,013 millibars (Carr et al., 1980). Goody and Belton (1967) recognized that such an atmosphere would respond strongly and quickly to variations in solar heating and radiative cooling during the day, thus, causing changes in pressure that would result in diurnal wind systems.

Because of the tenuous atmosphere of Mars, much stronger winds than those on Earth are required to set particles into motion. Arvidson (1972) estimated that saltating grains of a given diameter will travel 20 times faster on Mars than on Earth. High-velocity winds combined with relatively low settling velocities permits fine particles to remain aloft in the martian atmosphere sufficiently long to result in global dust storms (Mutch et al., 1976).

Even before the Mariner and Viking missions, telescopic observations showed that major dust storms are fairly common on Mars. Antoniadi (1930) was the first to suggest that wind might be modifying the surface of Mars. He proposed that increased solar heating of the atmosphere during perihelion provided enough energy for wind to raise large amounts of dust.

Mars observers, for more than a century, have been able to distinguish between yellow clouds (i.e., dust clouds) and white clouds (Snyder, 1979). Several types of white clouds have been observed: morning and evening hazes, recurrent localized clouds (i.e., in the Tharsis, Olympus Mons, and Elysium regions), and polar hoods. Generally, most of these clouds are believed to be composed of water; however, some may consist of carbon dioxide (Briggs et al., 1977).

During the winters the polar regions cool to extremely low temperatures, forming an extensive cloud cover known as a polar hood. North of about 60° latitude, the polar hood is believed to be partially composed of carbon dioxide ice particles. This cloud cover disappears in late winter to reveal a surface covered largely with carbon dioxide frost or snow (Leovy and Briggs, 1974).

Wind Features

Mariner 9 arrived at Mars during one of the more intense planet-wide dust storms. After the dust settled, Mariner cameras revealed a wide variety of landforms that can be attributed to wind. These features include dune fields, yardangs, and varied light and dark markings that are interpreted as surficial wind streaks (McCauley, 1973). The Viking mission has provided additional information about the eolian regime.

The most common eolian features observed on Mars are wind streaks. These streaks are almost always associated with impact craters or other topographic obstacles. Although wind streaks occur in a variety of shapes, sizes, and topographic settings, most can be grouped into one of three categories: (1) bright depositional streaks, (2) dark erosional streaks, or (3) dark depositional streaks (Thomas et al., 1981). Presumably, the orientations of wind streaks relect both global flow patterns and slope-controlled winds.

A vast field of transverse and barchan dunes, several hundred kilometers across, surrounds the north polar cap (Tsoar et al., 1979). Smaller fields of transverse dunes occur in craters and in canyons and valleys all over the planet (Ward et al., 1982). Wind directions can be derived from dune shape and orientation of the slip faces.

Crater splotches are irregular, dark deposits that occur on the downwind interior sides of craters. Many of these dark splotches have been resolved to be fields of dunes, through image enhancement. The occurrence of dark crater splotches increases with increased latitude (Thomas et al., 1981).

Yardangs are streamlined erosional landforms aligned with the strongest regional winds (Ward, 1978); other wind-erosion features on Mars include pits and grooves. Ward et al., (1980) considered these erosional features to be indicators of long-term wind trends. Most of the erosional landforms occur in the equatorial region of Mars, i.e., the area swept clean of eolian debris (Soderblom et al., 1973b).

The global wind pattern can be derived from systematic mapping of the orientation of eolian features (Ward et al., 1980). Of particular interest to this investigation is the circulation pattern in the northern hemisphere.

Coriolis-type winds appear to dominate near the pole (above 80°N). Between 80°N and 40° - 50°N, most streaks and dunes trend northwest-southeast showing no coriolis affect. Ward et al., (1980) suggested that the mid-latitude trend may be the result of storm winds locally generated form thermal contrast produced by the retreating ice cap during the spring. South of 40° - 50°N latitude the winds may be influenced by the coriolis effect as they change to a northeast-southwest orientation (Ward et al.,1980).

Channels

The channels on Mars have been the subject of considerable controversy since their discovery during the Mariner 9 mission; however, most workers have concluded that they are fluvial features. The main question is whether significant quantities of water could have existed in the past on the planet's surface (Mutch et al., 1976). Presently, the surface is too cold (Leighton and Murray, 1966), and the atmospheric pressure is too low at the lower latitudes (Fanale, 1976) for liquid water to be stable at the martian surface. These problems led to the suggestion that different atmospheric and climatic conditions existed in the past (Mutch et al., 1976; Carr, 1980b).

The two types of channels that are important to the present study are the small runoff channels that occur in the cratered terrain and the large outflow channels that occur around the Chryse basin. Runoff channels are commonly simple gullies or troughs a few tens of kilometers long. Their number and length tend to decrease toward the high latitudes (Carr and Clow, 1981). Masursky et al. (1977) suggested that the water that cut the channels may have been derived from rainfall. Alternatively, Pieri (1980) concluded that sapping or seepage from the groundwater system was more probable. Several of these small channels occur in the old cratered terrain in Mare Acidalium quadrangle.

The outflow channels are very wide, have few, if any, tributaries, and commonly extend for more than 100 km (Fig. 1). Scour patterns and teardrop-shaped islands are commonly associated with the channels (Carr and Clow, 1981). These large outflow channels have been interpreted as having been formed by catastrophic flooding (McCauley et al., 1972; Masursky, 1973; Masursky et al., 1977; Milton, 1973; Baker and Milton, 1974; Nummedal, 1976; Carr, 1979; Baker, 1982).

Carr and Clow (1981, Fig. 7) mapped the planetwide distribution of the outflow channels, the largest of which are around Chryse Planitia. Scours from the channels that enter the Chryse region from the south extend northward into Acidalia Planitia before they disappear between 35°N and 40°N. Channel deposits of Kasei Vallis occur in the southwestern part of Mare Acidalium quadrangle.

Volcanism and Ice

The effects of volcanism on surface ice have been investigated by Allen (1979b) and by Hodges and Moore (1978, 1979). Mesa-like structures on the martian surface resemble Icelandic tablemountains believed to be the result of volcanic eruption beneath an ice layer. Moberg ridges, thought to be subglacial fissure eruptions, have also been tentatively identified in the northern plains of Mars (Allen, 1979b). Frey et al. (1979) have identified what they believe to be pseudocraters in the Cydonia region. Pseudocraters are small domes with or without summit craters that develop from steam venting when lava flows over wet ground (Lucchitta, 1981).

GEOLOGY OF MARE ACIDALIUM QUADRANGLE

Impact Craters

In the present investigation, craters have been assigned to one of four morphologic categories based on crater preservation state according to the guidelines adapted for the Mars Geologic Mapping Program of the U.S. Geological Survey. A c_4 classification indicates young crater material; the rims are sharp, and the floors are deep. Small c_4 craters (< 10 km) generally have a bowl shape whereas the larger c_4 craters have central peaks. The ejecta blankets are fresh and extensive. Craters of c_3 classification are moderately fresh, although they have been somewhat modified. The crater rims are relatively sharp. The larger c_3 craters may or may not have a central peak, but the floor is still lower than the surrounding terrain. The ejecta blankets show somewhat less detail than c_4 craters. Moderately old or degraded craters are designated as c_2 craters. The crater rims are rounded, the floors are generally flat, and they have no central peak. The ejecta blankets may have been partly buried or stripped away. A c_1 crater is highly degraded; the crater rims are subdued, and the floors are flat and shallow and usually filled with younger material. The ejecta may have been completely obscured or removed, and only parts of the rim still exist. Greeley et al. (1977), in mapping the Chryse Planitia region, emphasized that the rate of degradation of craters is probably not uniform on a global scale but may be considered fairly uniform over a limited area.

To determine possible age relationships between units, crater counts were made on all material units of sufficient size to provide a valid statistical sample. The cumulative crater size-frequency is defined as the number of craters per unit area with diameters equal to, or greater than, a specific diameter (Nuekum and Hiller, 1981). The data are presented on plots of log crater frequency (number per unit area) versus log crater diameter (Fig. 8). The frequency plots should shift to higher crater densities as the surface-rock units become older. The relationship is demonstrated in Figure 8; the cratered plateau unit is believed to be the oldest in the quadrangle based on the abundance of large (> 20 km) impact craters. Utilization of larger craters in size-frequency plots is preferable because large craters are less susceptible to destruction than smaller ones.

Plateau Province

The elevated plateau province contains the oldest exposed surfaces in the quadrangle based on the crater size-frequency distributions and marks the northern extent of the ancient southern highlands. Plateau material occurs in three areas: the southeast corner, containing cratered plateau material (302,000 km^2); the central region, containing dissected and fractured plateau material (25,000 km^2); and the southwest corner, containing rugged plateau material (270,000 km^2), ridged plateau material (95,000 km^2), fractured plateau material (46,000 km^2) and small patches of lower plateau material.

Cratered Plateau.--The surface of the elevated cratered plateau in the southeast corner of the quadrangle appears to be the oldest in the map

ORIGINAL PAGE IS
OF POOR QUALITY

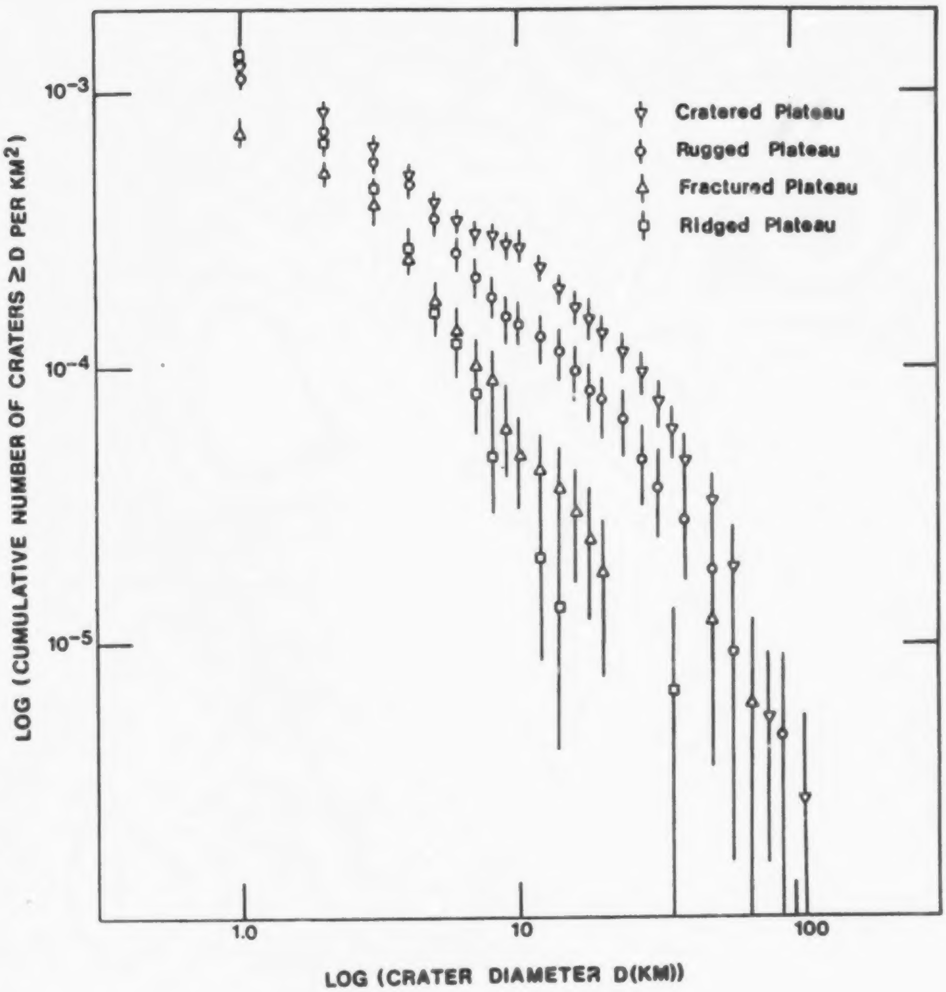

Figure 8. Cummulative crater size-frequency distributions for the plateau units. Number of craters are cummulated from largest to smallest size; vertical lines indicate one standard deviation, 1σ, confidence intervals for each data point plotted, calculated by assuming the crater populations are Poisson distributed. The 1σ is approximated by using $N = \pm \sqrt{N}$ where N is the number of craters (Arvidson et al., 1978).

area based on the abundance of large (> 20 km) impact craters (Fig. 8). The cratered plateau material is characterized by many flat-floored, degraded and partly buried c_1 and c_2 impact craters. Craters of c_3 age and younger are superposed on the cratered plateau surface. The age of the material forming the cratered plateau surface and burying the older craters must, therefore, be older than the craters of c_3 age. The lithology of these deposits is unknown but may comprise thin volcanic lava flows and eolian material.

Processes of eolian deposition and erosion appear to be currently active. Dark material commonly occurs on the floors of larger craters, and in a few places the dark material seems to have been blown out of the crater interior, forming a dark plume downwind from the crater. Light streaks of light material also are present but are less common.

Several small sinuous channels occur on the cratered plateau surface (Fig. 9) and are included on Carr and Clow's (1981) global-distribution map. These authors use the term "valley networks" for these features. Pieri (1980) suggested that these features may imply immature drainage from restricted source regions as a result of mobilization of volatile material in the subsurface, e.g., through sapping or seepage from permeable strata.

Shultz and Glicken (1979) used the term "floor-fractured crater" to describe impact craters, commonly found along the plateau-plains boundary, that have apparently been heavily modified by processes restricted to the crater interiors. Several of these modified craters occur on the cratered plateau in MC-4 (Fig. 10). Because modification occurs only in certain

Figure 9. Small channels on cratered plateau. (a) Dendritic network of channels (large arrow) associated with rim material of the large c_2 craters near the plateau-plains boundary; small trough along the rim of old c_1 crater indicated by arrow; small c_4 craters occur with or without central peaks; several north-northeast trending ridges occur on the cratered plateau; compare the texture of the smooth plains (ps) and the cratered plateau (plc); see Figure 11 for regional setting; image artifacts occur along the eastern and western margins of the image; Viking frame 218S20 (36.4°N, 8.5°W).

(b) Sinuous channels at plateau-plains escarpment; channels on cratered plateau (plc) indicated by arrows; northeast channel discontinuous, partially covered in one area by small impact crater; channel originates from circular depression; irregular rimless depressions that may be thermokarst features occur on cratered plateau; knobby material (k) occurs on smooth plains (ps); image artifacts occur along east and west margins of the image; Viking frame 205A02 (30.9°N, 14.7°W).

a.

b.

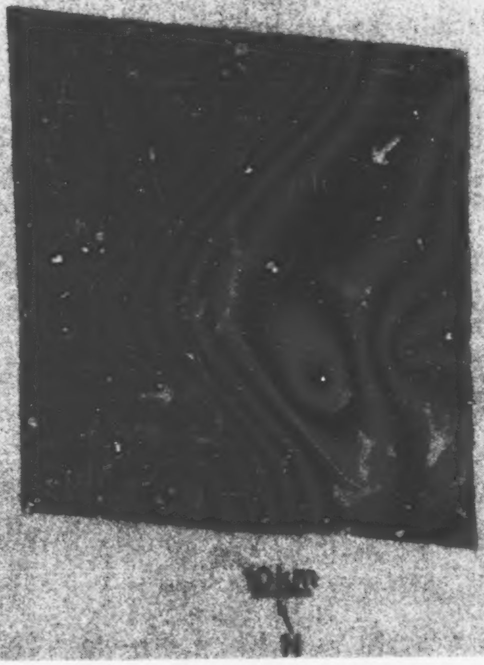

Figure 10. Floor-fractured crater on cratered plateau. See Figure 11 for regional setting; compare the floor morphology of the 20 km diameter c_1 floor-fractured crater in the center of the mosaic and the larger c_1 crater only partially shown along the western margin of the image with smaller c_1 craters to the west; small bowl-shaped c_4 crater occurs just south of the floor-fractured crater; note the three smaller (10 km diameter) craters north of the floor-fractured crater; a rim is still visible on the crater farthest south, whereas the two craters to the north exhibit only faint circular outlines; angularity of some crater outlines, e.g. western-most c_1 crater that is only partially shown, may be result of regional fracture pattern; low ridges and faintly visible irregular depressions (small arrows) give the intercrater surface a rough appearance; small sinuous channel indicated by the large arrow; image artifact occurs along the eastern margin of the mosaic; Viking frames 216S06, 218S19, 218S21 (35°N, 8.5°W).

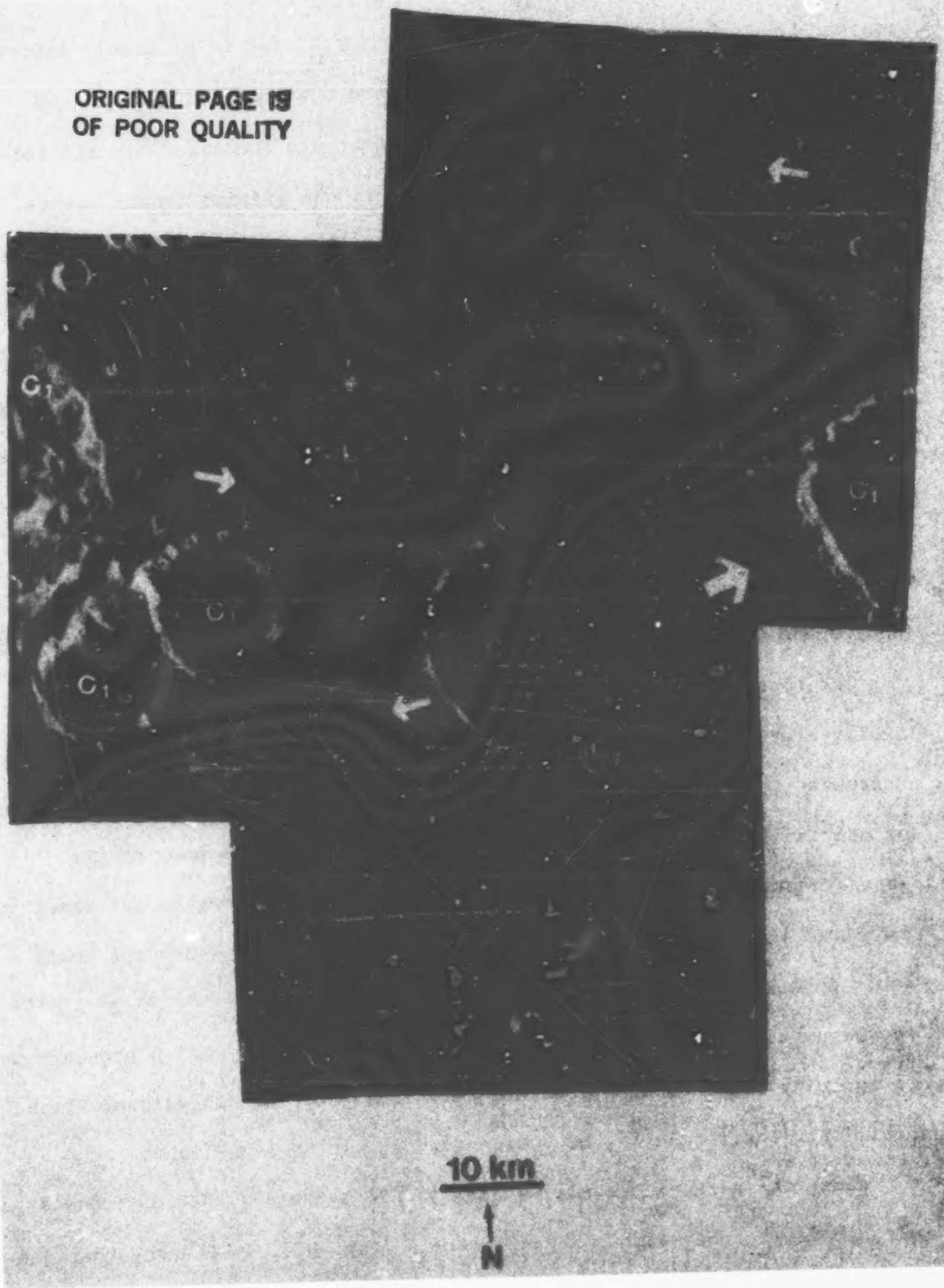
C1
C1
C1
C1
C1
10 km
N

craters in a given region (Fig. 10) and affects craters of widely different formation ages, Shultz and Glicken suggested that modification of the craters is directly related to processes that are localized beneath certain crater floors and not necessarily related to the initial impact events. They suggested that these craters are sites of localized intrusions; the injection of the intrustion is assumed to lift the crater floor and cause fracturing and slumping of the wall material. During advanced stages of intrusion, concentric grabens surrounding the floor and polygonal fractures in the central floor plate may form. Heat released by the intrusion beneath the brecciated zone of the impact crater could thaw permafrost resulting in the release of water or vapor through the fractures. This release of water may result in further surface deterioration and modification (Shultz and Glicken, 1979).

The boundary between the heavily-cratered plateau material and the lightly-cratered, smooth plains is varied. In the southern region, an escarpment several hundred meters high characterizes the boundary. There are many small channels, fractures, and irregular depressions on the plateau near the escarpment (Fig. 9b). These features may be the result of removal of water ice trapped in the plateau layers. This removal would result in collapse depressions and in scarp retreat. Franke et al. (1981) have begun a survey of slope features along the plateau-plains boundary and are applying standard equations and techniques for the analysis of slope stability. Their results, however, have not yet been published.

Along the northern boundary, dark plains materials that may consist of volcanic flows embay old c_1 and c_2 craters (Fig. 11), indicating that the boundary in this region may be partly depositional. Numerous mesas and knobs, interpreted as erosional remnants of plateau material, occur along the entire plateau-plains boundary, indicating that the plateau material may have, at one time, covered much more of this region. Scott (1978) reported that, in many areas along the plateau-plains boundary, lava flows of the lowland plains embay older highland rocks, and remnants of the highland surface project as islands above the lava-covered plains. From the data of the Great Escarpment of Basutoland Plateau in Africa, Scott (1978) extrapolated a 0.16 cm/yr rate of scarp retreat for the martian escarpment. Scott estimated that a minimum of 200 million years would have elapsed between the beginning of lateral erosion of the highlands and the extrusion of lava in the lowlands.

Dissected and Fractured Plateau Material.--The dissected and fractured plateau material covers a small area in the center of the quadrangle. The plateau surface is smooth and is cut by a number of fractures and troughs that commonly trend north-south. This region was mapped in detail, and the geologic map is included as Appendix II. Only a few impact craters occur on the areally restricted plateau surface, thus crater statistics for relative age determination would be unreliable.

The remnants of degraded impact craters occur along the southern margin and are commonly embayed by dark plains materials (Fig. 12). The lack of ejecta or crater rims associated with these crater forms suggest that they were partially buried or that erosional stripping has left only the circular depressions. The plateau may consist of light eolian material

Figure 11. Cratered plateau - smooth plains boundary. (a) Compare the number of craters and the surface roughness of the cratered plateau (plc) and the smooth plains (ps); smooth plains materials embay the three large (40 km diameter) craters in the center of the image; knobby material (k), thought to be erosional remnants of the cratered plateau, can be seen scattered across the smooth plains in the northwest portion of the image; several of the intermediate-size craters in this region have linear sections of walls that may reflect a regional fracture pattern; the area shown in Figure 9a is delineated by the box; the floor-fractured craters shown in Figure 10 are indicated by arrows; image artifacts occur along the eastern and western margins of the image; Viking frame 561A07 (36.9°N, 11.0°W). (b) Schematic cross-section showing the smooth plains - cratered plateau boundary from A to A'.

a.

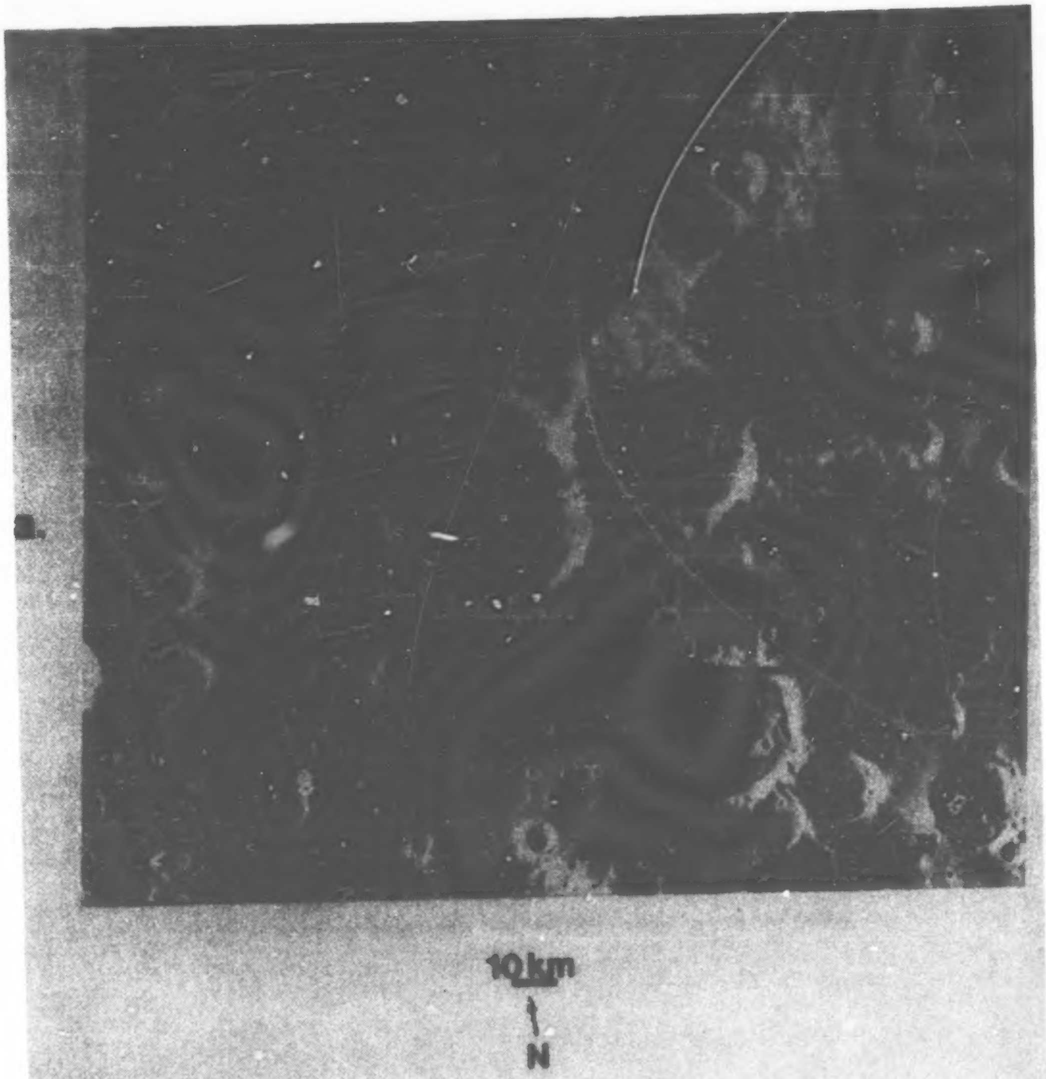

b.

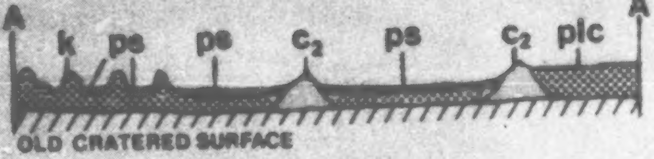
A
k
ps
ps
c_2
ps
c_2
plc
A′
OLD CRATERED SURFACE

Schematic Cross-Section
Large Vertical Exaggeration

ORIGINAL PAGE IS
OF POOR QUALITY

Figure 12. Dissected and fractured plateau material. Numerous fractures and troughs trend north, northwest, and northeast; patterned, and subdued patterned mottled plains materials (pmp, pmps) surround this isolated remnant of dissected and fractured plateau material (pldf). The small arrows indicate areas where subdued patterned mottled plains materials have filled depressions in the plateau. The two large circular depressions in the lower left corner may be old impact craters; small dome with summit knob (large arrow) occurs in the center of low-albedo material on the dissected and fractured plateau; knobby material (k) occurs to the north, east, and south of the plateau; image artifact occurs along eastern margin of image; Viking frame 670B16 (48°N, 24.5°W); for a more detailed map and cross-section, see Appendix II.

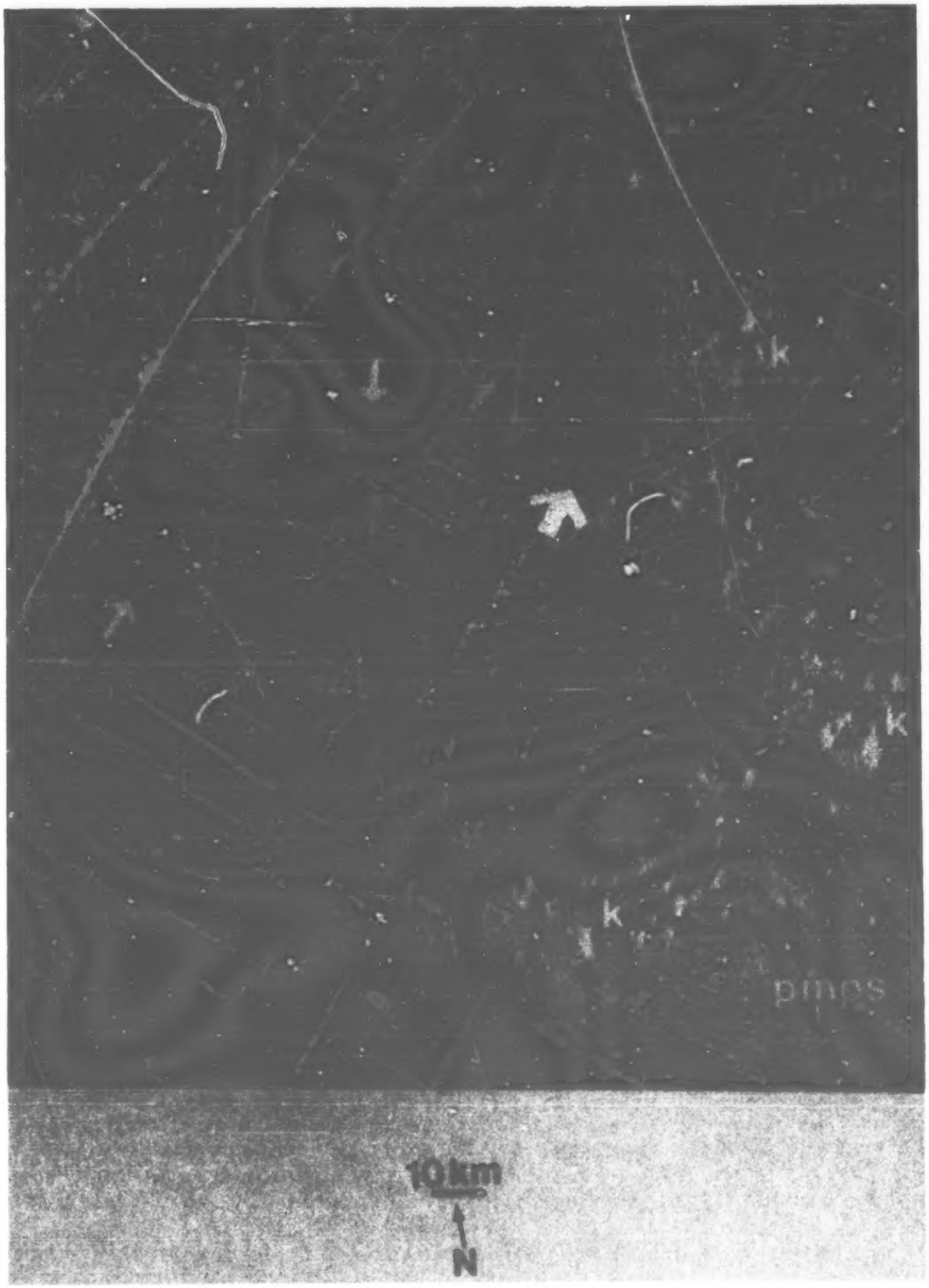
k
k
k
pmps
10 km
N

blanketing an older, cratered surface.

Along the northern boundary, there is a large region of knobby terrain; the knobs are interpreted as erosional remnants of a higher surface. Plains materials overlie and embay fractures and depressions in the plateau along the eastern and western boundaries. An escarpment marks the plateau boundary to the south. The knobs and isolated plateaus that occur near this escarpment are erosional remnants of plateau material.

Igneous processes have been active in this central region as indicated by the presence of several lava flows, a number of small domes with summit craters, and structures that have been interpreted by Allen (1979b) as tablemountains produced by volcanic eruptions beneath an ice sheet. The fractures that cut the plateau may, in some way, be tectonically related to this pulse of igneous activity. Alternatively, they may be the result of more regional stresses.

Rugged Plateau Material.--The rugged plateau material covers a large portion of eastern Tempe Plateau. The unit is characterized by many degraded flat-floored c_1 craters and crater ghosts. The intercrater area is rough, with many irregular scarps (up to 0.5 km in height), channels, and depressions (Fig. 13). Crater statistics (Fig. 8) indicate that the surface is older than the associated ridged or fractured plateau material but may be slightly younger than the cratered plateau material in the southeast corner of the quadrangle. The unit is interpreted to be volcanic and eolian material that has resurfaced the old, heavily-cratered terrain, leaving exposed only the partially buried outlines of the larger craters. The region was subsequently disrupted by faulting.

Based on Mariner 9 data, a large volcanic center was recognized along the western border of Mare Acidalium quadrangle (Underwood and Trask, 1978) and the eastern boarder of Arcadia quadrangle (Wise, 1979). The radial etched-mountain material was described by Wise (1979) as radial, flat-bottomed, bifurcating, discontinuous valleys interspersed with steep-walled closed depressions and was interpreted as basaltic flows from a major volcanic center. High-resolution Viking images show that the radial channels do not extend into Mare Acidalium quadrangle, and thus the materials in this region are mapped as rugged plateau material.

Gatto and Anderson (1975) pointed out the similarity between the rugged intercrater region and terrestrial thermokarst topography. Thermokarst is produced by the melting of ground ice and accompanying collapse of the ground surface. On Earth, thermokarst topography consists of pits, dry gullies and valleys, small hummocks and closed depressions (Fairbridge, 1968). Gatto and Anderson (1975) suggested that the water produced during melting of ground ice continued to flow, forming the "stream" channels that are seen in the area. Subsequent wind erosion may have enlarged some of the depressions.

Other distinctive features of the rugged plateau surface are the circular structures with unusual interior morphology, that appear to be old, degraded impact craters. Several of these flat-floored depressions have an annular moat just inside the rim wall; other irregular depressions

Figure 13. Rugged plateau material. The numerous irregular escarpments and depressions give the surface a rugged appearance; lettered bars indicate locations of topographic profiles shown in Figure 14; compare the interior morphology of the craters indicated by the lettered bars with the crater interiors seen in some of the other figures or with the c_3 crater seen in the southwest corner of the image; most of the craters seen on the rugged plateau have interior moats, although none of the crater interiors is exactly alike; small crater occurs in center of larger crater at A-A'; the channel-like depressions in the center of the image that may be somewhat radial to the circular mound at D-D' have been interpreted as thermokarst features; other irregular depressions on the rugged plateau may also be thermokarst depressions; the large circular mound shown at D-D' has been interpreted as a possible volcanic center (Scott, personal communication, 1981); ghost crater occurs to the east of the mound; small, unusual mesas (arrows) occur in the northern region; one of the mesas has an elongate summit depression; knob (k) may be volcanic intrusion or more resistant remnant of an underlying unit. Northeast trending fracture system occurs in the central region; mare-type ridges occur in the southeast corner of the mosaic; Viking frames 704B38-39 (45°N, 56.5°W).

C-4

ORIGINAL PAGE IS
OF POOR QUALITY

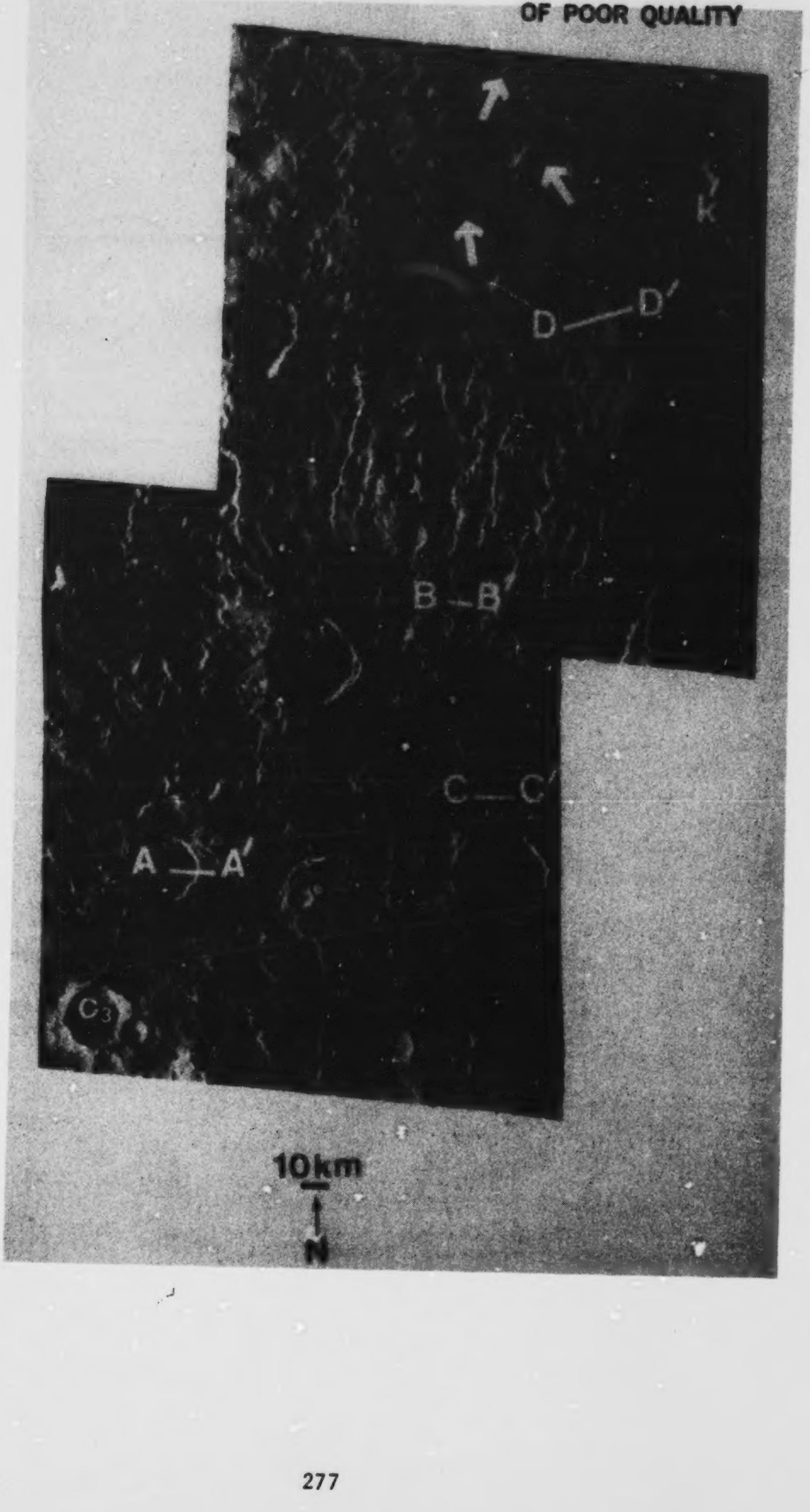
K
D
D′
B
B
C
C′
A
A′
C₃
10km
N

ORIGINAL PAGE IS
OF POOR QUALITY

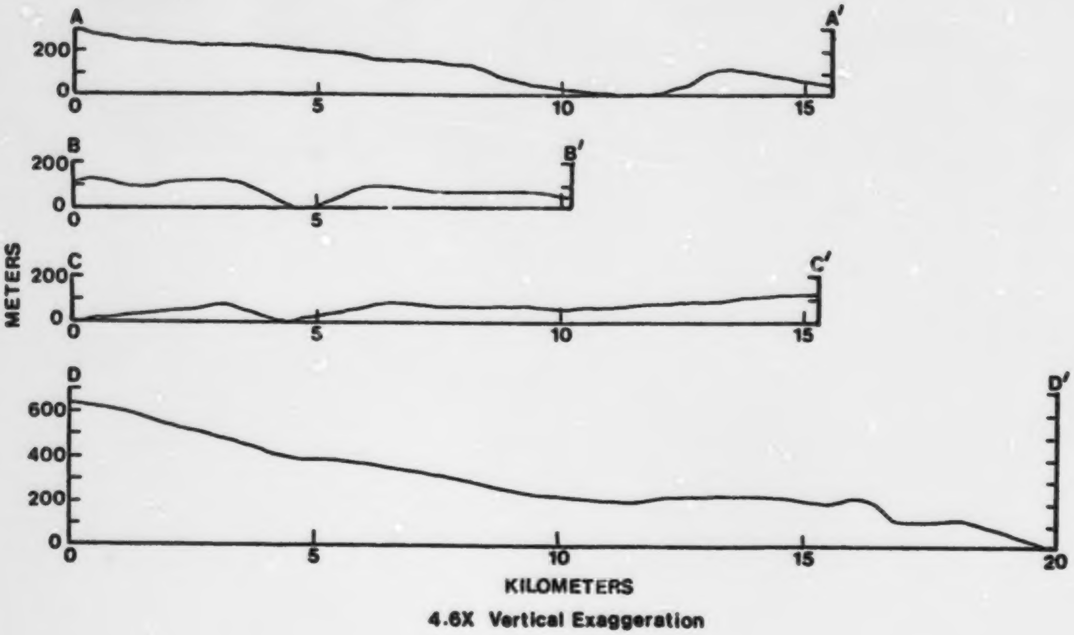

Figure 14. Relative-height profiles of crater forms shown in Figure 13. The profiles are constructed by computer from a program developed to extract topographic data directly from the Viking orbiter digital-image files. From Davis et al. (1981).

contain circular ridges. Figure 13 shows examples of these unusual features. Relative-height profiles of three "moat" craters were plotted by Davis et al., (1981) and are shown in Figure 14a-c.

The circularity of these features strongly suggests that they are impact craters; the lack of sharp crater rims or ejecta blankets indicates later resurfacing or exhumation. The unusual morphology may be related to the target material. Roddy (1977) reported complex internal structure, including moat-like topography, from explosion experiments in unconsolidated alluvium overlying water-saturated clays. Alternatively, Fagen et al. (1981) suggested that these circular depressions result from surface subsidence rather than from impact onto the surface. These authors proposed that either the entire central region sank downward as one mass along fracture lines, or the central region broke into a number of small segments which eventually deteriorated leaving the depression. They do suggest, however, that the location of the collapse depression may depend on the existence of the impact craters and other topographic features of a more ancient terrain that underlies the plateau strata.

A large (40 km) circular feature with positive relief also occurs in this region, and a profile was produced by Davis et al. (1981) (Fig. 14d). Scott (personal communication, 1981) suggested that this feature may be the remains of an ancient volcanic center similar to the radially etched mountain material in MC-3 (Wise, 1979). Another alternative is that the feature is an exhumed, filled impact crater.

The boundary between the rugged plateau and the smooth plains is varied. To the south, the boundary is marked by a steep escarpment. This escarpment may partially be a result of fluvial erosion associated with Kasei Vallis. Farther to the north, the boundary appears to be depositional; smooth plains material overlies the plateau material, embaying or completely burying old craters. The boundary of the rugged plateau material with the other smoother plateau units is morphologically distinct.

Ridged Plateau Material.--The ridged plateau material occurs in the southern region of Tempe Plateau in MC-3 (Wise, 1979) and MC-4. This unit forms a relatively smooth surface with many north-northwest trending mare-type ridges (Fig. 15a, b). The crater size-frequency distribution curve for the ridged plateau material (Fig. 8) indicates that this unit is younger than the adjacent rugged plateau material and the cratered plateau material in the southeast corner of the quadrangle. The ridged plateau, however, may be similar in age to the fractured plateau material to the north inasmuch as their crater-density plots are similar.

A possible flow front occurs on the ridged plateau surface near the boundary with the rugged plateau terrain (Fig. 16a). Other flow fronts have been reported on the ridged plateau surface in MC-3 (Fig. 16b) (Wise, 1979). These features led to the interpretation of this material as volcanic flow rock.

Many north-northwest trending mare-type ridges occur on this ridged plateau surface. Mare ridges were first observed on the Moon and were defined as broad, elongate arches or swells associated with narrower, steeper crenulated ridges or spines (Strom, 1972). Individual ridges on Mars may be as long as several hundred kilometers, ranging in width from 1-20 km, and as high as several hundred meters (Gifford, 1981).

The origin of mare ridges remains controversial. The two general hypotheses advanced to explain the origin of these ridges on the Moon involve igneous processes that produce such features as plutons, pressure ridges, squeeze-ups of lava, and fissure eruptions (Strom, 1972; Quaide, 1965; Hodges, 1973), or tectonic processes, such as faulting or folding (Lucchitta, 1976, 1977; Sharpton and Head, 1980; Howard and Muehlberger, 1973). The controversy is similar for Mars. From studying the mare-type ridges in Chryse Planitia (directly south of Acidalia Planitia), Greeley et al. (1977) favored the volcanic origin for the mare-type ridges because of their association with plains of volcanic origin and because none of the mare-type ridges truncated impact craters as would be expected if the ridges were tectonic. Alternatively, Lucchitta and Klockenbrink (1981) and Gifford (1981) found that the planet-wide trend of the ridges is predominantly north-south and concluded that the ridges were tectonic.

Although many mare-type ridges in MC-4 occur on the ridged plateau unit, they are not restricted to this unit. Some of the ridges extend into the rugged plateau material, a few ridges occur on the smooth plains, and one ridge can be traced across the higher ridged plateau unit and the lower smooth plains (Fig. 15b). This tends to support a tectonic origin for the ridges in this region. The occurence of the ridges on both plateau and plains material indicate that the ridges were formed after the development of the highlands-lowlands boundary.

ORIGINAL PAGE IS
OF POOR QUALITY

Figure 15. Ridged plateau material. (a) High-resolution image showing several mare-type ridges; the ridges are asymmetric, with steeper flanks to the east, lunar mare ridges are commonly asymmetrical (Lucchitta, 1976); ridges trend approximately north-south; several of the small (< 1 km diameter) craters have distinct, high-albedo wind plumes indicating that the winds are from the east; image artifacts occur along the eastern and western margins of the image; Viking frame 668A06 (34.7°N, 58.7°W).

(b) Mare-type ridge cutting across the plateau-plains boundary (arrow); the difference in topographic expression of the ridge between the plateau (plr) and the smooth plains (ps) may be a function of material strength; the effects of differential erosion are apparent i.e. the ejecta blanket of the large c_3 impact crater in the center of the image is only visible on the plateau; the crater rim is particularly resistant to erosion; dark patches, interpreted as eolian material, are confined to low-lying areas on the upwind side of scarps and on the floor of the large crater (the wind is from the north-northeast); image artifacts occur along the eastern and western margins of the image; Viking frame 558A34 (34.6°N, 52.5°W).

ORIGINAL PAGE IS
OF POOR QUALITY

a.

b.

Figure 16. Flow fronts on ridged plateau. (a) Numerous flow fronts (arrows) on the ridged plateau (plr) along the boundary with the rugged plateau (plrg); fresh, bowl-shaped c_4 crater with radial, ballistic- and flow-ejecta deposits occur in the center of the image; knobby material (k) occurs in the northern portion of the image; relict crater indicated with large arrow; image artifact occurs along the western margin of the image; Viking frame 668A10 (33.9°N, 56.9°W).

(b) Flow fronts on the ridged plateau in MC-3; well-defined flow lobe are indicated by arrows; large impact craters at the top of the image obscure possible source areas for the two flows; both flows have been cut by en echelon grabens trending northeast-southwest; a few mare-type ridges can be seen in the southern region; Viking frame 704B58 (37.5°N, 65.6°W).

b.

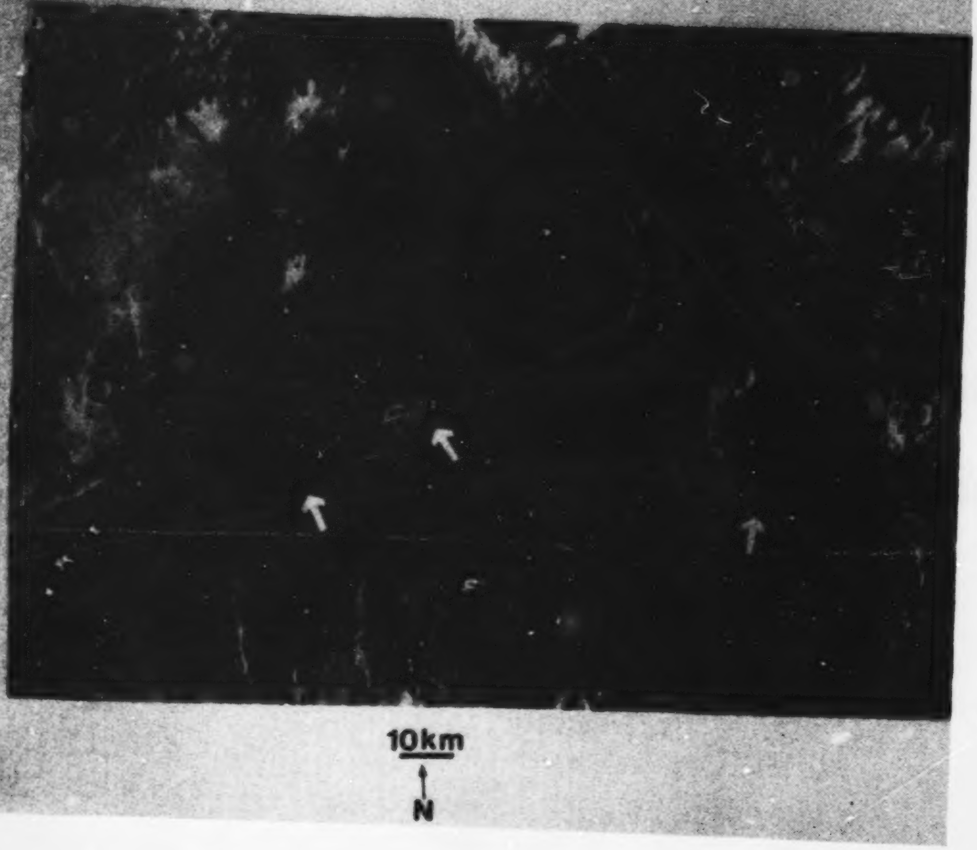

The boundary between the relatively smooth ridged plateau material and the rugged plateau material is fairly distinct. Volcanic flow rock of the younger ridged plateau surface may have completely buried the older, rugged plateau surface. To the south, the ridged plateau - smooth plains boundary is erosional, with an escarpment separating the higher plateau material from the lower smooth plains. North of latitude 37°N, the boundary appears to be depositional with smooth plains material overlying and embaying grabens cut into the ridged plateau material. In some areas, a small channel filled with light, possibly alluvial material lies along the plateau-plains boundary (see Appendix I; see also Fig. 37).

Fractured Plateau Material.--Fractured plateau material occurs along the northern edge of Tempe Plateau in MC-4 and extends south and west into MC-3 (Wise, 1979). The unit forms a relatively smooth surface interrupted by numerous northeast-trending horsts and grabens. Individual troughs range in width from 1-10 km and are as long as 200 km. The grabens cut older c_1 and c_2 craters, but do not cut younger c_3 and c_4 craters. The crater size-frequency distribution curve for the fractured plateau material (Fig. 8) indicates that the unit is younger than the adjacent rugged plateau material but may be equivalent in age to the ridged plateau material to the south.

Wise (1979) suggested that the fractured uplands (fractured plateau material) consists of lava rock similar to the Lunae Planum material (ridged plateau material) to the south. The material that makes up the fractured plateau is interpreted in the present study to be volcanic and eolian material that was later disrupted by faulting.

The fractures in this region cut all but the freshest impact craters indicating that the fractures are relatively recent features. To the west in MC-3, the faults extend north into the plains material. In MC-4, however, the fractures terminate at the plateau-plains boundary. Regionally, the fractures of the Tempe Fossae system are part of the semiradial fault system of the Tharsis province. This fault system may reflect an extensive zone of deep crustal weakness (Wise, 1979).

The boundary region between the fractured plateau material and plains material was mapped in detail and is included as Appendix I. Rim walls of degraded and embayed craters form the plateau-plains boundary in several places. Grabens that cut into the higher plateau surface terminate at the plains boundary and are also embayed by smooth, dark plains material.

A sinuous channel, oriented normal to the fracture trend, is cut into the plateau material (Fig. 17). In the same area, other sinuous channels within a graben deposited outwash or flood plain material onto the plains (Fig. 17). This indicates that there was drainage and a redistribution of material from the plateau.

Lower Plateau Material.--The lower plateau material occurs in small patches along the southeast margin of Tempe Plateau. This unit forms a rough surface at an elevation intermediate between the lower smooth plains material and the higher ridged or rugged plateau material (Fig. 18). A

Figure 17. Fractured plateau material. Boundary region between fractured plateau (plf) and smooth plains (ps); large (17 km wide) graben that cuts into the plateau trends northeast across the southeast corner of the image; smooth plains materials cover the floor of this large graben; debris also appears to bury fractured plateau material to the west of the large graben; smaller faults occur within the large graben; small arrows indicate smaller grabens cutting the fractured plateau; a sinuous 3-4 km-wide channel extends across the western portion of the image; the light-colored fan-shaped material (large arrow) on the smooth plains, has been interpreted as outwash or flood plain material from drainage of the plateau; compare the differences in the preservation of the craters and ejecta on the fractured plateau and on the smooth plains; especially note the c_3 flow-ejecta crater in the northern part of the image; Viking frame 61B52 (53.1°N, 60.5°W); for a more detailed map, see Appendix 1.

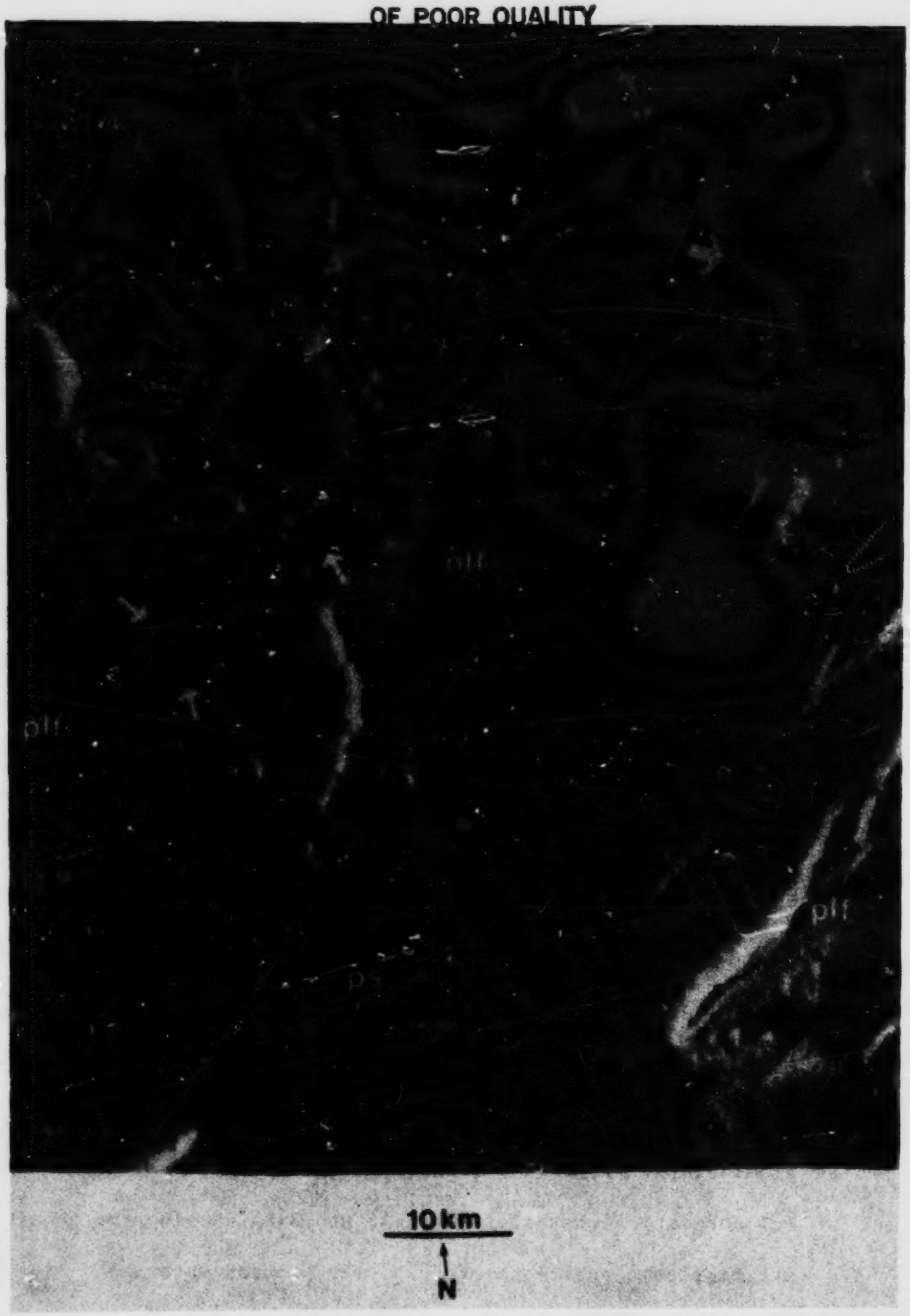
plf
plf
plf
ps
10 km
N

Figure 18. Lower plateau material. (a) Lower plateau material (pll) at southwest margin of Tempe Plateau is bounded by higher rugged plateau material (plrg) and lower smooth plains material (ps); the lower plateau material appears to underly stratigraphically the rugged plateau material; alternatively, the lower plateau material here may be a down-faulted block of rugged plateau material; the dark patches on the smooth plains are thought to be eolian accumulations; notice that the ejecta blanket of the c_4 crater in the southeast corner of the image has been partially stripped away; image artifact occurs along the eastern and western margins of the image; Viking frame 558A17 (31.5°N, 55°W). (b) Lower plateau material (pll) is shown in relationship to smooth plains material (ps) and an isolated remnant of ridged plateau material (plr); lobate flows of lower plateau material appear to embay a circular depression on the ridged plateau (arrow) indicating that the lower plateau material is a younger, possibly volcanic flow unit; compare the surface roughness of the lower plateau material with that of the smooth plains; north-south ridge is truncated by lower plateau material just west of isolated remnant of ridged plateau material; image artifacts occur along the eastern and western margins of the image; Viking frame 668A27 (31.1°N, 49.6°W).

(c) Schematic cross-sections A-A' and B-B' showing two possible stratigraphic positions of the lower plateau material.

ORIGINAL PAGE IS
OF POOR QUALITY

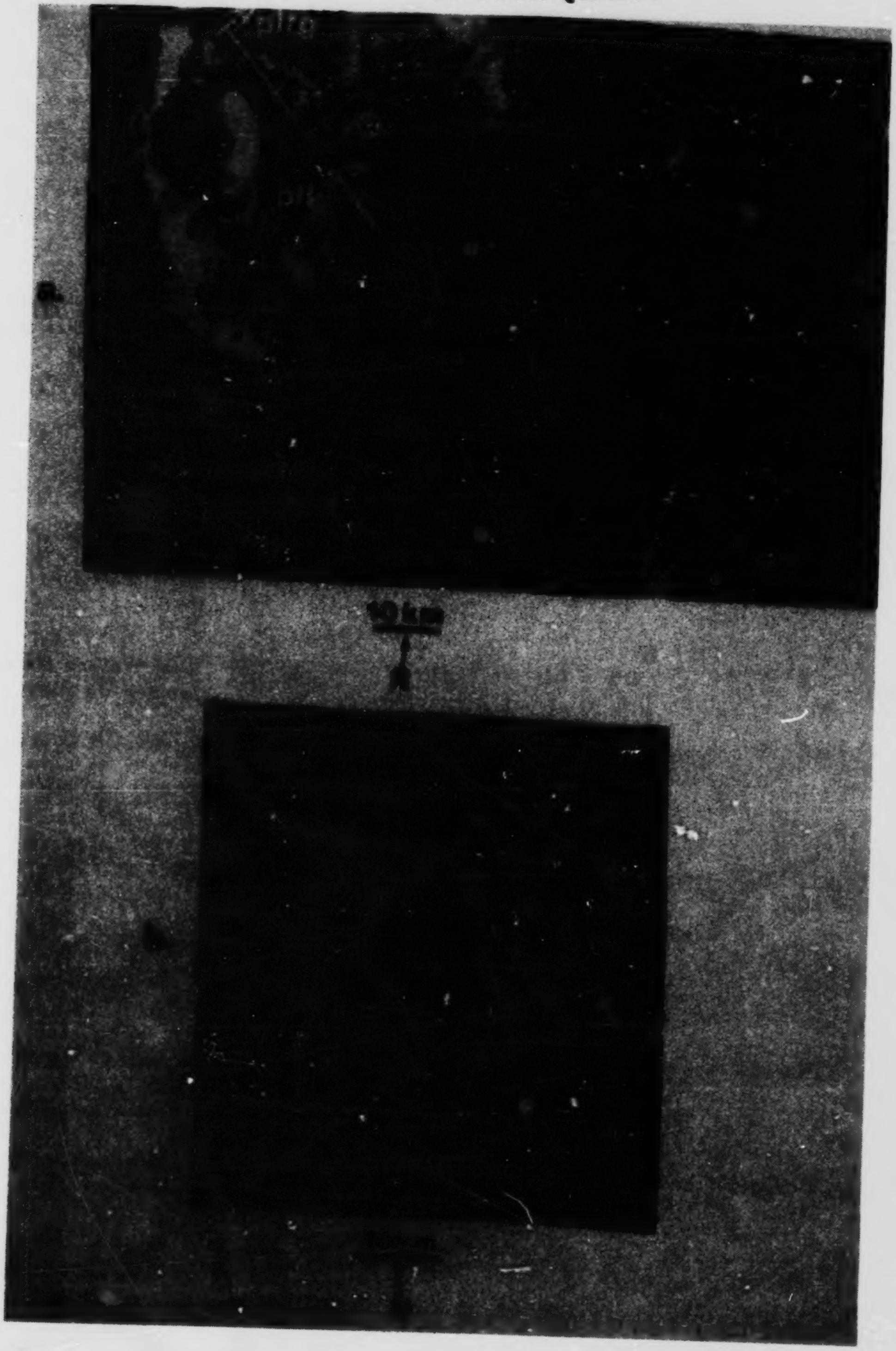

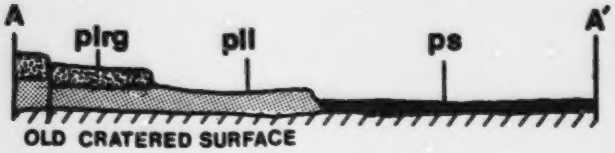
A
plrg
pll
ps
A'
OLD CRATERED SURFACE

Lower Plateau Material Older Than Smooth Plains Material

C. **Schematic Cross-Sections
Large Vertical Exaggeration**

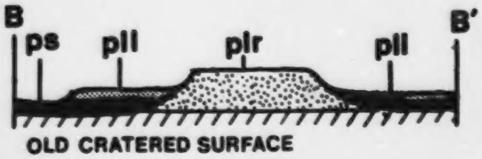
B
ps
pll
plr
pll
B'
OLD CRATERED SURFACE

Lower Plateau Material Younger Than Smooth Plains Material

few c_3 and c_4 impact craters (< 10 km) occur on this surface indicating that it is relatively young.

Exposures of lower plateau material, such as that seen in Figure 18a, indicate that stratigraphically the lower plateau material underlies the other plateau materials and has been exposed by erosion and scarp retreat. Other areas (Fig. 18b) show lower plateau material embaying a circular depression in the higher ridged plateau material, indicating that some of the lower plateau material was emplaced after the highlands-lowlands boundary developed and was subsequently modified by erosion.

In several places small channels cut the lower plateau material, creating streamlined remnants up to 40 km long trending east-northeast (Fig. 19). Aqueous erosion is indicated by the presence in these channels of streamlined landforms.

The main channels of Kasei Vallis occur to the south and west between latitude 20° - 30°N, longitude 50° - 75°W (Fig. 1). Kasei Vallis has been interpreted as the site of catastrophic floods of great depths and high velocity (Baker and Milton, 1974; Baker and Kochel, 1979). The erosional and depositional effects associated with running water in Kasei Vallis appear to have extended into the southwestern region of MC-4 (Scott and Tanaka, 1980; Carr and Clow, 1981).

Plains Province

Lowland plains material covers approximately 80 percent of the area of MC-4. On the basis of Mariner 9 data, Underwood and Trask (1978)

Figure 19. Streamlined remnants of lower plateau material. Channels that cut into lower plateau material (pll) created streamlined landforms such as those seen in the southwest corner of the image; large arrows indicate possible fluvial bars or erosional grooves; the ejecta of a c_3 crater on the lower plateau has been partially stripped away; isolated remnants of ridged plateau material (plr) surrounded by smooth plains material (ps) do not appear to be streamlined; in many places, escarpments bounding the ridged plateau are linear and may be structurally controlled; dark material accumulates on the upwind sides of many topographic obstacles; light streaks associated with several of the small craters indicate that the wind is from the north-northeast; a continuation of the mare-type ridge seen in Figure 15b is indicated by the small arrow in the northeast corner of the image; image artifact occurs along the western margin of the image; Viking frame 558A15 (32.2°N, 52°W).

ORIGINAL PAGE IS
OF POOR QUALITY

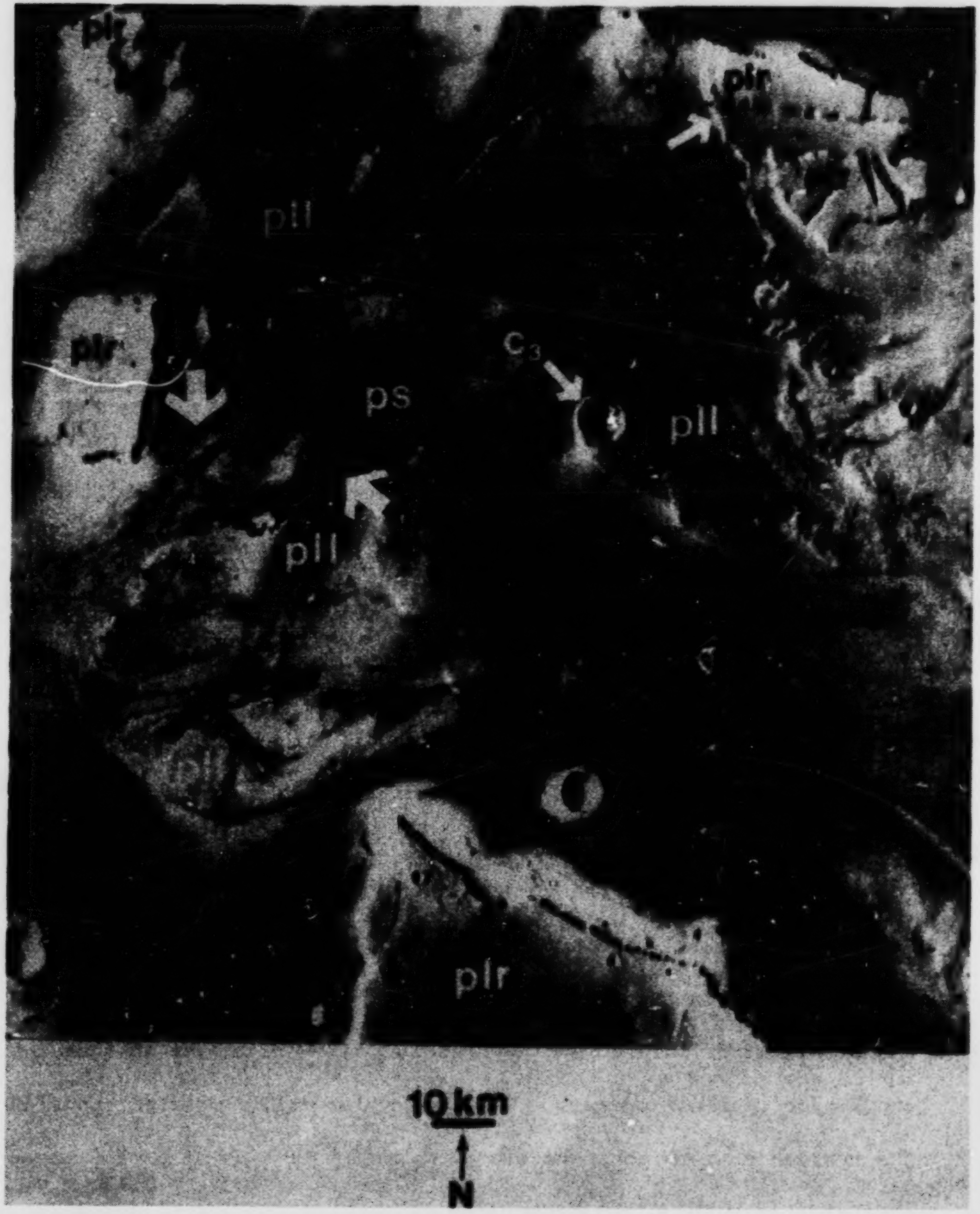
plr
plr
pll
plr
ps
c3
pll
pll
pll
plr
10 km
N

subdivided the lowland plains into three basic geologic terrain types: mottled plains material, plains material, and plains and dissected plateau material - undivided. Results from the present investigation using Viking data indicate that nine subdivisions can be recognized within these lowland plains. Wherever possible, the descriptive modifiers used by Underwood and Trask (1978) were incorporated into the names of the units in the present investigation. These units are: mottled plains material - undivided (991,000 km^2), hummocky mottled plains material (386,500 km^2), patterned mottled plains material (458,200 km^2), subdued patterned mottled plains material (37,000 km^2), fractured plains material (23,000 km^2), knobby plains material (193,000 km^2), smooth plains material (1,162,400 km^2), patterned smooth plains material (60,000 km^2), and variegated plains material (128,000 km^2).

Mottled Plains Region.--The mottled plains extend almost entirely around the planet between latitudes 50° - 70°N (Scott and Carr, 1978). The term "mottled plains" was first used by members of the Mariner 9 imaging team (Carr et al., 1973). Soderblom et al. (1973b), in mapping the geologic terrain of the north polar region, described the mottled cratered plains as characterized at Mariner A-frame resolution ($\cong$ 3 km) by an abundant population of small craters ($<$ 20 km) and a highly mottled appearance. The mottled pattern consists of a complex of streaks of bright material and concentrations of bright material highlighting the interior and exterior parts of crater rims and ejecta blankets. Soderblom et al. pointed out that the mottled cratered plains has a lower average albedo than most of Mars and that it is one of the few regional units intrinsically characterized by its albedo.

The cause of the extreme albedo contrast between the ejecta blankets and the intervening plains is uncertain. Soderblom et al. (1973a) suggested that the bright materials are remnants of the debris mantle that, at one time, buried the mottled plains. Subsequently, the debris has been removed leaving patches of light materials trapped in the coarser-textured parts of the craters, such as their rims and ejecta blankets. High-resolution Viking data have commonly revealed fine detail on some of the ejecta blankets and bright crater rays, similar to those seen on the Moon. These fresh craters show little or no eolian modification, thus, it is difficult to interpret these bright-ejecta patterns as the result of trapped particles. Another explanation that was suggested by Carr (1981) is that impacting meteorites excavated higher-albedo material from below the dark surface.

The mottled plains occur in the northern two-thirds of MC-4. On the basis of variations in surface texture and detail, the mottled plains were subdivided into four units: mottled plains material - undivided, hummocky mottled plains material, patterned mottled plains materials, and subdued patterned mottled plains material.

Mottled Plains Material - Undivided.--The mottled plains material - undivided covers most of the northern region. The unit is characterized by high-albedo zones surrounding many of the impact craters; the intercrater plains have very low albedo. The crater size-frequency distribution of craters $\geq$ 1 km (Fig. 20) indicate that the mottled plains material - undivided may be similar in age to the rest of the mottled plains units. The mottled plains material may consist of volcanic rock and eolian debris.

The western part of the mottled plains is characterized by a distinct northwest-southeast eolian grain. Many light streaks occur downwind from impact craters, and dark eolian material occurs in craters and forms splotches on the intercrater plains. Many of the smaller craters on these plains, north of latitude 45°N, appear to be filled or partially filled with light material (Fig. 21a). Soderblom et al. (1973a) reported that craters filled with light debris are common poleward from 30°N. These authors pointed out that it would be difficult to imagine a process that would fill only the crater interiors, so they suggested that the entire northern region was, at one time, mantled with light-colored debris thick enough to bury the craters. Subsequently, erosion has removed most of this mantle, leaving only materials protected within the crater interiors (Soderblom et al., 1973a).

The Vikings' data generally are superior to those obtained by the Mariner 9 spacecraft. However, the majority of Viking images north of approximately 40° are low- to-medium resolution (220 meters/pixel), equivalent to the Mariner B-frames. Many of the surface details are at the resolution point. One of these surface textures is a reticulate pattern that occurs in the intercrater region (Fig. 21b). It is difficult to determine the topographic

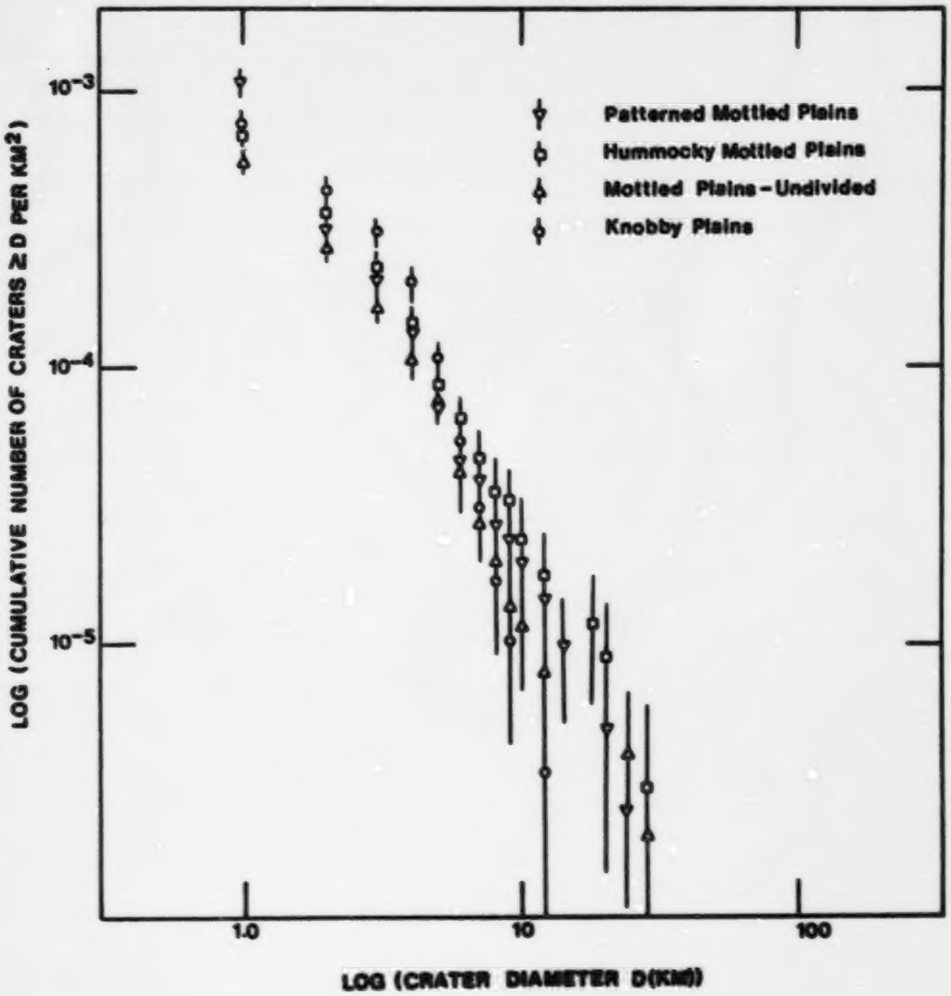

Figure 20. Cummulative crater size-frequency distributions for the mottled plains units and knobby plains. Numbers of craters are cummulated from largest to smallest size; vertical lines indicate one standard deviation, 1σ, confidence intervals for each data point plotted, calculated by assuming the crater populations are Poisson distributed. The 1σ is approximated by using $N = \pm \sqrt{N}$ where N is the number of craters (Arvidson et al., 1978).

Figure 21. Mottled plains material - undivided, example 1.

(a) Low-resolution image of the mottled plains material - undivided; high-albedo ejecta blankets extend outward 2-3 crater diameters and are surrounded by low-albedo plains; the arrows show some of the impact craters with interiors that appear to be filled with light-colored material; the light-colored material is believed to be the remnant of a debris mantle that, at one time, blanketed the northern region (Soderblom et al., 1973a); small-scale patterned ground occurs in the intercrater region; scattered dark hummocks occur in the north-central part of the image; dark streaks occur in the southern portion of the image; the wind is from the northwest; Viking frame 672B74 (60°N, 25.7°W).

(b) Enlargement showing the small-scale detail of the mottled plains material - undivided; faint reticulate pattern of varied scale occurs in the intercrater region; this pattern may be similar to that seen farther south in the patterned mottled plains or the fractured plains; compare the filled or partially filled impact craters in the southwest corner of the image with the fresh bowl-shaped crater indicated by the arrow; the fresh crater also has light-colored ejecta; scattered dark hummocks occur throughout the area; Viking frame 672B76 (60°N, 20.9°W).

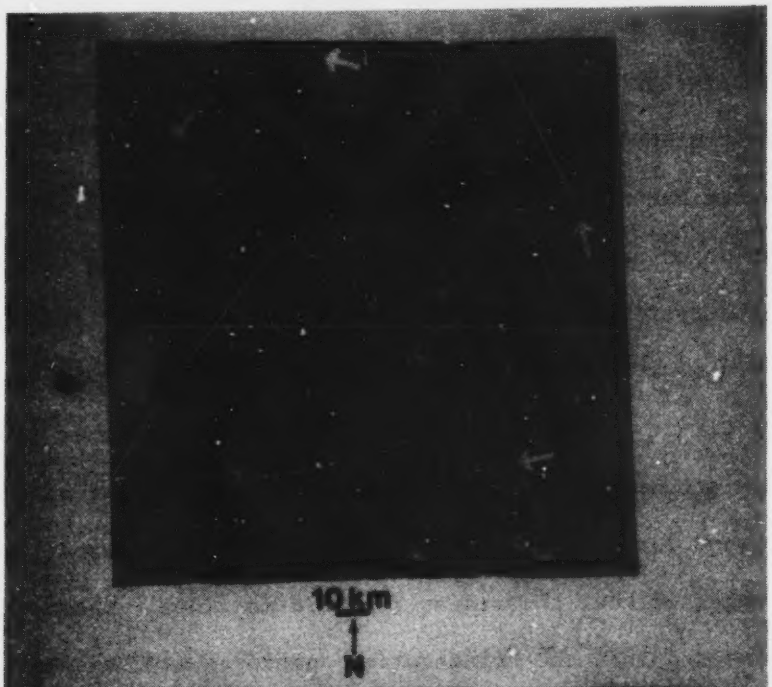
10 km
N

10 km
N

relief of these surface features that have produced this pattern, but it may be similar to that of the fractured plains and patterned mottled plains to the south.

Another pattern that is equally perplexing is a series of concentric arcs that occur near the mottled plains - smooth plains boundary (Fig. 22a). As with the reticulate pattern, the topographic relief cannot be determined. The pattern of arcs vaguely resemble the patterned ground that occurs in MC-5 at latitude 45°N, longitude 354°W. Carr and Schaber (1977) suggested that these arcuate features marked successive positions of the retreat of an escarpment during removal of a former mantle. Alternatively, Lucchitta (1981) suggested that the ridges resemble moraines. Rossbacher and Judson (1981) proposed that the "fingerprint" patterns may be solifluction lobes and ice-cored ridges similar to those observed in the Canadian arctic.

The boundaries with the other mottled plains units are gradational. The mottled plains - hummocky mottled plains boundary is marked by increased numbers of small, dark hills that characterize the hummocky mottled plains. The boundary between the mottled plains material - undivided and the patterned mottled plains has been placed at the first recognition of the polygonal troughs, the detection of which may be a result of resolution. The boundary with the lighter, dissected and fractured plateau material is generally recognized by contrasts in albedo and in morphology. The boundary between the mottled plains and smooth plains is commonly recognized by a textural and albedo variation: to the east, the smooth plains have higher albedo than the mottled plains; to the west, the

ORIGINAL PAGE IS
OF POOR QUALITY

smooth plains have much lower albedo. A narrow, high-albedo line runs along the contact in places (Fig. 22b). To the west, a sinuous channel filled with light material runs along the mottled plains - smooth plains boundary.

Hummocky Mottled Plains Material.--The hummocky mottled plains material occurs along the northern border of MC-4 and extends north into MC-1. Botts (1980) used the name "bulbous plains" for a unit with similar characteristics that occurs at 70°N latitude. The hummocky mottled plains are characterized by many small (< 1 km) dark hills surrounded by lighter-colored material. These dark hills, in combination with high-albedo ejecta blankets, give the surface a mottled appearance (Fig. 23a). The crater size-frequency distribution (Fig. 20) indicates that the hummocky mottled plains may have a slightly greater abundance of large (> 10 km) craters than the other mottled plains units. Because the boundary between the mottled plains - undivided and the hummocky mottled plains is gradational, and because several of these large craters lie in this transition zone, this variation may not be significant. The light material that constitutes most of the surface is interpreted to be eolian. The darker material that occurs in the intercrater plains may be volcanic. Botts (1980) came to a similar conclusion for the origin of the bulbous plains in MC-1.

Similar to the mottled plains material - undivided, the hummocky mottled plains have many craters that are filled or partially filled with light material. There are also several large, fresh craters with high-albedo

Figure 22. Mottled plains material - undivided, example 2.

(a) Faint curvilinear features of undetermined origin can be seen in the center of the image; these curvilinear features are located near the mottled plains - smooth plains boundary; unusual troughs with central ridges are indicated by the arrows; a pedestal crater (p) occurs in the northeast corner of the image; the extreme albedo contrast is a function of image processing; Viking frame 670B30 (43.7°N, 42.8°W).

(b) Boundary between the mottled plains material - undivided (pm) and the smooth plains material (ps) near Tempe Plateau; smooth plains are low albedo in this region; high-albedo line marks the boundary; high-albedo wind streaks associated with some craters indicate the wind is from the northwest; streak formation may be related to the topographic relief of the crater rims; note the narrow trough on the smooth plains (arrow); Viking frame 670B01 (53.1°N, 50.3°W).

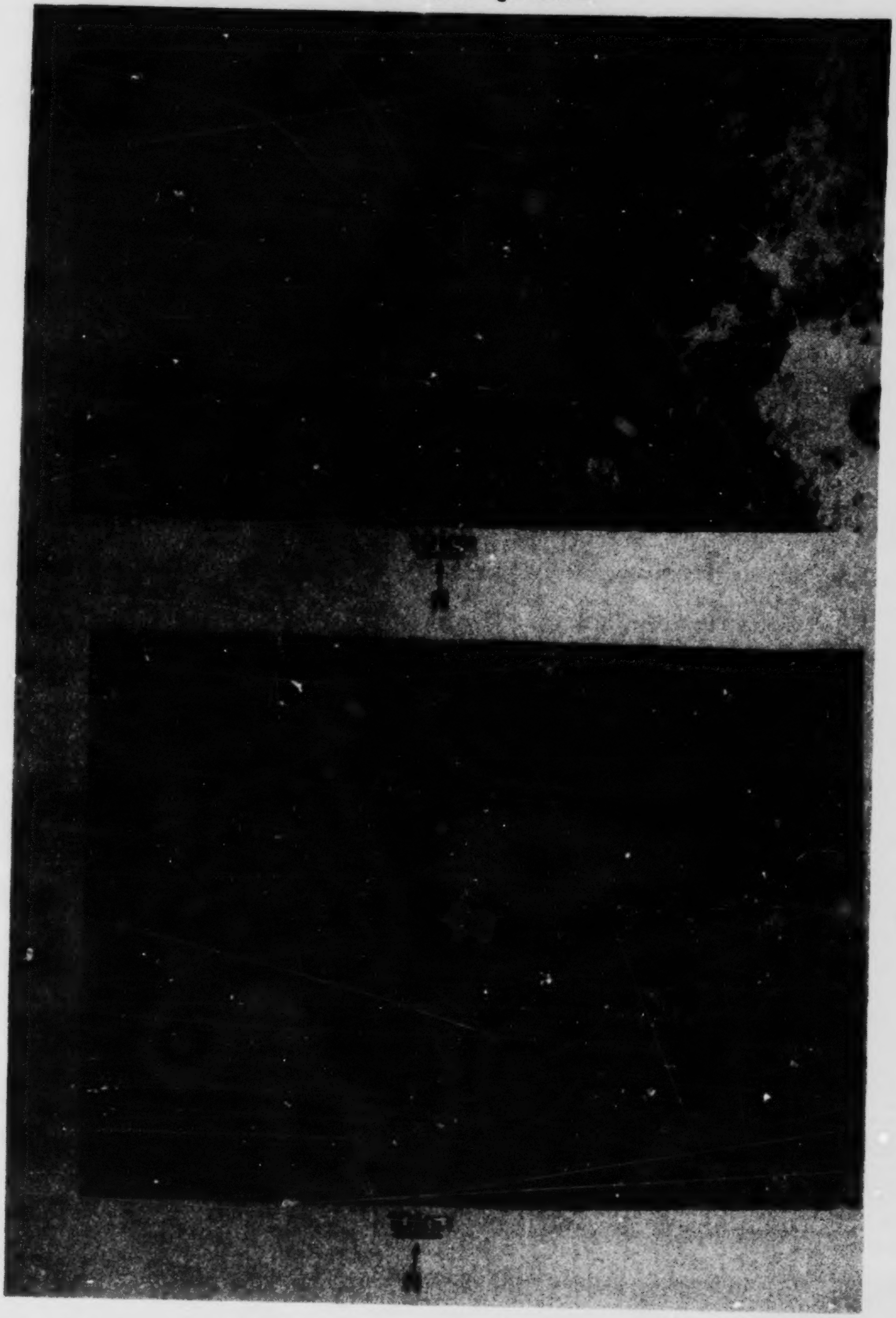

ORIGINAL PAGE IS
OF POOR QUALITY

Figure 23. Hummocky mottled plains material. (a) Dark irregularly spaced hills and knobs are scattered throughout the inter-crater region; the unit has a mottled appearance, with high-albedo ejecta blankets surrounded by low-albedo plains; the craters in the eastern part of the image are filled with light-colored material; the interior of the freshest crater in the northwest corner of the image contains a dark splotch presumed to be eolian material; compare this image with Figure 21a and notice that the eolian grain is not as obvious on the hummocky mottled plains; image artifact occurs along the eastern margin of the image; Viking frame 672B77 (62.7°N, 18.2°W).

(b) Large fresh impact crater on hummocky mottled plains shows little evidence of subsequent modification; two ejecta types surrounding this crater; thin, high-albedo, ray-forming ejecta extends out more than 5 crater diameters and thick flow-ejecta deposits occur close to the crater; compare this crater with the filled craters in the south-east portion of the image; the surrounding plains have a hummocky appearance; some of the dark hummocks appear to have summit depressions (small arrow) and, in places, the hummocks appear to coalesce (large arrow); image artifact occurs along the eastern margin of the image; Viking frame 669B30 (65.9°N, 43°W).

(c) Schematic cross section showing possible origins of the knobs or hummocks on the hummocky mottled plains.

ORIGINAL PAGE IS
OF POOR QUALITY

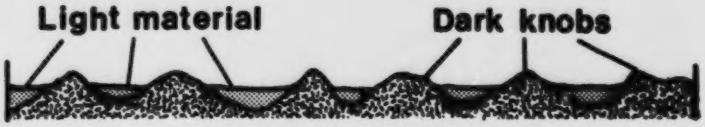
Light material
Dark knobs

C. Schematic Cross-Sections
Large Vertical and Horizontal Exaggeration

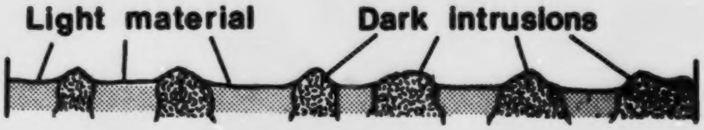
Light material
Dark intrusions

ejecta blankets and rays (Fig. 23b). These larger, fresh craters commonly have deposits of dark material in the interior of the crater. The eolian grain, however, is not as apparent as in the mottled plains region to the south.

The features that characterize the hummocky mottled plains material are the small, irregularly spaced, dark hills and the low albedo crater rims. The knobs may be plutons, volcanic domes, volcanic necks, cinder cones, or permafrost features such as pingos. Alternatively, these knobs may represent a lower hummocky, cratered surface that has been mantled with lighter material leaving only the tops of the dark hills and crater rims exposed. This lower dark unit may or may not be volcanic. The presence of similar dark hummocks or knobs in the large c_2 crater, Lomonosov, weakens the hypothesis that the knobs may be high hills on a hummocky, low-albedo surface largely mantled with lighter material. There are no high-resolution images of this region, so no definite interpretations on the origin of the dark hummocks can be made.

The boundary with the mottled plains material - undivided to the south is gradational. The boundary between the mottled plains material and the lighter knobby plains is based on albedo, which may be the result of a thicker debris mantle covering the knobby plains.

Patterned Mottled Plains Material.--The patterned mottled plains materials cover a large part of east-central MC-4. The unit, as with other mottled plains units, is characterized by high-albedo ejecta blankets that extend out 2-3 crater diameters, surrounded by low-albedo intercrater plains. A polygonal pattern of troughs is superimposed on the low-albedo, intercrater plains. The impact crater density ($\approx$ 1000 craters ≥ 1 km/10^6 km^2) for this unit is slightly higher than that of the other plains units; however, the crater size-frequency curve (Fig. 20) is very similar to the other plains units indicating that there probably is little age variation between the units. The patterned mottled plains material probably consists of dark volcanic material that was subsequently disrupted to form the polygonal pattern of troughs (Fig. 24).

Patterned or fractured terrain occurs over extensive areas of the northern plains and has been the subject of considerable controversy since its discovery during the early stages of the Viking mission. Proposed mechanisms for the polygonal pattern include: permafrost activity, desiccation of water saturated sediments, cooling of lava, and tectonic deformation.

Carr and Schaber (1977), Coradini and Flamini (1979), Helfenstein and Mouginis-Mark (1980), and Helfenstein (1980) suggested that the fractures were created by ice-wedging processes such as those that occur in terrestrial periglacial regions. The major objection to the hypothesis is scale. The martian patterns are as much as two orders of magnitude larger than ice-wedge polygons on Earth. Morris and Underwood (1978) pointed out that the largest polygonal fractures on Earth ($\approx$ 1 km diameter) are associated with desiccation of thick, formerly water-saturated playa sediments. Helfenstein and Mouginis-Mark (1980) suggested that the smaller polygons (2-5 km diameter) were formed by ice-wedging and later desiccation processes caused some of the smaller polygons to coalesce, producing the 10-20 km polygons.

Morris and Underwood (1978) and Masursky and Cradbill (1976) suggested that the troughs may be large-scale lava cooling cracks. As with the ice-wedge hypothesis, the origin of the polygonal fractures by contraction and cooling of lavas faces a scale problem. Pechmann (1980) pointed out that few lava flows on Earth are thick enough to accommodate tension cracks that are hundreds of meters deep.

Pechmann (1980) investigated the possibility that the polygonal pattern of troughs was caused by deep-seated tension of tectonic origin that resulted in normal faulting. He reported that troughs in Acidalia Planitia locally exhibit preferred orientations. He compared the fractures on Mars to troughs of similar scale and morphology in the Caloris Basin on Mercury and suggested that both sets of troughs are grabens formed in response to a nearly isotropic horizontal tensional stress.

All of the proposed theories on the origin of the polygonal pattern have their limitations. It is possible that the troughs are polygenetic, that is, formed by more than one process. The larger fractures may be tectonic, whereas the smaller polygons closer to the pole may be the result of permafrost activity. Some of the troughs may have originally been formed by one or more processes and extended or enlarged, or both, by other processes.

Common on the patterned mottled plains are numerous small, dome-like

Figure 24. Patterned mottled plains material. (a) Enlargement showing the crudely polygonal pattern of troughs superimposed on low-albedo plains; the sun is from the west; few of the polygons are closed; the large circular feature may reflect a buried impact crater; unusual ridge with summit trough (arrow) appears to eminate from a small crater and cuts across the circular trough; numerous small (< 1 km) craters can be seen on this image especially in the western region; Viking frame 32A18 (44.1°N, 18.3°W). (b) Numerous small (< 1 km) dome-like structures with or without summit craters are common throughout the patterned mottled plains; they may occur in clusters or chains as seen on this image; compare the morphology of the cratered domes with that of the small impact craters in the southeast corner of the image; the dark circle in the northwest corner is an artifact of the imaging system; Viking frame 9A44 (43.4°N, 13.6°W).

ORIGINAL PAGE IS
OF POOR QUALITY

structures with summit craters (Fig. 24b). Several origins have been suggested for these features. Wood (1979) and Hodges (1979) suggested that these features were products of volcanic activity, i.e., cinder cones; Frey et al. (1979) interpreted them to be pseudocraters produced by lava flowing over water-saturated ground. Lucchitta (1981) and Wood (1979) suggested that these domes resemble terrestrial pingos produced by the arching of frozen ground forced upward by the intrusion of water under pressure. Masursky and Cradbill (1976) and Carr (1981) offered yet another explanation; small impact craters were eroded to inverted relief.

Unlike those of the mottled plains units to the north, i.e., mottled plains material - undivided and hummocky mottled plains material, few of the impact craters on the patterned mottled plains are filled with light material. Fine detail is observed on the ejecta blankets, and there is little evidence for eolian modification. This suggests that the blanket of light-colored debris that once covered the mottled plains and knobby plains to the north did not extend southward into the patterned mottled plains region. The lack of the partly eroded debris mantle in this area may also explain the higher density of small impact craters, i.e., they have not been covered by the debris mantle as in the north.

Boundaries with all surrounding units are gradational. The boundaries with all the non-mottled plains units (variegated plains, fractured plains, smooth plains, patterned smooth plains) are based on albedo; the patterned mottled plains have much lower albedo than the other units (Fig. 25). In identifying the variegated plains and the smooth plains, the occurrence of the polygonal trough pattern also was a criterion. The boundary with the mottled plains material - undivided was difficult to define because of the poor quality of the images, but the boundary is based on the occurrence of the polygonal troughs. The boundary between the patterned mottled plains and the subdued patterned mottled plains is placed where the troughs decrease in abundance, probably because they have been filled or partially filled by lava flows.

Subdued Patterned Mottled Plains Material.--The subdued patterned mottled plains material occurs in close proximity to the central plateau. The unit exhibits the same characteristics, at medium resolution, as the patterned mottled plains material. At higher resolution, however, the troughs are observed to be more discontinuous. Crater counts were not made on this surface because of its limited area, but the crater density is assumed to be slightly less than that of the patterned mottled plains material. The presence of flow fronts, pressure ridges, and possible volcanic cones led to the interpretation of this unit as volcanic flows that fill or partially fill pre-existing troughs.

A portion of the subdued patterned mottled plains was mapped in detail, and the geologic map is included as Appendix II. Figure 26 shows examples of lava flows that occur on this surface. The source of these lavas is somewhat uncertain. The flows may have originated from fissures that were subsequently buried, or from central vents. Several small, low-albedo domal structures that resemble pedestal craters, may, in fact, be small

Figure 25. Patterned mottled plains - variegated plains boundary. Compare the texture and albedo change between the patterned mottled plains (pmp) and the variegated plains (pv); a white line marks the boundary; the large (40 km diameter) c_4 flow-ejecta crater covers the boundary in the eastern region; rugged ejecta occurs near the crater rim; a small pedestal crater (p) occurs on the west side of the image; large (30 km diameter) circular structure similar to that seen in Figure 24a is indicated by the arrows; a less distinct circular feature occurs to the right of the pedestal crater (arrow); the impact craters in this region appear fresher than those on the mottled plains to the north (Fig. 21); Viking frame 673B34 (47.3°N, 2.5°W).

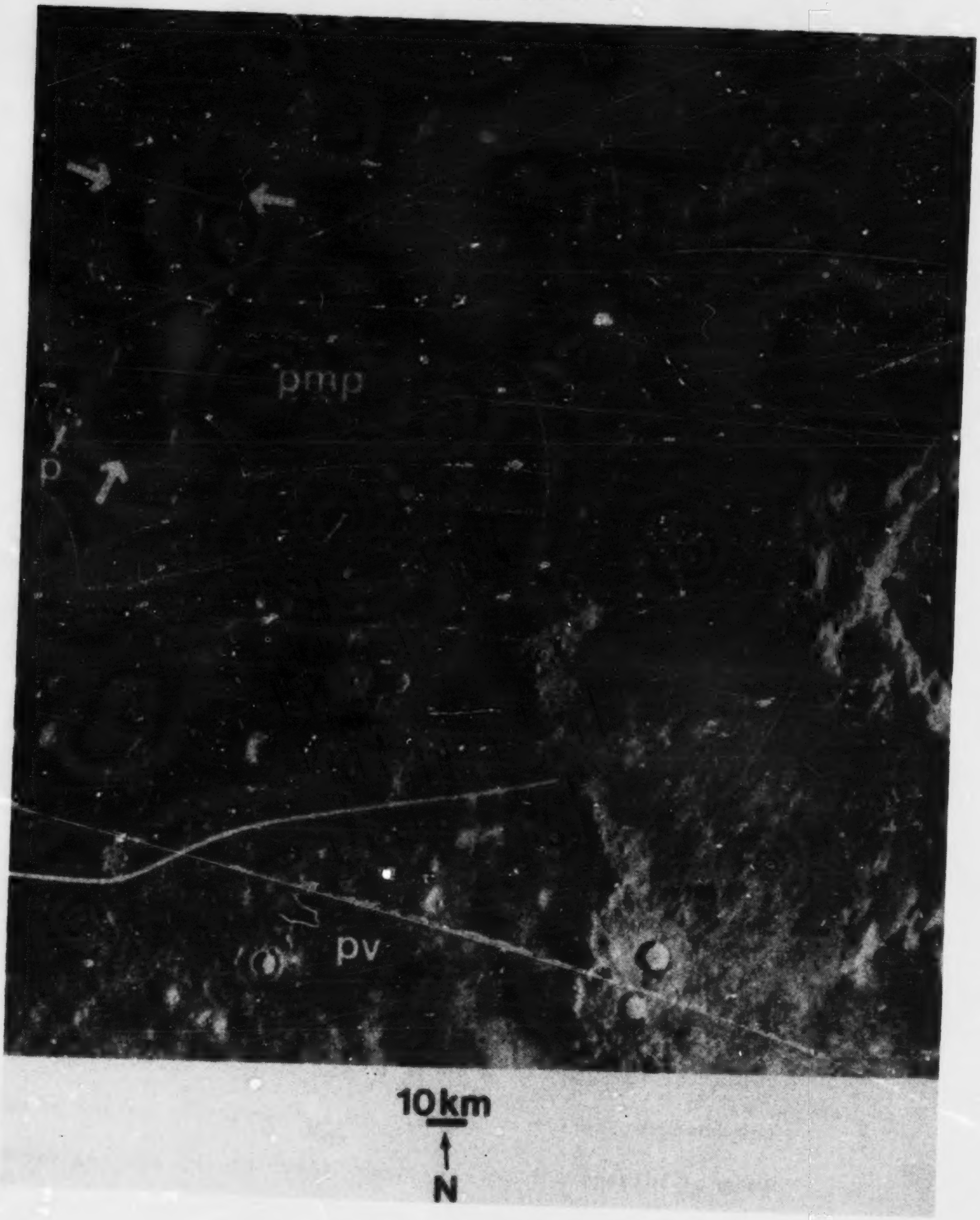
pmp
p
pv
10km
N

Figure 26. Lava flows on subdued patterned mottled plains. (a) A large low-albedo lava flow can be seen in the center of the image; small arrows mark distinct flow lobes; another flow can be seen in the northwest corner of the image; the ejecta of the large impact crater in the center of the image may have been buried by older lava flows; lava flows may have originated from fissures that were subsequently buried, or from domal structures that are indicated by the large arrows; alternatively, these domal structures also resemble pedestal craters; smaller domes, seen as white dots in the southern part of the image, may be similar to those seen in Figure 24b; knobby material (k), from the breakdown of the plateau, occurs to the north and south of the large lava flow; two north-south trending fractures can be seen in the northeast corner of the image; Viking frame 35A32 (45.4°N, 28.4°W).

(b) Possible pressure ridges on a lava flow are indicated by arrows; a source for this flow is uncertain; note the clusters of small domes in the northeast corner and the larger dome (d) in the southeast corner of the image; if these domes are volcanic, they may be a local source for the flows; note the obscure pattern of troughs in the northeast corner of the image; isolated patches of knobby material (k) are scattered throughout the region; Viking frame 35A41 (46.5°N, 22.2°W).

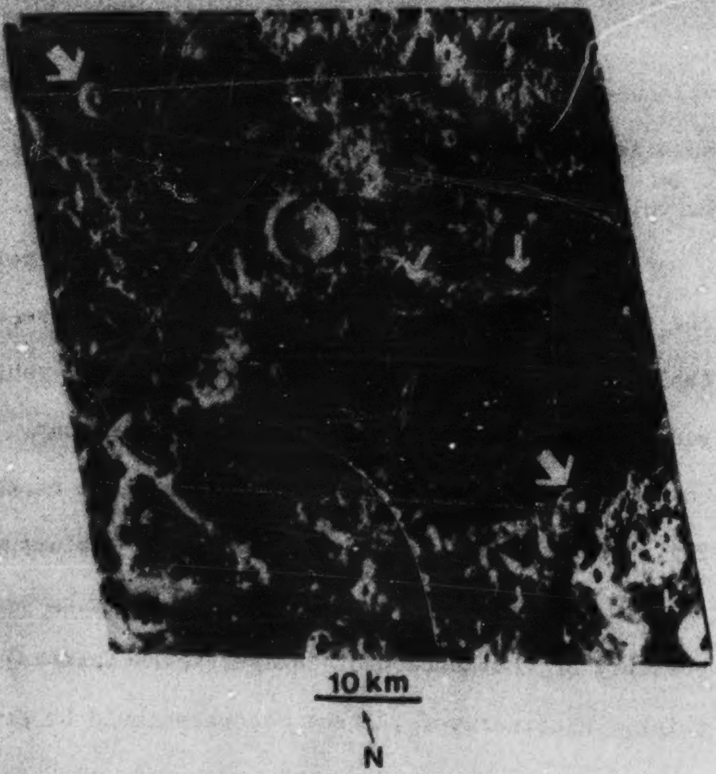
k
k
10 km
N

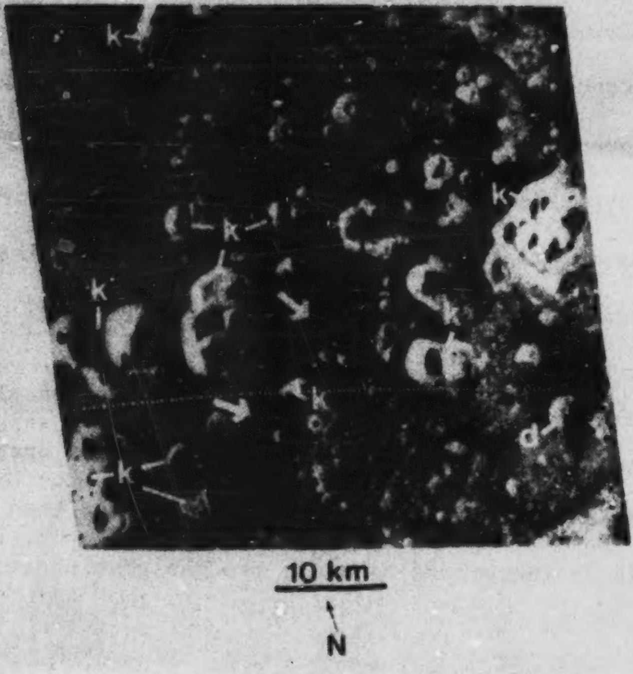
k
k
k
k
k
k
k
d
k
10 km
N

volcanoes (Fig. 26a). There are also numerous small, cratered domes, such as those that occur on the patterned mottled plains, that could be volcanic cones (Figs. 26, 27).

Hodges and Moore (1979) and Allen (1979b) believed that several of the small mesas and buttes in this region may be analogous to Icelandic tablemountains produced by subglacial central-vent eruptions and moberg ridges produced by subglacial fissure eruptions. These structures are commonly a few kilometers across and several hundred meters high (Fig. 27). If these martian features are true tablemountains and moberg ridges, then at one time this region must have been covered by a layer of ice, or possibly a combination of ice and rocky material, several hundred meters thick. Alternatively, these features could be erosional remnants of the dissected and fractured plateau material.

The boundary between the subdued patterned mottled plains and the dissected and fractured plateau boundary is commonly expressed by an escarpment with lava flows embaying incomplete impact-crater depressions on the plateau surface (Fig. 12). The boundary with the patterned mottled plains material is marked by an increase in trough abundance on the patterned mottled plains (Fig. 28).

Fractured Plains Material.--The fractured plains cover a small area between the patterned mottled plains and the cratered plateau in southeastern MC-4. The unit has a higher albedo than the mottled plains units and is characterized by wider troughs than those of the patterned mottled plains and the patterned smooth plains. Crater counts were not made on this surface because of its limited area, but visual estimates indicate a fairly low crater density. No craters larger than 5 km in diameter exist on the fractured plains surface. The fractured plains material may consist of volcanic and eolian material.

The troughs of the fractured plains may be as wide as 2 km, as opposed to the troughs on the other patterned plains units that are generally less than 1 km wide. Commonly the troughs are shallow and have flat floors (Fig. 29). Pechmann (1980) reported that some of the troughs on the fractured plains have one or two smooth terraces along a portion of the wall. He also reported vertical offset in several of the troughs and concluded that these features were the result of normal faulting (Pechmann 1980; Figs. 1-3).

A small section of the fractured plains was mapped at higher resolution (Appendix III). In this region, the fractured plains nearest the large remnant of cratered plateau material (mesa material on the high-resolution map) may have been partially resurfaced by lava flows, as indicated by the presence of several possible flow fronts and by the subdued and discontinuous pattern of fractures.

The presence of a scarp forming the boundary between the fractured plains and the higher variegated plains and the presence of knobs and mesa material on the fractured plains led Guest et al. (1977) to conclude that the fractured plains material is an old unit that stratigraphically underlies the plateau material. Figure 29b shows a part of the scarp

Figure 27. Subdued patterned mottled plains material. (a) Small mesas (m) with or without summit knobs may be tablemountains or erosional remnants; many small cratered domes are at the limit of resolution; ejecta from the large c_4 crater is not cut by the arcuate fracture at the eastern side of the image, the smaller craters and ejecta blankets in the southern part of the image also are not cut by the fracture, indicating that the fractures are older than the c_4 craters; northwest-southeast and northeast-southwest fracture grid occurs; Viking frame 26A30 (44.8°N, 20.4°W); for a detailed map and cross-section, see Appendix II.

(b) The small mesa (m) in the northwest corner of the image is cited by Allen (1979b) as a possible tablemountain; from shadow-length measurements, Allen estimated that the mesa is 470 m high; numerous small cratered domes can be seen as white dots in the northern part of the image; a possible flow is indicated by arrows; the polygonal pattern of fractures is more obvious in this region than the region to the west (Figure 26b); Viking frame 26A28 (44.8°N, 21.7°W); for a detailed map and cross-section, see Appendix II.

ORIGINAL PAGE IS
OF POOR QUALITY

Figure 28. Patterned mottled plains - subdued patterned mottled plains boundary. The boundary (white line) is marked by a rapid change in the abundance of troughs; also the subdued patterned mottled plains (pmps) may be slightly lower albedo; the image is too low in resolution to detect individual lava flows on the subdued patterned mottled plains, but the proposed tablemountain shown in Figure 27b is indicated by a small arrow in the southern part of the image; knobby material (k) is scattered throughout both the patterned mottled plains (pmp) and the subdued patterned plains (pmps); large circular trough on the patterned mottled plains occurs in the east-central portion of the image (large arrow); image artifact occurs along the eastern margin of the image; Viking frame 670B18 (47.2°N, 21.2°W); part of the area of this image was mapped in greater detail and is included as Appendix II.

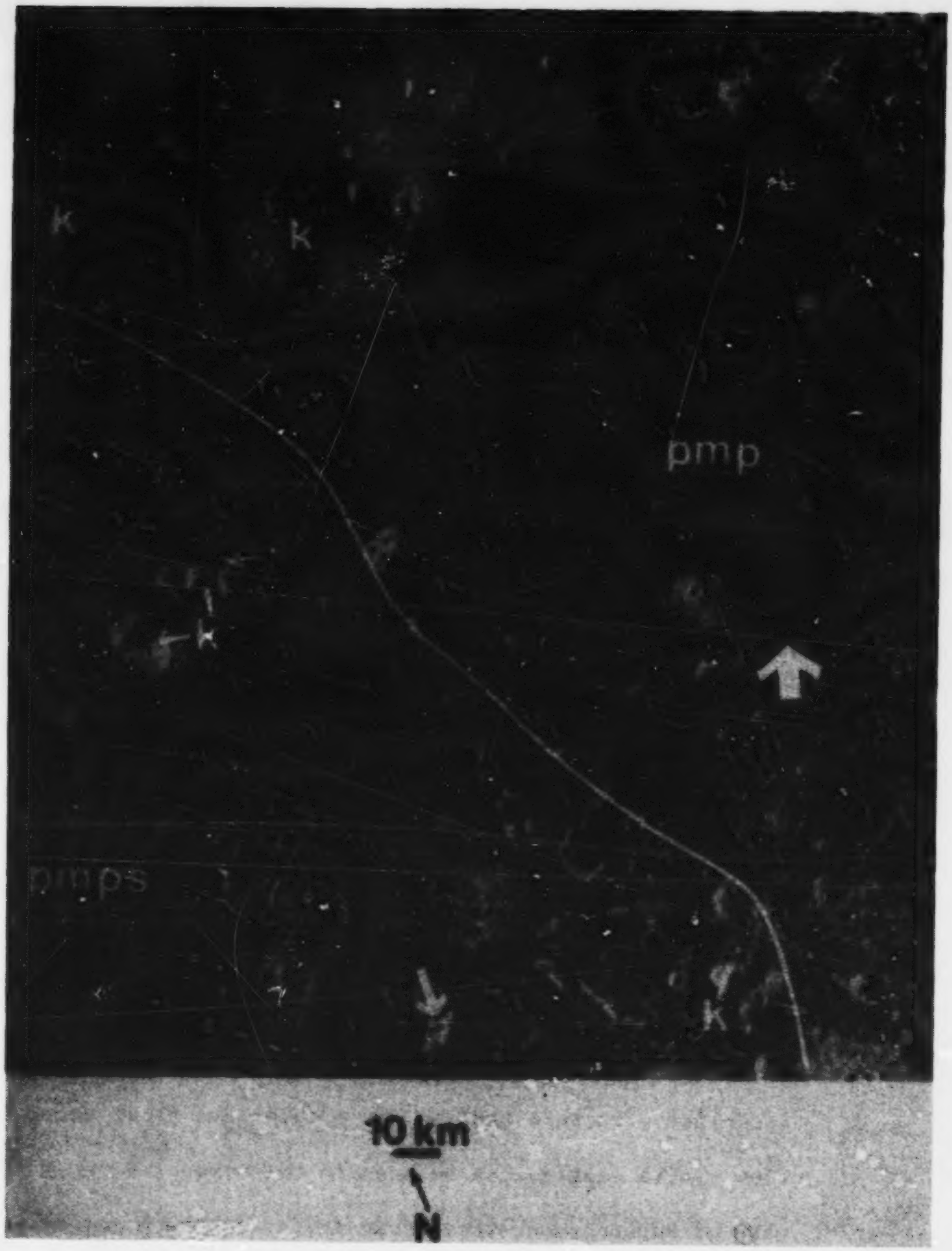
k
k
pmp
k
pmps
k
10 km
N

Figure 29. Fractured plains material. (a) Compare these troughs with those seen on the patterned mottled plains (Fig. 24); troughs on the fractured plains can be as large as 2 km wide (troughs on the patterned mottled plains are generally less than 1 km wide); the wider troughs have flat floors and steep sides that Pechmann (1980) believed are consistent with either formation by downdropping of the trough floor or by separation of the trough walls followed by infilling; matching irregularities in some of the opposite walls of the troughs suggest tensional separation of the walls; arrow indicates the region where Pechman reported downward offset at the trough walls; numerous small domes occur in the southern portion of the image; knobby terrain (k) occurs in the southeast corner of the image; impact craters on the fractured plains unit do not have high-albedo ejecta blankets; Viking frame 35A64 (40.4°N, 13.9°W).

(b) Sinuous escarpment along the boundary between the fractured plains (pf) and the variegated plains (pv); the low albedo fractured plains material appears to terminate 2-3 km away from the escarpment; the arrow indicates a lobe-like structure that may be a thin lava flow; three fresh flow-ejecta craters can be seen in this image; several clusters of secondary craters occur in the southern and eastern regions; the knobs in the southwest corner of the image appear to be layered; image artifacts occur along the eastern and western margins of the image; Viking frame 35A73 (41.6°N, 8.7°W).

a.

b.

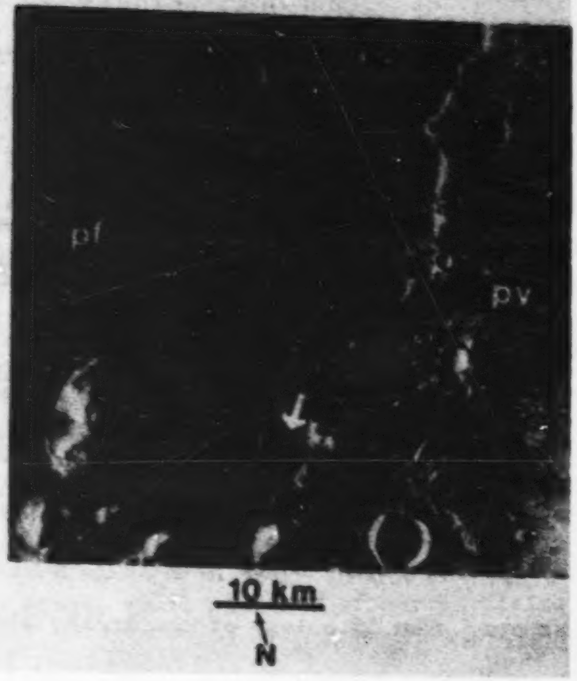

boundary. It appears as though the darker fractured plains materials do not always come in contact with the scarp. Guest et al. (1977) suggested that scarp retreat occurred by a breakdown of the rocks as a result of sapping and other ground ice activity and that as the scarp retreated, it left piles of lighter debris on the rocks stratigraphically below the smooth plains material. Alternatively, the lower fractured plains may have been partially resurfaced by thin lava flows, with the albedo boundary marking the extent of these flows.

In some areas a small escarpment marks the boundary of the fractured plains and the higher knobby terrain. If these knobs are erosional remnants of the higher cratered plateau material, then the escarpment boundary would suggest that the fractured plains lie stratigraphically underneath the cratered plateau and were exposed be erosion. The boundary with the darker mottled plains unit to the north is based on an albedo difference.

Knobby Plains Material.--The knobby plains material occurs in the northeast corner of MC-4 and extends eastward into the adjacent quadrangle, MC-5. The unit exhibits characteristics similar to those of the adjacent mottled plains including the filled and partly filled impact craters. The knobby plains, however, have much higher albedo (Fig. 30a). The crater size-frequency distribution curve for the knobby plains is very similar to that of the mottled plains units (Fig. 20), suggesting that the units are of similar age. The lithology of the knobby plains is interpreted to be eolian material blanketing a lower, possibly volcanic surface.

Knobs similar to those on the hummocky mottled plains are common on the knobby plains. These dark hummocks are present on the floor of the large crater Lomonosov (64°N, 9°W) (Fig. 30b). These darker knobs may be volcanic or permafrost features. It is not likely that they represent a lower, darker unit that has been partially mantled with lighter material.

The knobby plains - mottled plains boundary is a sharp albedo contrast (Fig. 30a). This contrast may be the result of a thicker layer of debris that still mantles the knobby plains, i.e. has not been eroded as completely as it was in the mottled plains region. Alternatively, the albedo contrast may be the result of variations in surface lithologies.

<ins>Smooth Plains Material</ins>.--The smooth plains cover a large portion of the southern region of MC-4 and are relatively featureless at medium resolution. Patches of knobby terrain are scattered throughout the smooth plains region, including several places where the knobs form a circular outline (Fig. 31a). The albedo varies; in the east, the smooth plains are intermediate to high albedo, whereas to the west, especially along the northern and southern margin of Tempe Plateau, the smooth plains are low albedo. Bright and dark wind streaks are common throughout the smooth plains region. The crater size-frequency curve for the smooth plains (Fig. 32) is very similar to those of the mottled plains units, suggesting they may be equivalent in age. The smooth plains are believed to consist of eolian and alluvial deposits that buried an older, cratered surface.

In two areas, small sections of smooth plains were mapped at high

Figure 30. Knobby plains material. (a) Boundary between the knobby plains (pk) and the lower-albedo mottled plains (pm) (lower white line); the smooth light-colored material in the northwest corner of the image is ejecta from a large c_4 crater to the northwest; the knobby plains do not exhibit the same albedo contrast between the plains and ejecta blankets as do the mottled plains; a sinuous ridge on the mottled plains is indicated by the arrow; image artifact occurs along the eastern margin of the image; Viking frame 673B08 (54.3°N, 5.2°W).

(b) Large (130 km diameter) c_2 impact crater, Lomonosov, occurs on the knobby plains near the northern boundary of MC-4; small (< 1 km) dark hills occur on the floor of the crater; these knobs are similar to those seen in the inter-crater region of the knobby plains and hummocky mottled plains (Fig. 23); the large patch of dark material on the crater floor may be a field of dunes; the wall of this large crater consists of a complex of short ridges; the striped pattern in the lower right corner is an image artifact; Viking frame 672B56 (65.1°N, 9.8°W).

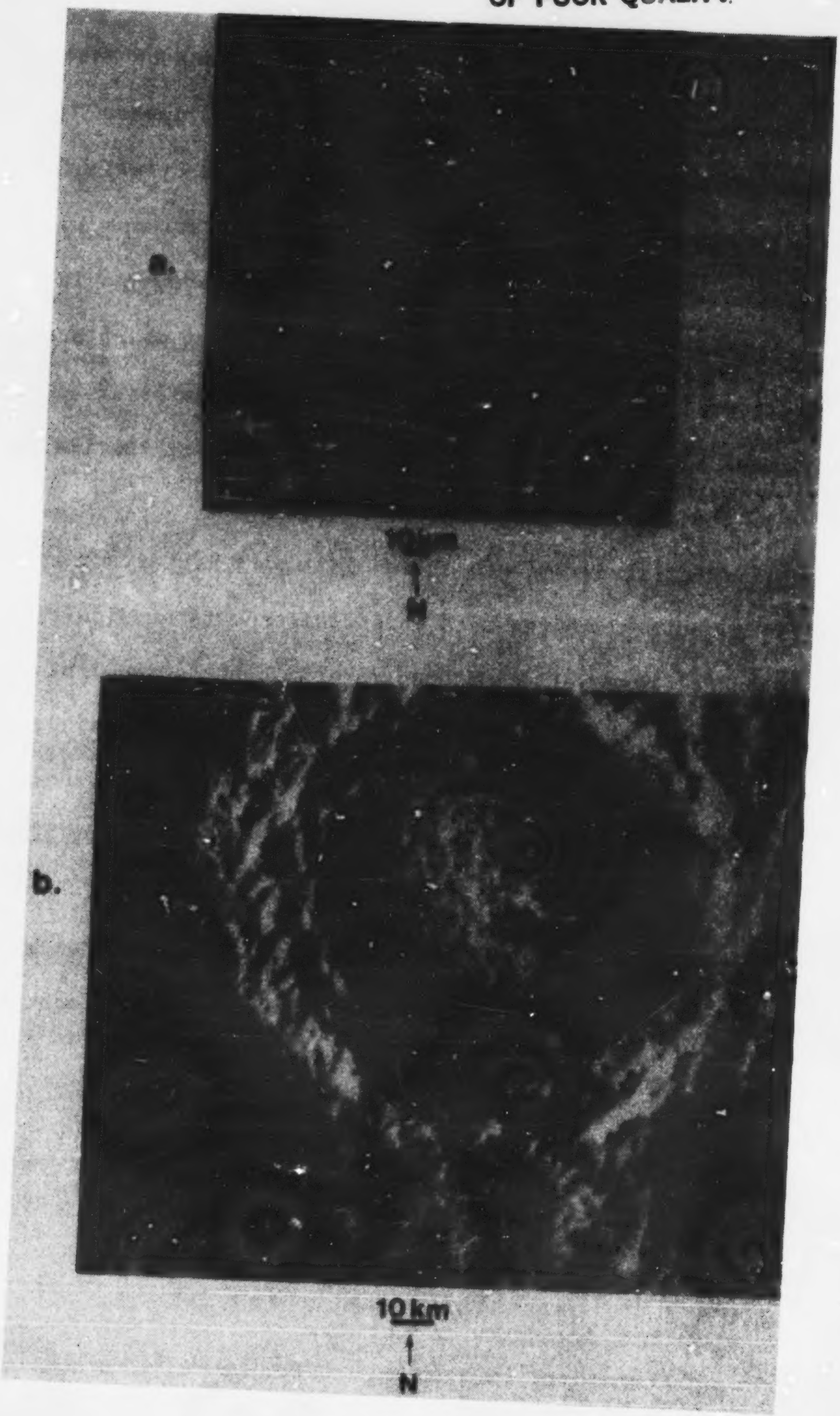
a.
10 km
N
b.
10 km
N

Figure 31. Smooth plains material. (a) Circular outlines of knobby material mark the positions of partly buried impact craters; the varied albedo pattern is caused by a shifting eolian mantle; both the light and dark wind streaks are scattered throughout the region; the arrow shows a discontinuous sinuous ridge and trough, many of which are scattered throughout the smooth plains; image artifacts occur along the eastern and western margins of the image; Viking frame 524A15 (34.5°N, 38.4°W).

(b) Streamlined remnants of an old impact crater; crater rim material is often much more resistant to erosion than is other, less well-compacted material; the streamlining of this feature is in a direction opposite to the wind; two unusual curvilinear troughs can be seen in the southern portion of the image (arrows); the mouths of several large outflow channels occur to the south of this region; the wind direction is from the northeast as indicated by the numerous light streaks formed downwind from impact craters; Viking frame 558A07 (32.7°N, 40.5°W).

a.

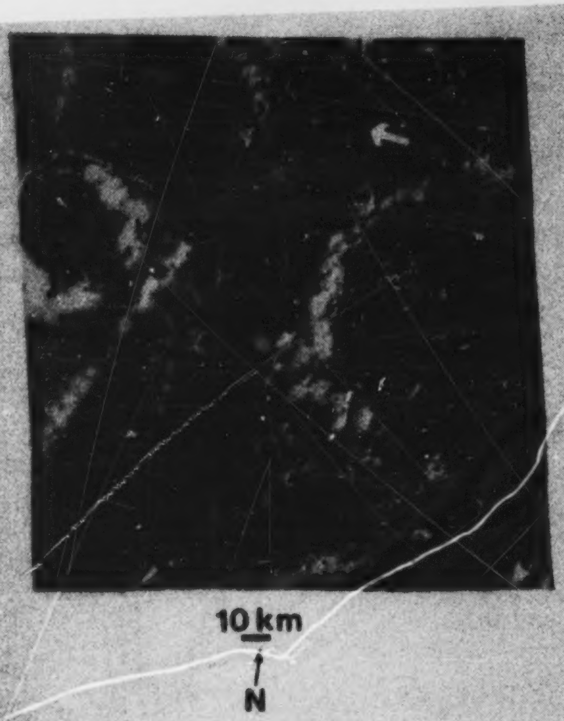

b.

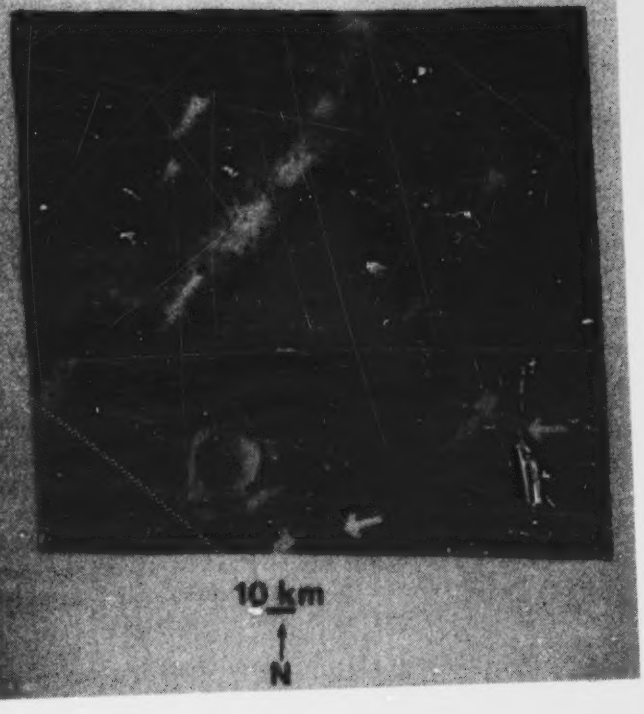

ORIGINAL PAGE IS
OF POOR QUALITY

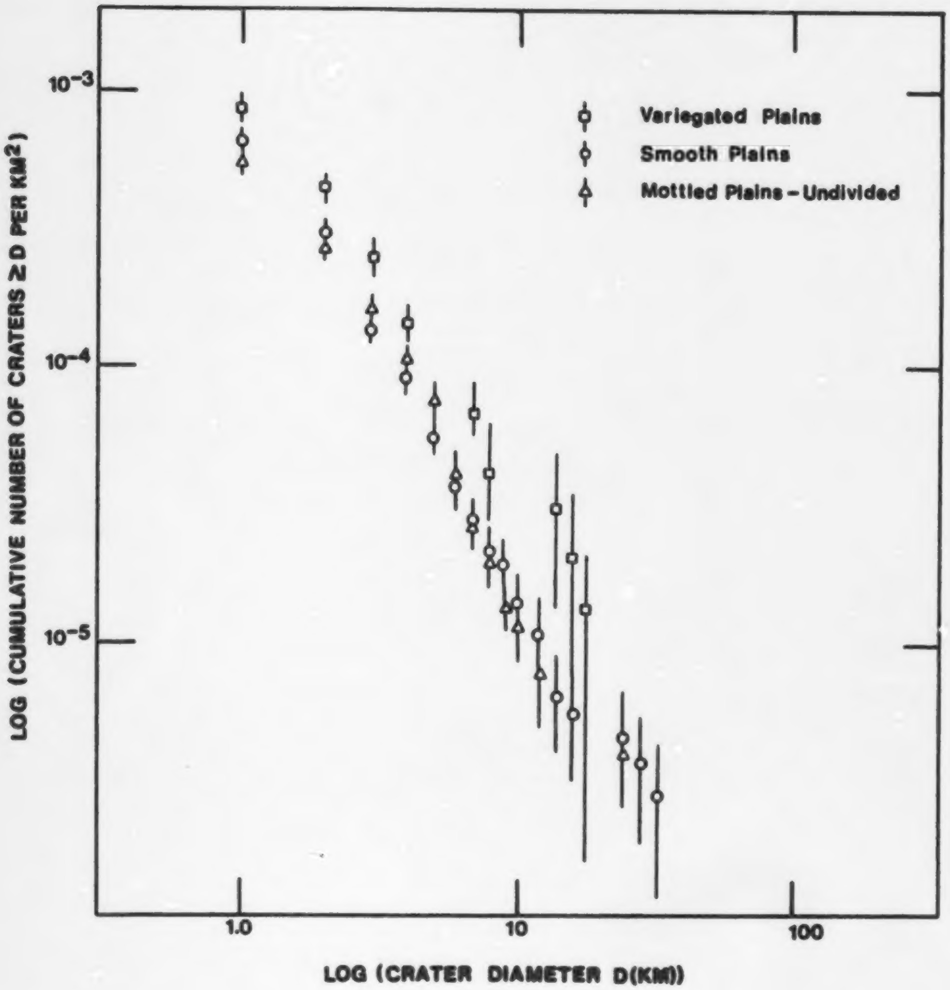

Figure 32. Cummulative crater size-frequency distributions for the variegated plains, smooth plains, and mottled plains - undivided. Number of craters are cummulated from largest to smallest size; vertical lines indicate one standard deviation, 1σ confidence intervals for each data point plotted, calculated by assuming the crater populations are Poisson distributed. The 1σ is approximated by using $N = \pm\sqrt{N}$ where N is the number of craters (Arvidson et al., 1978).

resolution (Appendix I, III). One area occurs along the northwest margin of the cratered plateau in the southeast corner of the quadrangle (Appendix III). Numerous small (< 1 km) cratered domes similar to those that occur on the patterned and subdued patterned mottled plains and on the variegated plains are scattered across the smooth plains surface in this region. Frey and Jarosewich (1981) discovered a definitive bimodal distribution of cratered dome diameters on the smooth plains. They suggested that if the domes are pseudocraters, the bimodal distribution may be the result of variations in the thickness of lava flows. Alternatively, the bimodal distribution may indicate that these domes have formed from more than one process. If these domes are volcanic edifices (Wood, 1979) or pseudocraters (Frey et al., 1979), the smooth plains in this region may consist partly of volcanic material.

The other area that was mapped using high-resolution data occurs along the northern margin of Tempe Plateau. In this region, smooth plains material embays troughs and channels that are cut into the higher plateau. Scott (1978) recognized lobate scarps and small convex cones and suggested that the smooth plains in this region are basalt flows. In the present investigation, most of the "small convex cones" are interpreted as impact craters, and the lobate scarps were not recognized. As a result, the smooth plains in this region have been interpreted as alluvial sediment from erosion and drainage off the highland block and as eolian material.

Scours and streamlined features oriented northeast occur in the southern smooth plains region (Fig. 31b) and disappear near 35°N. These features have been interpreted to be the result of erosion associated with the release of water from the large outflow channels to the south (Carr and Clow, 1981). Much of the smooth plains material in this southern region may consist of debris deposited during the flooding.

Several mare-type ridges occur on the smooth plains in the southwestern region. Figure 33a shows one of these ridges that was cut by faults that are aligned with the faults of Tempe Plateau. Another mare-type ridge cuts across both the higher plateau and lower smooth plains material (Fig. 15b). The occurrence of these ridges on units with varied lithology and different elevation supports the hypothesis that the mare-type ridges in this region are tectonic.

Other unusual ridges of more uncertain origin occur throughout the smooth plains (Fig. 33b, 34). The sinuous ridges near the plateau plains boundary in the southeast region show no preferred orientation and can be more than 60 km long (Fig. 33b). Several of these ridges subdivide into two or more branches. Figure 34a shows a meandering pattern of troughs with ridges running down the center. Less well-preserved examples of this pattern occur as far north as 40°N. Scott (personal communication, 1982) suggested that these may be meander scrolls from shifting stream channels. A wider and more subdued pattern of ridges or swells occurs on the smooth plains around 37°N, 17°W (Fig. 34b). These subdued swells form a more regular pattern of branches.

Light wind streaks and patches of dark eolian material are common throughout the smooth plains region. The streaks record north and northwest winds at north latitudes greater than 40°. Farther south, the streaks record a more northeasterly wind direction.

The boundary of the smooth plains with the darker mottled plains units to the north is based on albedo. The smooth plains - patterned smooth plains boundary is more gradational and is placed where trough abundance increases. To the southeast and southwest, the boundary between the smooth plains and the higher plateau units is a steep escarpment. Farther northwest, the escarpment is not always present, and smooth plains material embays and rests on the plateau units.

Patterned Smooth Plains Material.--The patterned smooth plains material occurs in the central region adjacent to the patterned mottled plains. The unit is characterized by a crudely polygonal pattern of troughs that is approximately the same size as that which occurs on the patterned mottled plains. The lack of high-albedo ejecta blankets and the overall higher albedo distinguishes the patterned smooth plains unit from the patterned mottled plains. No crater counts were made on this unit because of its limited extent and gradational boundary with the smooth plains, but crater density is assumed to be similar to that of the smooth plains. The lithology of the patterned smooth plains material is thought to be similar to that of the smooth plains material to the south, i.e., predominantly eolian material blanketing an older cratered surface (Fig. 35).

There are several possible explanations for the presence of the troughs on the smooth plains. Patterned mottled plains material may have, at one time, extended farther south and been subsequently blanketed with

Figure 33. Ridges on the smooth plains, example 1. (a) A mare-type ridge on the smooth plains near Tempe Plateau is truncated by east-west trending faults; faint traces of the ridge (arrow) extend to the impact crater; isolated remnants of plateau material can be seen along the western margin of the image; dark patches are interpreted as eolian material; well preserved c_4 flow-ejecta crater occurs in the center of the image; image artifacts occur along the eastern and western margins of the image; Viking frame 558A31 (37.0°N, 49.1°W).

(b) A sinuous ridge near the plateau-plains boundary in the southeastern region; the ridge bifurcates at the knobby material then continues on the other side; a smaller ridge (arrow) cannot be seen as well because it runs parallel to the sun angle, and thus, no shadow is formed; the sun is from the top right; the mesas (m) and knobs (k) are believed to be erosional remnants of cratered plateau material; well-preserved c_4 bowl-shaped crater occurs in the northeast corner of the image; Viking frames 218S01-02 (33.0°N, 14.5°W).

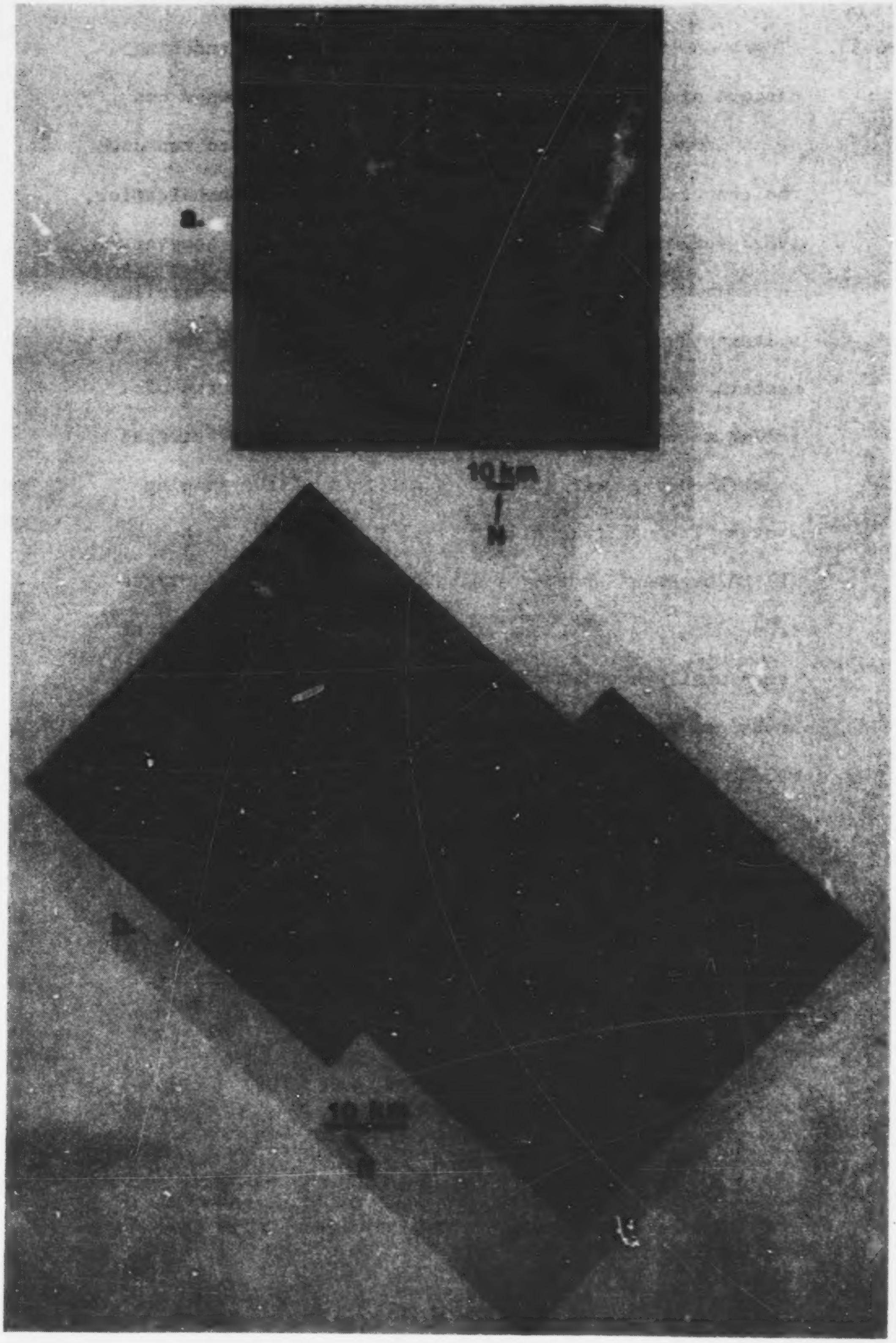
a.
10 km
N
b.
10 km
N

Figure 34. Ridges on the smooth plains, example 2. (a) Meandering pattern of troughs with ridges; the shallow troughs can be as large as 2 km wide; narrow ridges appear to run down the center of these troughs; Scott (personal communication, 1982) suggested that these are meander scrolls, however orthogonal intersections are atypical of meander scrolls; a large (20 km diameter) impact crater occurs on the eastern side of the image; dark patches and streaks of eolian material occur in the central region; the striped pattern on the west side is an artifact of the imaging system; Viking frame 524A28 (29.1°N, 28.0°W).

(b) Enlargement showing a subdued pattern of wide ridges or swells; some of these swells are 3-4 km wide; many of these swells subdivide into two or more branches; isolated knobs are scattered throughout the region; Viking frame 597A12 (37.5°N, 17.4°W).

a.

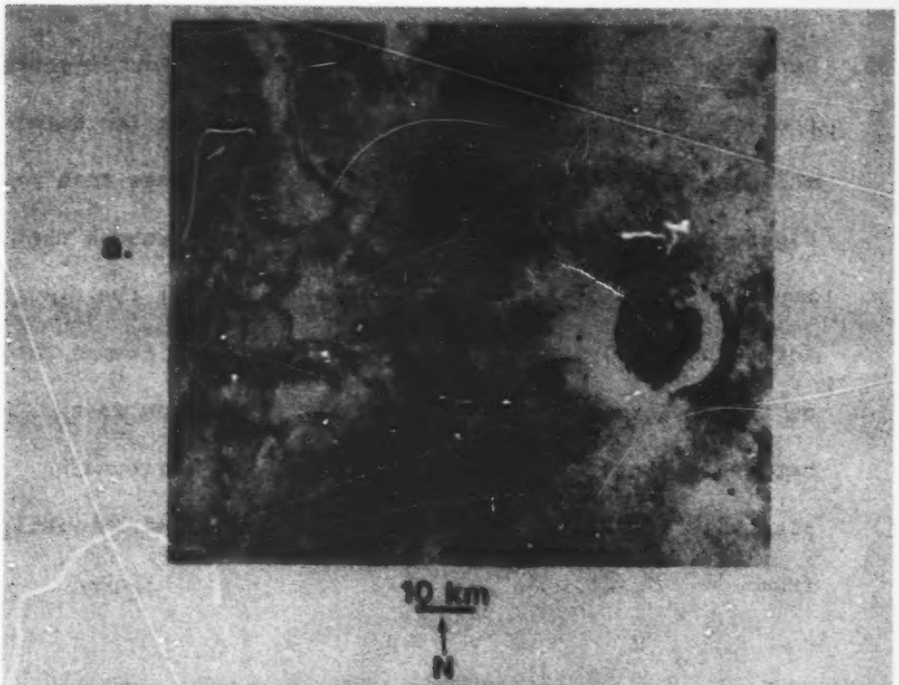

b.

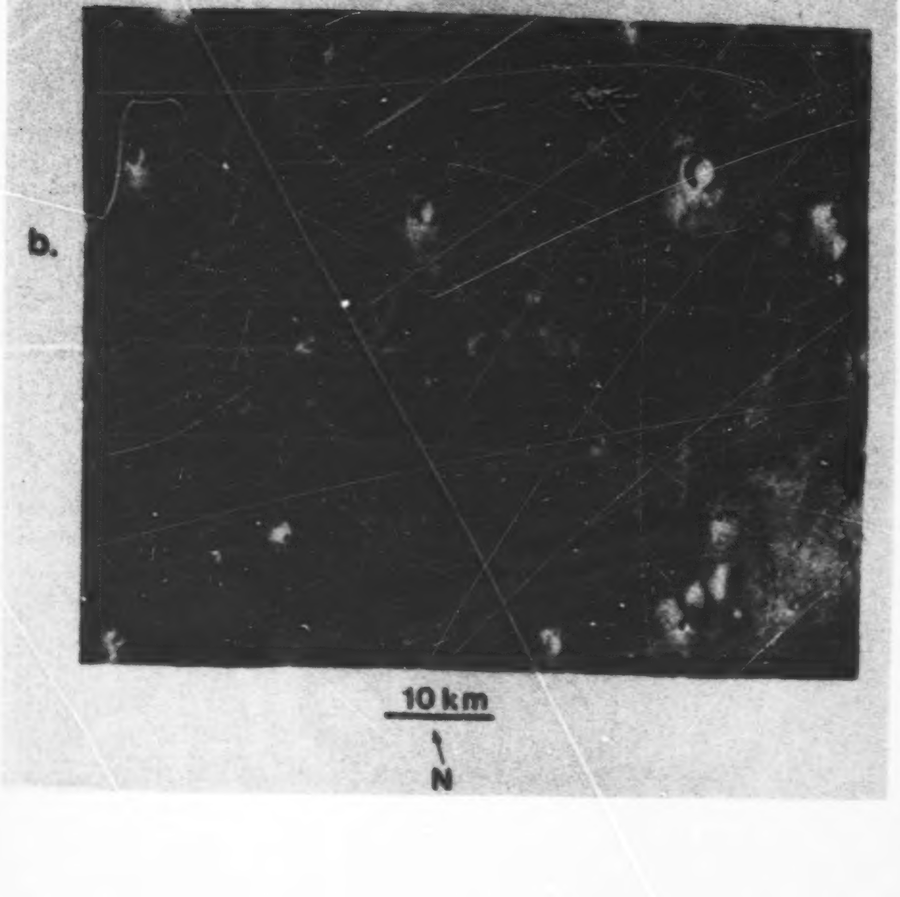

Figure 35. Patterned smooth plains material. This enlargement shows the subdued pattern of troughs superimposed on the intermediate-albedo smooth plains; compare this image with Figure 24, which shows a similar pattern of troughs that bound polygons of slightly larger size; few of the troughs form closed polygons; circular forms are less common than on the patterned mottled plains; the albedo contrast between the crater ejecta blankets and the surrounding plains is not as extreme as on the mottled plains; Viking frame 597A05 (39.6°N, 24.2°W).

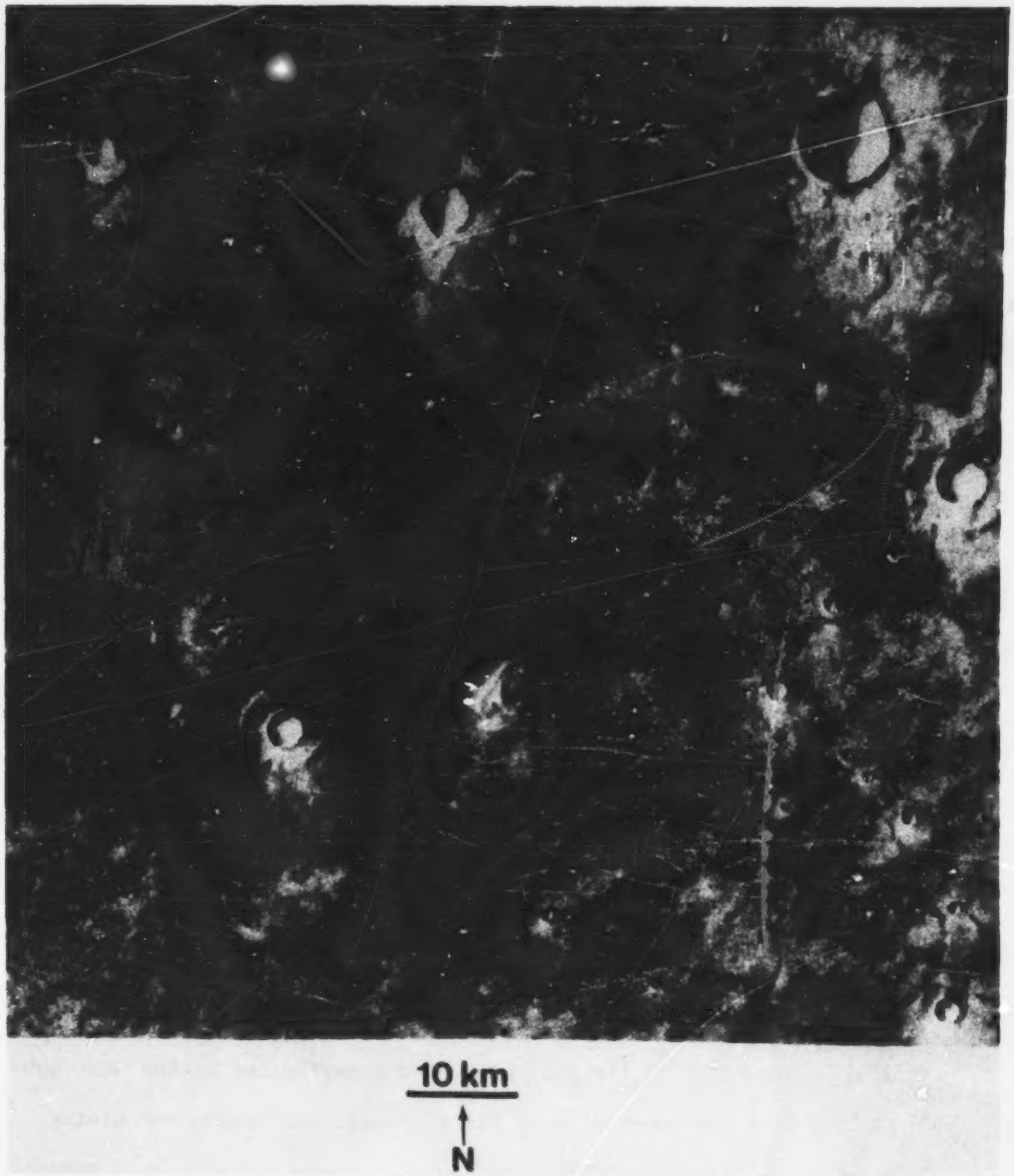
10 km
N

a thin mantle of lighter smooth plains material that slightly obscured the trough pattern. More feasible is the hypothesis that the smooth plains materials were subjected to the same mechanisms that produced the troughs on the adjacent mottled plains, i.e., permafrost activity, desiccation, or tectonism.

The boundary of the patterned smooth plains with the darker mottled plains material to the north is based on albedo. The occurrence of the trough pattern marks the smooth plains - patterned smooth plains boundary.

Variegated Plains Material.--The variegated plains material occurs along the eastern border of MC-4 and extends into MC-5. These plains are smooth, relatively featureless, and at medium resolution display a patchy albedo pattern. The crater size-frequency distribution (Fig. 32) for the variegated plains indicates that this unit may have a slightly higher number of larger craters, but the standard error bars are large and the difference may not be significant. The variegated plains are believed to be composed of volcanic and alluvial material (the latter only occurs near the plateau-plains boundary). These plains are blanketed by a thin mantle of shifting eolian material that forms the patchy albedo patterns.

A small section of the variegated plains around Bamberg crater (40°N, 3°W) was mapped using high-resolution data, and the map is included as Appendix III. On the geologic map the variegated plains are subdivided into the rough plains, hilly plains, and variegated plains. The rough plains are located adjacent to the ejecta deposits from Bamberg crater. The rugged texture is produced by the presence of many small

(< 1 km diameter) depressions that are believed to be secondary impact craters. The hilly plains are characterized by small (< 1 km wide) domes with summit craters similar to those that occur on the patterned and subdued patterned mottled plains and in places on the smooth plains. Clusters of these cratered domes are scattered throughout the variegated plains.

There are several small streamlined features on the variegated plains near the plateau-plains boundary along the eastern edge MC-4. Small channels occur on the cratered plateau near the plains boundary. The variegated plains material appears to blanket a portion of the ejecta deposits from Bamberg crater. These features suggest that the variegated plains in this region may consist of alluvial material deposited by channels draining the plateau to the south. Alternatively, the streamlined features may have been produced by wind erosion, and the variegated plains in this region may consist of eolian material.

Structures resembling Icelandic tablemountains occur in several places on the variegated plains. Figure 36a shows one of these steep-sided, flat-topped mesas with a summit knob. Alternatively, the features have been interpreted as erosional remnants of a higher, probably layered surface (Guest et al., 1977).

The variegated plains - cratered plateau boundary is in many places expressed as a low escarpment. In other areas the boundary is textural, between the relatively rugged, highly-cratered plateau unit and the smoother, variegated plains unit (Fig. 36b). A small irregular escarpment marks the

Figure 36. Variegated plains material. (a) Smooth, featureless plains with few topographic irregularities; two small irregularly shaped secondary craters from a large crater occur in the southeast corner of the image; a small mesa with a summit knob (m) resembles Icelandic tablemountains (Allen, 1979b); alternatively, the mesa may be an erosional remnant of layered plateau material; two smaller knobs (k) occur in the southern region; dark circle in the center of the image is an image artifact; Viking frame 36A44 (43°N, 4.2°W).

(b) Boundary between the cratered plateau (plc) and the variegated plains (pv); compare the differences in crater densities between the two units; an escarpment (large arrow) marks the plateau-plains boundary; to the west of the escarpment, the circular outline of two old impact craters can be seen; many irregular depressions occur on the cratered plateau (small arrows) and are believed to be collapse features from the breakdown of the plateau; Bamberg, a c_3 crater approximately 50 km in diameter, occurs along the left side of the image; numerous secondary craters occur east of Bamberg; Viking frame 673B60 (40.5°N, 0.9°W); part of this region was mapped in greater detail and is included as Appendix III.

a.

b.

pv
plc
10 km
N

boundary with the lower fractured plains materials (Fig. 29b), suggesting that the variegated plains material may be younger and, therefore, overlie the fractured plains material (Guest et al., 1977). The boundary between the variegated plains and the darker patterned mottled plains is based on albedo and the presence of the polygonal pattern on the mottled plains (Fig. 25).

Other Material

Dark Material.--Dark material occurs in patches through the quadrangle but is particularly abundant on the smooth plains near the southern margin of Tempe Plateau. Commonly these dark patches are associated with some sort of topographical barrier. Dark material occurs in and around craters on the plateaus and the plains (Figs. 15a, 30a), in valleys (Fig. 37a), along escarpments (Figs. 15a, 19), and in the inter-crater regions of the plains (Figs. 21a, 31a). These low-albedo materials are believed to be accumulations of eolian debris that reflect the present wind direction. In certain areas these dark patches have been resolved as fields of transverse dunes (Fig. 37a).

Light Material.--Light material is not as abundant as dark material. It occurs only in two areas: (1) along the northern margin of the southeast cratered plateau, and (2) along the northern margin of Tempe Plateau (Fig. 37b). A fan-shaped deposit of light-colored material is seen on the smooth plains adjacent to the fractured plateau (Fig. 17). The northern Tempe Plateau region was mapped in greater detail and is included as

Appendix I. This unit is interpreted as eolian material and alluvial material from drainage of the highland block.

Channel Material.--High-albedo channel material occupies an elongate, sinuous depression along the smooth plains - mottled plains boundary north of Tempe Plateau (Fig. 37b). The channel ranges in width from 10-25 km and extends approximately 200 km. A very narrow trough can be traced another 100 km before it pinches out. This region was mapped in detail and is included as Appendix I. The unit is interpreted as alluvium filling an old stream channel (Scott and Tanaka, 1980).

Knobby Terrain Material.--Knobby terrain material occurs throughout the lowland plains but is particularly common in close proximity to the cratered plateau in the southeast region and the dissected and fractured plateau material in the central region. The terrain consists of irregular hills of knobs that rise above the level of the plains. These knobs vary in size; the largest are 15 km across and are approximately 3000 m high (Fig. 38a). Most of the knobs are much smaller.

The origin of the knobs is varied and depends on the location. Knobs and mesas that occur close to the highlands probably are erosional remnants of the plateau material left by scarp retreat. Many of the knobs in this region appear to have basal debris accumulations (Fig. 38b). Squyres (1978) suggested that these debris flows may be similar to terrestrial rock glaciers.

Numerous patches of knobs occur on the smooth plains. In several areas, the knobs form a circular outline (Fig. 31a). These knobs are

Figure 37. Dark, light, and channel material. (a) Dark material occurs on the smooth plains between two plateaus; the small field of transverse dunes is indicated by the arrow; other dark material has accumulated on the upwind side of the small isolated plateau; this region is included on the low-resolution image shown on Figure 15b; Viking frame 668A17 (33.2°N, 53.6°W).

(b) High-albedo channel material (ch) can be seen along the boundary between the smooth plains (ps) and the mottled plains (pm); fractured plateau material (plf) occurs in the southwest corner of the image; patchy light material (lt) can be seen on the mottled plains in the northwest corner; several high-albedo wind streaks associated with some small craters indicate that wind is from the northwest; the smooth plains in this region are lower albedo than the mottled plains; the pattern on the east side of the image is an artifact of the imaging system; Viking frame 669B76 (53.9°N, 53.4°W); high-resolution map and cross-section of this area are included as Appendix I.

ORIGINAL PAGE IS
OF POOR QUALITY

a.

b.

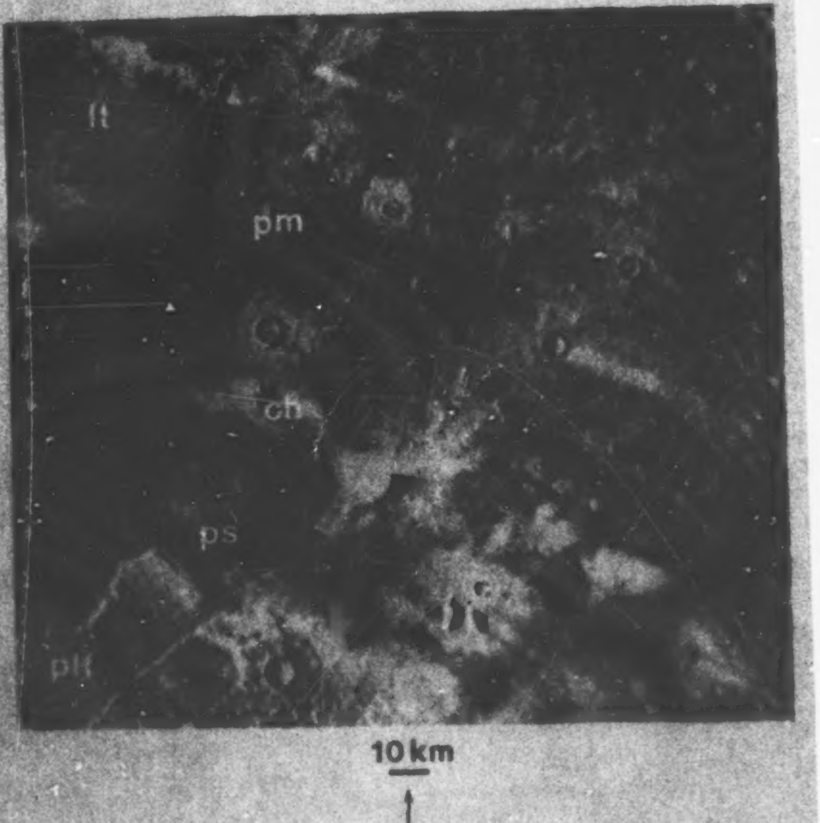
lt
pm
ch
ps
pl
10 km
N

Figure 38. Knobby terrain material. (a) Largest knobs in the quadrangle occur near Kunowsky crater, a large c_4 crater on the boundary between the knobby plains (pk) and the mottled plains (pm); these knobs are as much as 15 km across and more than 3000 m high; smaller knobs lie south of the large knobs; this image overlaps with the image in Figure 30b; a sinuous ridge is indicated by the arrow; pattern at the right side of the image is an artifact of the imaging system; Viking frame 673B06 (54.7°N, 9.2°W). (b) Knobby terrain near the plateau-plains boundary in the Cydonia region; many of the knobs appear to have basal debris accumulations; the arrow marks apparent flow lobe; Squyres (1978) interpreted the striations on the flow as the result of compression and contraction from movement; the knob with a summit crater (C) may be a cinder cone; stratification of the knobs is obvious in a few places; subdued pattern of troughs occurs on the plains; Viking frame 70A09 (40.4°N, 11.0°W); this area was mapped in greater detail and is included as Appendix III.

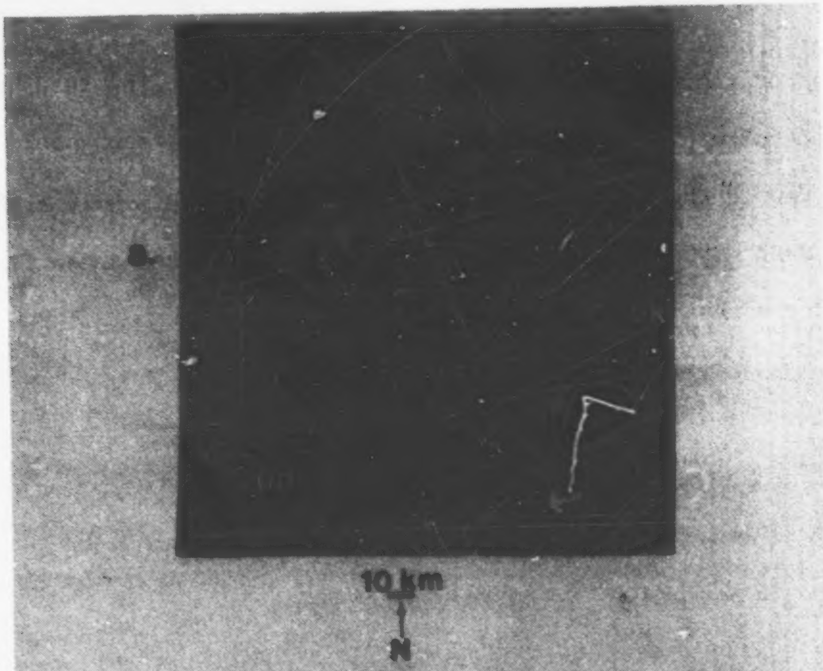
a
10 km
N

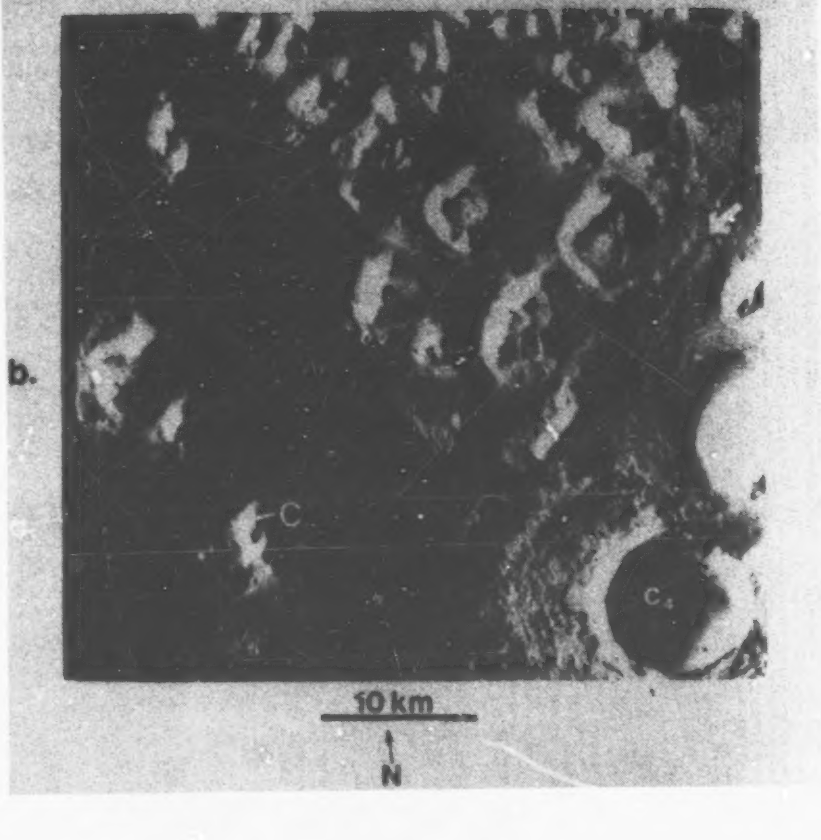
b.
C
C4
10 km
N

believed to represent more resistant remnants of an underlying heavily cratered terrain.

A few of these knobs in the Cydonia region have summit craters (Fig. 38b). West (1974) and Frey et al. (1979) interpreted these features as cinder cones.

GEOLOGIC HISTORY

Before concluding with an interpretation of the geologic history of the quadrangle, it is important to mention a point that was brought up by Milton (1976) and re-emphasized by Guest et al. (1977). Milton indicated that it is often difficult to distinguish between the age of an erosional surface and the rock units exposed on that surface. From mapping in the Cydonia region, Guest et al. (1977 p. 4119) concluded: "The northern 'plains' are composed of an intricate mixture of young rock units, young surfaces cut in old rocks that have been modified by surface processes such as wind, permafrost, etc., and old exhumed rock surfaces probably equivalent in age to units exposed in the southern cratered highlands of Mars."

Early Cratering

The process that dominated throughout the early history of the Mare Acidalium quadrangle was undoubtedly impact cratering. The oldest surfaces exposed in the quadrangle, as indicated by crater density, are the cratered plateau to the southeast and the slightly younger rugged plateau to the southwest. Both units have many large (up to 120 km) degraded craters of c_1 and c_2 age. Many of the old craters, however, were subsequently buried or partly buried by volcanic or eolian material or both. This resurfacing took place before the craters of c_3 age were formed inasmuch as c_3 craters are superimposed on the surface and show little evidence of modification.

Outgassing

Soderblom and Wenner (1978) suggested that during planetary outgassing water was injected into the upper few kilometers of the crust by subsurface igneous activity, surface volcanic eruptions, and lateral migration of liquid and vapor. Many geomorphic features that occur on these older plateau surfaces such as the small channels, irregular depressions, and floor-fractured craters, suggest that the materials that make up these two surfaces were rich in volatile substances.

Early Volcanism

Sometime after the rugged plateau surface was formed, the lavas and eolian materials that formed the fractured plateau and the ridged plateau were emplaced. The faults of the fractured plateau are a part of the Tempe Fossae system that extends to the southwest. This fault system is relatively old because it predates the emplacement of the smooth plains material. Other faults to the south that are oriented in a more east-west direction cut both plateau and plains materials, and, therfore, are considerably younger. Wise (1979), based on mapping of the adjacent MC-3 quadrangle stated: "The cause for localization of the older fault system of Tempe Fossae is unknown, although the alignment of three younger giant volcanoes of Tharsis southwestward along this line suggests that the fault system may reflect an extensive zone of deep curstal weakness."

Scarp Formation

The formation of the boundary between the intensely cratered southern hemisphere and the lightly cratered northern lowlands must have occurred sometime after the emplacement of the youngest plateau material. This boundary may be the result of collapse and erosion of an ice-rich layer in the northern region (Soderblom and Wenner, 1978), the result of more global processes such as differentiation that produced a crust of varied thickness (Mutch et al., 1976; Carr, 1980a), or sub-crustal erosion and subsidence of the northern region (Wise et al., 1979). The large depression of Acidalia Planitia was suggested to be the result of crustal subsidence caused by uplifting and volcanism of the Tharsis region to the southwest (Carr, 1974; Phillips and Saunders, 1975).

Scarp Retreat and Formation of Plains Units

The knobby terrain materials that occur in large patches near the southeast plateau-plains boundary have been interpreted as erosional remnants of the higher plateau material that were left by erosion and scarp retreat. Dissected and fractured plateau materials and associated knobby terrain exist 800 kilometers northwest of the southwest cratered plateau and 1000 kilometers east of the southwest plateau province. These materials may also be erosional remnants of the plateau suggesting that the highlands material, at one time, extended over much of the plains region. This supports the mechanism of deterioration of an ice-rich layer and concomitant scarp retreat proposed by Soderblom and Wenner (1978) for the formation of the plateau-plains boundary. Much of the material that forms some of the plains units may have been derived from the breakdown of the plateau.

The age relationships between the plains material are difficult to determine for several reasons. Boundary escarpments or embayment relationships are rare. The boundaries between the units are commonly gradational, reflecting only albedo or textural variations, or both.

Crater size-frequency distributions for all the plains units tend to follow the same general trend suggesting that most of the plains surfaces were exposed or emplaced during the same general time interval. Alternatively, the crater statistics may not represent accurate age relationships because of the complexity of the depositional and erosional events that have occurred. Almost all of the craters that occur on the plains are c_3 or younger.

Although the mottled plains occur some 1,000 km north of the highlands, Scott (1979, p. 3052) proposed that the plains may be a part of this surface. He stated:"Possibly the mottled plains unit represents lower, more deeply eroded remnants of the highlands that have survived an ancient episode of crustal separation caused by drifting or downfaulting and followed by volcanism with flood basalts filling the intervening region and forming smoother plains between the segregated parts of the crust." It is apparent that the mottled plains - undivided and the hummocky mottled plains have been blanketed with a light-colored debris mantle that has been partially stripped away. Whether the underlying darker material is an old erosional surface or younger, volcanic material is uncertain. The knobby plains resemble these northern mottled plains units in that the knobby plains are rocks of uncertain age that have subsequently been blanketed with a layer of light material.

The patterned mottled plains are more likely to represent younger plains material rather than old rock exposed by erosion. The low albedo and the presence of many small, cratered domes suggest that these may be vast volcanic plains that were subsequently fractured by tectonic, desiccation, or permafrost processes. The pattern, however, appears to be fairly old because few of the superimposed impact craters were affected by the fracturing.

The subdued patterned mottled plains represent a more recent period of volcanic activity that caused lava flows to bury partially some of the troughs of the patterned mottled plains. These flows embayed and partially buried parts of the dissected and fractured plateau material that occurs in this central region.

The fractured plains are another example of the problem of material age vs. surface age. Guest et al. (1977) suggested that the fractured plains material is an old unit stratigraphically underlying the plateau material. The fractured plains surface was exposed by erosion and scarp retreat, with the fractures forming after the surface was exposed. The present investigation suggests that part of the fractured plains surface may consist of younger volcanic or eolian material. Boundary escarpments, where the fractured plains form the lower surface, indicate that the fractured plains are old in relation to some of the adjacent units.

The pattern of troughs on the smooth plains adjacent to the patterned mottled plains and in close proximity to the fractured plains suggest that some of the smooth plains material was emplaced at approximately the same time as the patterned mottled plains. Part of the material that makes up the smooth plains may have been derived from the breakdown of the plateau. The presence of relics of large circular structures suggest that the smooth plains material in the central region buried a lower, more heavily cratered surface.

To the southwest, large-scale flooding and erosion associated with Kasei Vallis and other large outflow channels to the south were occuring either during or shortly after the emplacement of the majority of the plains material. This flooding may have contributed a large quantity of alluvial material to the smooth plains. Fluvial erosion created streamlined landforms, scours, and channels, and exposed layers of lower plateau material along the plateau-plains escarpment.

Tectonism

Tectonic stresses, probably the result of the Tharsis-related stress system, created north-south trending mare-type ridges that occur on both the plateau and the smooth plains in the southwestern region. Later, more tectonic activity resulted in east-west trending fractures that occur on both the plateau and the plains, as these fractures also extend across the mare-type ridges.

Farther north, the plateau-plains escarpment, streamlined landforms, erosional remnants, and tectonic features do not occur. Smooth plains material covers a narrow region between northeast Tempe Plateau and the mottled plains. Circular outlines on the smooth plains together with the embayment of grabens on the plateau by smooth plains materials, suggest that the smooth plains material buried the older plateau material in this region. Perhaps the smooth plains material was deposited in a gentle depression that existed along the plateau - mottled plains boundary. Also occurring in this region are sinuous channels and fan-shaped deposits of light material. These features are believed to be the result of subsequent small-scale drainage and deposition of material from the highland block.

In the Cydonia region, the smooth plains differ from those to the west. A high density of small cratered domes and the gradational boundary with the subdued fractured plains, which are believed to be lava flows that partially fill the troughs, suggest that the smooth plains in this region may consist of volcanic material.

The origin of the variegated plains to the east is probably similar to that of the smooth plains, i.e., some of the material that constitutes these plains may be volcanic, whereas the variegated plains along the plateau-plains boundary may be partly alluvial and colluvial material deposited from drainage of the highland block. The emplacement of the variegated plains is believed to postdate the creation of the fractured plains because of the escarpment boundary; however, the age-relationship between the variegated plains and the patterned mottled plains to the north is uncertain.

Late Volcanism

Many of the volcanic features, i.e., lava flows, pressure ridges, and domes, that are scattered throughout the plains region appear to have formed recently because they show little subsequent modification. The proposed tablemountains and moberg ridges are associated with these young volcanic features and require the presence of an ice-rich unit to form. Clifford (1980) and Hodges and Moore (1979) proposed that a primitive ice sheet may have, at one time, covered a significant portion of the planet's surface. The ice sheet subsequently retreated in response to climatic changes, and the water from this ice sheet is presently stored in the groundwater system and in the polar caps. If this hypothesis is correct, then many of the unusual surface textures and features that occur on the lowland plains could be explained by the breakdown and removal of this ice-rich layer.

Recent Processes

Currently eolian erosion and deposition and mass wasting are the dominant processes within this region. Although many other processes are active, they do not play the determining role they once did. The margins of the plateaus and the knobby terrain are areas where permafrost decay and mass movement processes are creating collapse pits and debris flows. Freezing and thawing of the surface continue to produce small-scale permafrost features such as pingos and ice-wedge polygons. Tectonism and volcanism may also be active geologic processes.

SUMMARY AND CONCLUSIONS

High-resolution Viking orbiter images show the geology of the Mare Acidalium quadrangle to be much more complex than previously had been suspected from the lower-resolution Mariner 9 images. Two major terrain types exist within the quadrangle; the higher, heavily-cratered plateau province, and the lower, lightly-cratered plains province. Both provinces can be subdivided into a number of material units. The plateau province consists of six units: (1) cratered plateau material, (2) dissected and fractured plateau material, (3) rugged plateau material, (4) ridged plateau material, (5) fractured plateau material, and (6) lower plateau material. The plains province consists of nine units: (1) mottled plains material - undivided, (2) hummocky mottled plains material, (3) patterned mottled plains material, (4) subdued patterned mottled plains material, (5) knobby plains material, (6) fractured plains material, (7) variegated plains material, (8) smooth plains material, and (9) patterned smooth plains material.

The oldest surfaces in the quadrangle occur in the southeast and southwest plateau regions. These surfaces record an early period when large impacts were extremely common. Subsequently, these regions were partially or completely buried by younger materials. To the west, the Tempe Plateau region was disrupted by faulting, possibly related to an early stage of Tharsis tectonism.

The central part of the quadrangle may have subsided in response to uplift of the Tharsis region to the southwest. Plateau material that once covered a large portion of the quadrangle began to break down and erode, leaving only erosional remnants of the higher surface scattered throughout the lowland region.

Volcanic, eolian, and alluvial sediments resurfaced a large portion of the lower plains. Processes such as wind, permafrost, mass movement, and tectonism created unusual and varied surface textures. Episodic floods of water from the large outflow channels to the south and west modified the surface in the southwest region, creating streamlined landforms and exposing the lower units of the plateau. Also, in this southwest region, tectonic activity associated with Tharsis-related stresses created mare-type ridges and east-west trending fractures. At the present time, wind erosion and deposition are the major processes active at the surface, although other processes such as tectonism, volcanism, mass movement, and periglacial activity may still play a role in molding the martian surface.

REFERENCES CITED

Allen, C. C., 1979a, Areal distribution of martian rampart craters: Icarus, v. 39, p. 111-123.

Allen, C. C., 1979b, Volcano-ice interactions on Mars: Jour. Geophys. Res., v. 84, no. B14, p. 8048-8059.

Allen, C. C., 1980, Volcano-ice interactions on the Earth and Mars: NASA Tech. Memo. 81979, p. 261-264.

Anders, E., and Owen, T., 1977, Mars and Earth: Origin and abundance of volatiles: Science, v. 198, p. 453-465.

Anderson, D. M., Gaffney, E. S., and Low, P. F., 1967, Frost phenomena on Mars: Science, v. 155, p. 319-322.

Anderson, D. M., Gatto, L. W., and Ugolini, F., 1973, An examination of Mariner 6 and 7 imagery for evidence of permafrost terrain on Mars: in Permafrost: The North American Contribution to the Second International Conference, Nat. Acad. Sci., U.S.A., p. 449-508.

Antoniadi. E. M., 1930, La planète Mars: Herman et Cie, Paris, p. 1659-1929.

Arvidson, R. E., 1972, Aeolian processes on Mars: Erosive velocities, settling velocities, and yellow clouds: Geol. Soc. America Bull., v. 83, p. 340-350.

Arvidson, R. E., Boyce, J. M., Chapman, C., Cintala, M., Fulchignoni, M., Moore, H., Neukum, G., Schultz, P., Soderblom, L., Strom, R., Woronow, A., and Young, R., 1978, Standard techniques for presentation and analysis of crater size-frequency data: NASA Tech. Memo. 79730, 20 p.

Arvidson, R. E., Carusi, A., Coradini, A., Fulchignoni, M., Federico, M., Funicello, R., and Salomone, M., 1976, Latitudinal variation of wind erosion of crater ejecta deposits on Mars: Icarus, v. 27, p. 503-516.

Baker, V. R., 1982, The channels on Mars: University of Texas Press, Austin, 198 p.

Baker, V. R., and Kochel, C., 1979, Martian channel morphology: Maja and Kasei vallis: Jour. Geophys. Res., v. 84, no. B14, p. 7961-7983.

Baker, V. R., and Milton, D. J., 1974, Erosion by catastrophic floods on Mars and Earth: Icarus, v. 23, p. 27-41.

Bates, R. L., and Jackson, J. A., eds., 1980, Glossary of geology: Am. Geol. Inst., Falls Church, Virginia, 749 p.

Biemann, K., Oro., J., Toulmin, P., Orgel, L. E., Nier, A. O., Anderson, D. M., Simmonds, P. G., Flory, D., Diaz, A. V., Rushneck, D. R., Biller, J. E., and Lafleur, A. L., 1977, The search for organic substances and inorganic volatile compounds in the surface of Mars: Jour. Geophys. Res., v. 82, no. 28, p. 4641-4662.

Botts, M. E., 1980, The stratigraphic sequence of volcanic and sedimentary units in the north polar region of Mars: NASA Tech. Memo. 81979, p. 265-326.

Briggs, G. A., Klausen, K., Thorpe, T., Wellman, J., and Baum, W., 1977, Martian dynamical phenomena during June-November 1976: Viking orbiter imaging results: Jour. Geophys. Res., v. 82, no. 28, p. 4121-4149.

Carr, M. H., 1974, Tectonism and volcanism of the Tharsis region of Mars: Jour. Geophys. Res., v. 79, no. 26, p. 3943-3949.

Carr, M. H., 1979, Formation of martian flood features by release of water from confined aquifers: Jour. Geophys. Res., v. 84, no. B14, p. 2295-3007.

Carr, M. H., 1980a, The geology of Mars: Am. Sci., v. 68, p. 626-635.

Carr, M. H., 1980b, The morphology of the martian surface: Space Sci. Rev., v. 25, p. 231-284.

Carr, M. H., 1981, The surface of Mars: Yale University Press, New Haven and London, 226 p.

Carr, M. H., Baum, W. A., Blasius, K. R., Briggs, G. A., Cutts, J. A., Duxbury, T. C., Greeley, R., Guest, J., Masursky, H., Smith, B. A., Soderblom, L. A., Veverka, J., and Wellman, J. B., 1980, Viking orbiter views of Mars: NASA SP-441, p. 1-181.

Carr, M. H., and Clow, G. D., 1981, Martian channels and valleys: Their characteristics, distribution, and age: Icarus, v. 48, p. 91-117.

Carr, M. H., Crumpler, L. S., Cutts, J. A., Greeley, R., Guest, J. E., and Masursky, H., 1977, Martian impact craters and emplacement of ejecta by surface flow: Jour. Geophys. Res., v. 82, no. 28, p. 4055-4065.

Carr, M. H., Masursky, H., and Saunders, R. S., 1973, A generalized geologic map of Mars: Jour. Geophys. Res., v. 78, no. 20, p. 4031-4036.

Carr, M. H., and Schaber, G. G., 1977, Martian permafrost features: Jour. Geophys. Res., v. 82, no. 28, p. 4039-4054.

Clifford, S. M., 1980, A model for the removal and subsurface storage of a primitive martian ice sheet: NASA Tech. Memo. 82385, p. 405-407.

Coradini, M. and Flamini, E., 1979, A thermodynamical study of the martian permafrost: Jour. Geophys. Res., v. 84, no. B14, p. 8115-8130.

Davis, P. A., Roddy, D. J., and Witbeck, N. E., 1981, Martian crater-form topography on Tempe Terra: NASA Tech. Memo. 84211, p. 99-101.

Dial, A., 1982, Geologic map of the Mare Boreum quadrangle of Mars: U.S. Geol. Survey Misc. Geol. Inv. Map (in preparation).

Fagen, J. J., Weiss, D., Steiner, J., and Franke, O. L., 1981, Subsidence depressions on martian plateau terrains: NASA Tech. Memo. 84211, p. 308-311.

Fairbridge, R. H., ed., 1968, The encyclopedia of geomorphology: Reinhold Book Corporation, New York, 1295 p.

Fanale, F. P., 1976, Martian volatiles: Their degassing history and geochemical fate: Icarus, v. 28, p. 179-202.

Farmer, C. B., and Doms., P. E., 1979, Global seasonal variation of water vapor on Mars and the implications for permafrost: Jour. Geophys. Res., v. 84, no. B14, p. 2881-2888.

Franke, O. L., Steiner, J., Weiss, D., and Fagen, J. J., 1981, A preliminary survey of slope and related features at and near the boundary between the plateau-fretted terrain and northern plains of Mars: NASA Tech. Memo. 84211, p. 319-320.

Frey, H., and Jarosewich, M., 1981, Small cones on Mars: Distribution and properties: in Papers Presented to the Third International Colloquium on Mars: Lunar Planet. Inst. Contribution 441, p. 84-86.

Frey, H., Lowry, B. L., and Chase, S. H., 1979, Pseudocraters on Mars: Jour. Geophys. Res., v. 84, no. B14, p. 8075-8086.

Gatto, L. W., and Anderson, D. M., 1975, Alaskan thermokarst terrain and possible martian analog: Science, v. 188, p. 255-257.

Gault, D. E. and Greeley, R., 1978, Exploratory experiments of impact craters formed in viscous liquid targets: Analogs for martian rampart craters?: Icarus, v. 34, p. 486-495.

Gifford, A. W., 1981, Ridge systems of Mars: NASA Tech. Memo. 84412, p. 221-363.

Goody, R., and Belton, J. J. S., 1967, Radiative relaxation times for Mars: A discussion of martian atmospheric dynamics: Planet. Space Sci., v. 15, p. 247-256.

Greeley, R. and Spudis, P., 1978, Volcanism in the cratered terrain hemisphere of Mars: Geophys. Res. Lett., v. 5, p. 453-455.

Greeley, R., and Spudis, P. D., 1981, Volcanism on Mars: Rev. Geophys. Space Phys., v. 19, no. 1, p. 13-41.

Greeley, R., Theilig, E., Guest, J. E., Carr, M. H., Masursky, H., and Cutts, J. A., 1977, Geology of Chryse Planitia: Jour. Geophys. Res., v. 82, no. 28, p. 4093-4109.

Guest, J. E., Butterworth, P. S., and Greeley, R., 1977, Geological observations in the Cydonia region from Viking: Jour. Geophys. Res., v. 82, no. 28, p. 4111-4120.

Head, J. W., and Roth, R., 1976, Mars pedestal crater escarpments: Evidence for ejecta related emplacement: in Papers presented to the Symposium on Planetary Cratering Mechanics, Lunar Sci. Inst., Houston, p. 50-52.

Head, J. W., Wood, C. A., and Mutch, T. A., 1977, Geologic evolution of the terrestrial planets: Am. Sci., v. 65, p. 21-29.

Helfenstein, P., 1980, Martian fractured terrain: Possible consequences of ice-heaving: NASA Tech. Memo. 82385, p. 373-375.

Helfenstein, P. and Mouginis-Mark, P. J., 1980, Morphology and distribution of fractured terrain on Mars: abs., Lunar Planet. Sci. Conf. 11th, p. 429-431.

Hodges, C. A., 1973, Mare ridges and lava lakes, Apollo 17 Preliminary Science Report: NASA SP-330, p. 31-12 to 31-21.

Hodges, C. A., 1979, Some lesser volcanic provinces on Mars: NASA Tech. Memo. 80339, p. 248-249.

Hodges, C. A., and Moore, H. J., 1978, Tablemountains of Mars: abs., Lunar Planet. Sci., Conf. 9th, p. 523-525.

Hodges, C. A., and Moore, H. J., 1979, The subglacial birth of Olympus Mons and its aureoles: Jour. Geophys. Res., v. 84, no. B14, p. 8061-8074.

Howard, K. A., and Muehlberger, W. R., 1973, Lunar thrust faults in the Taurus-Littrow region, Apollo 17 Preliminary Science Report: NASA SP-330, p. 31-22 to 31-25.

Hoyt, W. G., 1976, Lowell and Mars: University of Arizona Press, Tucson, 376 p.

Kieffer, H. H., Martin, T. Z., Peterfreund, A. P., and Jakosty, B. M., 1977, Thermal and albedo mapping of Mars during the Viking primary mission: Jour. Geophys. Res., v. 82, no. 28, p. 4249-4291.

Leighton, R. B., and Murray, B. C., 1966, Behavior of carbon dioxide and other volatiles on Mars: Science, v. 153, p. 136-144.

Leovy, C. B., and Briggs, G. A., 1974, Clouds of Mars: in Mars as viewed by Mariner 9: NASA SP-329, p. 149-161.

Lucchitta,B. K., 1976, Mare ridges and related highland scarps-result of vertical tectonism?: Proc. Lunar Planet. Sci. Conf. 7th, p. 2761-2782.

Lucchitta, B. K., 1977, Topography, structure, and mare ridges in southern Mare Imbrium and northern Oceanus Procellarum: Proc. Lunar Planet. Sci. Conf. 8th, p. 2691-2703.

Lucchitta, B. K., 1978, Geologic map of the Ismenius Lacus quadrangle of Mars: U.S. Geol. Survey Misc. Geol. Inv. Map, I-1065.

Lucchitta, B. K., 1981, Mars and Earth: Comparison of cold-climate features: Icarus, v. 45, p. 264-303.

Lucchitta, B. K., and Klockenbrink, J. L., 1981, Ridges and scarps in the equatorial belt of Mars: Moon and Planets, v. 24, p. 415-429.

Masursky, H., 1973, An overview of geological results from Mariner 9: Jour. Geophys. Res., v. 78, no. 20, p. 4009-4030.

Masursky, H., Boyce, J. M., Dial, A. L., Schaber, G. G., and Strobell, M. E., 1977, Classification and time of formation of martian channels based on Viking data: Jour. Geophys. Res., v. 82, no. 28, p. 4016-4038.

Masursky, H., and Cradbill, N. L., 1976, Search for the Viking 2 landing site: Science, v. 194, p. 62-68.

McCauley, J. F., 1973, Mariner 9 evidence for wind erosion in the equatorial and mid-latitude regions of Mars: Jour. Geophys. Res., v. 78, no. 20, p. 4123-4137.

McCauley, J. F., Carr, M. H., Cutts, J. A., Hartmann, W. K., Masursky, H., Milton, D. J., Sharp, R. P., and Wilhelms, D. E., 1972, Preliminary Mariner 9 report on the geology of Mars: Icarus, v. 17, p. 289-327.

McElroy, M. B., Kong, T. Y., and Yung, Y. L., 1977, Photochemistry and evolution of Mars' atmosphere: A Viking perspective: Jour. Geophys. Res., v. 82, no. 28, p. 4379-4388.

McGill, G. E., 1977, Craters as "fossils": The remote dating of planetary surface materials: Geol. Soc. America Bull., v. 88, p. 1102-1110.

Milton, D. J., 1973, Water and processes of degradation in the martian landscape: Jour. Geophys. Res., v. 78, no. 20, p. 4037-4047.

Milton, D. J., 1976, Geologic map of the Lunae Palus quadrangle of Mars: U.S. Geol. Survey Misc. Geol. Map, I-894.

Morris, E. C., and Underwood, J. R., Jr., 1978, Polygonal fractures of the martian plains: NASA Tech. Memo. 79729, p. 97-99.

Mouginis-Mark, P. J., 1979, Ejecta emplacement of the martian impact crater Bamberg: Proc. Lunar Planet. Sci. Conf. 10th, p. 2651-2668.

Mouginis-Mark, P. J. and Carey, D. L., 1980, Crater studies in the northern plains of Mars: Thickness estimates of fluidized ejecta deposits: NASA Tech. Memo. 81776, p. 105-107.

Mutch, P. and Woronow, A., 1980, Emplacement of martian rampart and pedestal ejecta blankets: NASA Tech. Memo. 81776, p. 96-98.

Mutch, T. A., Arvidson, R. E., Head, J. W., Jones, K. L., and Saunders, R. S., 1976, The geology of Mars: Princeton University Press, Princeton, 400 p.

Neukum, G., and Hiller, K., 1981, Martian ages: Jour. Geophys. Res., v. 84, no. B4, p. 3097-3121.

Neukum, G., and Wise, D. U., 1976, Mars: A standard crater curve and possible new time scale: Science, v. 197, p. 1381-1387.

Nummedal, D., 1976, Fluvial erosion on Mars, a review paper presented at Colloquium on Water in Planetary Regoliths: Planet. Geol. Program, NASA, Hanover, N.H., p. 47-54.

Owen, T., and Biemann, K., 1976, Composition of the atmosphere at the surface of Mars: Detection of Argon-36 and preliminary results: Science, v. 193, p. 801-803.

Pechmann, J. C., 1980, The origin of polygonal troughs on the northern plains of Mars: Icarus, v. 42, p. 185-210.

Phillips, R. J., and Saunders, R. S., 1975, The isostatic state of martian topography: Jour. Geophys. Res., v. 80, no. 20, p. 2893-2898.

Pieri, D. C., 1980, Geomorphology of martian valleys: NASA Tech. Memo. 81979, p. 1-160.

Pollack, J. B., and Black, D. C., 1979, Implications of the gas composition measurements of Pioneer Venus for the origin of planetary atmospheres: Science, v. 205, p. 56-59.

Quaide, W., 1965, Rilles, ridges, and domes - clues to maria history: Icarus, v. 4, p. 374-389.

Roddy, D. J., 1977, Large scale impact and explosion craters: Comparison of morphological and structural analogs, in Impact and Explosion Cratering, Pergamon Press, New York, p. 185-246.

Rossbacher, L. A., and Judson, S., 1981, Ground ice on Mars: Inventory, distribution, and resulting landforms: Icarus, v. 45, p. 39-59.

Schiaparelli, G. V., 1878, Osservazioni astronomiche e fisiche sull' asse di rotazione e sulla topografia del planete Marte: Atti della R. Academia dei Lincei Memoria della ce. di Scienze Fisiche. mem. 1, ser. 3, v. 10, p. 308-439.

Schultz, P. H., and Glicken, H., 1979, Impact craters and basin control of igneous processes on Mars: Jour. Geophys. Res., v. 84, no. B14, p. 8033-8047.

Scott, D. H., 1976, Geologic maps of the Cydonia region of Mars: Prime B Viking landing site: Open File Rep., 76-500, U.S. Geol. Survey, Reston, VA.

Scott, D. H., 1978, Mars, highlands-lowlands: Viking contribution to Mariner relative age studies: Icarus, v. 34, p. 279-285.

Scott, D. H., 1979, Geologic problems in the northern plains of Mars: Proc. Lunar Planet. Sci. Conf. 10th, p. 3039-3054.

Scott, D. H., and Carr, M. H., 1978, Geologic map of Mars: U. S. Geol. Survey Misc. Geol. Inv. Map, I-1083.

Scott, D. H., and Tanaka, K. L., 1980, Mars stratigraphy: Lowland plains and Valles Marineris: NASA Tech. Memo. 82385, p. 104-106.

Sharp, R. P., 1973, Mars: Fretted and chaotic terrains: Jour. Geophys. Res., v. 78, no. 20, p. 4073-4083.

Sharp, R. P., 1974, Ice on Mars: Jour. Glaciology, v. 13, no. 68, p. 173-185.

Sharpton, V. L., and Head, J. W., 1980, Lunar mare arches and ridges: Relation of ridge lobes to small pre-existing craters: abs., Lunar Planet. Sci. Conf. 11th, p. 1024-1026.

Snyder, C. W., 1979, The planet Mars as seen at the end of the Viking mission: Jour. Geophys. Res., v. 84, no. B14, p. 8487-8519.

Soderblom, L. A., Kreidler, J. J., and Masursky, H., 1973, Latitudinal distribution of a debris mantle on the martian surface: Jour. Geophys. Res., v. 78, no. 20, p. 4117-4122.

Soderblom, L. A., Malin, M. C., Cutts, J. A., and Murray, B. C., 1973, Mariner 9 observations of the surface of Mars in the north polar region: Jour. Geophys. Res., v. 78, no. 20, p. 4197-4210.

Soderblom, L. A., and Wenner, D. B., 1978, Possible fossil water liquid-ice interfaces in the martian crust: Icarus, v. 34, p. 622-637.

Soderblom, L. A., West, R. A., Hesman, B. M., Kreidler, J. J., and Condit, C. D., 1974, Martian planetwide crater distributions; Implications for geologic history and surface processes: Icarus, v. 22, p. 239-263.

Solomon, S. C., and Chaiken, J., 1976, Thermal expansion and thermal stress in the Moon and terrestrial planets: Clues to early thermal history: Proc. Lunar Planet. Sci. Conf. 9th, p. 3229-3243.

Squyres, S. W., 1978, Martian fretted terrain: Flow of erosional debris: Icarus, v. 34, p. 600-613.

Strom, R. G., 1972, Lunar mare ridges, rings, and volcanic ring complexes: The Moon, p. 187-215.

Thomas, P., Veverka, J., Lee, S., and Bloom, A., 1981, Classification of wind streaks on Mars: Icarus, v. 45, p. 1214-1253.

Tsoar, H., Greeley, R., and Peterfreund, A. P., 1979, Mars: The north polar sand sea, and related wind patterns: Jour. Geophys. Res., v. 84, no. B14, p. 8167-8180.

Toksoz, M. N., and Hsui, A. T., 1978, Thermal history and evolution of Mars: Icarus, v. 34, p. 537-547.

Underwood, J. R., Jr., and Trask, N. J., 1978, Geologic map of the Mare Acidalium quadrangle of Mars: U.S. Geol. Survey Misc. Geol. Inv. Map, I-1048.

U.S. Geol. Survey, 1975, Shaded relief map of Mare Acidalium quadrangle of Mars, 1:5,000,000: U.S. Geol. Survey Misc. Inv. Map I-958.

U.S. Geol. Survey, 1976, High resolution Mariner 9 pictures in the Cydonia region of Mars, 1:250,000: U.S. Geol. Survey Misc. Inv. Map I-990.

U.S. Geol. Survey, 1976, Topographic map of the Cydonia region of Mars, 1:1,000,000: U.S. Geol. Survey Misc. Inv. Map I-988.

U.S. Geol. Survey, 1976, Topographic map of the Mare Acidalium quadrangle of Mars, 1:5,000,000: U. S. Geol. Survey Misc. Inv. Map I-979.

U.S. Geol. Survey, 1976, Topographic map of Mars, 1:25,000,000: U.S. Geol. Survey Misc. Inv. Map I-966.

U.S. Geol. Survey, 1981, Controlled photomosaic of the Mare Acidalium northwest quadrangle of Mars, 1:2,000,000: U.S. Geol. Survey Misc. Inv. Map I-1347.

U.S. Geol. Survey, 1981, Controlled photomosaic of the Mare Acidalium northeast quadrangle of Mars, 1:2,000,000: U.S. Geol. Survey Misc. Inv. Map I-1348.

U.S. Geol. Survey, 1981, Controlled photomosaic of the Mare Acidalium southwest quadrangle of Mars, 1:2,000,000: U.S. Geol. Survey Misc. Inv. Map I-1349.

U.S. Geol. Survey, 1981, Controlled photomosaic of the Mare Acidalium south-central quadrangle of Mars, 1:2,000,000: U.S. Geol. Survey Misc. Inv. Map I-1350.

U.S. Geol. Survey, 1981, Controlled photomosaic of the Mare Acidalium southeast quadrangle of Mars, 1:2,000,000: U.S. Geol. Survey Misc. Inv. Map I-1351.

Ward, A. W., 1978, Windforms and wind trends on Mars: An evaluation of martian surficial geology from Mariner 9 and Viking spacecraft television images: Ph.D. thesis, University of Washington, 201 p.

Ward, A. W., Doyle, K. B., Helm, P. J., Weisman, M. K., and Witbeck, N. E., 1982, Global map of eolian features on Mars: Jour. Geophys. Res., (in preparation).

Ward, A. W., Helm, P. J., Witbeck, N. E., and Weisman, M., 1980, Global digital map of eolian features on Mars: NASA Tech. Memo. 82385, p. 330-332.

C-2

West, M., 1974, Martian volcanism: Additional observations and evidence for pyroclastic activity: Icarus, v. 21, p. 1-11.

Wilhelms, D. E., 1976, Geologic map of Oxia Palus quadrangle of Mars: U.S. Geol. Survey Misc. Geol. Inv. Map, I-895.

Wise, D. U., 1979, Geologic map of the Arcadia quadrangle of Mars: U.S. Geol. Survey Misc. Geol. Inv. Map, I-1154.

Wise, D. U., Golombek, M. P., and McGill, G. E., 1979, Tectonic evolution of Mars: Jour. Geophys. Res., v. 84, no. B14, p. 7934-7939.

Wood, C. A., 1979, Monogenetic volcanoes of the terrestrial planets: Proc. Lunar Planet. Sci. Conf. 10th, 2815-2840.

ACKNOWLEDGMENTS

I would like to thank my thesis advisor, Dr. James R. Underwood, Jr. and members of my committee, Dr. George Clark, Dr. Charles Walters, and Dr. Larry Weaver for their valuable advice and criticism. I would also like to thank Dr. David H. Scott of the U.S. Geological Survey for his support and review of my thesis.

This research was funded by NASA and the U.S. Geological Survey. The research was conducted at Kansas State University and at the NASA Regional Data Center at the U.S. Geological Survey in Flagstaff, Arizona. I would like to thank Jody Swann and Anthony Sanchez of the U.S. Geological Survey for helping provide the needed images and photomosaics.

Finally, I would like to thank Joseph M. Boyce at NASA Headquarters for originally informing me of this project and his continued encouragement throughout the project.

APPENDIX

Three areas were mapped using high resolution photomosaics, and these maps are included as Appendices I - III. These areas are: (1) the Tempe Plateau region (centered at 52°N, 58°W); (2) the Central Plateau region (centered at 46°N, 26°W); and (3) the Cydonia region (centered at 40°N, 7°W). See Figure 7 for locations of high-resolution maps. Caution must be used when comparing the photomosaics with maps because the maps are larger scale to enable more detial to be shown. Appendix IV contains five subquadrangle maps and descriptions of all the units in Mare Acidalium Quadrangle. For reference purposes, representative Viking frame numbers are included in all map unit descriptions. Some of these images are included in the text and are so indicated. For reasons of space and cost, not all of the representatives images could be included.

ORIGINAL PAGE IS
OF POOR QUALITY

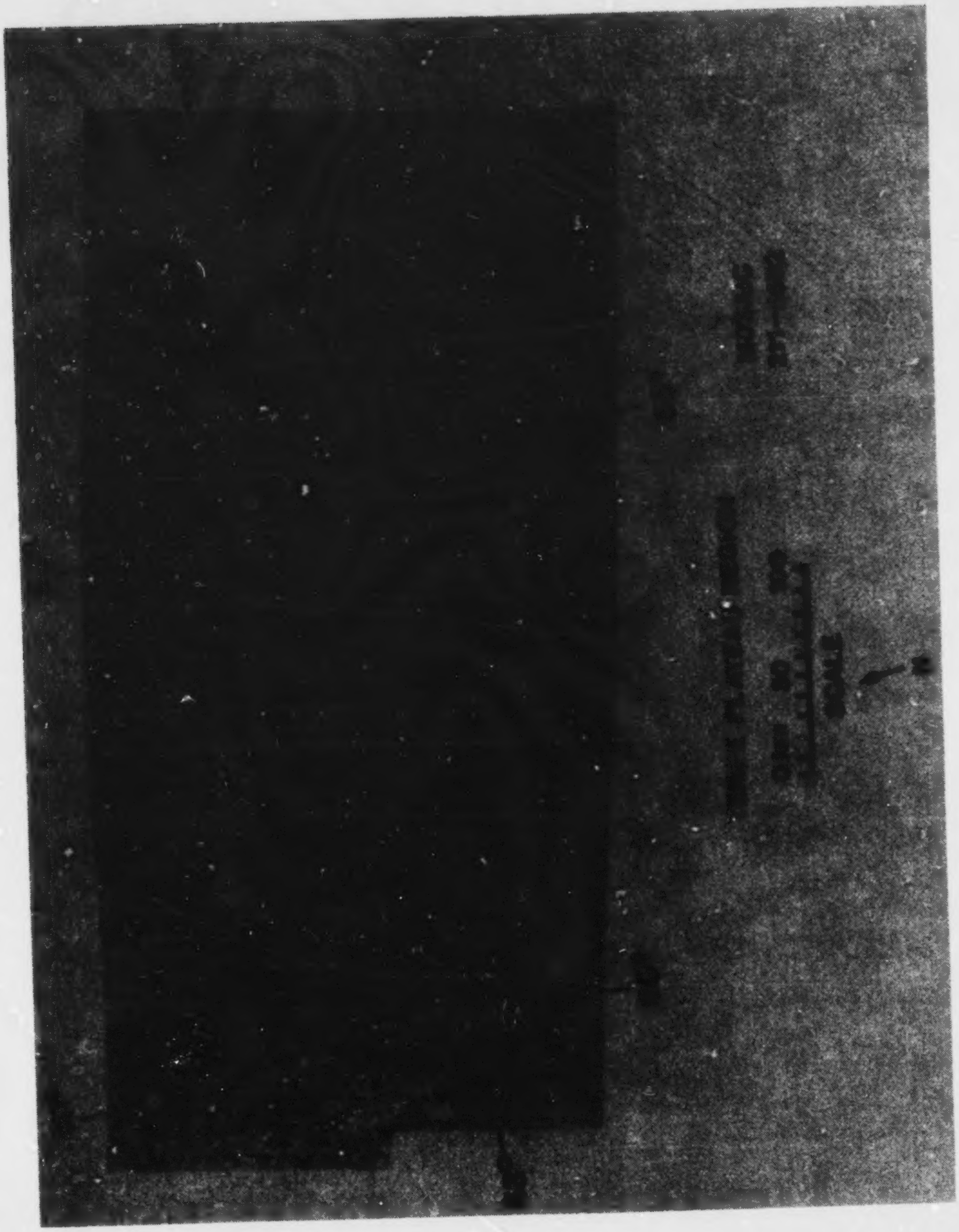

Figure 39. Photomosaic of the Tempe Plateau Region.

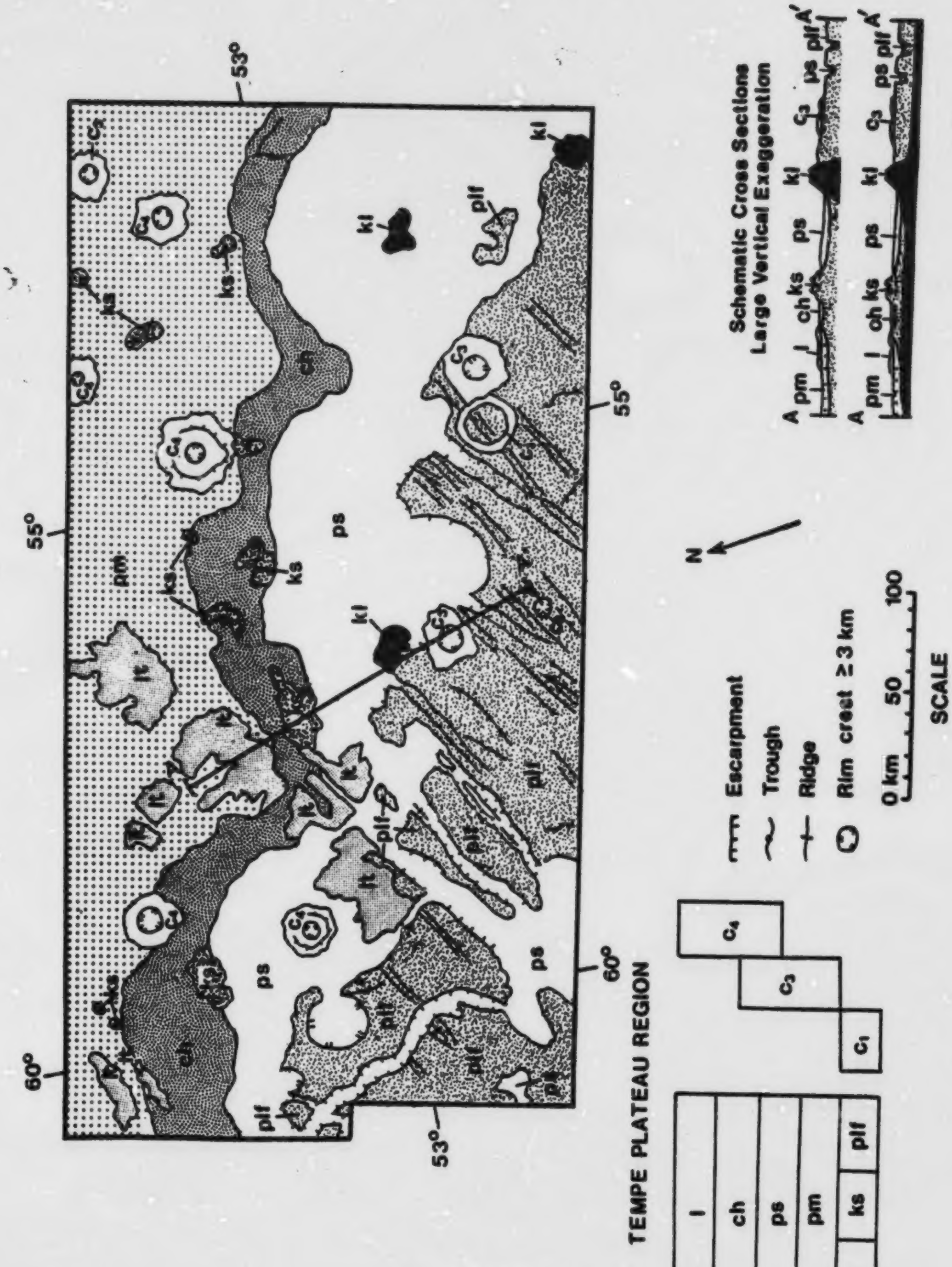
TEMPE PLATEAU REGION
l
ch
ps
pm
kl
ks
plf
c4
c3
c1
Escarpment
Trough
Ridge
Rim crest ≥ 3 km
0 km 50 100
SCALE
N
Schematic Cross Sections
Large Vertical Exaggeration
A
A'
53°
55°
60°

Figure 40. Geologic map of the Tempe Plateau region.

APPENDIX I - TEMPE PLATEAU REGION

plf	FRACTURED PLATEAU MATERIAL - Occurs in southern half of region; intermediate albedo; moderate crater density; forms high surface cut by numerous faults trending northeast-southwest; northwest-southeast trending sinuous depression cuts fractured plateau material at 53°N, 60°W (Fig. 17); boundary with lower smooth plains materials marked by escarpment; smooth plains materials embay grabens cut into fractured plateau material; representative image 61B56. INTERPRETATION: Volcanic and eolian material covering ancient crustal deposits; subsequently disrupted by Tempe Plateau faulting; faults cut older (c_1) impact craters.
kl	LARGE KNOBBY MATERIAL - Occurs in three locations close to, or at, the boundary between fractured plateau and smooth plains; forms small, elongate and equidimensional, steep-sided mountains (largest $\cong$ 10 km across) that rise above both plains and plateau material; representative image 61B56. INTERPRETATION: Volcanic material; alternatively may represent resistant volcanic, or other, material underlying fractured plateau and smooth plains material.
ks	SMALL KNOBBY MATERIAL - Occurs in small patches on plains north of fractured plateau; forms small ($<$ 1 km across), rounded hills or knobs that stand above surrounding plains materials;

representative image 61B55.

INTERPRETATION: Erosional remnants of higher surface material.

pm MOTTLED PLAINS MATERIAL - Occurs in northern part of area; low albedo; moderate crater density; relatively smooth plains with variegated-albedo pattern; ejecta blankets surrounding craters are generally higher albedo than surrounding plains; pedestal craters common; older c_3 craters partially filled with material; boundary with channel material marked by abrupt change to higher albedo; representative image 61B57.

INTERPRETATION: Volcanic and eolian plains; some small hills with summit craters may be volcanic; craters filled with eolian material suggest earlier existence of widespread eolian mantle, now largely deflated.

ps SMOOTH PLAINS MATERIAL - Occurs between fractured plateau and channel material; low albedo; low crater density; forms smooth plains; smaller craters (< 1 km diameter) partially filled with debris; small hills with summit craters at limit of resolution; escarpment commonly marks boundary with higher fractured plateau material; albedo change marks boundary with high-albedo channel material; representative image 61B52.

INTERPRETATION: Alluvial, eolian, and volcanic deposits; small hills with summit craters may be volcanic (Scott, 1978); plains materials fill sinuous channel cut into plateau and deeply embay grabens in fractured plateau; eolian material partially buries small impact craters.

ch CHANNEL MATERIAL - Occurs between mottled and smooth plains (Fig. 37b);high albedo; low crater density; fills elongate, sinuous, gentle depression ranging in width from 10 - 25 km; representative image 61B57.

INTERPRETATION: Stream channel containing alluvium (Scott and Tanaka, 1980).

lt LIGHT MATERIAL - Occurs in patches close to fractured plateau in western region; high albedo; very low crater density; light-colored material appears to overlie plains materials; fan-shaped deposit at 53.2°N, 58.8°W; representative image 61B52 (Fig. 17)

INTERPRETATION: Outwash of flood-plain deposits, the result of drainage of higher plateau surface.

Crater Material

All craters mapped believed to have been produced by impact; subdivisions based on morphologic characteristics believed to reflect relative age.

c_4	YOUNG CRATER MATERIAL - Sharp, complete rim crests; steep walls; deep, rough floors; bowl shape; extensive ejecta deposits; representative image 61B59. INTERPRETATION: Relatively recent impact-crater material.
c_3	MODERATELY YOUNG CRATER MATERIAL - Rim crest high, complete; walls relatively steep; floor may be rough and lower than adjacent terrain; ejecta deposits less extensive than c_4 craters; representative image 61B56. INTERPRETATION: Moderately young but slightly degraded impact-crater material.
c_1	OLD CRATER MATERIAL - Rim crest low, incomplete or nearly absent; shallow flat floors generally filled with younger material; commonly forms rugged and partially buried ring; little or no ejecta deposits; representative image 61B58. INTERPRETATION: Oldest, degraded impact-crater material.

Figure 41. Photomosaic of the Central Plateau Region.

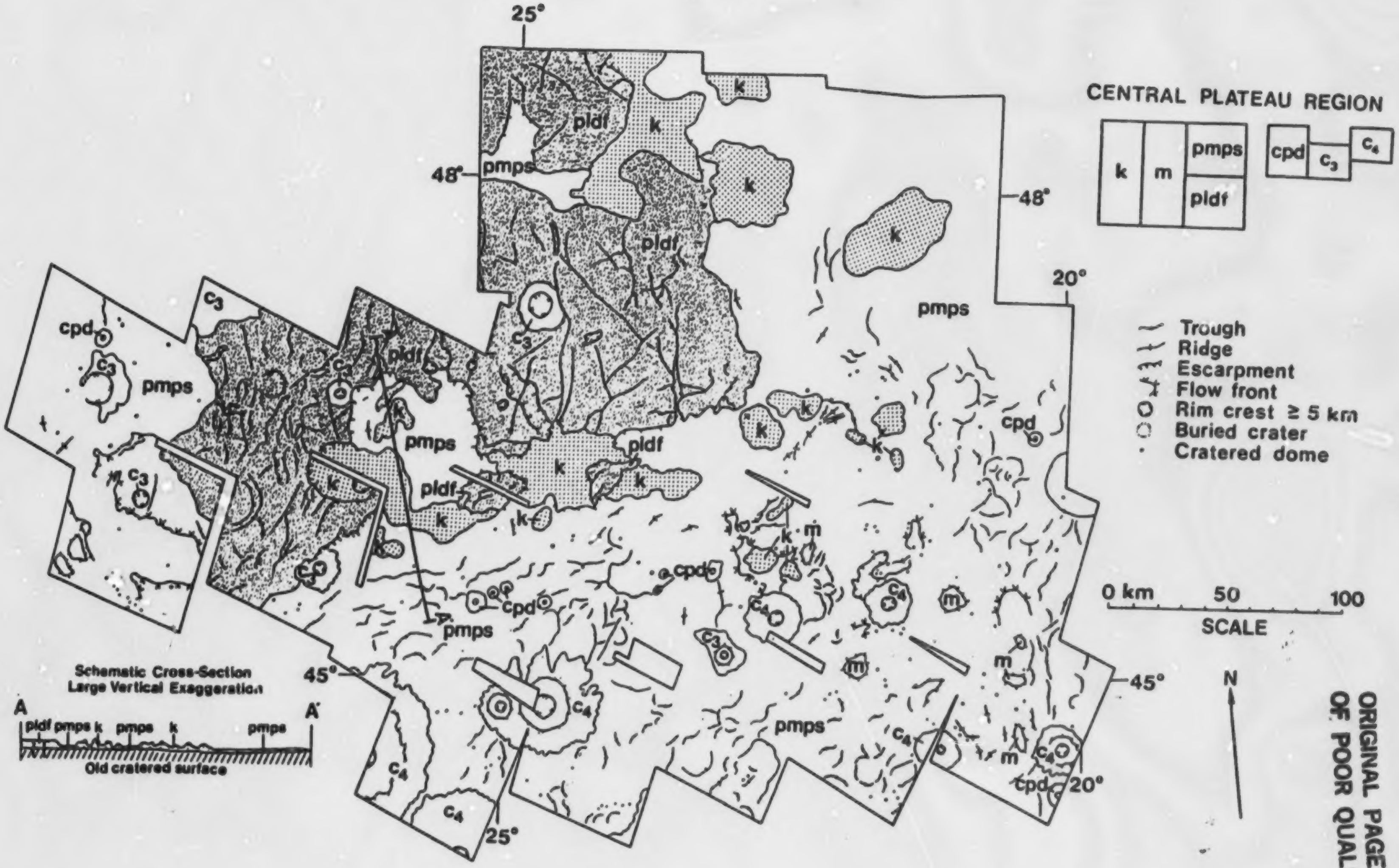
CENTRAL PLATEAU REGION
k
m
pmps
pldf
cpd
c_3
c_4
Trough
Ridge
Escarpment
Flow front
Rim crest ≥ 5 km
Buried crater
Cratered dome
0 km
50
100
SCALE
N
25°
48°
20°
45°
Schematic Cross-Section
Large Vertical Exaggeration
A
A'
pldf
pmps
k
Old cratered surface

Figure 42. Geologic map of the Central Plateau region.

ORIGINAL PAGE IS OF POOR QUALITY

APPENDIX II - CENTRAL PLATEAU REGION

pldf	DISSECTED AND FRACTURED PLATEAU MATERIAL - Forms high surface between 46° - 49°N and 22° - 28°W; intermediate to high albedo; low crater density; relatively smooth surface cut by many fractures that generally trend N - S; fracture width ranges from few hundred meters to more than 2 km; very few impact craters; escarpment characteristically marks the boundary of the plateau material with surrounding plains materials; representative image 35A35. INTERPRETATION: Remnants of higher unit that may have, at one time, covered region; circular depressions mark locations of large degraded craters; resurfaced by eolian and volcanic material; subsequently disrupted by faulting.
k	KNOBBY MATERIAL - Occurs adjacent to fractured and dissected plateau and in scattered patches on plains; low crater density; knobs are small, irregularly shaped hills (average 2 km across) similar in height to that of plateau; knobs occur individually and in clusters and stand above plains material; some conical hills have summit craters; representative image 35A41 (Fig. 26b). INTERPRETATION: Erosional remnants of plateau material; locally may be small volcanoes.
pmps	SUBDUED PATTERNED MOTTLED PLAINS MATERIAL - Surrounds dissected and fractured plateau and occupies circular depression bounded

by plateau and knobby material; very low albedo; moderate crater density; relatively smooth, dark plains cut by many discontinuous arcuate troughs generally < 1 km wide; pedestal craters common; high albedo flow-ejecta craters superimposed on plains; small (< 1 km wide) domes with summit craters common; representative image 26A27.

INTERPRETATION: Volcanic flow rock; possible flow fronts and pressure ridges occur in several areas (Figs. 26a, b); domes may be cinder cones; low dark hills with summit craters may be small shield volcanoes; volcanic material fills or partially fills pre-existing pattern of troughs.

m MESA MATERIAL - Forms isolated plateaus in region of subdued patterned mottled plains materials; low albedo; low, steep-sided, flat-topped mesas generally < 8 km across and several-hundred-meters high; several mesas have small knob or ridge on top; representative image 26A28 (Fig. 27b).

INTERPRETATION: Tablemountains resulting from subglacial volcanic eruptions; may have small cinder cones on top; alternatively may be erosional remnants of dissected and fractured plateau material

Crater Material

All craters mapped believed to have been produced by impact; subdivisions based on morphologic characteristics believed to reflect relative age.

c_4 YOUNG CRATER MATERIAL - Sharp, complete rim crests; steep walls; deep rough floors; bowl shape; extensive ejecta deposits; representative image 26A24.

INTERPRETATION: Relatively recent impact-crater material.

c_3 MODERATELY YOUNG CRATER MATERIAL - Rim crest high, complete; walls relatively steep; floors may be rough and lower than adjacent terrain; ejecta deposits less extensive than c_4 craters; representative image 26A26.

INTERPRETATION: Moderately young but slightly degraded impact-crater material.

cpd PEDESTAL CRATER MATERIAL - Small (< 5 km diameter) bowl-shaped crater; ejecta extends outward 2 - 3 crater diameters; ejecta forms platform that stands above surrounding terrain; representative image 35A36.

INTERPRETATION: Impact-crater material with associated viscous ejecta flow; flow too viscous to form lobes (Mutch and Woronow, 1980).

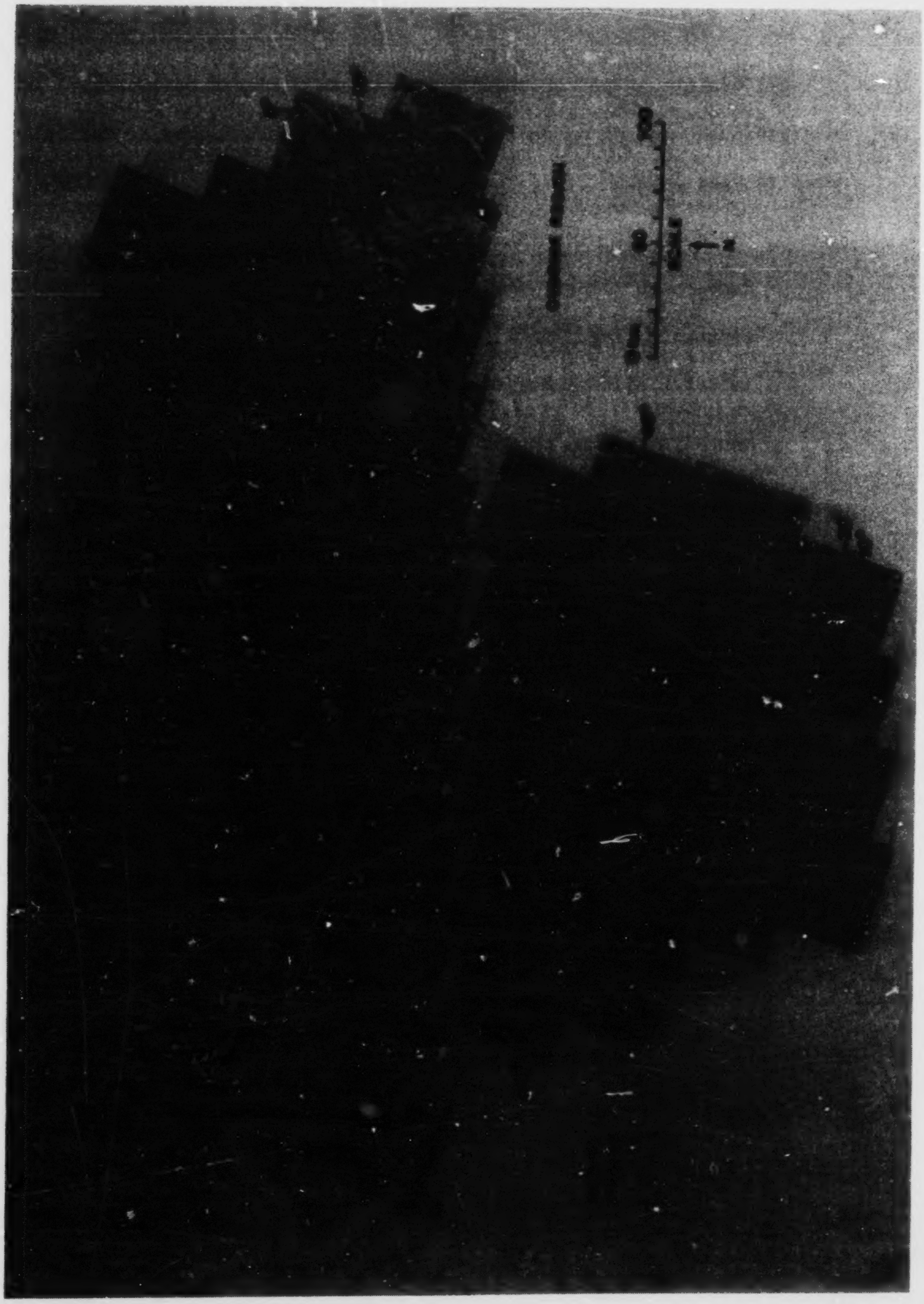

Figure 43. Photomosaic of the Cydonia Region.

ORIGINAL PAGE IS
OF POOR QUALITY

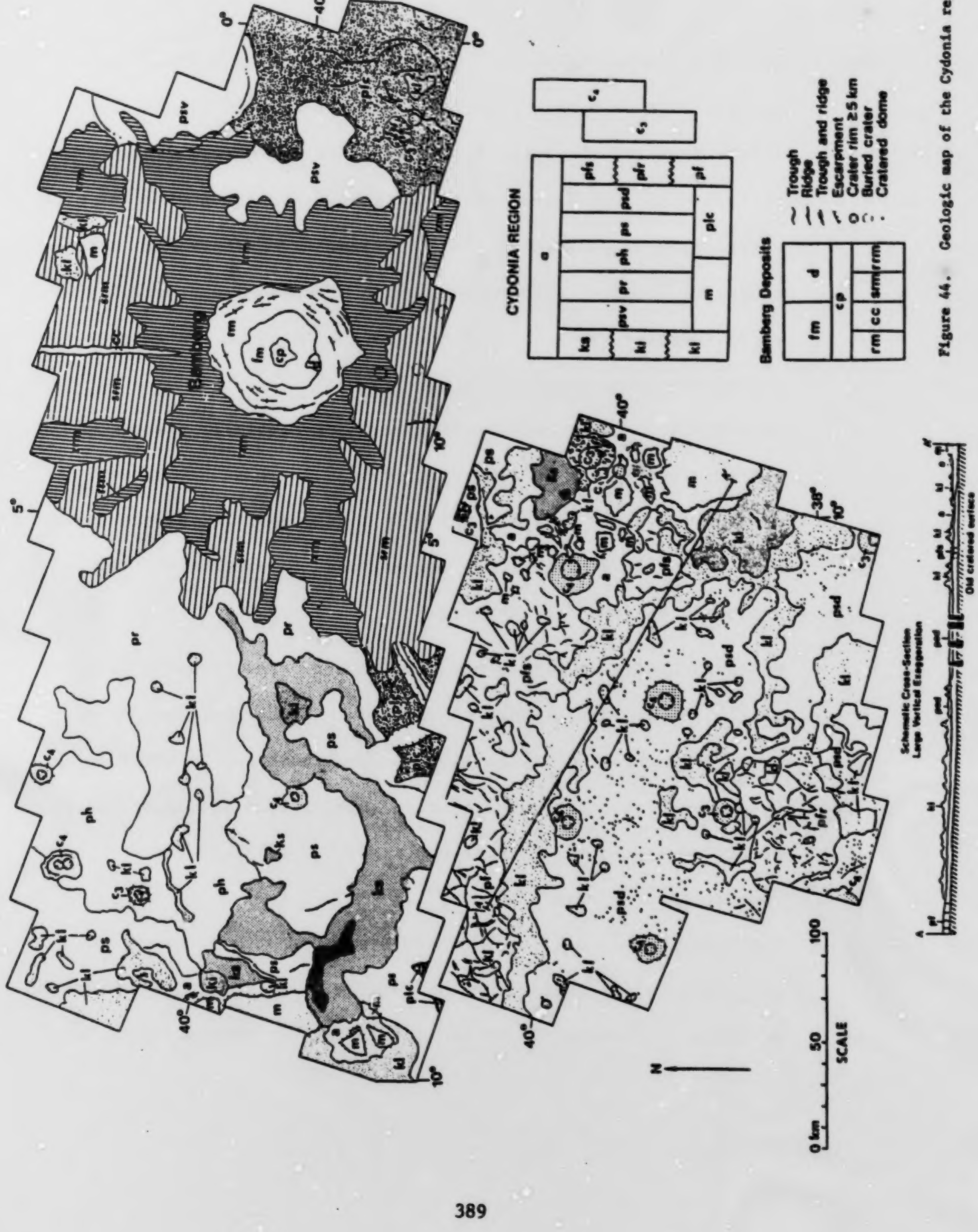
CYDONIA REGION
a
ks
pvv
pr
ph
ps
psd
pfs
kl
m
plc
pfr
pf
c4
c3
Bamberg Deposits
fm
d
cp
rm
cc
sm
rrm
Trough
Ridge
Trough and ridge
Escarpment
Crater rim ≥5 km
Buried crater
Cratered dome
Bamberg
40°
0°
5°
10°
38°
N
0 km
50
100
SCALE
A
A'
Schematic Cross-Section
Large Vertical Exaggeration
Old cratered surface

Figure 44. Geologic map of the Cydonia region.

APPENDIX III - CYDONIA REGION

plc CRATERED PLATEAU MATERIAL - Occurs east of Bamberg crater at eastern edge of mosaic area; intermediate to high albedo; high crater density; characterized by many large degraded impact craters with flat floors; intercrater area relatively smooth with varied albedo; many small (< 1 km diameter) craters and crater clusters; boundary with variegated smooth plains expressed by rapid increase in density of craters and in places, a gentle escarpment; representative image 72A30.

INTERPRETATION: Ancient crustal deposits partially resurfaced by volcanic and eolian depostis; removal of volatile substances trapped in mantle deposits may have caused collapse depressions and debris flows; many small craters and crater clusters may be secondary craters from Bamberg.

m MESA MATERIAL - One large mesa and several smaller mesas lie near 39.5°N, 10°W; intermediate albedo; low crater density; size of mesas range from 10 km^2 to 1400 km^2 and mesas may be several-hundred-meters high; rough texture superimposed on larger mesas; irregular pits occur on mesa centered at 39.85°N, 9.8°W; representative image 72A09.

INTERPRETATION: Outliers and erosional remnants of cratered plateau material that occur approximately 150 km south; breakdown of lenses of layers of ice produced irregular collapse pits.

kl LARGE-KNOB MATERIAL - Occurs mainly to west between 10° - 15°N and 39° - 42°N; irregular knobs and ridges generally 1 - 2 km across; heights of knobs similar to heights of mesas; spacing between knobs ranges from 0.5 - 4 km; low crater density; conical knobs with summit craters occur (Fig. 38b); some knobs appear layered or resting on top of lower mesa; small domes (< 1 km wide) with summit craters occur throughout knobby region; inter-knob area smooth, low albedo; discontinuous, low escarpment forms boundary of knobby terrain with fractured plains material to north; smooth plains material surrounds knobs; representative image 70A05.

INTERPRETATION: Small volcanoes or erosional remnants of cratered plateau material, or both; embayed by smooth plains material.

ki INTERMEDIATE-KNOB MATERIAL - Occurs along west side of large mesa at approximately 39°N, 10°W; forms low irregular hills and knobs; width of knobs ranges from 0.5 - 1.5 km; heights of knobs generally < 500 m, and lower than surrounding large-knobs; inter-knob spacing ranges from 0.2 - 1.5 km; low crater density; representative image 72A09.

INTERPRETATION: Erosional remnants of cratered plateau-material; intermediate size and apparently lower height represent erosion to a lower unit or layer of cratered plateau material.

ks SMALL-KNOB MATERIAL - Occurs primarily in arc east of mesa material at 38.5°N, 8.5°W; forms low, small hills and knobs ranging from 0.1 - 0.8 km across; spacing between knobs very close, generally < 0.1 km; circular pattern of knobs occurs at boundary with smooth plains material; low crater density; representative image 72A14.

INTERPRETATION: Erosional remnants or debris from breakdown of overlying cratered plateau material; locally may represent more resistant remnants of crater rims.

pf FRACTURED PLAINS MATERIAL - Occurs north of large-knob material to west; moderately-high albedo; low crater density; characterized by crudely polygonal pattern of troughs cutting smooth plains; troughs range in width from 0.2 - 1.5 km and are 5 - 10 km apart; depth ranges from 30 ± 10 m to 100 ± 10 m (Pechmann, 1980); wider troughs commonly have flat floors; in some areas, boundary of large-knob material with lower fractured plains material characterized by escarpment (40°N, 12.6°W); escarpment not present in other areas (40°N, 13°W); fractures terminate abruptly at contact with low-albedo inter-knob plains material; representative image 70A03.

INTERPRETATION: Fractured material may be old unit stratigraphically underlying cratered plateau and mesa material (Guest et al., 1977); overlying units subsequently stripped away; alternatively, may be younger plains material; fractures may have occurred after erosional stripping or after deposition and may be result of permafrost activity (Carr and Schaber, 1977), desiccation (Morris and Underwood, 1978), or tectonism (Pechmann, 1980).

pfr RADIALLY FRACTURED PLAINS MATERIAL - Occurs only in southwest, centered at 38°N, 13°W; low albedo; low crater density; fractures range in width from 0.2 - 0.8 km and extend radially outward approximately 25 km from 2 x 6 km ridge; two fracture traces aligned from one side of ridge to the other; numerous small (< 1 km) domes with circular summit depressions occur on radially fractured plains; fractures do not cut knobby material; gradational boundary with surrounding smooth plains; representative image 72A02.

INTERPRETATION: Ridge may be moberg ridge (Allen, 1980) or erosional remnant of plateau material; domes probably volcanic (Allen, 1980; Frey et al., 1979; Wood, 1979); fractures may be tectonic and may have influenced location of intrusions of igneous material.

pfs SUBDUED FRACTURED PLAINS MATERIAL - Occurs north of, and surrounding large knobs west of mesa material between 39.5°N - 41°N and 10° - 12°W; moderately-high albedo; very low crater density; fractures narrow, generally < 0.5 km wide and discontinuous; some small domes < 1 km wide with summit craters; gradational boundary with smooth plains and fractured plains; representative image 70A07 (Fig. 38b).

INTERPRETATION: Volcanic flow rock that fills or partially fills fractures; cratered domes may be small volcanoes.

psv VARIEGATED SMOOTH PLAINS MATERIAL: Occurs only at east margin adjacent to cratered plateau material; high and low albedo; low crater density; smooth, featureless surface; several small (≅ 5 km long) dark streamlined features oriented SE-NW occur close to boundary with cratered plateau material; boundary with cratered plateau marked by rapid decrease in crater density on smooth plains; in places boundary is expressed as gentle escarpment overlooking lower smooth plains; boundary with rough radial material of Bamberg crater is abrupt textural change; representative image 72A29.

INTERPRETATION: Sedimentary blanket and channel deposits originating from highlands to the south during plateau breakdown and scarp retreat.

pr ROUGH PLAINS MATERIAL - Occurs between 39° - 42° N and 5° - 8° W; low albedo; high density of small craters < 1 km diameter; surface appears rough at high resolution; gradational boundaries with adjacent hilly plains material and rough radial material; more distinct textural boundary with smooth radial material; representative image 70A21.

INTERPRETATION: Plains of unknown origin with many secondary craters from adjacent c_3 impact crater, Bamberg; presence of many secondary craters makes crater counts unreliable.

ph HILLY PLAINS MATERIAL: Occurs between 39° - 41.5°N and 7° - 9°W; low albedo; low crater density; characterized by high density (30 - 40/100 km^2) of small ($<$ 500 wide) hills; many hills appear to have summit craters although craters are at limit of resolution; boundary with smooth plains is distinct albedo and morphologic change; gradational with rough plains; representative image 70A15.

INTERPRETATION: Volcanic plains with small cinder cones (Wood, 1979) or pseudocraters (Frey et al., 1979; Lucchitta, 1981); alternatively, hilly plains may represent fields of pingos (Wood, 1979).

ps SMOOTH PLAINS MATERIAL - Occurs in several regions between 38° - 40°N and 7° - 11°W; intermediate albedo; very low crater density; smooth, featureless plains; most impact craters < 1 km diameter; 6 conical hills approximately 2 km diameter occur on smooth plains between 38.8° - 39.2°N and 8.5° - 9°W; some hills appear to have summit craters; in same area a 25 km-long, ≈ 500 m-wide, straight trough oriented NW-SE traverses smooth plains; another more sinuous trough of similar width oriented approximately parallel occurs 30 km west; trough originates from 2 km-wide conical hill with summit depression and meanders northward approximately 60 km through narrow region of smooth plains bounded on both sides by knobby terrain; boundary with knobby terrain in most places gradational; representative image 72A12.

INTERPRETATION: Volcanic and eolian plains; conical hills may be small volcanoes; troughs may be collapsed lava tunnels or tubes analogous to lunar sinuous rilles (Greeley and Spudis, 1981).

psd SMOOTH PLAINS MATERIAL WITH DOMES - Occur mainly west of mesa material between 38° - 40°N and 10° - 13°W; low albedo; moderate crater density; relatively smooth plains with many small

(< 1 km across) domes with summit craters; gradational boundary with subdued fractured plains and with radially fractured plains; dark smooth plains material and domes surround knobs; representative image 70A04.

INTERPRETATION: Volcanic and eolian deposits; small domes may be cinder cones, pingos (Wood, 1979), or pseudocraters (Frey et al., 1979; Lucchitta, 1981).

a APRON MATERIAL - Surrounds knobs and occurs at base of mesa escarpments; intermediate albedo; very low crater density; valley fill between knobs and mesas commonly has ridges and troughs parallel to escarpment; distal margins of apron material lobate; representative image 70A11.

INTERPRETATION: Lobate debris flows from escarpment; ridges and troughs parallel to escarpment are compressional features from flows (Squyres, 1978); young age indicated by scarcity of impact craters.

Crater Material

All craters mapped believed to have been produced by impact; subdivisions based on morphologic characteristics believed to reflect relative age.

c_4 YOUNG CRATER MATERIAL - Sharp, complete rim crests; steep walls; deep rough floors; bowl shaped; extensive ejecta deposits; representative image 70A02.

INTERPRETATION: Relatively recent impact-crater material.

c_3 MODERATELY YOUNG CRATER MATERIAL - Rim crests high, complete; walls relatively steep; floors may be rough and lower than adjacent terrain; ejecta deposits less extensive than c_4 craters; representative image 70A12.

INTERPRETATION: Moderately young but slightly degraded impact-crater material.

Bamberg Deposits

cp	CENTRAL PEAK MATERIAL - Peak centrally located in Bamberg crater; diameter approximately 10 km; summit pit diameter approximately 6 km; no stratification observed, representative image 72A25. INTERPRETATION: Formed by elastic rebound following impact; central pit may be collapse pit created by release of trapped volatile material.
fm	FLOOR MATERIAL - Smooth and relatively featureless; varied albedo; no impact craters; terminates at ridges of rim material; representative image 72A25. INTERPRETATION: Eolian or slumped material fills interior of crater.
d	DUNE MATERIAL: Series of dark parallel ridges; occurs near south margin of floor material; representative image 72A25. INTERPRETATION: Small field of transverse dunes.
rm	CRATER RIM MATERIAL - Consists of many ridges and hills; rim material may be as wide as 18 km with very low crater density; representative image 72A25. INTERPRETATION: Rim formed during impact process.
cc	CRATER CHAIN MATERIAL - Extends north of Bamberg crater for approximately 70 km; maximum width 3 km; consists of 40 small craters or depressions (Mouginis-Mark, 1979); representative image 70A27. INTERPRETATION: Chain of secondary craters formed during impact.

rrm	ROUGH RADIAL MATERIAL - Forms rough surface radial to Bamberg crater; extends outward up to 3 crater diameters from rim material; many closely spaced pits and depressions; boundary with smooth radial material is abrupt textural change; representative image 70A25. INTERPRETATION: Ejecta deposit of Bamberg crater; some flow lobes; many secondary craters and crater clusters produced by impact.
srm	SMOOTH RADIAL MATERIAL - Forms relatively smooth surface radial to Bamberg crater; extends outward 2 - 3 crater diameters from crater-rim material; varied albedo; low crater density; representative image 70A27. INTERPRETATION: Ejecta deposits of Bamberg crater possibly more volatile-rich than rough radial material and thus with a smoother surface.

APPENDIX IV - MARE ACIDALIUM QUADRANGLE

Crater densities are given for units for which crater counts have been made. Number refers to the cumulative number of craters 1 km in diameter and greater per 10^6 km^2 as determined from crater size-frequency distribution curves. All numbers were derived directly from the size-frequency curves and not extrapolated. Crater densities $> 1,000/10^6$ km^2 are considered moderate; crater densities $\leq 1,000/10^6$ km^2 are considered low.

Plateau Materials

plc CRATERED PLATEAU MATERIAL - Occurs in southeast corner of quadrangle between lat 30° - 40°N, long 0° - 20°W; low albedo, moderate crater density (1460 craters $\geq$ 1km/10^6 km^2); characterized by many large (up to 120 km diameter), flat floored, c_1 and c_2 craters; intercrater areas contain irregular depressions and low escarpments; irregular depressions are common near plateau-plains boundary; escarpment commonly marks boundary with lower plains units; representative image 561A07 (Fig. 11).

INTERPRETATION: Ancient crustal deposits partially resurfaced by volcanic and eolian material that also fills large craters.

pldf DISSECTED AND FRACTURED PLATEAU MATERIAL - Occurs between lat 46° - 49°N, long 22° - 28°W, intermediate to high albedo; low crater density (few craters observed); relatively smooth surface cut by numerous fractures and troughs trending north-south; fracture widths up to 2 km; fracture lengths up to 50 km; escarpment marks the boundary of plateau unit in some places; other areas, sharp change from high-albedo plateau material to low-albedo plains material; representative image 670B16 (Fig. 12).

INTERPRETATION: Remnants of a higher unit that earlier may have covered the region; large circular depressions mark the location of degraded and filled craters; resurfaced by eolian and volcanic materials; subsequently disrupted by faulting.

plrg RUGGED PLATEAU MATERIAL - Occurs in western region between lat 31° - 52°N, long 50° - 60°W; intermediate albedo; moderate crater density (1150 craters ≥ 1 km/10^6 km^2); forms rough surface with numerous shallow, flat-floored c_1 craters up to 90 km diameter; intercrater area contains many rimless, irregular depressions and escarpments; several channel-like depressions trending north-south with openings to the north; northeast trending fractures; boundary with surrounding smoother units generally morphologically distinct; representative image 704B38-39 (Fig. 13).

INTERPRETATION: Volatile-rich volcanic flow rock and eolian material resurfacing ancient crustal deposits; melting of ground ice caused local collapse and formation of depressions that were later modified by the wind; local disruption by faults of the Tempe Plateau.

plr RIDGED PLATEAU MATERIAL - Occurs between lat 31° - 40°N, long 50° - 60°W; intermediate albedo; moderate crater density (1300 craters $\geq$ 1 km/10^6 km^2); forms smooth surface with north-northwest trending mare-type ridges, oriented similarly to those ridges in MC-10; few fracture traces; boundary with rugged plateau material is morphologic change from smooth, ridged plateau surface to rough, rugged plateau surface; representative image 668A06 (Fig. 15a).

INTERPRETATION: Volcanic flow rock with mare-type ridges; locally disrupted by faults of the Tempe Plateau.

plf FRACTURED PLATEAU MATERIAL - Occurs in western region between lat 48° - 52°N, long 52° - 60°W; intermediate albedo; low crater density (700 craters $\geq$ 1 km/10^6 km^2); relatively smooth surface cut by many northeast trending flat-floored depressions up to 17 km wide; escarpment generally forms boundary with lower plains material; distinct morphologic boundary between relatively smooth fractured plains material and rugged plains material; representative image 61B52 (Fig. 17).

INTERPRETATION: Volcanic flow rock and eolian material cut by many faults of Tempe Plateau.

pll LOWER PLATEAU MATERIAL - Occurs in small patches between lat 30° - 36°N, long 49° - 60°W; varied albedo; few craters observed; forms rough surface at elevation intermediate between smooth plains and plateau units; cut by channels creating mid-channel, streamlined, erosional remnants up to 40 km long; boundary with smooth plains commonly marked by low escarpment with lobate pattern in places (Fig 18b); escarpment marks boundary with higher plateau units; representative image 668A27.

INTERPRETATION: Remnants of a lower, more resistant plateau layer exposed and eroded by fluvial activity; may also be eroded lava flows or plains material.

Plains Materials

pm MOTTLED PLAINS MATERIAL - UNDIVIDED - Covers large area between lat 40°N - 63°N, long 15° - 60°W; varied albedo; low crater density (550 craters $\geq$ 1 km/10^6 km^2); high-albedo zones extend out 2-3 crater diameters; low-albedo intercrater plains; small craters filled or partially filled with light material; distinct northwest-southeast eolian grain indicated by wind plumes and streaks; boundary with other mottled plains units gradational; boundary with smooth plains marked by change from intermediate-albedo smooth plains material to low-albedo mottled plains material; representative image 672B74 (Fig. 21a).

INTERPRETATION: Volcanic and eolian material; former blanket of light material now being stripped away by wind; ejecta blankets may act as trap for fine-grained windblown particles.

pmh HUMMOCKY MOTTLED PLAINS MATERIAL - Occurs in northern part of quadrangle between lat 58° - 65°N, long 5° - 60°W; extends northward into MC-1; varied albedo; low crater density (675 craters $\geq$ 1 km/10^6 km^2); high albedo zones surround impact craters; intercrater plains characterized by low dark hummocks or knobs (generally < 1 km wide) surrounded by lighter material; many craters are filled or partially filled with light material; gradational boundary with all surrounding units; representative image 672B77 (Fig. 23a).

INTERPRETATION: Volcanic and eolian plains; small dark knobs or hummocks are volcanic, plutonic, or permafrost features such as pingos; alternatively, knobs may represent a lower hilly, irregular surface mantled with light material leaving only dark summits of once-buried hills exposed; ejecta blankets may act as trap for fine-grained, light-colored windblown material.

pmp PATTERNED MOTTLED PLAINS MATERIAL - Occurs between lat 40° - 50°N, long 0° - 30°W; varied albedo; low crater density (1000 craters ≥ 1 km/10^6 km^2); high-albedo ejecta blankets extend outward 2-3 crater diameters; intercrater region very low albedo; crudely polygonal pattern of troughs; troughs generally < 10 km long, < 1 km wide, and $\approx$ 100 m deep; pedestal craters common; small (< 1 km wide) domes with summit craters common; boundary with all surrounding units gradational; representative image 32A18 (Fig. 24a).

INTERPRETATION: Volcanic plains; domes are small cinder cones; high-albedo zones surrounding impact craters are result of impact excavating lower material having high albedo; troughs originated through permafrost (Carr and Schaber, 1977), desiccation (Morris and Underwood, 1978), or tectonic (Pechmann, 1980) processes.

pmps SUBDUED PATTERNED MOTTLED PLAINS MATERIAL - Occurs around dissected and fractured plateau near center of quadrangle; crater density observed to be similar to patterned mottled plains; low albedo; relatively smooth dark plains cut by many discontinuous, arcuate troughs generally < 1 km wide and averaging 5 km long;

small (< 1 km) domes with summit craters common; boundary with patterned mottled plains gradational; boundary with higher dissected and fractured plateau marked by escarpment; representative image 35A41 (Fig. 26b).

INTERPRETATION: Volcanic flow rock; flow fronts and pressure ridges occur in several places; domes are small cinder cones; volcanic material fills or partially fills pre-existing troughs.

pf FRACTURED PLAINS MATERIAL - Occurs between lat 40° - 43°N, long 10° - 15°W; intermediate albedo; no craters larger than 5 km; characterized by crudely polygonal pattern of troughs cutting smooth plains; trough widths range from 0.2-2.0 km, are as long as 20 km, and are 5-10 km apart; depth of troughs range from 30-100 m (Pechmann, 1980); wider troughs mostly have flat floors; decrease in trough abundance marks boundary with surrounding units; representative image 32A36.

INTERPRETATION: Fractured materials may be old unit stratigraphically underlying the plateau materials exposed by scarp retreat; alternatively, may be young volcanic and eolian material; fractures are post depositional and are the result of tectonism (Pechmann, 1980), desiccation (Morris and Underwood, 1978), or permafrost activity (Carr and Schaber, 1977).

pk KNOBBY PLAINS MATERIAL - Occurs in the northeast corner of quadrangle, lat 52° - 65°N, long 0° - 15°W; extends eastward into MC-5; intermediate to high albedo; low crater density (750 craters ≥ 1 km/10^6 km^2); small craters (< 2 km) mostly filled with light material; ejecta blankets of 2-10 km craters obscured by light material; numerous small (< 1 km) irregularly spaced knobs give surface rough appearance; boundary with mottled plains material marked by distinct albedo change from high-albedo knobby plains to low-albedo mottled plains; representative image 673B08 (Fig. 30a).

INTERPRETATION: Volcanic plains blanketed with light-colored eolian material; knobs are eroded volcanic material or partially buried impact craters.

ps SMOOTH PLAINS MATERIAL - Covers large portion of southern region between lat 30° - 40°N, long 10° - 50°W; intermediate to high albedo; low crater density (760 craters $\geq$ 1 km/10^6 km^2); patches of knobby terrain material are scattered throughout smooth plains; large (up to 120 km) circular features are outlined by knobs; grooves and streamlined features oriented east and northeast are common to the southwest; boundary with higher plateau units marked by escarpment, boundary with mottled plains marked by albedo change form intermediate- to high-albedo smooth plains to low-albedo mottled plains; representative image 558A07 (Fig. 31b).

INTERPRETATION: Eolian fill and, especially to south, alluvial fill from large outflow channels to south and west; locally may be volcanic material; overlies older cratered surface; shifting eolian material results in varied albedo.

psp PATTERNED SMOOTH PLAINS MATERIAL - Occurs between lat 37° - 40°N, long 18° - 31°W; intermediate albedo; low crater density assumed to be similar to smooth plains materials; characterized by subdued pattern of discontinuous troughs only a few hundred meters wide and averaging 5 km long; high-albedo wind streaks associated with many craters; decrease in fracture abundance marks boundary with smooth plains material; change from intermediate albedo to low albedo marks the boundary with mottled plains; representative image 597A05 (Fig. 35).

INTERPRETATION: Thin mantle of light-colored eolian material blanketing patterned mottled plains, partially filling troughs; mantle thickness increases to the south; alternatively, fractures may be result of permafrost activity (Carr and Schaber, 1977), desiccation (Morris and Underwood, 1978), or tectonic activity (Pechmann, 1980) and may have occurred after smooth plains materials were emplaced.

pv VARIEGATED PLAINS MATERIAL - Occurs between lat 38° - 46°N, long 0° - 10°W; varied albedo; low crater density (880 craters $\geq$ km/10^6 km^2); smooth, featureless plains; patchy albedo pattern; scattered occurrences of small (< 1 km wide) domes with summit craters; small patches of knobs and mesas occur; boundary with patterned mottled plains occurs where troughs begin; boundary with cratered plateau changes from rough plateau material to smoother plains material; representative image 36A44 (Fig. 36a).

INTERPRETATION: Volcanic plains; domes may be cinder cones; alternatively, these plains may consist of alluvial and eolian material; small knobs and mesas erosional remnants of plateau material to south.

Other Materials

d DARK MATERIAL - Very low-albedo material; forms patches in and around craters, in valleys, along escarpments, and on plains units; representative image 558A15 (Fig. 19).

INTERPRETATION: Eolian material aligned with present wind circulation; locally may be small dune fields.

lt LIGHT MATERIAL - High-albedo material; forms patches near plateau-plains boundary; representative image 669B76 (Fig. 37b).

INTERPRETATION: Eolian and alluvial material.

ch CHANNEL MATERIAL - Occupies elongate depressions near plains-plateau boundary in western region; high albedo; very few craters; representative image 669B76 (Fig. 37b).

INTERPRETATION: Alluvial deposits of former streams.

k KNOBBY TERRAIN MATERIAL - Irregular hills or knobs rising above level of plains; may be up to 15 km across and 3000 km high but generally smaller; locally knobs form circular pattern; at high resolution, some knobs appear to have summit craters; representative image 70A09 (Fig. 38b).

INTERPRETATION: Erosional remnants of higher surface of plateau material; in some areas may represent crater rims and more resistant facies of lower cratered unit; locally may represent exposed igneous intrusions or small volcanic cones or mountains.

Crater Materials

All craters mapped believed to have been produced by impact; craters with diameters < 10 km not mapped; subdivisions based on morphologic characteristics believed to reflect relative age.

c_4	YOUNG CRATER MATERIAL - Sharp, complete rim crest; central peak; steep walls; deep rough floors; extensive ejecta deposits; representative image 558A31 (Fig. 33a). INTERPRETATION: Relatively recent impact-crater material.
cr	CRATER RAY MATERIAL - High-albedo material that surrounds several large (> 20 km) c_4 craters on mottled plains (units pm, pmh, pmp); representative image 670B36. INTERPRETATION: Fine-grained, light-colored primary and secondary ejecta material.
c_3	MODERATELY YOUNG CRATER MATERIAL - Rim crests high, complete; may have central peak; walls relatively steep; floor may be rough and lower than adjacent terrain; ejecta deposits less extensive than c_4 craters; representative image 673B60 (Fig. 36b). INTERPRETATION: Relatively young but slightly degraded impact-crater material.
cp	CENTRAL PEAK MATERIAL - Rugged, irregular peaks centrally located in c_3 and c_4 craters; representative image 597A46. INTERPRETATION: Formed by rebound following impact.

cpd	PEDESTAL CRATER MATERIAL - Small (generally < 5 km) bowl-shaped craters; ejecta extends outward 3 crater diameters; ejecta forms platform that stands above surrounding terrain; convex slope at distal edge of ejecta blanket; representative image 26A56 (Fig. 6b). INTERPRETATION: Impact crater with associated viscous ejecta flow (flow too viscous to form lobes; Mutch and Woronow, 1980); alternatively may represent preferential retention of eolian debris in and around craters as intercrater debris is eroded away (Carr, 1981).
c_2	MODERATELY OLD CRATER MATERIAL - Rim crests low, rounded, complete or imcomplete; no central peak; floors generally flat; may be partially flooded or filled with younger material; ejecta deposits show little or no surface texture, or are partially stripped away; representative image 672B56 (Fig. 30b). INTERPRETATION: Moderately old and partially degraded impact-crater material.
c_1	OLD CRATER MATERIAL - Rim crest low, incomplete, or nearly absent; no central peak; shallow flat floors generally filled with younger material; commonly forms rugged and partly buried rings; little or no ejecta deposits; representative image 218S19 (Fig. 10). INTERPRETATION: Oldest, highly degraded impact-crater material.

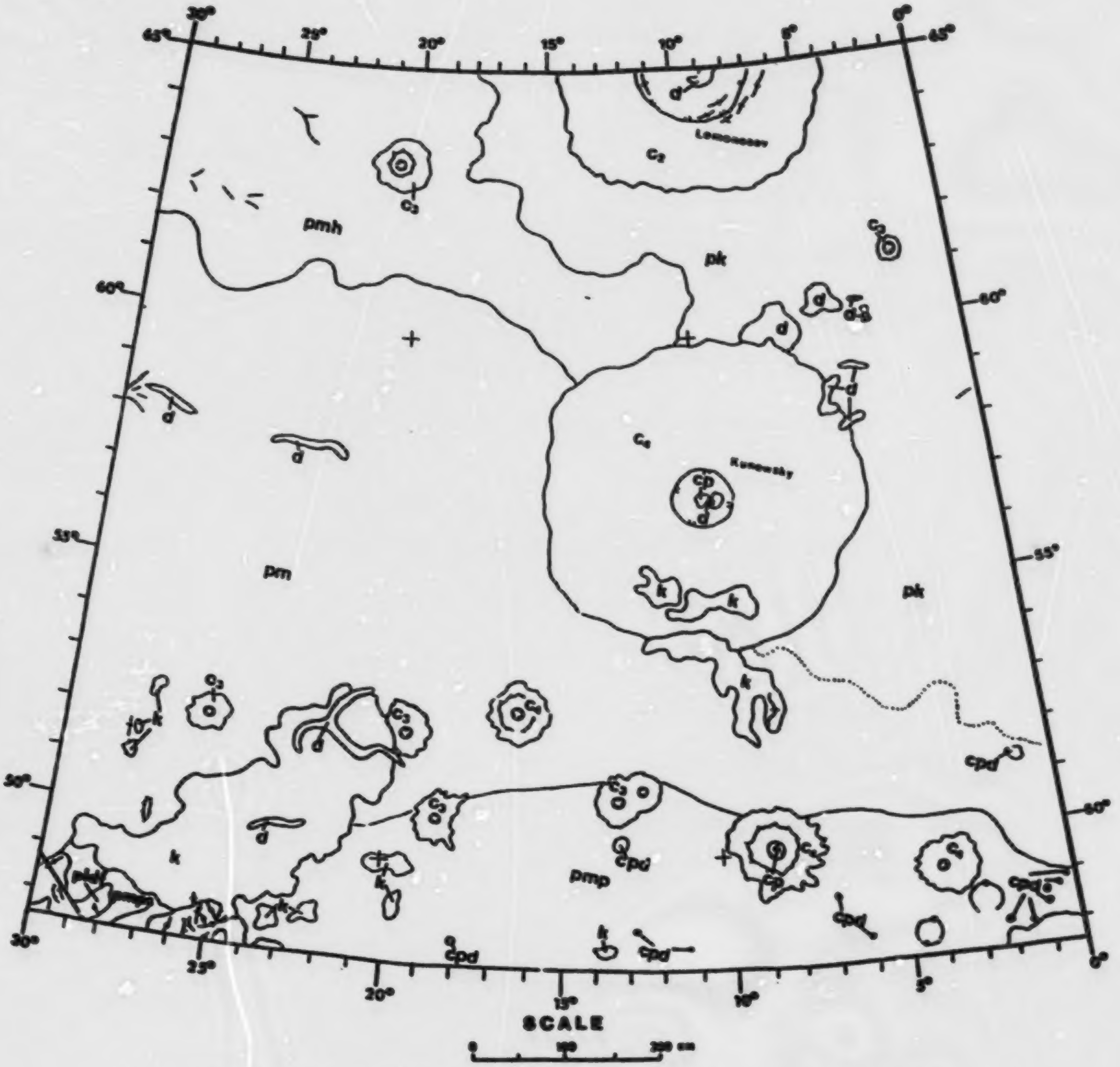
65°
30°
25°
20°
15°
10°
5°
0°
65°
60°
55°
50°
Lomonosov
C2
C3
pmh
pk
d
C4
Kunowsky
cp
pm
k
cpd
pmp
SCALE
0
100
200 km

GEOLOGIC MAP OF MARE ACIDALIUM QUADRANGLE - NE

ORIGINAL PAGE IS
OF POOR QUALITY

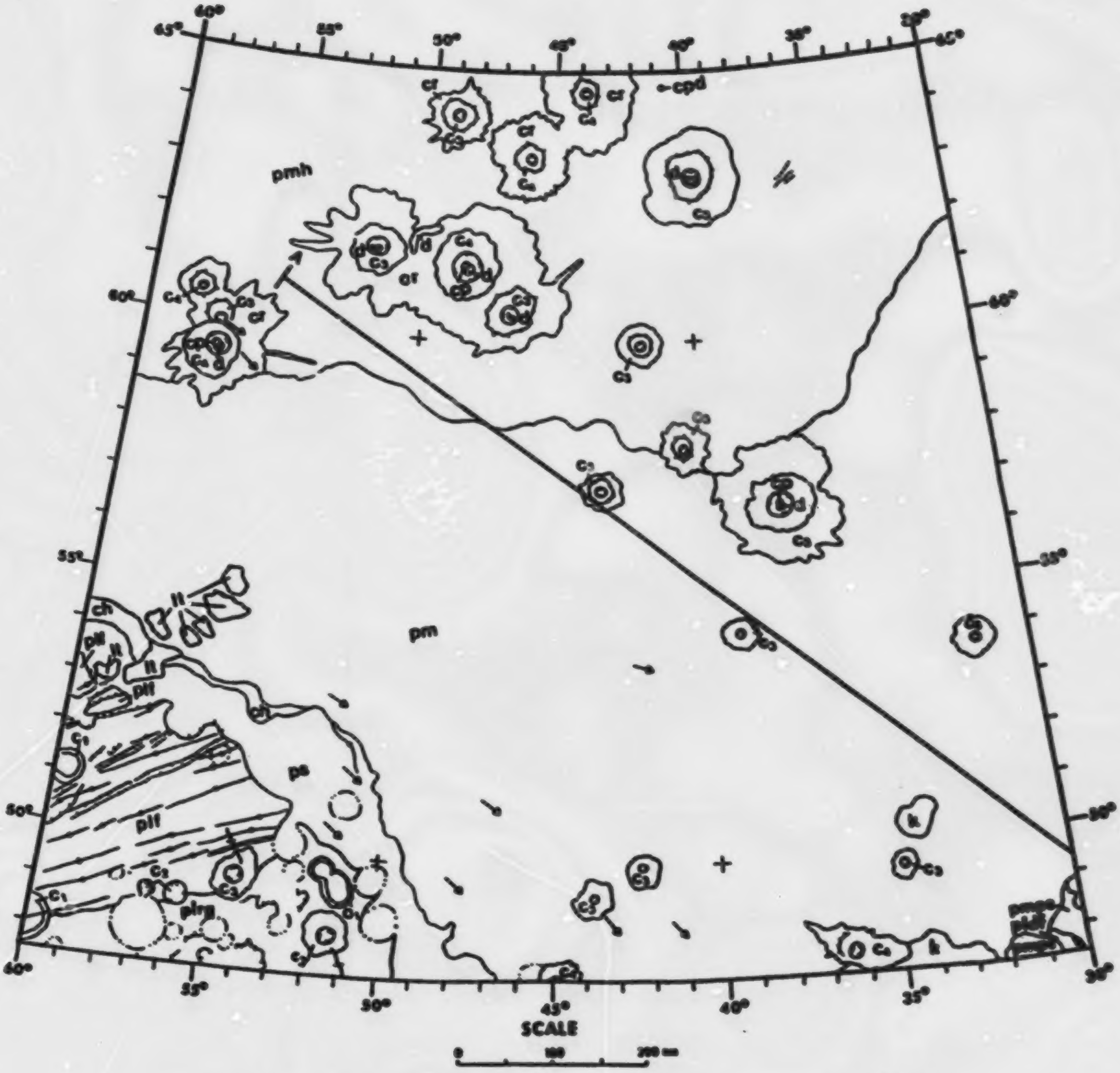
65°
60°
55°
50°
45°
40°
35°
30°
60°
55°
50°
pmh
pm
ps
plf
ch
ll
plrg
cf
cpd
C3
C4
C1
C2
k
pmpa
SCALE
0
100
200 km

GEOLOGIC MAP OF MARE ACIDALIUM QUADRANGLE - NW

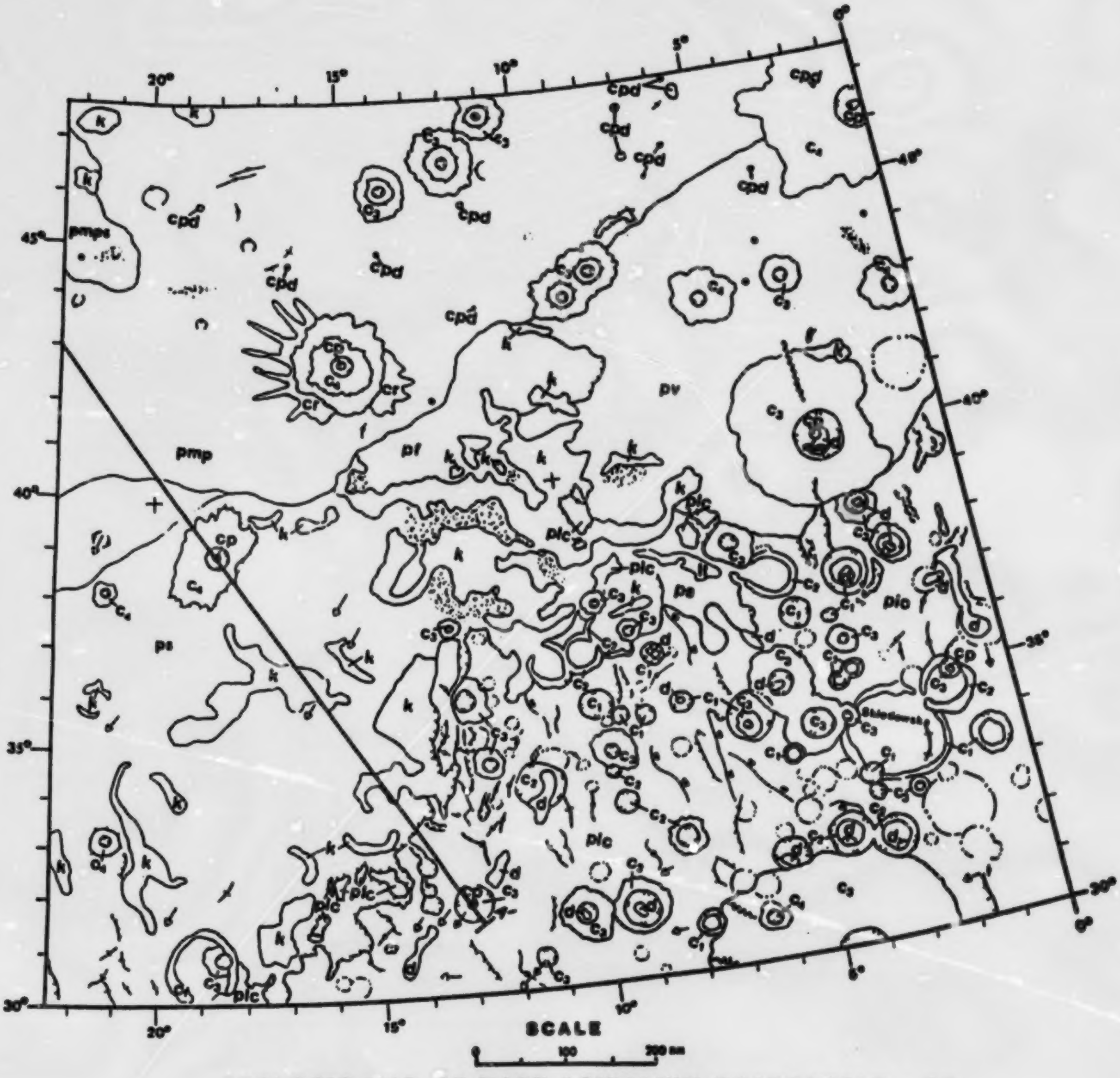
20°
15°
10°
5°
0°
45°
40°
35°
30°
cpd
pmps
pmp
pv
pf
plc
ps
k
cp
cr
d
Stiedowsky
SCALE
0
100
200 km

GEOLOGIC MAP OF MARE ACIDALIUM QUADRANGLE - SE

ORIGINAL PAGE IS
OF POOR QUALITY

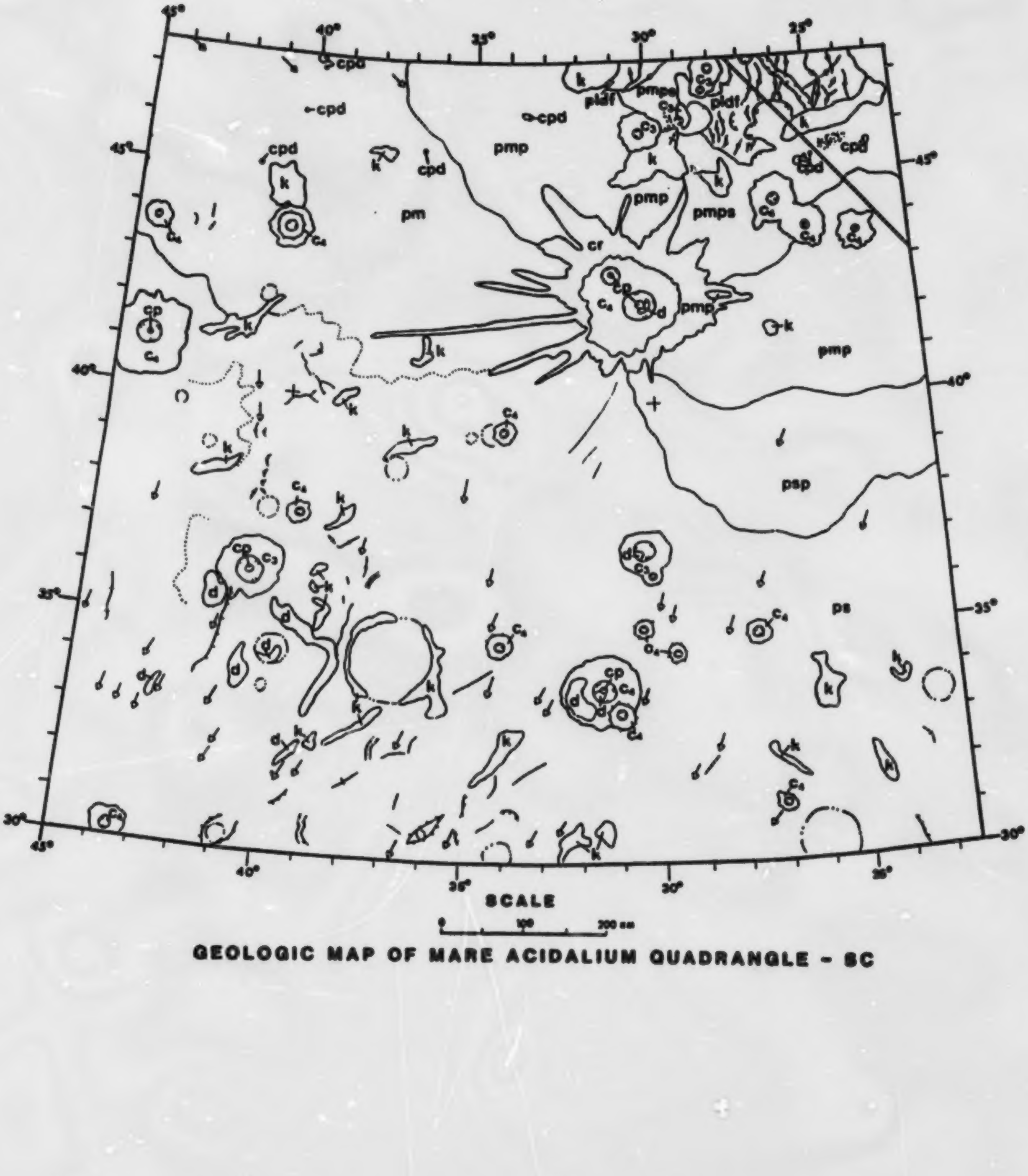
45°
40°
35°
30°
25°
cpd
pmp
pm
pmps
pldf
k
cr
cp
d
psp
ps
C₃
C₄
SCALE
0
100
200 km

GEOLOGIC MAP OF MARE ACIDALIUM QUADRANGLE - SC

ORIGINAL PAGE IS
OF POOR QUALITY

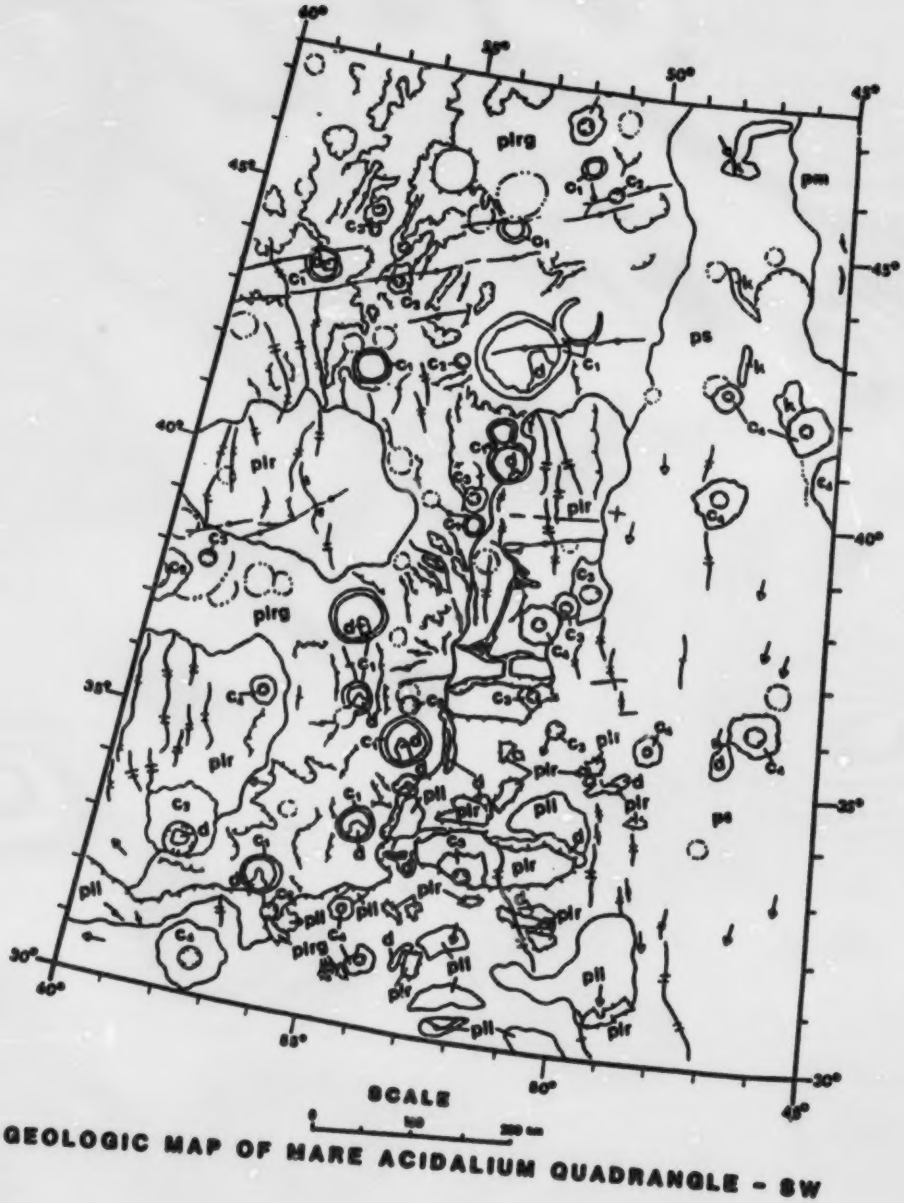
40°
50°
45°
40°
35°
30°
60°
55°
plrg
pm
ps
plr
pll
c1
c2
c3
c4
d
k
SCALE
0
100
200 km

GEOLOGIC MAP OF MARE ACIDALIUM QUADRANGLE - SW

ORIGINAL PAGE IS
OF POOR QUALITY

CORRELATION OF MAP UNITS

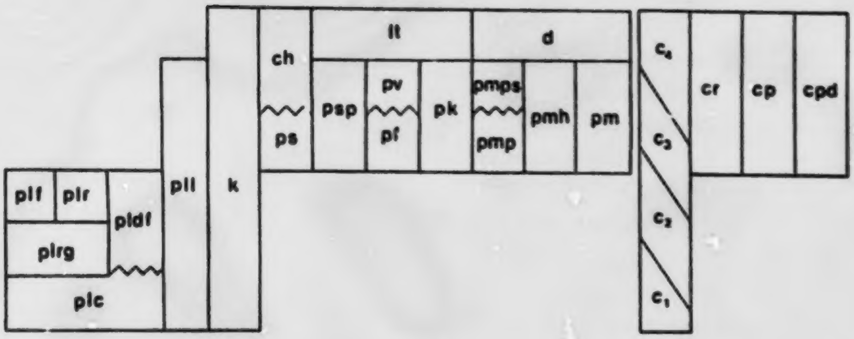
plf
plr
pldf
pll
k
plrg
plc
ch
ps
lt
psp
pv
pf
pk
d
pmps
pmp
pmh
pm
c_4
c_3
c_2
c_1
cr
cp
cpd

MAP UNITS

PLAINS MATERIALS

pv	Variegated Plains Material
psp	Patterned Smooth Plains Material
ps	Smooth Plains Material
pk	Knobby Plains Material
pf	Fractured Plains Material
pmps	Subdued Patterned Mottled Plains Material
pmp	Patterned Mottled Plains Material
pmh	Hummocky Mottled Plains Material
pm	Mottled Plains Material - Undivided

PLATEAU MATERIALS

plf	Fractured Plateau Material
plr	Ridged Plateau Material
plrg	Rugged Plateau Material
pll	Lower Plateau Material
pldf	Dissected and Fractured Plateau Material
plc	Cratered Plateau Material

OTHER MATERIALS

d	Dark Material
lt	Light Material
ch	Channel Material
k	Knobby Terrain Material

CRATER MATERIALS

c_4	Young Crater Material
cr	Crater Ray Material
c_3	Moderately Young Crater Material
cp	Central Peak Material
cpd	Pedestal Crater Material
c_2	Moderately Old Crater Material
c_1	Old Crater Material

14

SYMBOLS

∼ - -	Contact; albedo contact dotted
┴┴┴	Steep scarp; used as contact in places; hachures point downslope
┬	Gentle scarp; barb points downslope
∼	Narrow depression; graben, channel, trough
—+—	Low ridge
—‡—	Mare-type ridge
—	Lineament; topographic or tonal
⋯	Sharp albedo variation
→	Light wind streak; arrow shows orientation of streak
→	Dark wind streak; arrow shows orientation of streak
≡	Dune field
•	Mesa with ridge or knob; may be tablemountain
▨	Region with cratered domes <1 km diameter; domes may be volcanic cones
○	Crater rim crest ≥10 km diameter; hachures point toward center of depression
◌	Partially buried or highly degraded crater rim crest
∘∘∘	Secondary crater chain
⬭	Irregular, rimless depression; hachures point toward center of depression

★U.S. GOVERNMENT PRINTING OFFICE:1984 -739 -010/ 5 REGION NO. 4

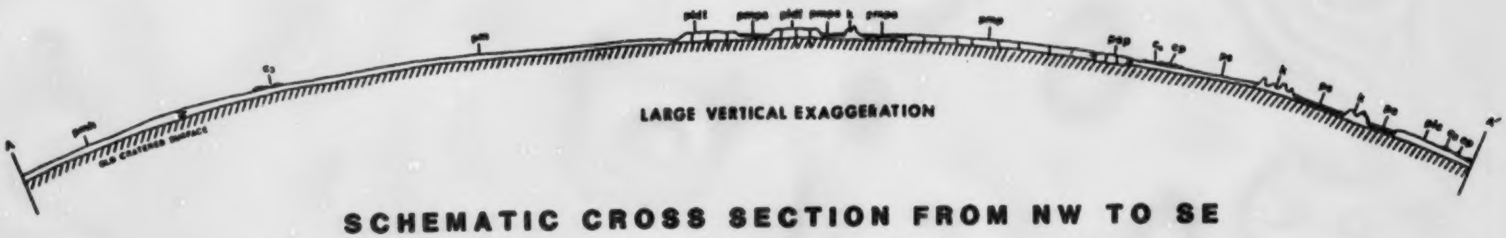
A
OLD CRATERED SURFACE
LARGE VERTICAL EXAGGERATION
A'

SCHEMATIC CROSS SECTION FROM NW TO SE